

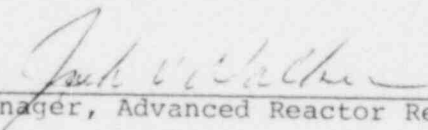
NUREG/CR-0983
SAND79-1566
Vol. 9
R-7

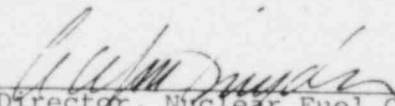
ADVANCED REACTOR SAFETY RESEARCH COMBINED
QUARTERLY REPORT
OCTOBER 1978-MARCH 1979

Advanced Reactor Research Department
Sandia National Laboratories, Albuquerque, New Mexico 87185

Printed: August 1980

APPROVED:


Manager, Advanced Reactor Research


Director, Nuclear Fuel Cycle Programs

Sandia National Laboratories
Albuquerque, New Mexico 87185
operated by
Sandia Corporation
for the
U. S. Department of Energy

Prepared for
Division of Reactor Safety Research
Office of Nuclear Regulatory Research
U. S. Nuclear Regulatory Commission
Washington, DC 20555
Under Interagency Agreement DOE 40-550-75
NRC FIN Nos. A-1016, -1172, -1180,
-1186, -1054, -1181, -1032, -1058, -1198, -1197

8011040342

CONTENTS

	<u>Page</u>
FOREWORD	13
EXECUTIVE SUMMARY	15
1. ENERGETICS	45
1.1 Prompt Burst Energetics (PBE)	45
1.2 Irradiated Fuels Response	66
2. FUEL DYNAMICS	101
2.1 Transition Phase	101
2.2 Initial and Extended Fuel Motion (IEFM)	128
2.3 Fuel-Motion Detection (FMD)	146
3. CORE DEBRIS BEHAVIOR - INHERENT RETENTION	161
3.1 Molten-Core Containment	161
3.2 PAHR Debris Bed	203
3.3 PAHR Molten Pool	219
3.4 Containment Analysis	225
3.5 Fragmentation	229
3.6 Sodium Containment and Structural Integrity	234
3.7 Aerosol Source Normalization	247
4. ELEVATED TEMPERATURE DESIGN ASSESSMENT	253
4.1 Uniaxial Creep-Fatigue Behavior Program	253
4.2 Creep-Fatigue Damage Analysis	259
4.3 Structural Analysis	263
4.4 Structural Evaluation	264
4.5 General	266
5. LMFBR ACCIDENT DELINEATION	267
5.1 Introduction	267
5.2 Engineered Systems	267
5.3 Accident Phenomenology	270
5.4 Postaccident Phenomenology	274

CONTENTS (cont)

	<u>Page</u>
6. TEST AND FACILITY TECHNOLOGY	277
6.1 ACRR Fuel-Motion Detection System	277
6.2 Large-Scale Test Assessment	290
6.3 ACRR Status	297

ILLUSTRATIONS

Figure

1.1-1	PBE Single-Pin Capsule	48
1.1-2	Energy Deposition in PBE Experiments as a Function of Polyethylene Thickness	49
1.1-3	Energy Deposition Profile for 14% Enriched Fuel With 0.063-in. Polyethylene	49
1.1-4	CHARTD Model of PBE Vessel	50
1.1-5	PBE Vessel Response - Effective Stress vs Time (inner wall)	51
1.1-6	PBE Vessel Response - Position vs Time (inner wall)	52
1.1-7	PBE Vessel Response - Radial Stress as a Function of Radius	52
1.1-8	PBE Vessel Response to 250 MPa Spike-Effective Stress vs Time (inner wall)	53
1.1-9	PBE Vessel Response to 250 MPa Spike Position vs Time (inner wall)	54
1.1-10	PBE Vessel Response to 250 MPa Spike-Radial Stress as a Function of Radius	54
1.1-11	Tentative PBE Seven-Pin Capsule	57
1.1-12	PBE-5S Simmer Model	61
1.1-13	Comparison of the Pressure Trace Characteristics for the First 1.5 ms	62
1.1-14	Pressure vs Time in Sodium Channel (0 to 1 ms)	64

ILLUSTRATIONS (cont)

<u>Figure</u>	<u>Page</u>
1.1-15 Pressure vs Time in Sodium Channel (1 to 2 ms)	64
1.2-1 Slab Geometry	70
1.2-2 Droplet Geometry	70
1.2-3 Illustration of Eq (1.1)	73
1.2-4 Calculated Maximum CO-Partial Pressures vs Time for Different Capsule Conditions and Fuel Geometries	79
1.2-5 Oxygen Diffusion in the Condensed Phase	80
1.2-6 CO Film Formed as Oxygen Diffusion Proceeds	80
1.2-7 System of Homogeneously Distributed Liquid-Fuel Droplets of Uniform Radius R_d	83
1.2-8 FGR 39* Adjusted to Exclude Early Gas Release	90
1.2-9 Comparison of Energy Required and Energy Available for Crack Propagation Between Intragranular Bubbles in FD 1.6	92
1.2-10 Views of Inner Can, Internal Parts, Image of Fuel (front and rear)	95
1.2-11 Comparison of FISCAS Prediction of Gas Release to FGR 39 Test Data	98
2.1-1 Schematic of Liquid-Liquid Ablation Experiment Apparatus	103
2.1-2 Observed Melting Pattern During Liquid-Liquid Ablation Experiments	104
2.1-3 Development of Flow Channel in Ice Pipe	107
2.1-4 Closeup of Inlet Section: Test 31VU-005-1/4	108
2.1-5 Flow at the Ice-Pipe Outlet, Test 31HO-006-1/4, Horizontal Flow	110
2.1-6 Interfacial Waves in Downward Flow Near the Flooding Limit: Test 31VD-004-1/4	113
2.1-7 Typical Temperature Trace for an Experiment	116

ILLUSTRATIONS (cont)

<u>Figure</u>		<u>Page</u>
2.1-8	Semilog Plot of Temperature vs Distance for a Test in Upward Vertical Flow	116
2.1-9	Physical Picture of the Water-Refrigerant System	119
2.1-10	Model Agreement With Experimental Results (1)	126
2.1-11	Model Agreement With Experimental Results (2)	126
2.1-12	Model Agreement With Experimental Results (3)	127
2.2-1	Interim In-Pile Sodium Loop Conceptual Design	133
2.2-2	Fission Couple Detector - CABRI	138
2.3-1	Typical Output Voltage of a Pt-SPD When the Voltage is Shunted Through a 2-k Ω Resistor in the In-Core FMD Experiments	148
2.3-2	Candidate Coded Apertures	155
2.3-3	Typical Arrangement Used to Record the Shadowgram Produced by an Arbitrary Object and an Arbitrary Coded Aperture	156
3.1-1	Heat Capacity vs Temperature With Heat Effects	174
3.1-2	Heat Capacity vs Temperature Without Heat Effects but Including Mass-Loss Effects	174
3.1-3	Comparison of Harmathy's Estimates and Results of Modeling	175
3.1-4	Comparison of Model Calculations With Harmathy's and Peeh's Data	178
3.1-5	Comparison of Model Calculations With Harmathy's Data	178
3.1-6	Top Surface of Solidified Steel in Test BURN No. 0	181
3.1-7	Concrete/Steel Interface in Test BURN No. 0	182
3.1-8	Under-Surface of Steel Showing Included Refractory Material	182
3.1-9	Alloyed Electrodes Used in Test BURN No. 0	183

ILLUSTRATIONS (cont)

<u>Figure</u>		<u>Page</u>
3.1-10	Level Swell in Test BURN No. 1, Mean Pool Depth	185
3.1-11	Level Swell in Test BURN No. 1, Maximum Pool Depth	185
3.1-12	Gas Flow Data for Test BURN No. 1	186
3.1-13	Schematic Diagram of Gas Evolution at a High-Temperature Melt/Concrete Interface	187
3.1-14	Contact Times - Test BURN 1, Position 1	188
3.1-15	Contact Times - Test BURN 1, Position 2	188
3.1-16	Contact Times - Test BURN 1, Position 3	189
3.1-17	Contact Times - Test BURN 1, Position 4	189
3.1-18	Contact Times - Test BURN 1, Position 5	190
3.1-19	Contact Times - Test BURN 1, Position 6	190
3.1-20	Contact Times - Test BURN 1, Position 7	191
3.1-21	Contact Times - Test BURN 1, Position 8	191
3.1-22	Contact Times - Test BURN 1, Position 9	192
3.1-23	Contact Times - Test BURN 1	192
3.1-24	Schematic of Lined Basaltic Concrete Crucible	195
3.1-25	Borax Test Penetration Data, 0 Degrees	197
3.1-26	Survey TGA High-Alumina Cement	199
3.1-27	MgO Crucible Used in Final Test	200
3.2-1	Liquid Fraction vs Dimensionless Heat Flux, Both at the Top of the Bed (Sodium-UO ₂ bed)	205
3.2-2	Liquid Fraction vs Dimensionless Height With Heat Source in the Particles (bed depth is 10-mm, permeability is 10^{-10}m^2 ; system is Na-UO ₂)	207
3.2-3	Liquid Fraction vs Dimensionless Height With Heat Source in the Liquid Only	208
3.2-4	Bottom-Insulated Bed With Saturated Sodium Above	212

ILLUSTRATIONS (cont)

<u>Figure</u>		<u>Page</u>
3.2-5	Model Predictions of Zone Thicknesses for a 100-mm-Thick Bed Cooled Above and Below by Sodium 500 and 300 K Below Saturation, Respectively	215
3.2-6	Specific Power at Incipient Dryout for Beds Cooled Above by Sodium 400 K Below Saturation and Cooled Below by Various Amounts	216
3.2-7	Computer Simulation of a Steady-State Debris Bed Design	217
3.3-1	Model Predictions of Ultrasonic Thermometer Readings for the Top, Middle, and Bottom of the Bed for MP-2	223
3.3-2	Model Predictions and Experimental Data for the Average of the Five Elements of One Ultrasonic Sensor in the MP-2 Bed	223
3.3-3	Experimental Data and Model Predictions for Temperatures at the Side Midpoints of the Inner and Outer Crucibles in MP-2	224
3.4-1	Schematic Logic Flow for CONTAIN	227
3.5-1	Comparison of a Melt-Attacked Crucible and a New Crucible	231
3.5-2	Large Fragments From Test FRAG 6	232
3.5-3	Fragments From FRAG 4 Showing Internal Voids	233
3.5-4	Fragment Size Distribution	234
3.6-1	Test 13 Crucible	236
3.6-2	Progress of the Reaction Front Through Firebrick and Concrete	237
3.6-3	Penetration of the Sodium Reaction Front into the Firebrick and Concrete of Test 13	238
3.6-4	Description of Test 13 Reaction Products Samples	240
3.6-5	Pretest Estimates of Plate Centerline Deflection	245
3.6-6	Experimental Centerline Deflection Data - 100 W/cm ²	245

ILLUSTRATIONS (cont)

<u>Figure</u>		<u>Page</u>
3.6-7	Comparison of Analytical and Experimental Plate Centerline Deflection - 100 W/cm^2	246
3.6-8	Comparison of Analytic and Measured Strain Near Plate Centerline - 100 W/cm^2	246
4.1-1	Lineshape Parameter vs Step-Annealing Temperature for 25% and 75% Cold-Worked Type 316 Stainless Steel	255
4.1-2	Microhardness vs Step-Annealing Temperature for 25% and 75% Cold-Worked Type 316 Stainless Steel	255
4.1-3	Isochronal Annealing Curve for Pure (99.995%) Nickel	256
4.1-4	Surface Positron Annihilation Values of Deformed Samples Using the Angular-Correlation Technique	257
4.1-5	Lineshape Parameters vs Number of Fatigue Cycles for Type 316 Stainless Steel	258
4.2-1	Finite Element Model for the Tubular Specimen	260
4.2-2	Displacement Pattern for the Room Temperature Multi-axial Specimen Under Imposed Axial Displacement Only	261
4.2-3	Contours of Effective Plastic Strain for the Room Temperature Multi-axial Specimen Under Imposed Axial Displacement	261
4.2-4	Displacement Pattern for the Room Temperature Multi-axial Specimen Under Imposed Axial Displacement and Internal Pressure (2750 psi)	261
4.2-5	Contours of Effective Plastic Strain for the Room Temperature Multi-axial Specimen Under Imposed Axial Displacement and Internal Pressure (2750 psi)	261
4.2-6	Test Section Strain Variations for the Room Temperature Multi-axial Specimen Under Imposed Axial Displacement and Internal Pressure (2750 psi)	262
4.2-7	Test Section Strain Variation for the Room Temperature Multi-axial Specimen Under Imposed Axial Displacement Only	263
6.1-1	ACRR Fuel-Motion Detection System	278

ILLUSTRATIONS (cont)

<u>Figure</u>		<u>Page</u>
6.1-2	Assembled System Seen From Side Facing Reactor	279
6.1-3	Lead Barrier With Instrumentation Chamber Behind	279
6.1-4	Lead Pig Used in Collimation Test Module Experiments of 1977	282
6.1-5	Densitometer Scan Across the X-ray Film (15 opaque zones between the axis and one edge)	286
6.1-6	Densitometer Scan Across the X-ray Film (Ta Code with 10 opaque zones)	286
6.1-7	Instrumentation Chamber: Cameras, Intensifiers, and Mirrors - No. 1	288
6.1-8	Instrumentation Chamber: Cameras, Intensifiers, and Mirrors - No. 2	288
6.1-9	Instrumentation Chamber: Cameras, Intensifiers, and Mirrors - No. 3	289
6.2-1	Clearance Between Adjacent Cylindrical Pins	292
6.2-2	Dimensionless Representation of Fuel-Element Pitch Requirements	292
6.2-3	Centerline Fuel and Clad Temperature for \$3.00 Pulse, Heat-Transfer Coefficient = $3.119 \text{ ergs/cm}^2\text{-s-}^\circ\text{C}$, Velocity of He Flow 1.219 cm/s. (Based on a core average fuel element)	294
6.2-4	Centerline Fuel and Clad Temperature for \$3.00 Pulse, Heat-Transfer Coefficient = $3.119 \text{ ergs/cm}^2\text{-s-}^\circ\text{C}$, Velocity of He Flow 1.828 cm/s. (Based on a core average fuel element)	295

TABLES

<u>Table</u>		
1-1	PBE-5S Comparison of Calculated and Measured Results	63

TABLES (cont)

<u>Table</u>		<u>Page</u>
1-2	Nomenclature for Section 1.2.3.2.1	71
1-3	Oxygen Diffusion Coefficients for Fresh Fuel Experiments	77
1-4	Oxygen Diffusion Coefficients for Irradiated-Fuel Experiments	77
1-5	Summary of the Investigated Oxygen Diffusion Problems	85
2-1	Test Data for Experiments Described in This Quarterly	106
2-2	Nomenclature for Section 2.1-2	112
2-3	Flow Areas for In-Pile Tests (cm ²)	130
2-4	Flow Times for In-Pile Tests (s)	131
2-5	Total Sodium-Flow Volume for In-Pile Tests (liters) (fluted area)	131
2-6	Tank Height (fc) to Hold Sodium in the Glory Hole (fluted area)	132
2-7	A2 Test Sensitivity Study	141
2-8	A1R Test Sensitivity Study	144
2-9	Fission-Couple and Pt-SPD Sensitivities	150
3-1	Weight Losses for Three Concrete Types	168
3-2	Chemical Compositions of Default Concretes	169
3-3	Engineering Composition of Default Concrete	170
3-4	Chemical Compositions of Concrete Constituents	170
3-5	Thermal Effects Values for Concrete Decomposition	171
3-6	COIL Test-Steel Compositions	179
3-7	Percent of Time Melt in Contact With Concrete at Various Locations and During Various Time Intervals	187
3-8	Examples of Core Retention Materials	194

TABLES (cont)

<u>Table</u>		<u>Page</u>
3-9	Qualitative Results of Melt/Core-Retention Material Interactions Tests	196
3-10	Test Conditions for FRAG Experiments	230
3-11	Description of Firebrick	236
3-12	Analysis of Reaction Products - Test 13	239
4-1	Creep-Fatigue Tests at Mar-Test, Inc.	253
5-1	LMFBR Accident Delineation Study - ESS Phase II Summary	269
5-2	Assignments of Phenomenology Categories, ULOF Accidents	274
6-1	Gamma-Ray Dose at Each Detector After One 277-MJ Burst	283
6-2	Comparison of R-Z and R- TWOTRAN-II Models	296

FOREWORD

Sandia Laboratories' Advanced Reactor Safety Research Program, initiated in FY 1975, is a comprehensive research activity conducted on behalf of the US Nuclear Regulatory Commission (NRC). It is part of NRC's confirmatory research effort to assure that the necessary safety data and theoretical understanding exist to license and regulate the Liquid Metal Fast Breeder Reactor (LMFBR) or other advanced converters and breeders which may be commercialized in the United States. The program includes a broad range of experiments to simulate accidental transient conditions in the LMFBR, provide the required data base for understanding the controlling accident sequences, and serve as a basis for verification of the complex computer-simulation models and codes used in accident analysis and licensing reviews. Such a program must include the development of analytical models, verified by experiment, that can be used to predict reactor performance under a broad variety of abnormal conditions. This work, along with that of other U.S. and international researchers, should provide the technology base on which licensing decisions can be made with confidence that the safety of the public is assured.

The early thrust of Sandia's program was designed to provide data associated with the hypothetical core disruptive accident, with emphasis on prompt-burst (≈ 1 -ms period) energetics and the behavior of postaccident core debris. The scope of the program was expanded in FY 1976 and 1977 to encompass other energetics and inherent-retention concerns such as large-scale sodium containment and structural integrity; aerosol source studies; transition-phase energetics; fuel failure and motion; and studies to quantify elevated temperature failure modes of critical component materials. A portion of the initial effort in the program was directed toward obtaining data to support the licensing review of the Clinch River Breeder Reactor (CRBR). Another important continuing thrust of the

program is the development of the test facilities and techniques. For FY79, the program is organized in the following subtasks, progress on which is reported herein.

TASK 1 Energetics

- 1.1 - Prompt Burst Energetics (PBE)
- 1.2 - Irradiated Fuels Response

TASK 2 Fuel Dynamics

- 2.1 - Transition Phase
- 2.2 - Initial and Extended Fuel Motion
- 2.3 - Fuel-Motion Detection
 - a. In-Core Systems
 - b. Coded Aperture Imaging

TASK 3 Core Debris Behavior - Inherent Retention

- 3.1 - Molten-Core Containment
- 3.2 - PAHR Debris Bed
- 3.3 - FAHR Molten Pool
- 3.4 - Containment Analysis
- 3.5 - Fragmentation
- 3.6 - Sodium Containment and Structural Integrity
- 3.7 - Aerosol Source Normalization

TASK 4 Elevated Temperature Design Assessment

TASK 5 LMFBR Accident Delineation

TASK 6 Test and Facility Technology

- 6.1 - ACRR Fuel-Motion Detection Systems
- 6.2 - Large-Scale Test Assessments
- 6.3 - ACRR Status

EXECUTIVE SUMMARY

Introduction

Sandia Laboratories, Albuquerque, New Mexico is conducting the Advanced Reactor Safety Research Program on behalf of the US Nuclear Regulatory Commission (NRC). The overall objective of the program is to provide NRC with a comprehensive data base essential to (a) defining key safety issues, (b) understanding the controlling accident sequences, (c) verifying the complex computer models used in accident analysis and licensing reviews, and (d) assuring the public that advanced power-reactor systems will not be licensed and placed in commercial service in the U.S. without appropriate consideration being given to their effects on health and safety.

The NRC program is carefully planned to complement the larger DOE program, but at the same time to satisfy the NRC obligation of independent confirmatory research.

Together with other programs, the Sandia effort is directed toward the soundness of the technology base upon which decisions are made, and includes experiments and model and code development.

Sandia has been tasked to investigate seven major areas of interest that are intimately related to overall NRC needs. These are:

- a. Energetics
- b. Fuel Dynamics
- c. Core-Debris Behavior - Inherent Retention
- d. Aerosol-Source Normalization
- e. Elevated Temperature-Design Assessment

f. LMFBR Accident Delineation

g. Test and Facility Technology

These major tasks are subdivided as necessary into subtasks to facilitate the organization of work and the interaction of subtask results into a body of coherent information that supports the requirements of the NRC.

EXECUTIVE SUMMARY

1. ENERGETICS

1.1 Prompt Burst Energetics (PBE)

Prompt Burst Energetics (PBE) experiments provide information on the energetic response of various reactor fuel-clad-coolant systems to superprompt critical excursions. This program is directed at characterizing the phenomena (which result in pressure generation and the conversion of thermal energy to work) and reactivity effects (arising from rapid coolant voiding and initial fuel motion). These experiments examine integral effects of fuel-clad-coolant interactions (FCI), fission gas release, and fuel and fission product-vapor pressures during superprompt critical-core-disruptive accidents. The experiments also determine the potential for damage to the primary containment. Furthermore, the rate of coolant voiding in a positive reactivity void-coefficient system determines the reactivity insertion rate and, hence, the magnitude of the transient under accident conditions. The experimental work is closely interfaced with analytical efforts to develop models that uniquely describe the observed phenomena for incorporation into predictive accident analysis as well as to provide data to verify existing accident-analysis codes. These experiments provide information about the thermodynamic states and spatial distribution of fuel, clad, and coolant following a superprompt excursion. These data serve as initial conditions for postaccident heat removal (PAHR) and molten-core containment analysis.

In tests performed to date, single fuel pins have been pulse-fission heated in the Annular Core Pulse Reactor (ACPR) (now modified and called the Annular Core Research Reactor (ACRR)) to temperatures resulting in fuel vaporization. The pins, which have been surrounded by helium or sodium, are contained in a rigid pressure vessel that is instrumented with thermocouples and pressure transducers, and fitted with a movable piston at its upper end. Estimates of the conversion of thermal energy to work result from comparisons of the kinetic energy of the piston to the fission

EXECUTIVE SUMMARY

energy input to the fuel. Pressure, temperature, and piston-displacement histories are determined for a variety of fuel-coolant systems and initial conditions. A series of experiments with fresh uranium-dioxide fuel and sodium coolant has been completed. Initial experiments with fresh uranium-carbide fuel and sodium have been performed. Future experiments will examine fission product effects in preirradiated fuel. A seven-pin test vehicle for PBE experiments is being developed.

During this period, preparations for upcoming experiments were completed including design modifications, procurement of fuel pins and capsule hardware, assembly of an expanded data-acquisition system, development of experiment safety analysis, and completion of the internal safety review. In-pile experiments were resumed late in the period.

Mass-spectrographic analysis has verified that the fuel pin in PBE-9S was 50% enriched. This result leads to slightly lower energy-conversion ratios than previously reported. (0.41% estimated from pressure integral.) The conclusion that FCI-induced sodium pressurization was responsible for the second pressure transient and the sustained pressurization, however, remains unchanged.

Results of applying SIMMER-II to a simplified model of PBE-5S (oxide/sodium, single pulse) predict about half the observed maximum pressure and a shorter acoustic period than in the experiment. No FCI pressure generation was observed in the initial pressure pulse. H. Jacobs, KfK, Karlsruhe, W. Germany visited Sandia to analyze the PBE-SG2 and PBE-9S experiments with MURTI, a FCI code developed at Karlsruhe. Preliminary results were in quantitative agreement with experiment.

The EXPAND clad model was compared to a more exact transient multiple-region treatment to determine if error was being introduced through use of average clad mechanical properties. No major error was observed and it was concluded that the present clad model is adequate. Work was initiated

EXECUTIVE SUMMARY

to extend the FCI code EPIC to include progressive fragmentation of fuel particles and to include a compressible treatment of the sodium slugs.

As part of the experimental safety analysis, response of the PBE-pressure vessel and rupture disk to sharp (0.1-ms rise time) pressure transients up to 250 MPa was investigated. Analysis indicated that the pressure vessel exhibited some permanent deformation (0.4%) but remained intact. The rupture disk exhibited a short delay (20 μ s) in response and thereafter tracked the internal pressure, thus surviving very short transients but protecting the capsule against sustained overpressure.

Current postmortem examination of oxide experiments is nearing completion and plans are being formulated for the carbide postirradiation examination (PIE). Preliminary results based on examination of a small amount of debris indicate that the average particle size is smaller in PBE-12S than in PBE-7S.

Evaluation of the pressure transducer response to mechanical vibration is being done as a result of the apparent triggering, in several experiments of an FCI by piston stoppage.

1.2 Irradiated Fuels Response

The Sandia Laboratories Irradiated Fuels Response program is aimed at determining the response of fresh and irradiated reactor fuels to both prompt burst (disassembly timescale) and loss-of-flow (LOF) heating conditions. On prompt-burst timescales, the pressure source from both fuel vapor and fission gases as well as the accelerations produced by these pressure sources are of central importance. Thus the program in this area centers on determination of the effective equation-of-state (EEO) of fresh and irradiated fuels, the dynamics of pressurization (rate effects), and the ability of this pressure to disperse fuel. On LOF timescales, the mode of initial fuel disruption and its timescale for both fresh and irradiated fuels are of crucial importance.

EXECUTIVE SUMMARY

1.2.1 Disassembly Timescale Phenomena

The SPR-III fresh UO_2 experiments and the four irradiated mixed-oxide experiments have been completed. Although results are preliminary, no great differences from fresh-fuel results have been obtained. Combined neutronics, heat-transfer, and fluid-flow calculations are underway for both sets of experiments, as well as for the ACRR fresh-fuel results of Reil.

The long unresolved question of anomalous pressures due to CO formation in the Sandia EEOS experiments is being investigated analytically. Preliminary results indicate that CO formation is probably not a problem in either the SPR-III or the REBA EEOS experiments.

An examination of the FD-1.6 fuel-disruption experiment in the original fuel disruption series shows that the fuel disrupted dramatically while still at or slightly below incipient melt. This has prompted an investigation of possible early termination of high-ramp disassemblies by fission-gas-driven fuel dispersal. To this end a calculational module has been developed (for eventual inclusion in FISCAS) that calculates gas release and fuel breakup. Also, a series of in-pile disassembly visualization experiments is under development in cooperation with the UKAEA. These experiments should determine the timescale for and strength of solid/liquid-state fuel dispersal during disassembly under LOF conditions.

The irradiated-fuel EEOS-experiments program will now continue on the ACRR which has much more adequate fluence capabilities than SPR-III for this purpose. The original set will be designed to determine the driving pressures operating in the disassembly visualization experiments.

1.2.2 LOF-Timescale Fuel Disruption

The FD-2 series of disruption experiments is essentially ready for execution. Canister design is complete; fabrication is nearly completed

EXECUTIVE SUMMARY

and the experiment matrix has been decided. Preliminary design calculations show that these experiments will successfully replicate the neutronic heating conditions of irradiated fuel under LOF conditions.

The FISCAS gas-release and fuel-swelling code has been compared with the HEDL FGR39 gas-release experiment. The experimental gas release at late times and high temperatures can be quite well duplicated, but the low-temperature release is greatly underestimated. The reason for this is not currently understood. However, the code overpredicts low-temperature swelling. Clearly the two effects are related.

2. FUEL DYNAMICS

2.1 Transition Phase

Following the loss of initial geometry in a core disruptive accident, and assuming that neither early shutdown nor rapid hydrodynamic disassembly takes place, the accident enters the transition phase. The progression of the transition phase toward possible second recriticalities may strongly influence the severity of the accident and it is therefore important to understand in detail the phenomena associated with this accident stage. Sandia work is currently directed toward the mechanics of fuel blockage formation since this defines conditions leading to recriticality.

The formation of fuel blockages by freezing is an important aspect of the transition phase since this phenomena controls the distance fuel penetrates through the upper core structure and hence the amount of negative reactivity available for accident termination. Heat transfer between flowing molten fuel and ablating steel walls ultimately controls fuel-penetration distance and is affected by transpiration as molten steel moves away from the solid wall and is ablated into the bulk flow. This

EXECUTIVE SUMMARY

effect was examined in greater detail this quarter. Expressions and descriptive equations are in Section 2.1 of the main text of this report.

The liquid-liquid ablation experiments currently underway facilitate the study of the mechanics of heat-transfer during the melting of a wall by a turbulently flowing liquid. Initial experiments with Refrigerant-11 and ice were performed with the Re-11 simulating molten UO_2 and the ice simulating stainless steel.

The approach to these experiments has been to include (to the extent possible) the important properties of the system while concentrating upon the underlying phenomenology.

Suffice it to say, the test apparatus performed as designed, allowing the experiments to proceed. Two main observations can be made concerning the results of the liquid-liquid ablation tests. First, the rate of ice-pipe meltout is quite slow at any fixed axial distance, slightly more than doubling the original size of the pipe during the test. Second, for any fixed time, the difference of the ice pipe's diameter change at different axial distances is small. The first observation indicates a quasi-steady melting process and the second indicates the ice pipe meltout rate is a weak function of the axial distance.

For the simple model used to predict experimental results, variations in the shear stress at the Re-11/ H_2O interface (the pipe wall) caused exaggerated fluctuations in various other values in the model resulting in poor agreement with the experimentally obtained values. If an improved model of interfacial shear stress is used, the agreement between experimental result and predicted result is much closer, although disagreements are not eliminated. The disagreement may be due to the constant-temperature boundary conditions at the water/refrigerant interface being unrealistic, or the models may not be applicable in the liquid-liquid system. Further work is necessary to reconcile and minimize the disagreements.

EXECUTIVE SUMMARY

2.2 Initial and Extended Fuel Motion (IEFM)

The purpose of the IEFM program is to investigate various phenomena associated with fast reactor-initiating accidents such as a loss of coolant flow (LOF) and transient overpower (TOP) without SCRAM. In these hypothetical accidents, dispersive fuel motion is a major source of negative reactivity insertion. However, depending upon failure location, failure mode, and final fuel relocation, positive reactivity effects are also possible. Therefore, it is important to identify and model phenomena such as fuel motion inside the clad prior to failure, axial fuel-failure location, mode of cladding failure, fuel disruption modes, rate of dispersal, fuel plateout, and extended fuel motion into the blanket (potential for blockage). Data to support model development and verification of these phenomena are severely limited. Irradiated fuel experiments are currently being planned that will use the newly developed coded-aperture fuel-motion detection system currently being installed in the ACRR. Investigators hope that, due to the considerably improved resolution of this diagnostic device, direct observations of these phenomena will be possible. These tests in the ACRR will require operating modes that allow preheats at nominal power followed by ramp, square wave or pulse power profiles. The required hardware to provide these modes is being constructed. This capability is expected to be available in late FY79 or early in FY80. An additional facility needed for these experiments is a flowing sodium loop. Design of a small prototype loop for single fresh-fuel pin tests is currently underway. Design of an advanced loop for larger irradiated fuel tests will begin in late FY79. Hot-cell and fuel-handling requirements are also being considered.

These experiments are somewhat complementary to those currently being performed in the CABRI reactor in France. Consequently, cooperative efforts are underway through the ACRR/CABRI exchange agreement to provide a continuing interchange of expected data and analysis results.

EXECUTIVE SUMMARY

During this reporting period, conceptual design work on the interim in-pile flowing-sodium loop continued with special emphasis on major components, functions, and features of the loop. The capability of providing high power-operating modes to the ACRR continued with the design of two prototype programmers to interface with the ACRR control console. In addition, a prototype transient-rod drive motor and power supply has been received. Tests of this system will continue during next quarter as will fabrication of the programmers. Preliminary work has begun to identify the characteristics of the relevant operational modes and their implications for the ACRR control system and reactor core.

Present large uncertainties in the energy deposition within the CABRI test fuel pin can lead to large errors in predicting the fuel-melt fractions, time of clad failure, fuel-vapor pressures, and other phenomena of interest. An energy-deposition-measurement program is underway with the objective of providing diagnostic tools that, together with French instrumentation, can measure energy depositions to within 3% to 5%. Several types of detectors will be used along with an unfolding algorithm to determine the energy deposited in the fuel pin. The detectors, to be effective, must be located close to the fuel; this is achieved by appropriate selection of detector placement.

As part of the multinational CABRI program, Sandia is providing pretest EXPAND calculations of A-Series (TOP) single-pin fresh-fuel tests. These calculations are aimed at predicting pin failure. The technical information interchange among CABRI partners appears to be molding the program into a much needed and useful technical exchange in reactor safety. This quarter has seen an active program in precalculating CABRI A-series tests; the actual tests are scheduled for performance in the near future. As a result of the CABRI precalculations, EXPAND has demonstrated its capability to deal with transients that occurred in tests A2 and A1R over a much longer period of time than the transients of tests previously performed in the ACRR. The experimental results, when compared to EXPAND precalculations, will serve either to validate the physical

EXECUTIVE SUMMARY

models in EXPAND for the kind of experiment or to point out areas in which EXPAND must be further refined.

2.3 Fuel-Motion Detection

2.3.1 In-Core Fuel-Motion Detection

The feasibility of in-core fuel-motion detection is being investigated at Sandia because many facilities that can be used for NRC fast reactor safety tests do not have instrumentation slots. Also, in those reactors that do not have slots, self-shielding may preclude the use of high-resolution techniques for large-scale tests. Consequently, 7-, 19-, and 37-pin experiments are being conducted in the SPR-III reactor to test both detectors and unfolding methods. Following the completion of these experiments, fuel-motion detection will be performed in the ACRR as part of prototypic accident situations generated during PBE experiments.

In the experiments performed during this period, 30 gamma-sensitive platinum self-powered detectors were placed in and around the 7-pin fuel bundle to observe the fuel motion. Typical observed signal levels were 15% to 20% of the background when all of the fuel was removed from the region near a detector. This result is encouraging since it is twice as large as anticipated for these detectors.

2.3.2 Coded-Aperture Imaging

2.3.2.1 Introduction--One of the main purposes of the Coded-Aperture-Imaging task is the study of imaging problems that arise in large reactor safety experiments (involving more than seven fuel pins). Imaging in these large tests is expected to differ considerably from single- or seven-pin tests because of the significant scattering and absorption of the imaging radiation within the larger test-fuel-pin bundles and the greater complexity of the image itself. Coded-aperture imaging of both gamma rays and neutrons is being studied.

EXECUTIVE SUMMARY

2.3.2.2 Gamma-Ray Coded-Aperture Imaging -- Gamma-ray coded-aperture imaging technology is being developed in order to measure fuel motion in experiments involving up to seven fast reactor fuel pins on the ACRR. This development is proceeding satisfactorily, and it is therefore attractive to consider extending this technology to larger fuel bundles. In larger fuel bundles, there will be much greater absorption and scattering of the fission gamma rays used for imaging than in single-pin or seven-pin cases. This scattering and absorption will tend to reduce the signals from the center and back surface of the fuel bundle.

During this period, the primary activity was planning and detailed design of the 37-pin bundle experiments to be conducted with the PARKA facility at LASL. Optical experiments were performed to aid selection of the coded apertures to be evaluated in the PARKA experiments. These optical experiments indicate that an off-axis Fresnel-code aperture can be used to image an object as wide as a 37-pin bundle.

2.3.2.3 Fast Neutron Coded-Aperture Imaging -- Little work was performed in this area because of concentration on the PARKA experiments. However, a large background in the LEXAN neutron detector was clearly identified and eliminated by a simple procedure. Scoping experiments on transient fast neutron detectors at the ^{252}Cf source showed that an image intensifier would be required for further experiments in this area.

3. CORE DEBRIS BEHAVIOR - INHERENT RETENTION

3.1 Molten Core Containment

If the core debris following a major reactor accident becomes uncoolable, it will ultimately penetrate the reactor pressure vessel and cascade into the reactor cavity. Interaction of the high-temperature core debris with structural material in the reactor cavity may lead to

EXECUTIVE SUMMARY

generation of huge quantities of gas, extensive release of radioactive materials in the form of aerosols, and possibly failure of the containment building. Evaluating the potential safety questions that arise from the core debris interactions with the containment structure is the focus of this task.

During the reporting period, large-scale tests of the interaction of hot (but not molten) core debris with concrete were conducted. These tests showed that solid debris at temperatures between the liquidus and solidus of the concrete will erode concrete and lead to gas generation.

Large-scale scoping tests were also conducted to study the interaction between molten steel and possible alternatives to concrete as reactor cavity materials. A transient interaction test of cast borax and stainless steel showed that borax could rapidly quench the high temperature melt. Sustained tests of molten stainless steel interacting with firebrick-lined basaltic concrete (FFTF design), high-alumina cement, and MgO were conducted. Firebrick-lined basalt was found to present only an insignificant barrier to a melt of core materials. The tests with high-alumina cement and MgO were prematurely terminated because of equipment failure. Both candidate materials did, however, show promise as core debris-retention materials.

Sandia Laboratories and Projekt Nukleare Sicherheit of the Kernforschungszentrum, Karlsruhe, FRG have agreed to perform a series of tests to assess the performance of computer models of melt/concrete interactions. Preliminary specifications of the sustained interaction test to be done at Sandia were established during the report period. Once this test is performed, the data necessary for model predictions of the test will be made available. Only after the predictions have been made will the test results be released.

Further analysis of data from tests BURN 1 and BURN 0 was conducted during the report period. Data from test BURN 1 quantified heretofore

EXECUTIVE SUMMARY

qualitative concepts of the extent of gas swelling of molten pool and the effect of gas generation on melt/concrete contact. The extent of molten-pool swelling due to gas generation increases with gas generation rate to a plateau. At higher gas-generation rates, no further increase in pool swelling occurs. Contact of the melt with concrete is also influenced by gas-generation rate. Data from test BURN 1 showed that localized sites of gas evolution may develop on both horizontal and vertical concrete surfaces in contact with concrete.

Refractory inserts mounted in the concrete crucible used in test BURN 0 were inspected during the report period. W_2B , Y_2O_3 , calcia stabilized ZrO_2 , and HfC were all found to be damaged by the sudden exposure to high-temperature core debris. Thermal shock and chemical dissolution of the refractories are likely mechanisms for the failures.

3.2 PAHR Debris Bed

Following a core-disruptive accident, molten-core materials may exit the core region and contact sodium where solid-fuel debris will be formed and collected on horizontal surfaces within the vessel. This debris is still capable of generating significant power through the decay of fission products. Should insufficient cooling be afforded by natural processes, the debris could remelt and threaten containment. The purpose of this task is to determine the natural cooling of such debris. Three major first-of-a-kind in-pile experiments have been performed at Sandia and have provided significant (and unexpected) data for modeling the behavior of debris beds.

The analysis of debris-bed behavior was performed by extending methods already appearing in the literature to one spatial dimension. Although this extension does not yield a new equation for the dryout heat flux of a nonsubcooled bed, it does offer insights into the heat-removal process. Two solutions ultimately emerge: one with a large liquid

EXECUTIVE SUMMARY

fraction, a small space for vapor flow, and inherent thermal stability; the other characterized by thermal instability.

The one-dimensional dryout model predicts complete bed dryout for any power above that required for incipient dryout. However, the D3 debris-bed experiment has refuted this. Thus an empirical postdryout model was developed to describe the stable partial dryout observed experimentally. This model was used to estimate the two-dimensional behavior of a proposed bottom-cooled debris-bed experiment.

The program devoted to the development of ultrasonic sensors and the establishment of areas for their application is continuing as it relates to the debris-bed experiments. So far, the results from the use of ultrasonic sensors promise improved knowledge of the conditions existing within debris-bed experiments. Ultrasonic techniques will be used in upcoming debris-bed experiments both to improve the experimental results and to further develop ultrasonics as well.

3.3 PAHR Molten Pool

In the assessment of postaccident heat removal (PAHR) possibilities, the case must be considered in which the debris formed by the hypothesized accident cannot be cooled and progresses to a molten state. Understanding the behavior of such pools is important in order to determine if a pool of given characteristics will be retained within engineered barriers and, if not, what retention times are afforded by these barriers to permit reduction of decay heat levels.

The in-core molten-pool experiments are aimed at investigating the short- and long-term behavior of internally heated pools of reactor materials. The studies will determine the exact nature of the progression to a molten state, the thermal and kinetic behavior of the pool, and the interaction of the pool with retention materials. Concurrent with the in-core program, high-temperature furnace experiments are conducted to

EXECUTIVE SUMMARY

provide the capability for extensive studies in support of the in-core experiment results. One important task in this program is the determination of the patterns of thermal-energy flow. The greater the downward heat flux, the more the structure supporting the pool is attacked. Therefore, the first goal of the molten-pool program has been to develop a versatile experiment in which heat flux and structural ablation can be studied using real materials under typical temperature and heating conditions.

Three in-core experiments were conducted in the first molten-pool series prior to the shutdown of the ACPR for up-grading. In the first fuel-only experiment (MP-1), the ultrasonic thermometry indicated fuel temperatures and axial temperature gradients that were similar to pretest calculations. In the second fuel-only experiment (MP-2), the on-line ultrasonic thermometry and posttest x-radiography indicated that a significant amount of fuel had melted. In MP-3S, a 220-g stainless-steel sample was melted by 628-g of overlying fission-heated UO_2 that reached 2673 K during the experiment. Thus, the three in-core experiments that have been run to date confirmed the operational capabilities of the experiment package design and demonstrated that fission-heating of enriched UO_2 to the desired temperatures could be achieved. Ultrasonic thermometry developed for this program has been shown to be a valuable diagnostic of temperatures and temperature gradients up to the UO_2 melting point.

During this period, the preparation for microscopic posttest analysis of a series of high-temperature furnace experiments was completed. The analysis to be performed next quarter will provide information on the sintering behavior of UO_2 and UO_2 -steel beds, the movement of molten steel within the bed, and the interactions of UO_2 and solid MgO (Harklase - a candidate core-retention material). A feasibility study was initiated to investigate the technology available to perform thermal-conductivity measurements of UO_2 beds at high temperatures. The thermal analysis of the MP-1 and MP-2 in-core experiments was completed. The development of

EXECUTIVE SUMMARY

ultrasonic thermometry for use in the debris-bed experiment program continued.

3.4 Fragmentation

Most severe accident scenarios for advanced sodium-cooled reactor systems involve the production of significant amounts of molten fuel and steel. The ultimate dispersal of this molten material often depends on either bulk freezing of the melt or the establishment of coolable particulate beds. Scenarios that differentiate between the dispersal modes involve questions of the fragmentation of substantial quantities of melt when contacted with coolant. Previous investigations yielded quantitative information involving very small quantities of fuel melt and left unanswered the question as to whether or not large quantities would yield different particulate-size distribution due to vapor blanketing of the bulk stream. A knowledge of particle-size distributions is crucial to the resolution of postaccident coolability of cores that have been reduced to rubble.

The test apparatus for the forward experiments was modified to accommodate dual ranges of transducers. The test apparatus for the reverse experiments is being assembled in preparation for the first such experiment. For the combined interaction experiments, the test apparatus was fabricated and three crucibles were cast.

This reporting period, the planned forward (melt into sodium) experiments were concluded with the performance of two additional fragmentation experiments. Each experiment used 20 kg of corium-producing metallogenic mixture and 23 kg of sodium, one with a sodium temperature of 523 K and the other with a sodium temperature of 963 K. No test exhibited a single coherent energetic event; rather, the interactions were all characterized by a series of pressure events occurring throughout the time period corresponding to the draining of the melt crucible. For all of the

EXECUTIVE SUMMARY

experiments performed, the corium melt consistently resulted in milder interactions than the steel melts.

In the first four fragmentation experiments, the MgO inner-reaction vessel was always cracked but no damage from melt attack was indicated. In FRAG 6, the crucible bottom showed evidence of melt attack, a part of which is attributed to thermal stress. Measurements of the apparent density of fragments and void fractions of the debris beds were made. The apparent fragment densities of FRAG 4 appear to be 4.93 g/cm^3 . The void fraction is calculated to be 0.56; that is, 56% of the bed volume is occupied by sodium.

3.5 Sodium Containment and Structural Analysis

In the event of a vessel or pipe rupture, large quantities of liquid sodium at temperatures in excess of 873 K come into contact with concrete or other containment materials. This task is aimed at identifying and quantifying the dominant phenomena involved in the erosion and possible breach of containment, and in the liberation of gas that may contribute to containment failure.

Any loop-type LMFBR system must account for the interaction of hot sodium with cell liners and, given either a failed liner or a Core Disruptive Accident (CDA), the interaction of hot sodium with concrete. The data base available for safety assessments involving these interactions is extremely limited, especially for the concrete and failed-liner interactions.

Large-scale sodium-basalt concrete interaction Test 13 was conducted during the last quarter of 1978 to present a one-dimensional sodium attack to the firebrick and concrete crucible. The test featured a steel insert in the crucible cavity; it is insulated from the concrete sidewall by 2.5 cm of magnesium-oxide powder. A layer of dense firebrick was next to

EXECUTIVE SUMMARY

the bottom plate of the insert and a layer of insulating firebrick was next to the concrete cavity bottom. The bottom plate was flawed to allow the sodium to contact the firebrick. The insert depth was increased to provide for more sodium so that the test would not be as sodium-limited as was Test 12. A 239-kg charge of sodium at 973 K was dumped into the lined crucible cavity. The sodium consumed both layers of firebrick and 25 to 30 cm of the bottom of the basalt-concrete crucible, totally penetrating the bottom in one area where the penetration was enhanced by cracking. The large volume of the reaction products caused severe horizontal cracking in the crucible.

The first physical separate-effects tests were completed. A charge of 4.5 kg of sodium was dumped into a steel pipe in which concrete has been cast. Tests were carried out at 873 K, 293 K, 973 K, and 1023 K on limestone concrete. The attack was progressively more apparent with each increase in temperature; however, even in the 1023-K test, the total attack was minor.

A series of chemical separate-effects tests has investigated the results of adding various amounts of water to molten sodium. The reaction process was monitored by measuring the hydrogen gas overpressure.

A flat-plate radiant-heat flux experimental series was completed. Thirty-eight-cm² steel plates were subjected to a centrally distributed heat flux of between 10 and 150 W/cm². The experiments were designed to simulate the structural response to localized molten-sodium spills exhibited by a steel liner in a concrete cell. These experiments serve to provide data for benchmarking analytical techniques; they also serve to evaluate the use of strain gages in a high-temperature environment.

EXECUTIVE SUMMARY

4. AEROSOL SOURCE NORMALIZATION

During an energetic hypothetical core-disruptive accident, fuel vapor may be produced that subsequently condenses to form small very particulated debris (molten or solid) that can be transported to the upper vessel regions and through breaks that may have occurred in the vessel. The possibility of transporting this material depends strongly on its initial character.

Aerosol produced from in-pile (ACRR) experiments is being characterized to determine the physical properties of fuel particles resulting from the vaporization and melt breakup of fuel pins subjected to simulated overpower excursions. The characteristics of these particles will be compared with those produced by out-of-pile experiments at ORNL that are part of the NRC-sponsored Aerosol Release and Transport (ART) program. Subsequent in-pile studies will examine the interaction of particles with the supporting structure and with sodium.

During this period, preparation continued on the second series of in-pile aerosol sampling experiments as well as on the first series of out-of-pile experiments at ORNL that began in March. The out-of-pile comparison tests at ORNL were designed to establish characteristics of debris produced by resistively heating the fuel to vapor. In addition to sampling this debris, fuel temperature profiles would also be measured. These temperature profiles would then be reproduced in fuel neutronically heated in the ACRR. Finally, fuel debris from these similar experiments would be compared. Techniques for sampling debris and photometrically measuring fuel radiance and temperature were verified in the first series of in-pile experiments.

EXECUTIVE SUMMARY

5. CONTAINMENT ANALYSIS

This task is directed toward developing a total containment system code (CONTAIN) that will analyze a variety of possible accident sequences, beginning at the point of a disrupted-core debris bed to the definition of the radiological release term in the event of multiple containment failure. Core-melt accidents, energetic disassemblies, reactor-vessel rupture, and large-scale sodium spills are addressed. Existing containment models are being adapted where feasible and new models are being developed in areas where suitable models do not exist. These new models are being supported by the test program described in previous sections. Major phenomenological factors are: (a) postaccident heat removal; (b) debris melt; (c) vessel failure; (d) concrete-sodium interactions; (e) concrete-melt interactions; (f) melt-sodium interactions; (g) liner response; (h) sodium pool/spray burning; (i) chemical reaction products and kinetics; (j) gas flow, pressurization, and venting characteristics; (k) heat transfer (pool/wall/atmosphere); (l) fission-product chemistry and inventory; and (m) aerosol-transport behavior.

The development of the advanced reactor containment code, CONTAIN, continued during this period. The major effort has been devoted to either evaluation or development of specific models for subsequent incorporation into CONTAIN. Development of some models has progressed to the stage where integration of selected models into the overall code structure is ready to begin.

A preliminary version of the cavity debris pool model, SINTER, has been compiled to model a one-dimensional sodium pool in an arbitrary structural configuration. Preliminary models for water release from concrete and the sodium/concrete reaction are included and are currently being upgraded. Initial efforts to interface SINTER with the overall code structure have begun in order to define data-storage and transfer requirements.

EXECUTIVE SUMMARY

The compartment atmosphere module basically performs mass and energy balances for the cell atmospheres and includes heat-transfer, sodium-burning, and aerosol-behavior models. The current version operates as a single-cell atmosphere with only a simple debris pool model incorporated to help define data-transfer requirements. The atmospheres of cell volumes interact based on pressure and energy gradients between cells. The state variables must be determined in each cell, while mass and energy exchanges between cells are accounted for. For reactor containment analysis, the transients occur over relatively long times requiring a transient solution that is stable for very long time steps. Appropriate equations are now being programmed for computer solution.

6. ELEVATED-TEMPERATURE DESIGN ASSESSMENT

The primary objectives of the elevated-temperature design assessment studies are (a) to develop correlative NDE techniques that can be used to monitor progressive creep, fatigue, and combined creep-fatigue damage in materials used in advanced reactor primary- and secondary-loop components; (b) to evaluate analytical methods (and correlate with experimental data) for creep buckling of advanced-reactor components operating at elevated temperatures; and (c) to design, fabricate, and operate a multiaxial creep-fatigue facility for the purpose of evaluation of creep-fatigue damage rules.

6.1 Creep-Fatigue Test Program (Uniaxial Loading)*

Creep Testing--No additional creep tests were conducted. Examinations using Positron Annihilation (PA) of a previously tested specimen was completed.

*All testing is performed on Type 316 Stainless Steel

EXECUTIVE SUMMARY

Creep-Fatigue Testing--Six additional creep-fatigue specimens of Type 316 stainless steel were sent to Mar-Test, Inc. to continue testing of longer term duration and with hold periods. Testing was completed on three specimens and was initiated on a fourth. Initial observations on surfaces of fatigued Type 316 stainless-steel specimens were completed.

6.2 Nondestructive Examination

A series of isochronal annealing measurements using the Doppler broadening PA technique was completed on 75% cold-worked Type 316 stainless steel. Results were in agreement with data reported previously on 25% cold-worked material. To better understand the individual roles of vacancies and dislocations in the PA response of metals, measurements were made on isochronally annealed cold-worked pure nickel.

6.3 Microstructural Analysis

No additional transmission-electron microscopy on deformed samples was carried out during this period.

6.4 Multiaxial Test Facility

Setup of the Multiaxial Test Facility was continued. Preparation of the necessary safety-related documents for the high-pressure system to obtain internal Sandia approval for operation was underway.

6.5 Creep-Fatigue Damage Analysis

The design and analysis of the biaxial specimen effort were continued. This work provides analytical support to the Multiaxial Test Facility being developed at Sandia. Two buckling analyses were completed using the MARC structural finite-element code.

6.6 Structural Analysis of Piping Elbow

Work continued on the assessment of creep-law behavior for use in piping analysis. Work to date has identified large differences in the

EXECUTIVE SUMMARY

creep response of piping elbows when different forms of creep laws are used.

6.7 Structural Evaluation

A technical review of the CRBRP piping document (Westinghouse-ARD report CRBRP-ARD-0185) was initiated. Preliminary assessments were made. A more in-depth study will be made in the next quarter.

7. LMFBR ACCIDENT DELINEATION

The principal objective of this program is to determine the applicability of event-tree methodology to all phases of LMFBR accidents. The results of the study are intended to (a) provide a demonstrated methodology for developing accident-sequence diagrams for an LMFBR, (b) identify and systematize the key phenomena and phenomenological or system uncertainties in the accident sequences, and (c) illustrate the methodology by determining the dominant accident sequences.

Over the past year, Sandia Laboratories initiated the LMFBR Accident Delineation Study to examine the applicability of event-tree methodology to the representation of fast reactor accident sequences. This project was a broad effort to review and evaluate available information on LMFBR accident sequences and to construct event trees delineating these accident sequences from accident initiation to radiological release from the containment. Qualitatively the event-tree methodology used here is similar in most respects to that demonstrated in WASH-1400 and the CRBR safety study.

In all of the major study areas (Engineered Systems, Accident Phenomenology, and Postaccident Phenomenology (Containment)) a significant portion of the available time during this period was spent in the

EXECUTIVE SUMMARY

preparation of summaries and reviews of the then-current status and results of the Delineation Study.

The Phase I Study in the Engineered Systems resulted in the formulation of event trees for 14 identified vital-subsystem failures that delineated a set of 15 initiating accident categories. From Phase I, two general objectives were established to identify promising areas for potential future investigation during Phase II. These objectives include scoping the requirements for a more realistic quantification of LMFBR initiating accident probabilities and providing feedback for evaluation of LMFBR safety research and development priorities.

Planning for future Accident Phenomenology work was strongly influenced by the major conclusions of the Interim Report, especially the following:

- a. Quantification of the event trees in this area is not likely to be feasible in the near term.
- b. Future containment-area work can probably demonstrate substantial risk mitigation provided very severe energetics can be assigned very low probabilities.

The proposed Accident Phenomenology work can be divided into two parts: continuation of general efforts required to bring the coverage offered in the Interim Report to a more uniform level; and the proposal of experimental and/or analytical studies to improve understanding of phenomenologies associated with the Unprotected Loss-of-Flow (ULOF) and Unprotected Transient Overpower (UTOP) accidents.

In the Postaccident Phenomenology area, efforts have been directed toward developing a work plan for improvements in the applicable event trees during the coming fiscal year. A draft work plan has been completed and initial tasks have been undertaken.

EXECUTIVE SUMMARY

8. TEST AND FACILITY TECHNOLOGY

8.1 ACRR Fuel-Motion Detection System

A coded-aperture fuel-motion detection system is under development for the ACRR. The design of the system has been based upon the experience gained in experiments with shielding, collimation, coded-aperture imaging, and time-resolved pseudoholography at the ACPR, SPR-II, and ^{252}Cf facilities. The system has been designed to facilitate high spatial and temporal resolution measurements of fuel motion in both transient and steady-state experiments, and to accommodate material-separation studies for the postaccident heat-removal experiments.

During this period, the various components of the ACRR fuel-motion detection system were assembled in the reactor tank. Only a few minor problems were encountered although over 500 individually designed pieces were fitted together to form the bulk shield, collimation, and detection systems. Some components not built to Sandia specifications had to be remanufactured. In particular, some of the collimation-system components developed leaks and had to be rewelded. Despite the resulting delay, some preliminary measurements were made to determine the effectiveness at the bulk shield; the bulk shield was far more effective than had been anticipated. No radiation background signals are likely to be generated in the camera or electronics.

During assembly and initial testing, the reactor safety committee imposed rigging guidelines for heavy-equipment handling above reactor components. Compliance required about 2-months additional work and results of initial proof tests will not be available until the next quarter.

8.2 Large-Scale Test Assessment

Large-scale test assessment efforts are directed toward the definition of an experimental program which will provide test data with

EXECUTIVE SUMMARY

the potential to confirm analysis and conclusions drawn from smaller scale CDA experiments. These considerations include the use of existing facilities as well as the definition of requirements for new facilities or modifications to existing ones.

A project for fuel-element design for the gas-cooled reactor concept was initiated. The complete design effort will include literature review, computational work, and design optimization. The fuel elements for a gas-cooled research reactor with full-length capability must be arranged in a fairly tight-packed array in order to yield large fuel-element volume fractions for minimum reactivity requirements. Clad thickness and bowing considerations for these extra long elements will also be important in choosing an appropriate packing fraction.

The separation distance between elements for a given fuel-element diameter and volume fraction can be increased by changing the fuel element from a cylindrical to a hexagonal shape. Large cans of fuel elements resulting in very small coolant volume fractions are also possible if steady-state operational requirements are of very low power or of short-time duration. This is the situation in the safety-test-facility (STF) reactor design where the coolant volume fraction in the converter is only 0.06 and the reactor is to be run only as an adiabatic machine.

The thermomechanical design effort during this quarter has involved assembling and checking out a computer code library that can be used to calculate transient or steady-state temperature and stress profiles in candidate HFFPR fuel elements. This library includes families of codes for one- and two-dimensional coupled thermomechanical response and for one-dimensional nonlinear heat transfer. These codes are intended to provide significant computational assistance in reactor design and analysis.

In the thermomechanical studies, there are two main areas of concern following a reactor pulse: clad temperature and fuel/clad hoop stress. One of the main thermomechanical design goals for the gas-cooled HFFPR is

EXECUTIVE SUMMARY

to provide a fuel-element design that will maximize fuel-volume fraction, and operate before maximum thermal and stress limits are reached for all anticipated transient and steady-state conditions.

A study to determine the sensitivity of maximum energy deposition in the test section as a function of the eigenvalue of the entire driver/test section in calculated assemblies was initiated, but results are too preliminary to report at this time.

Work on the neutronics evaluation of a high-volume percent Be_2C fuel has been dedicated to the production of cross-sections for the fuel and to the development of R- θ models that include an outer cavity, radial fuel-motion detection slots, and six control-rod locations. Development of the R- θ models was concurrent for both BeO and Be_2C systems. Normalization of the R- θ model to the R-Z TWOTRAN II code was accomplished through the use of zone- and energy-dependent terms (DB^2) reflecting Leakage \div Flux. The agreement between the R-Z and R- θ models for the effective neutror multiplication factor (k_{eff}) is approximately 1% difference. The difference in energy deposition is about 8%.

8.3 ACRR Status

Ascension-to-full-power and pulsing tests (ATPs) were performed with the completion of parts of ATP 1, 7, 11, 12 and 14. Other system checks were conducted. Several experiments were supported involving programs associated with basic research, weapon system reliability research, and reactor safety research. Initial steps were taken to order higher reactivity-worth transient rods. The current rods are worth \$2.95; the new rods will be worth approximately \$4.25. A second set of two rods will be ordered later for use with a slotted core (or experiments with fuel-motion diagnostics) as soon as a standard slotted core is developed. The slotted core was reconfigured to reduce the imbalance in reactivity-worth of the control and transient rods. The standard core also was reconfigured to facilitate the changeover to the slotted core and to minimize

EXECUTIVE SUMMARY

the influence on the core safety and control instrumentation. The core was then calibrated and dosimetry was performed for planned experiments.

In summary, all startup tests have been completed as has most of the reactor characterization. Major use of the facility has been for the fuel-motion detection system with other users being phased in around the slotted core operations. Operation of the ACRR is a designed.

ADVANCED REACTOR SAFETY RESEARCH PROGRAM
COMBINED QUARTERLY REPORT
OCTOBER 1978 - MARCH 1979

1. ENERGETICS

1.1 PROMPT BURST ENERGETICS (PBE) (K. O. Reil, 4423; M. F. Young, 4425;
J. T. Hitchcock, 4424)

1.1.1 Introduction

PBE experiments are designed to provide information on the energetic response of various reactor fuel-clad-coolant systems to superprompt critical excursions. This program is directed at characterizing the phenomena that result in pressure generation and the conversion of thermal energy to work, and reactivity effects arising from rapid coolant voiding and initial fuel motion. These experiments examine integral effects of fuel-clad-coolant interactions, fission-gas release, and fuel- and fission-product vapor pressures during superprompt critical core-disruptive accidents. The experimental work is closely interfaced with analytical modeling efforts to develop models that uniquely describe the observed phenomena for incorporation into predictive accident analysis. These experiments also provide information about the thermodynamic states and spatial distribution of fuel, clad, and coolant following a superprompt excursion. These data serve as initial conditions for postaccident heat-removal studies.

In tests performed to date, single fuel pins have been pulse-fission heated in the Annular Core Pulse Reactor (ACPR) to temperatures resulting in fuel vaporization. The pins, surrounded by helium or sodium, are contained in a rigid pressure vessel that is instrumented with thermocouples and pressure transducers, and is fitted with a movable piston at its upper end. Comparisons of the kinetic energy of the piston to the

fission energy input to the fuel enable estimates of the conversion of thermal energy to work.

Pressure, temperature, and piston-displacement histories are determined for a variety of fuel-coolant systems and initial conditions. A series of experiments with fresh uranium-dioxide fuel and sodium coolant has been completed. Initial experiments with fresh uranium-carbide (UC) fuel and sodium have been performed. Future experiments will examine fission-product effects in preirradiated fuel. A seven-pin test vehicle for PBE experiments is under development.

During this period, preparations for upcoming experiments were completed, including design modifications, procurement of fuel pins and capsule hardware, assembly of an expanded data-acquisition system, development of experiment safety analysis, and completion of the internal safety review. In-pile experiments were resumed late in the period.

Mass-spectrographic analysis has verified that the fuel pin in PBE-9S was 50% enriched. This result leads to slightly lower energy-conversion ratios that were previously reported (0.41% estimated from pressure integral). The conclusion that FCI-induced sodium pressurization was responsible for the second pressure transient and the sustained pressurization, however, remains unchanged.

The analysis of PBE experiments is continuing with application of SIMMER-II to experiment analysis and with work directed at modeling the fuel-coolant interactions observed in experiments. In preliminary studies, the MURTI FCI code (developed at Karlsruhe) was used to model PBE-9S and PBE-SG2. Work was initiated to extend the FCI code EPIC to include progressive fragmentation of fuel particles and to include a compressible treatment of the sodium slugs.

Current postmortem examination of oxide experiments is nearing completion and plans are being formulated for the carbide postirradiation

examination (PIE). Evaluation of the response of pressure transducers to mechanical vibration is under way.

1.1.2 Experiment Preparations

All preparations for the upcoming PBE experiments are complete, including capsule design and fabrication, procurement of other capsule components, expansion of data-acquisition system, completion of safety analysis, development of an experiment plan for the fresh oxide-sodium experiments, and the internal safety review of those experiments.

1.1.2.1 Single-Pin Capsule -- Figure 1.1-1 shows a cross section of the assembly for future single-pin, stagnant-coolant PBE experiments. The instrumented pressure vessel is essentially the same as that used in previous experiments (PBG-12S, -SG1, -SG2, and -SG3). The major difference is two independent radiological-containment boundaries instead of the single containment used in previous experiments. The double containment will be required for the irradiated mixed-oxide experiments and will be used for fresh-fuel experiments as well.

1.1.2.2 Neutronics -- As a necessary part of the experiment design and safety analysis, estimates have been made of fission-energy deposition attainable for different experiment configurations in the ACRR. The bulk of this analysis for PBE experiments has been done with DTF-IV¹⁻¹, using macroscopic neutron cross sections modified by artificial absorption cross sections (DB²) to correctly account for axial leakage. These artificial absorption cross sections were derived from an R-Z TWOTRAN-II¹⁻² calculation. A set of microscopic cross sections developed for the ACRR were used. The DTF-IV results were normalized to measured free cavity fluence.

The results of these studies are summarized in Figure 1.1-2 which shows predicted energy deposition in a PBE experiment as a function of polyethylene moderator thickness and fuel enrichment. The initial experiments in the ACRR will use 14%-enriched fuel and are designed to yield maximum radially averaged energy depositions of 2400 J/g. From the parametric study, a moderator thickness of 0.063 in. is indicated. The predicted energy deposition profile for that case is shown in Figure 1.1-3.

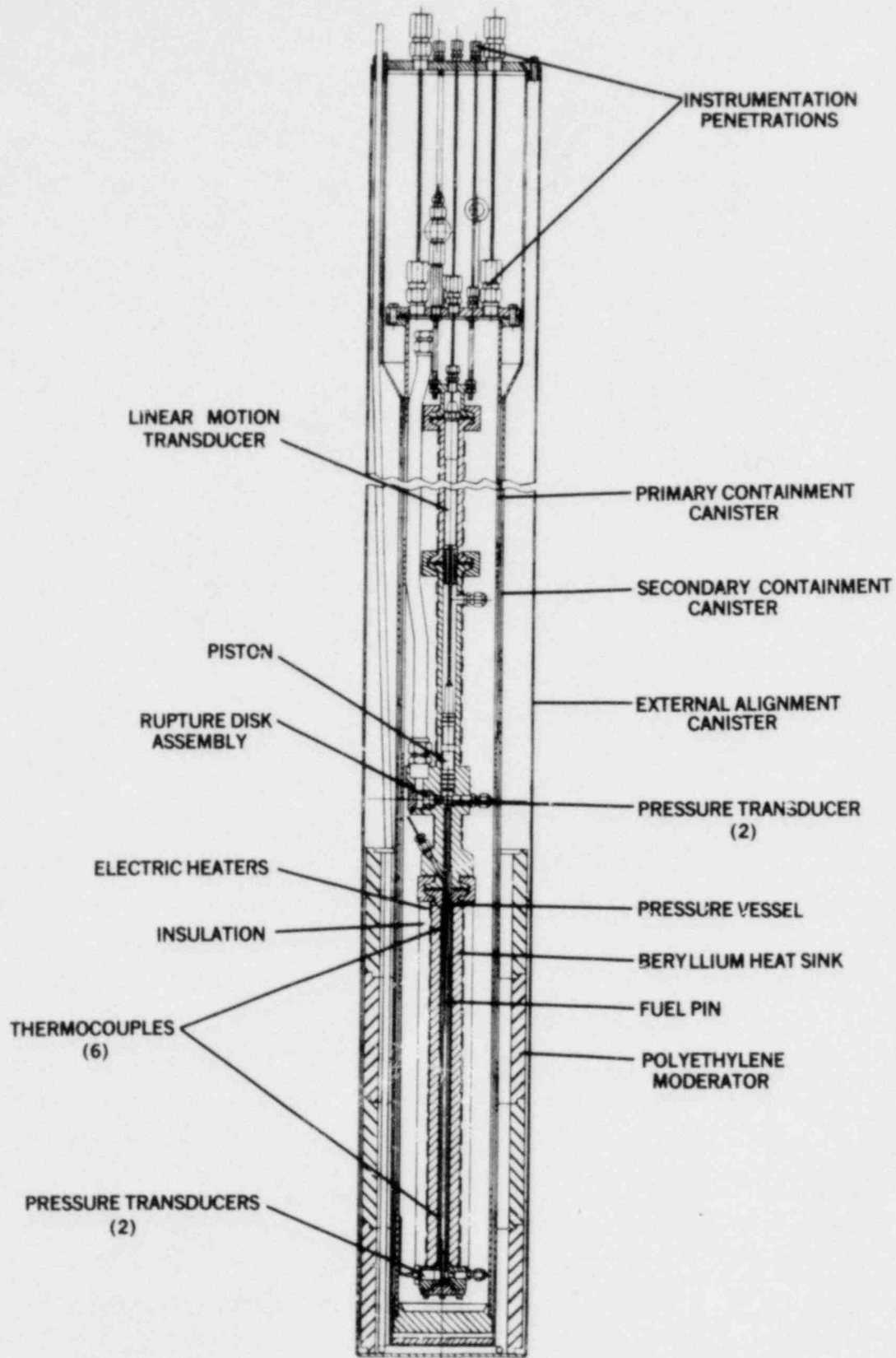


Figure 1.1-1 PBE Single-Pin Capsule

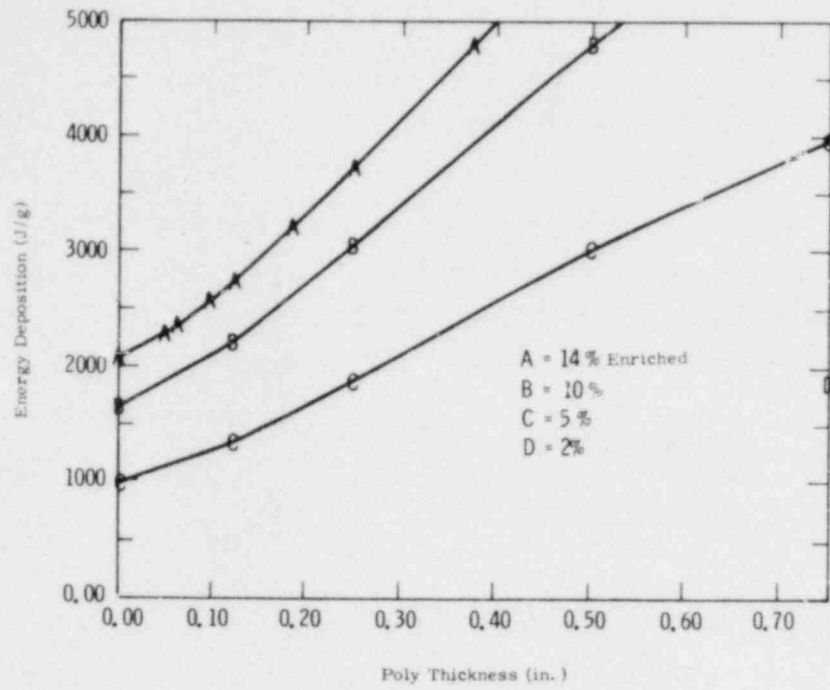


Figure 1.1-2 Energy Deposition in PBE Experiments as a Function of Polyethylene Thickness

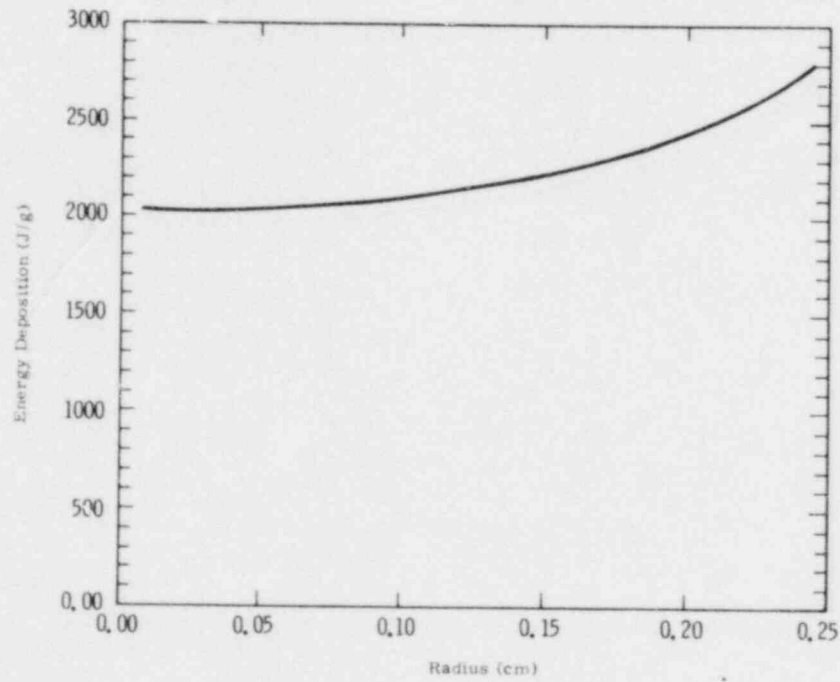


Figure 1.1-3 Energy Deposition Profile for 14%-Enriched Fuel With 0.063-in. Polyethylene

The validity of the normalization used will be evaluated by dosimetry experiments using uranium-loaded aluminum wire and fuel pins. Those dosimetry experiments and other characterization experiments will precede the first sodium experiment (PBE-13S).

1.1.2.3 Transient Pressure Response -- The response of the PBE capsule to an internal-pressure spike was investigated with CHARTD¹⁻³, a one-dimensional hydrodynamic code. The sodium, molybdenum liner, and Inconel vessel were modeled as shown in Figure 1.1-4. The sodium was treated as a hydrodynamic fluid, and the moly and Inconel are represented as elastic-plastic materials. The six-lobed moly sleeve is approximated as a 20-mil-thick cylinder fitted inside the Inconel vessel.

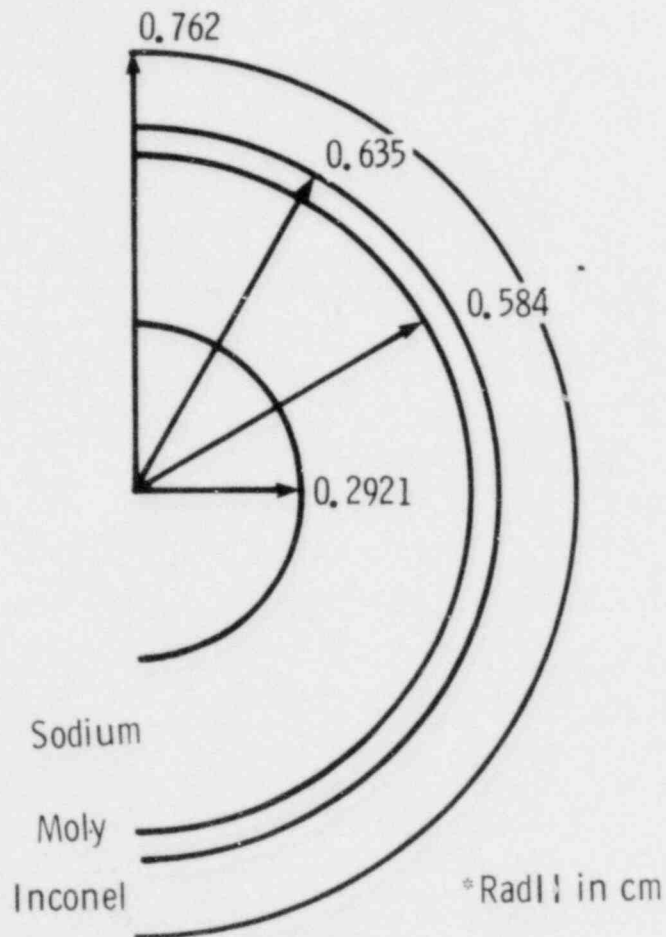


Figure 1.1-4 CHARTD Model of PBE Vessel

Response of the inner vessel wall to a 200-MPa spike (100- μ s rise time) is shown in Figures 1.1-5 and 1.1-6. The maximum effective stress is slightly less than the yield stress of the Inconel (9×10^2 MPa); the maximum displacement is 0.4%. The inner wall of the vessel is thus on the verge of going plastic, while the bulk of the vessel wall remains below the yield point and hence remains elastic. Both the effective stress and the radial displacement attain a maximum at the same time that the maximum internal pressure is applied (100 μ s) and decrease thereafter. Figure 1.1-7 shows the radial stress as a function of radius; it is apparent that the moly liner decreases the pressure applied to the inner wall by roughly 20% (to 160 MPa).

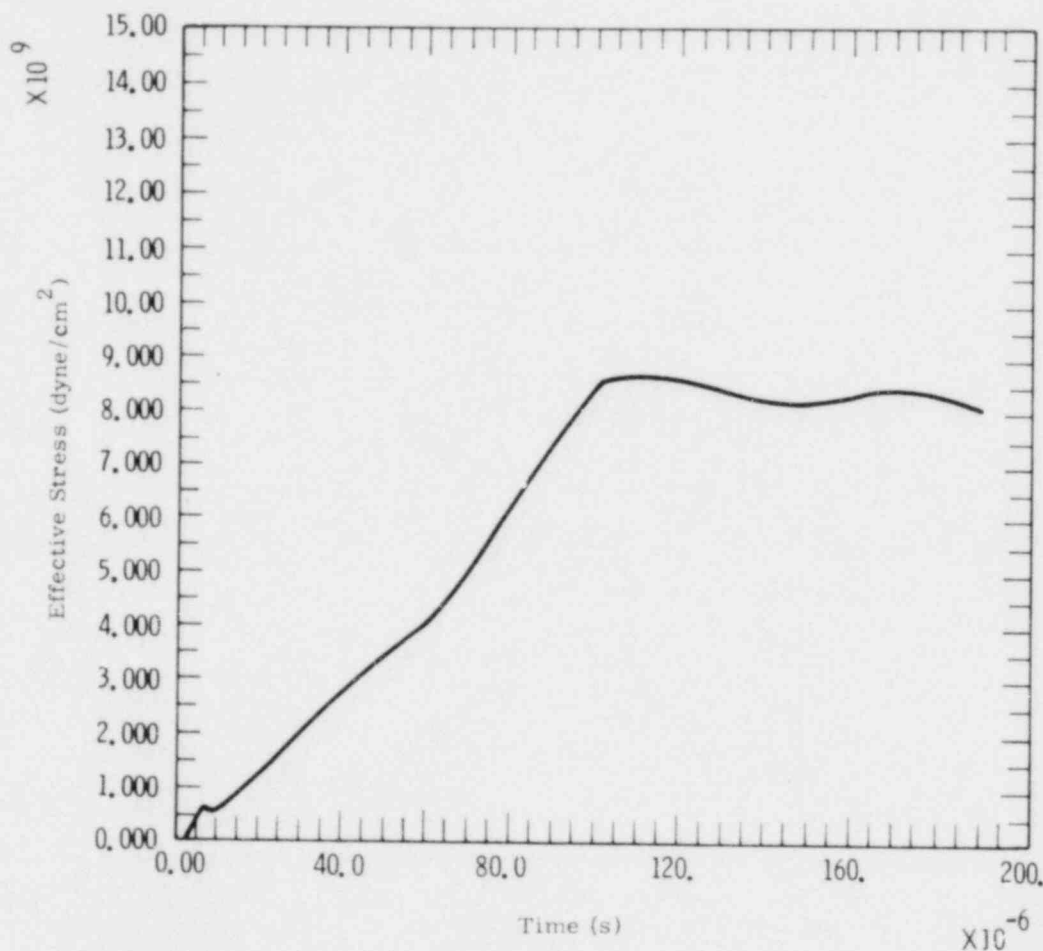


Figure 1.1-5 PBE Vessel Response - Effective Stress vs Time (inner wall)

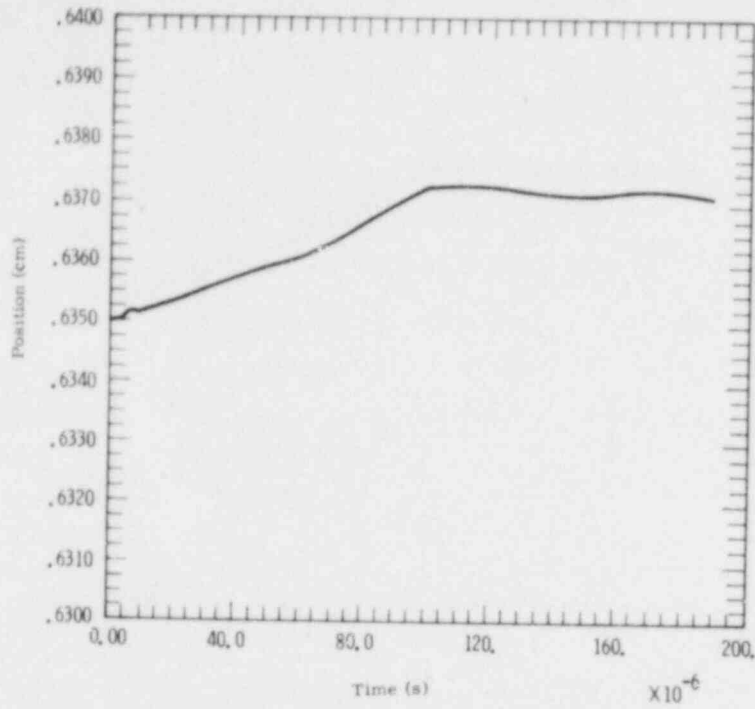


Figure 1.1-6 PBE Vessel Response - Position vs Time (inner wall)

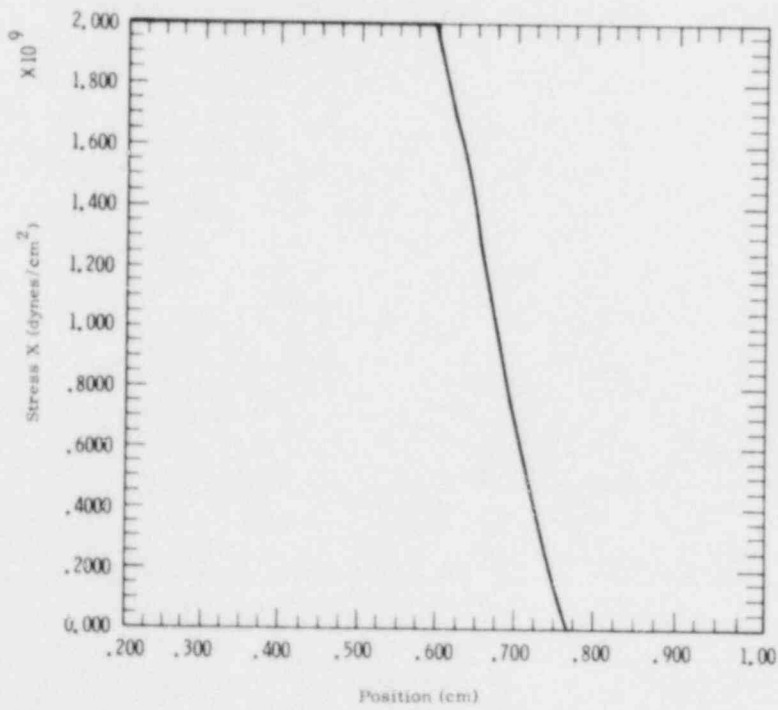


Figure 1.1-7 PBE Vessel Response - Radial Stress as a Function of Radius

A CHARTD calculation was also done with a 250-MPa spike (100- μ s rise time again) applied to the inner boundary. This resulted in essentially the same maximum displacement at inner and outer vessel walls (0.4%). The yield point was exceeded out to a radius of 7.342 mm, or 78% of the wall thickness. The vessel thus exhibits some permanent deformation but remains intact. Maximum instantaneous velocity on the outer surface was ≈ 0.060 m/s, which would be considerably reduced if the inertial restraint of the beryllium heat sink around the vessel were included in the calculation. The effective stress at the inner wall and inner wall radius are shown as functions of time in Figures 1.1-8 and 1.1-9. Radial stress is shown at 100 μ s in Figure 1.1-10. Again, the pressure applied to the wall is reduced below the actual internal pressure by the moly liner.

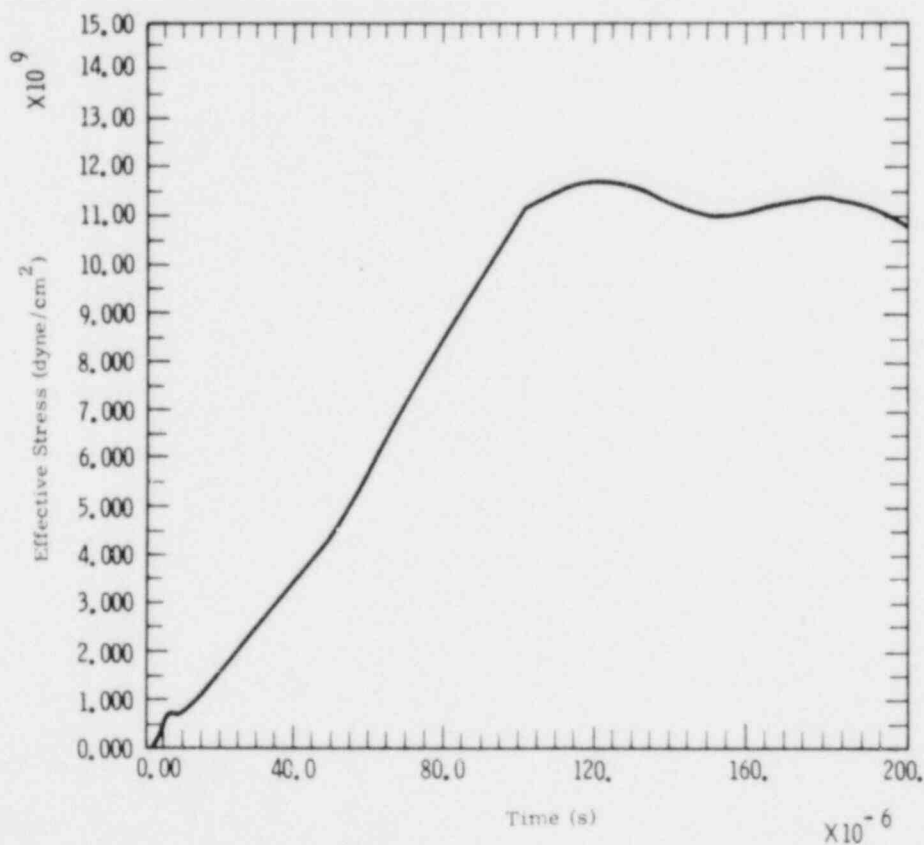


Figure 1.1-8 PBE Vessel Response to 50-MPa Spike - Effective Stress vs Time (inner wall)

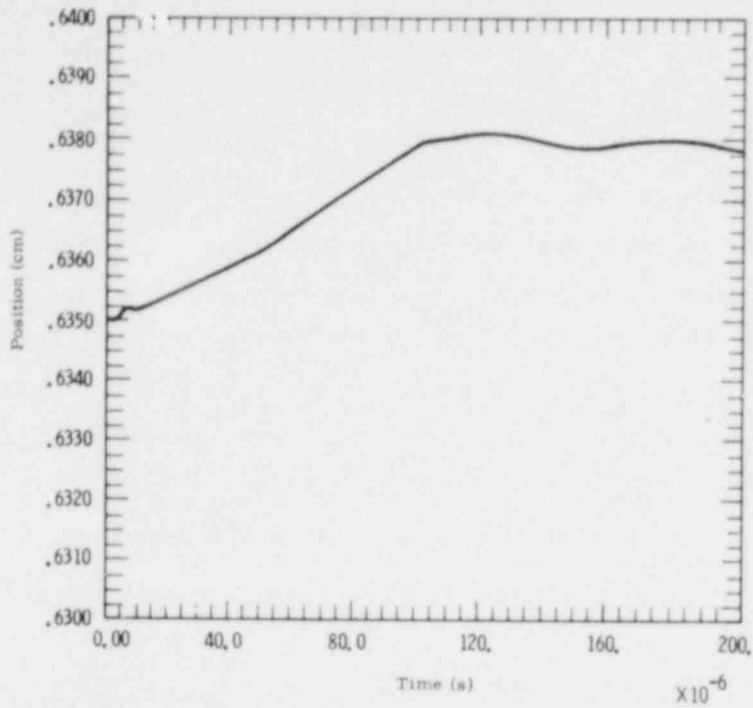


Figure 1.1-9 PBE Vessel Response to 250-MPa Spike - Position vs Time (inner wall)

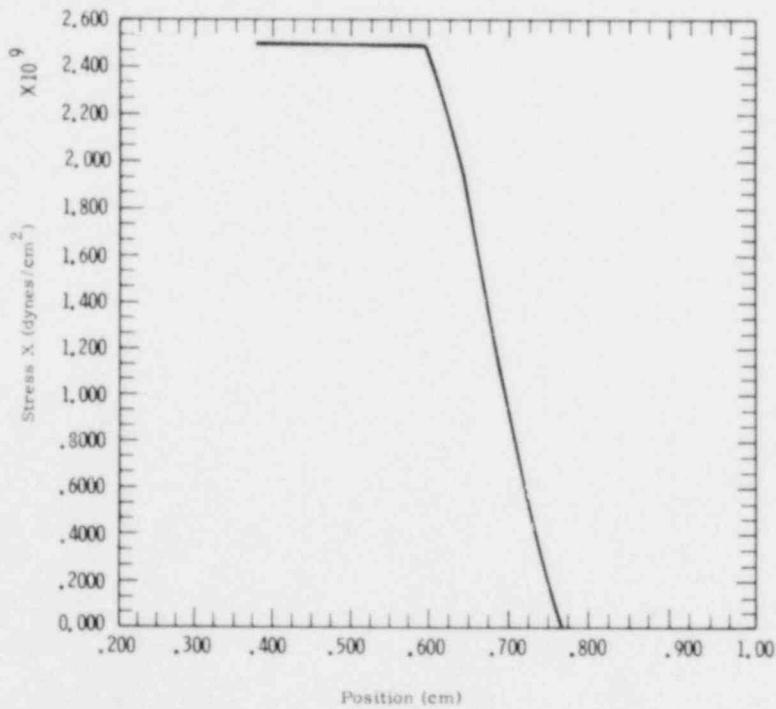


Figure 1.1-10 PBE Vessel Response to 250-MPa Spike - Radial Stress as a Function of Radius

Investigation of the rupture disk response to a fast transient revealed that a short delay (20 μ s), comparable to the acoustic transient time across the radius of the upper pressure-vessel channel, was introduced by the rupture disk geometry. After this delay, the rupture disk tracked the internal pressure. With a maximum rise time comparable to that observed in PBE experiments to date (2.5 MPa/ μ s in PBE-SG2), the rupture disk should vent before the internal pressure reaches 75 MPa. Thus the rupture disk should survive very short transients while still protecting the capsule against severe overpressure.

1.1.2.4 Containment Pressure -- To design containment canisters and to establish internal pressures for leak tests, it is necessary to establish an upper bound for the maximum pressure exerted against containment. The approach taken here was to assume a Hicks-Menzies-type FCI in the pressure-vessel volume followed by isentropic expansion of the sodium to the containment value.

This analysis assumed instantaneous total thermal equilibration between a mass of fuel and sodium and an average energy deposition of 4200 J/g in the fuel. Various combinations of fuel and sodium masses were examined. The greatest expanded pressure corresponded to mixing all the fuel with all the sodium. The volume of sodium (38.5 cm³) includes all of the sodium in the channel between the fuel pin and molybdenum liner, and the sodium between the top of the fuel pin and the piston. For an initial temperature of 773 K, this represents 32 g of sodium. The oxide fuel pins contain 64 g of fuel. The sodium was assumed to occupy a volume including the free volume derived from piston displacement (11.3 cm³). Thus the effective sodium density is 0.64 g/cm³ (32 g in 49.8 cm³). The total free volume of the internal containment canister is approximately 9800 cm³. Following expansion this yields a sodium density of 0.00327 g/cm³ (32 g in 9800 cm³).

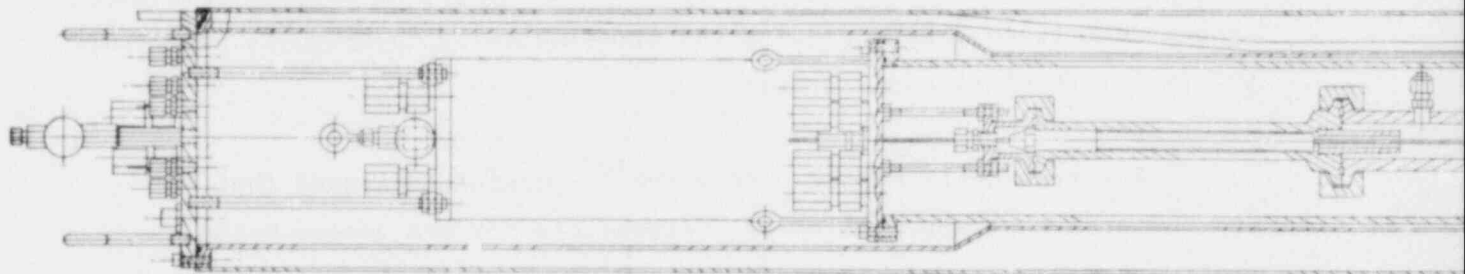
The sodium equation-of-state data used was ANEOS data for the CHARTD¹⁻³ code. The equation-of-state was evaluated using the CKEOS¹⁻⁴ program of the CHARTD package. The approach taken was a constant-volume heating of the fuel and sodium from 773 K in the pressure-vessel volume

until 268 kJ were added. The sodium was then expanded isentropically to the containment volume. Sodium data from the CKEOS output and UO_2 enthalpy data from ANL-CEN-RSD-76-1¹⁻⁵ were used to determine the equilibrium state. The compressed mixture was found to equilibrate at about 4280 K, corresponding to an entropy of about 5.3×10^7 ergs/g. When expanded along that isentrope, the expanded state was found to be at a temperature of 1395 K with a pressure of 0.58 MPa (82 psi).

This analysis neglects heat transfer to the clad, pressure vessel, or containment, all of which would reduce the final temperature and pressure. Further, no thermal interaction even approaching the efficiency described here has ever been observed. The analysis is thus extremely conservative. Based on this conservative analysis, the containment cans were designed for a working pressure of 100 psia and leak tests will be performed with a pressure differential of 100 psi.

The pressure in the compressed state at 4280 K is approximately 1840 MPa. Thus the rupture disk (rated at 34 MPa) would vent, permitting the sodium to expand into the receiver volume and reducing the density by more than a factor of 2. From the CKEOS results, the pressure after expansion to a density of 0.32 g/cm^3 is less than 17 MPa, well below the capsule design pressure.

1.1.2.5 Seven-Pin Capsule -- Work is under way to extend the single-pin PBE experiment technology to 7-pin assemblies. Figure 1.1-11 shows a tentative design for a stagnant-coolant 7-pin PBE capsule. The design is now being evaluated with regard to experiment goals and mechanical and instrumentation considerations.



POOR ORIGINAL

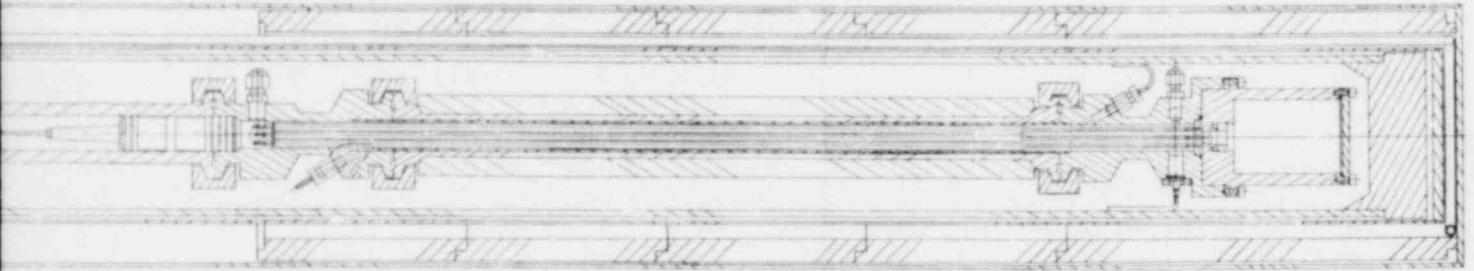


Figure 1.1-11 Tentative PBE Seven-Pin Capsule

1.1.3 PBE-9S Results

As noted in the previous quarterly,¹⁻⁶ there was evidence that the fuel pin in PBE-9S was greater than 20% enriched. Subsequent mass-spectrographic analysis of debris from that experiment showed the fuel to be 50% enriched. The maximum radially averaged energy deposition was thus 3520 J/g rather than 2900. The greater energy deposition, derived from dosimetry and neutron-transport calculations, yielded slightly lower thermal-to-mechanical energy-conversion ratios than previously reported.¹⁻⁷ The conversion factor derived from piston motion was 3.2×10^{-4} ; the estimate derived by integration of the measured pressure history was 0.41%. Using energy, the deposition level and distribution associated with 50% enriched fuel in the EXPAND¹⁻⁷ pin-failure model results in predicted clad failure 1.6 ms after the peak of the reactor power. Evidence of pin failure was observed 1.8 ms before the power peak. In terms of the reactor pulse width at half maximum (12 ms for PBE-9S), the agreement between EXPAND results and experimentally observed failure time is similar to other oxide results.

The previously stated conclusion¹⁻⁷ remains unchanged that FCI-induced sodium pressurization was responsible for the second high-amplitude pressure transient and the sustained pressurization.

1.1.4 PBE Analysis

1.1.4.1 Modifications of EPIC for PBE-FCI Analysis -- An experimental-analysis version of EPIC,¹⁻⁸ an FCI code similar to PLUTO,¹⁻⁹ was acquired from ANL and tested on the CDC 7600. Results of the test problems agreed with ANL results.

The possibility of using a compressible treatment of the sodium slugs in EPIC was investigated. This would allow a more detailed comparison of calculated results and PBE experimental data. A compressible model now exists, but has not yet been incorporated into EPIC.

The feasibility of incorporated progressive fragmentation of the fuel particles (presently a user-input fixed size) into EPIC was also investigated. The necessary changes were completed and a baseline comparison was made to the older EPIC version. The fragmentation process is controlled by a new subroutine added to EPIC; presently, the rate of fragmentation is parametrically determined from the Bond and Weber numbers. A more mechanistic treatment will be used as further experimental data on FCIs become available.

1.1.4.2 MURTI-Code Liaison -- Helmut Jacobs (KfK) visited Sandia for 2 wks in December to investigate PBE-9S and PBE-SG2 with the MURTI¹⁻¹⁰ fuel-coolant-interaction code developed at Karlsruhe. In this code the fuel and sodium are treated as a heat-conducting, compressible fluid. The code was set up on the Sandia computer system and the effects of various physical assumptions in modeling the PBE experiments were studied. This work is expected to lead to a better understanding of FCI phenomena in the PBE experiments.

Preliminary results were in qualitative agreement with PBE-9S and PBE-SG2 experiment results.

1.1.4.3 EXPAND Development -- A transient stress-strain model incorporating multiple regions was tested; different mechanical properties are allowed in the different regions. Comparisons between the multiple-region representation, a single region, and the present integral-plastic-clad model in EXPAND under similar fast-transient loading conditions show good agreement in calculated stress-strain conditions, especially at the outer clad surface. This comparison was done to determine if any major error was introduced in calculation by the use of average mechanical properties in the EXPAND clad model; the clad has a high thermal gradient across itself for PBE conditions and consequent large variations in mechanical properties. Results show that no large error is present and that the present EXPAND model is adequate.

1.1.4.4 SIMMER-II Analysis -- Current work with SIMMER-II¹⁻¹¹ is directed toward analysis of the PBE-5S experiment. The purpose is to (1)

investigate the applicability of SIMMER to these complex experiments and (2) provide information for model development and verification.

The first phase of the work examined modeling assumptions. Because the SIMMER code was developed to investigate the behavior of large reactor systems, the modeling of a single-pin experiment is not straightforward. Specifically, problems were encountered in modeling the cladding, the piston, and the heat transfer to the structure.

The initial model of the PBE-5S experiment, used to obtain a first look at the SIMMER hydrodynamics, represented only the dominant features of the experiment. This model is shown in Figure 1.1-12. It assumes a full circumferential break 1 cm high, constant sodium-flow area, a pseudo-sodium movable piston, a uniform initial-fuel temperature, and little or no heat transfer to the structure. The calculation was started at the point of pin failure with initial conditions obtained from M. Young's EXPAND predictions. Using Reil's upper-energy-bound UO_2 equation-of-state,¹⁻¹² the EXPAND code predicts pin failure with a peak fuel temperature between 4350 and 4550 K, and a corresponding fuel-vapor pressure of 6 to 10 MPa. In SIMMER a "best guess" UO_2 equation-of-state was used. This curve starts along the upper-energy-bound curve at low pressures then goes through the Benson data¹⁻¹³ at higher pressures. The initial fuel temperature in SIMMER was set at a uniform 4352 K resulting in a fuel-vapor pressure of 10 MPa. The fuel was modeled as a single-phase liquid at the point of pin failure. The temperature of the coolant and structural material was set at 770 K with a pressure of 0.28 MPa.

The SIMMER analysis using this simplified model of PBE-5S starts at pin failure and extends 2.0 ms into the transient. A comparison of the calculated and measured pressure traces and the predicted pressure-generation mechanisms was of specific interest in the initial hydrodynamic calculations. Figure 1.1-13 shows a direct comparison of the pressure-trace characteristics for the first 1.5 ms. This comparison is summarized in Table 1-1. The magnitudes of the calculated pressure peaks at both transducer locations are much lower than the measured values. These differences are not inconsistent with the uncertainties in the energy

deposition and the fuel equation-of-state. The calculated pressure was found to be predominantly due to fuel-vapor pressure up to about 1.2 ms. At this point, sodium-vapor pressure increased in the zone immediately above the break.

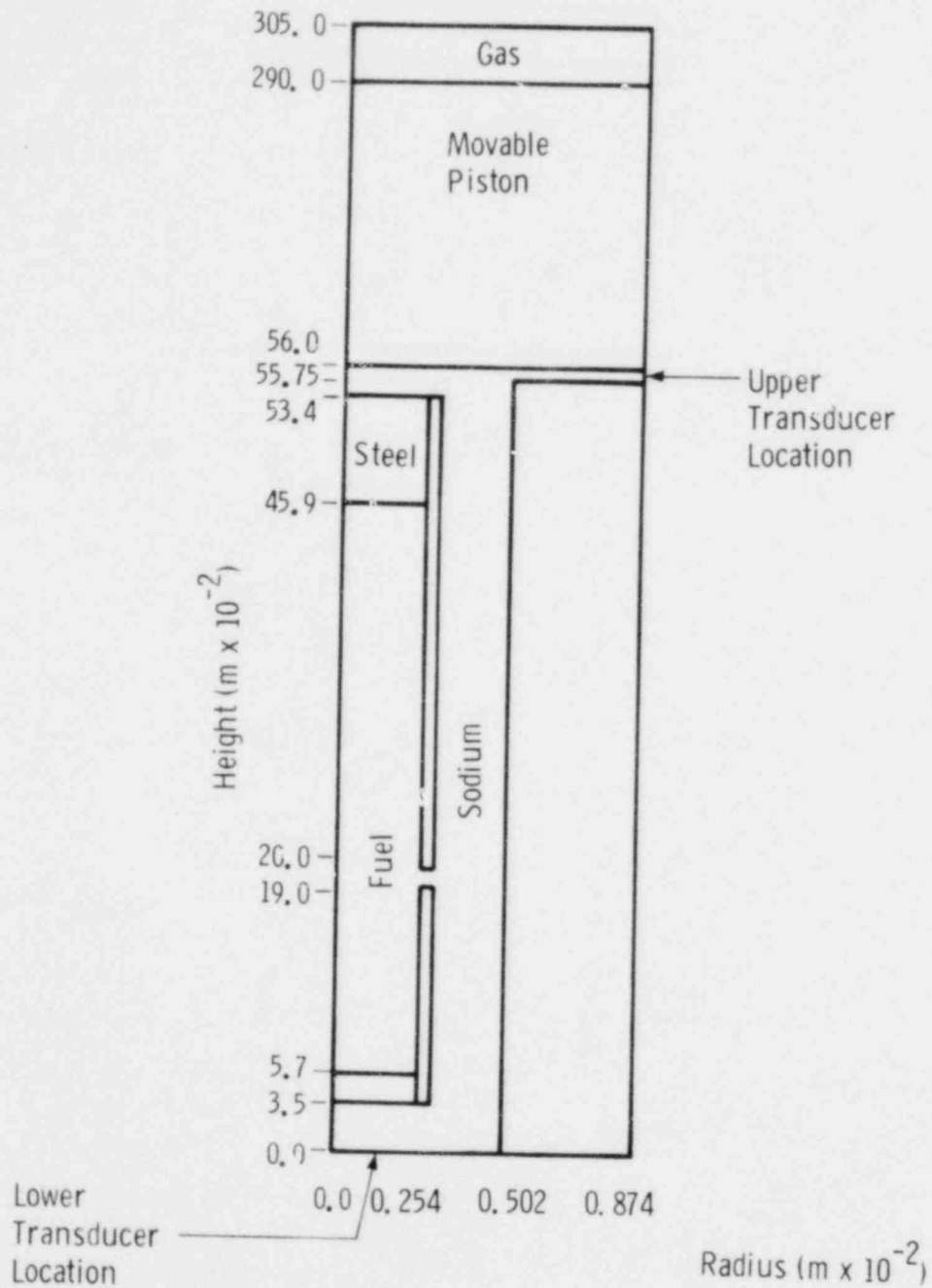


Figure 1.1-12 PBE-5S SIMMER Model

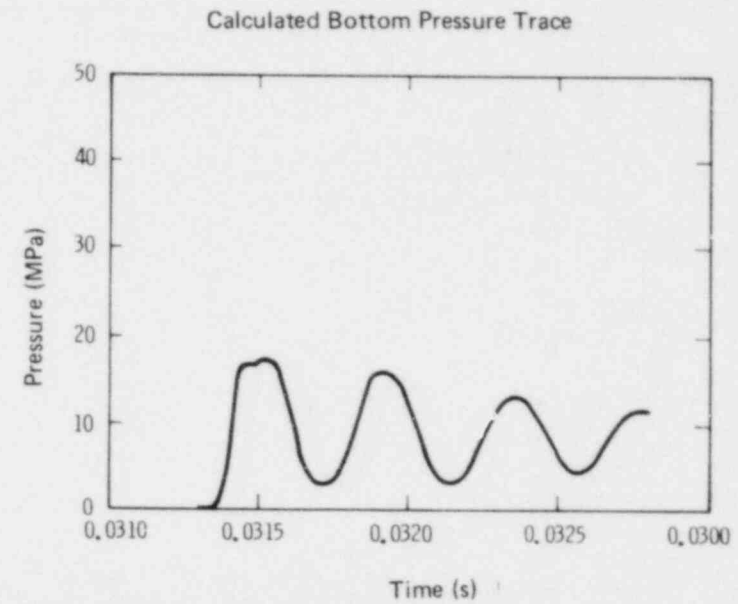
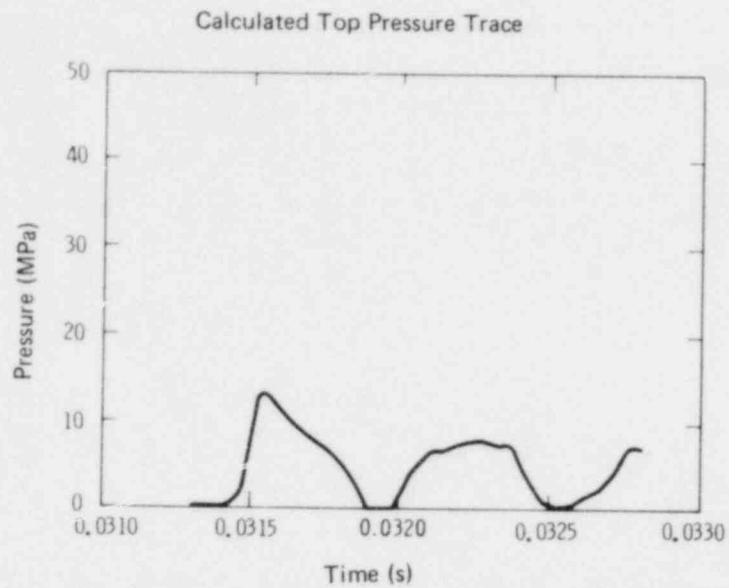
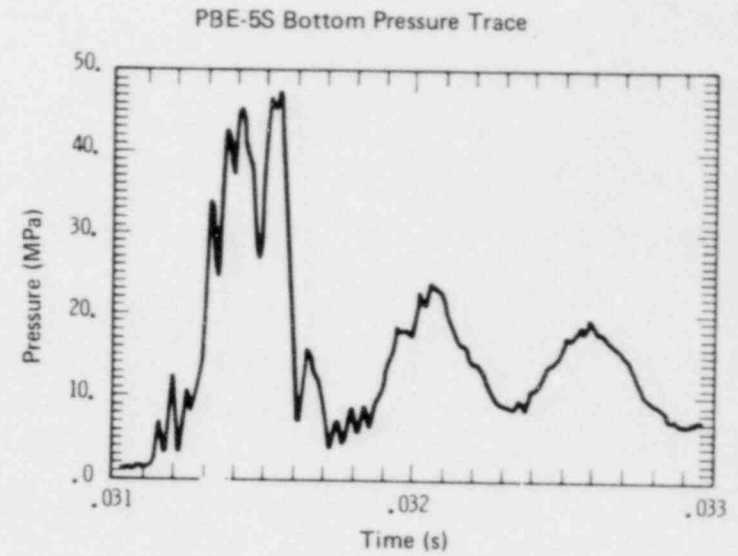
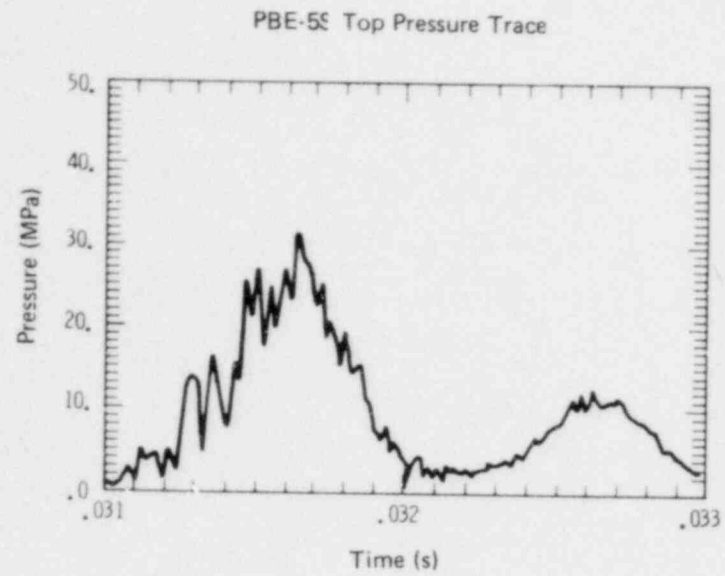


Figure 1.1-13 Comparison of the Pressure Trace Characteristics for the First 1.5 ms.

Table 1-1
PBE-5S Comparison of Calculated
and Measured Results

	Measured		Calculated	
	Top	Bottom	Top	Bottom
First Peak (MPa)	31.0	46.0	13.3	17.5
FWHM (ms)	0.35	0.28	0.28	0.22
Second Peak (MPa)	12.5	22.5	7.9	16.0
FWHN (ms)	0.40	0.32	0.39	0.24
First/Second Pressure Ratio	2.5	2.0	1.7	1.1
Period Between First and Second Peak	1.05	0.63	0.60	0.41
Bottom/Top Pressure Ratio of First Peaks	1.48		1.32	

At about 1.8 ms, a pressure wave caused by sodium vapor developed as can be seen in Figures 1.1-14 and 1.1-15, a 3-D pressure plot in the sodium channel. Although the calculations do not indicate any significant sodium-vapor pressure in the initial pressure pulses, its presence cannot yet be precluded because of the very simplistic liquid-to-liquid heat-transfer correlation in SIMMER. Further modeling and experimental work will be required to provide confirmatory evidence. The frequency of the calculated pressure oscillations is higher than the measured frequency for both transducer locations. This would indicate a lower than expected effective sonic velocity in the experiment. Also, the decay of the pressure train is slower in the calculations, perhaps due to the uniform fuel temperature approximation in SIMMER. As these results are very similar to earlier analysis done by M. Young using the CSQ-II code without heat transfer,¹⁻⁷ the effects of heat transfer are evidently not dominant in the early phase of the oxide cases. No comparison of the calculated and measured piston displacement has been made. The piston displacement is related to the integral of the top pressure curve. Given the underprediction of the pressure at the top of the pin, little displacement

is calculated to occur in the period out to 2.0 ms past failure as so far studied.

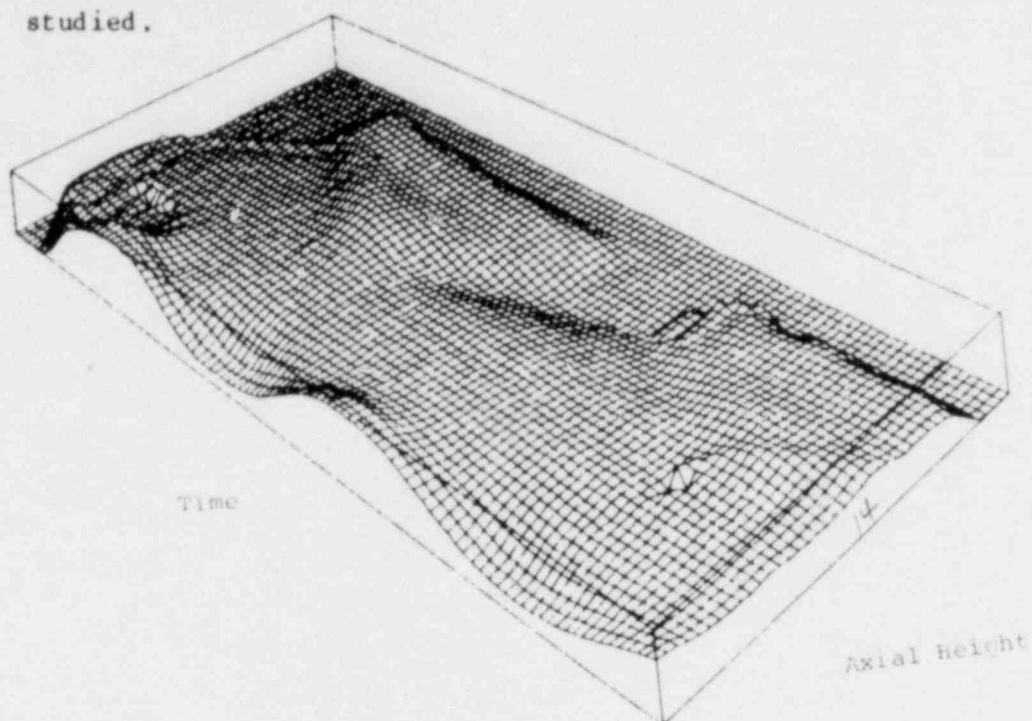


Figure 1.1-14 Pressure vs Time in Sodium Channel (0 to 1 ms)

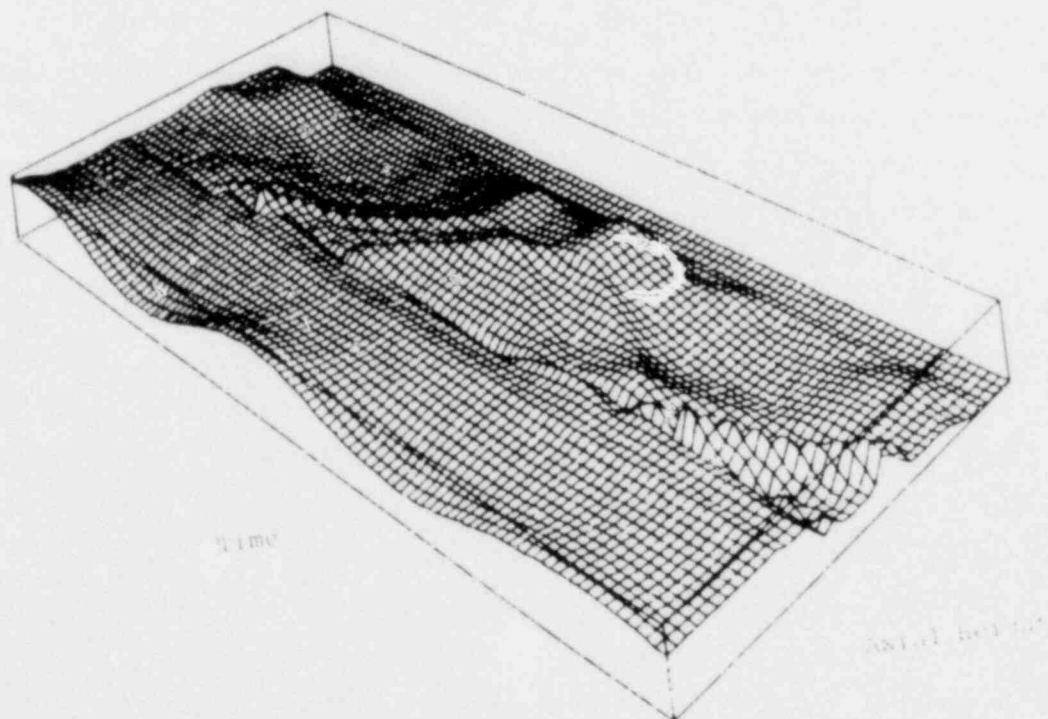


Figure 1.1-15 Pressure vs Time in Sodium Channel (1 to 2 ms)

The second (current) phase of the SIMMER work models the PBE-5S experiment more realistically. The objective is to observe the sensitivity of the calculated-pressure train and pressure-generation mechanisms to the modeling changes. The improved model contains a temperature profile and two-phase fuel in the pin at failure, area changes in the sodium channel, an improved liquid-structure heat-transfer correlation for low-liquid velocities, and variations in the initial fuel temperatures and pressures.

1.1.5 Pressure-Transducer Response

In several experiments pressure transients have been observed at the top of the test channel immediately following the deceleration of the piston. Based on these observations and other analysis, it was concluded that the pressure transient resulted from an FCI triggered by the low-amplitude pressurization produced by deceleration of the sodium slug moving with the piston.^{1-6, 1-7, 1-14}

Because of the coincidence of the pressure transient with piston stoppage (a mandrel on the piston plastically deforms a steel sleeve), work is in progress to evaluate the response of pressure transducers to this mechanical loading. A fixture has been designed and fabricated to aid in this study. This equipment will permit acceleration of a piston in the PBE experiment capsule to the velocities observed in experiments (up to 30 m/s). The output of the pressure transducers will be monitored as the piston impacts the absorber sleeve.

1.1.6 Postirradiation Examination (PIE)

PIE of PBE-7S is complete. Only complete assembly and documentation of the results remains to be completed.

Following repairs and modifications to the glove box and cutting equipment, the PBE-12S PIE is progressing. The package has been disassembled. Work is under way to remove the sodium from the cut pieces and work to recover the particulate and other debris will follow. Preliminary results from examination of a very small amount of particulate indicate

that the PBE-12S particulate is finer (smaller mean diameter) than that from PBE-7S.

PIE of the uranium-carbide experiments is dependent on the installation of a new large glove-box facility. Installation is scheduled for spring of 1979; the facility will be operational by summer. Discussions are under way with the staff of the Fast Breeder Reactor Project, KfK, Karlsruhe, West Germany, with regard to the types of analysis to be performed in the carbide PIE. KfK will send a staff member to participate in the PIE that is scheduled to begin in late August 1979.

1.1.7 Status

All preparations for the resumption of PBE experiments are completed. These include hardware and fuel procurement, expansion of the data-acquisition system, and internal safety reviews. The necessary diagnostic and dosimetry experiments will be completed in mid-April and PBE-13S will be completed in late April. Preparations for subsequent experiments, particularly PBE-14S, with tin coolant have been initiated.

Current PIE work for oxide-fueled experiments will be completed next quarter and an appropriate report will be prepared.

Work on developing an adequate FCI-analysis tool using the structure of the EPIC code will continue.

1.2 Irradiated Fuels Response (G. L. Cano, 4423; W. J. Camp, 4425; E. D. Bergeron, 4425; W. M. Breitung, 4425; D. H. Worledge, 4424; D. A. Benson, 5534; K. K. Murata, 4425; N. K. Hayden, 4425)

1.2.1 Introduction

The Sandia Laboratories Irradiated Fuels Response program is aimed at determining the response of fresh and irradiated reactor fuels to both prompt-burst (disassembly timescale) and loss-of-flow (LOF) heating conditions. On prompt-burst timescales, the pressure source from both fuel vapor and fission gases as well as the accelerations produced by

these pressure sources are of central importance. Thus the program in this area centers on determination of the effective equation-of-state (EEO) of fresh and irradiated fuels, the dynamics of pressurization (rate effects), and the ability of this pressure to disperse fuel.

On LOF timescales, the modes of initial fuel disruption and their timescales for both fresh and irradiated fuels are of crucial importance. Various mechanisms for disruption have been proposed: liquid-fuel slumping, rapid solid/liquid-state swelling, solid-state breakup, and liquid/gas-froth formation. Of these, the last two are dispersive and would tend to reduce reactivity, while the first two are not dispersive and thus would not diminish reactivity. Indeed, they could have deleterious effects on the accident progression. Thus, it is important to determine the disruption mechanisms operating under various LOF heating conditions. To accomplish this determination, the FD-1 series of fuel-disruption experiments has been performed. These experiments involved multipulse heating of single fresh and irradiated pellets in the ACPR. Film records of fuel behavior were obtained for all twelve experiments. Significant results from this series included the observation of rapid swelling as a disruption mechanism.

Currently, the experimental program in this area centers on the FD-2 series in which larger fuel sections (three pellets) are irradiated in the ACRR with heating conditions much more typical of LOF conditions than those that were obtainable in the ACPR. Additional improvements include filming of both sides of the pellet stack, gas sampling, dynamic two-color pyrometry, and contamination-free fuel handling facilities.

Analytical work in the EEO and the LOF/FD programs directly involves neutronic and thermohydrodynamic analysis of the experiments. In the case of the EEO program, the analytical work coupled to EOS theories and rate theories to unfold the equilibrium and dynamic pressure sources. In the case of LOF/FD experiments, this is coupled directly to the FISGAS code. FISGAS is intended to calculate fuel mechanics including swelling, cracking, frothing, and gas release. In its current form, it calculates swelling and gas release.

1.2.2 Disassembly Timescale EEOS Experiments

The SPR-III experiments on fresh UO_2 and irradiated mixed-oxide fuels have been completed. Analysis and modeling of the fresh-fuel experiments and modeling of the previous ACPR fresh-fuel experiments are now underway using a two-pronged approach. A simple heat-transfer analysis that ignores hydrodynamic effects is being performed using TAC2D. At the same time, CSQ-II is being employed to analyze heat transfer by conduction and radiation as well as hydrodynamic mass-transfer effects.

During January, the four SPR-III-irradiated UO_2 - PuO_2 experiments were performed using PNL-10 fuel. Powdered-fuel disks, surrounded on the radial extremities by gold filters, were irradiated with energy depositions varying up to 3000 J/g. The natural SPR-III pulse with polyethylene moderation was used yielding approximately 90% of the deposition in 0.5 ms. Experiment-unfolding for these tests is underway. The PNL-10 fuel employed was $\text{U}_{0.75}\text{Pu}_{0.25}\text{O}_2$ with 5.3% burnup. Pretest analysis of the fuel (performed in collaboration with LASL) shows that approximately 30% of the fission gases generated were retained in the fuel. Roughly 25% of this was lost when the mixed-oxide disks were reduced to 50- to 100- μ powder. This loss is potentially significant with regard to release rates during the transient.

During this period, a paper entitled "Measurement and Analysis of Transient Vaporization in Oxide Fuel Materials" was presented at the International Symposium on Thermodynamics of Nuclear Materials, Julich, FRG, on January 29, 1979. The paper discussed the effects of original sample stoichiometry, chemical interactions with the container, and non-equilibrium evaporation due to induced temperature gradients, and gave special attention to dynamic behavior in rapid heating and vaporization of the oxide due to chemical nonequilibrium.

The long-unresolved question of anomalous pressures created in the electron-beam experiments has been investigated. These pressures are considered to result from CO formation caused by the interaction of fuel with

the graphite walls. The results of these experiments are also relevant to SPR-III and planned ACRR irradiated-fuel EEOS experiments. Section 1.2.3 presents the investigational results.

1.2.3 Investigation of the Importance of CO Formation in Sandia In-Pile EEOS Experiments

1.2.3.1 Introduction -- All Sandia in-pile measurements of fuel EEOS data (ACPR, SPR-III) used pressure vessels with an inner graphite liner. With respect to the chemical equilibrium at the high temperatures involved, a strong tendency exists for oxygen to leave the liquid mixed-oxide and to combine with carbon to form gaseous CO. (The free energy of formation of this reaction is 80 kJ per mole CO at 3100 K and increases with increasing temperature.) Significant generation of CO could cause an additional, non-prototypical contribution to the measured vapor pressure of the fuel.

The three main processes influencing CO-generation rates are:

- a. The diffusion of oxygen via the gaseous phase to the graphite walls or out of liquid fuel that is in contact with graphite.
- b. The reaction of oxygen with graphite at the graphite surface.
- c. The release of the reaction product CO into the graphite container volume.

A thorough investigation of this combined mass-transfer problem is hindered by the unknown reaction kinetics of atomic oxygen with graphite and by the uncertain fuel geometries during the experiment. Therefore, investigators decided to examine only the possible oxygen-diffusion fluxes for different idealized fuel geometries. The resulting CO-pressure histories are consequently upper estimates for possible CO pressures.

When currently conducted experimental analysis and posttest examinations yield more information about fuel geometry, the maximum pressure of the CO generated during the experiments can be estimated by combining the calculated pressure histories of the ideal geometries.

The oxygen transport was investigated for two fuel geometries: a quiescent layer of liquid fuel resting on the container bottom (slab geometry, Figure 1.2-1) and a system of homogeneously distributed liquid droplets of uniform radius (droplet geometry, Figure 1.2-2).

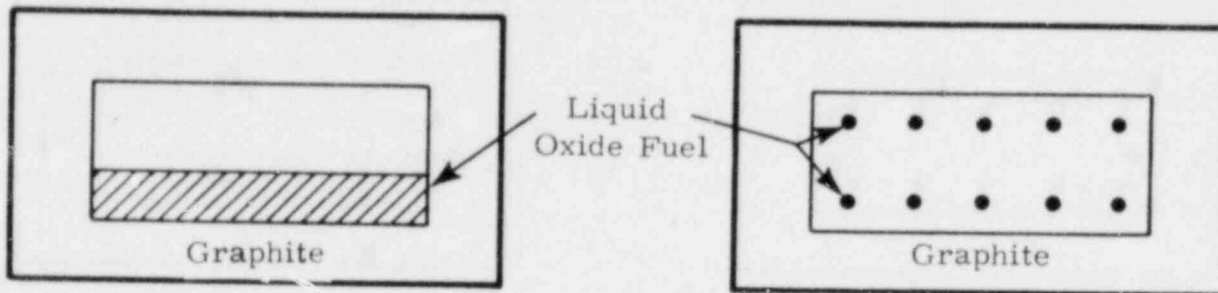


Figure 1.2-1 Slab Geometry

Figure 1.2-2 Droplet Geometry

The fundamental quantity describing the movement of oxygen is the diffusion coefficient. Therefore, values for the diffusion coefficient of gaseous oxygen in different atmospheres and the diffusion coefficient of oxygen in liquid-oxide fuel have to be estimated.

1.2.3.2 Oxygen Diffusion Coefficients

1.2.3.2.1 Oxygen Diffusion Coefficient in Liquid (U,Pu)O₂ -- Table 1-2 contains the nomenclature (definitions) for the development to follow.

Since the oxygen diffusion coefficient in condensed-oxide fuel depends exponentially on temperature, it is important to determine the temperature at the fuel-graphite interface.

Table 1-2
Nomenclature for Section 1.2.3.2.1

<u>Symbol</u>	<u>Physical Quantity</u>	<u>Dimension</u>
T_f^∞	Fuel temperature in the undisturbed region	K
T_i	Fuel-carbon interface temperature	K
T_c^∞	Carbon temperature in the undisturbed region	K
k	Thermal conductivity	J/s mK
ρ	Density	kg/m ³
C_p	Heat capacity	J/g • K
R	Gas constant	J/mol • K
μ_f	Viscosity of liquid fuel	cP
ϕ_f	Association parameter for liquid fuel (= 1 for unassociated solvents)	--
M_f	Molecular weight of fuel	kg/mole
V_b	Molal volume of fuel at normal boiling point	m ³ /mol
D_o	Self-diffusion coefficient of oxygen in condensed fuel	m ² /s
\tilde{D}_o	Chemical diffusion coefficient of oxygen in condensed fuel	m ² /s
x	Stoichiometry deviation of the oxide	--
σ	Collision diameter	Å
Ω_D	Collision integral, listed in (1)	--
V_c	Critical molar volume	m ³ /kg
T_c	Critical temperature	K
P_c	Critical pressure	Pa
D_o^{gas}	Oxygen diffusion coefficient in the gas phase	m ² /s
j_o	Oxygen flux	mole/sm ²
P_{CO}	CO-pressure	Pa

Table 1-2 (Cont)

<u>Symbol</u>	<u>Physical Quantity</u>	<u>Dimension</u>
$P_{O, surf}$	Oxygen partial pressure above liquid fuel	Pa
ΔZ	Diffusion distance	m
F	Diffusion area	m^2
t	Diffusion time	s
V_{free}	Free capsule volume	m^3
n_o	Diffused oxygen per unit area	mole/ m^2
C_m	Concentration of metal atoms in liquid fuel	mole/ m^3
h	Thickness of CO film	m
β	Relative contact area	m^2/m^2
d	Mean droplet distance	m
R_d	Droplet radius	m
α	Fuel volume fraction	m^3/m^3
V_{tot}	Total volume of capsule	m^3
O_{cr}	Inner capsule surface area	m^2

The following relationship results from semiinfinite heat-conduction calculations for two materials that are in perfect contact:¹⁻¹⁵

$$\frac{T_f^\infty - T_i}{T_i - T_c^\infty} = \frac{(k C_p)_c}{(k C_p)_f} \quad 1/2 \quad (1.1)$$

Figure 1.2-3 illustrates Eq (1.1).

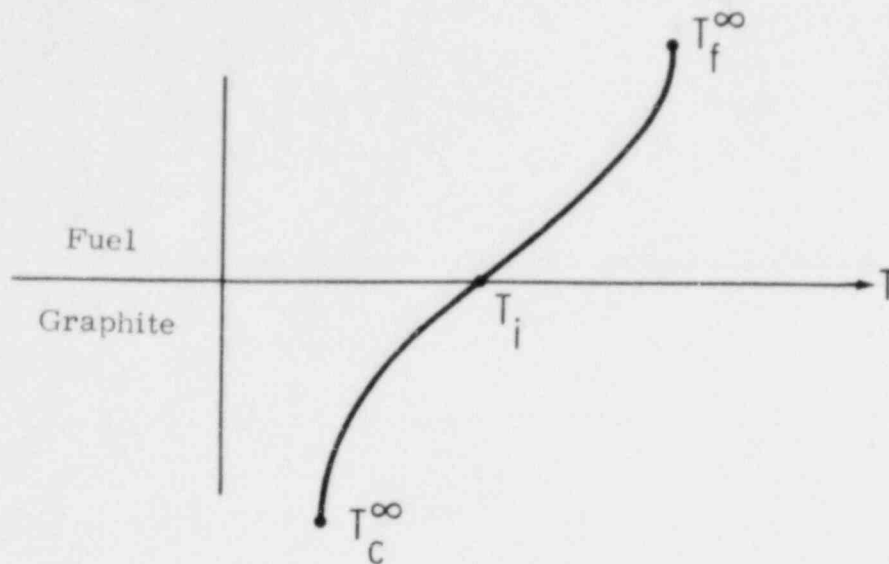


Figure 1.2-3 Illustration of Eq (1.1)

The interface temperature is established within microseconds and independent of time. With the appropriate material data, T_i becomes

T_{fuel}^{∞}	[K]	4000	5000	(1.2)
T_i	[K]	2730	3380	

No appreciable oxygen transfer is possible when the interface temperature (T_i) drops below the fuel-solidus temperature (3043 K) due to the separating of solid fuel and carbon by expanding CO. In addition, the oxygen mobility in solid fuels is too low¹⁻¹⁶ to result in measurable CO pressures. Significant CO pressures could be generated only when the contacting bulk fuel is at temperatures near 5000 K. Therefore, the oxygen diffusion coefficient will be determined for the respective interface temperature of 3380 K. The most verified correlation for the self-diffusion coefficient of nonelectrolytes in dilute solution is¹⁻¹⁷

$$D_o = \frac{T}{U_f} \frac{7.4 \times 10^8 (\phi_f M_f)^{1/2}}{V_f^{0.6}} \quad (1.3)$$

Assuming $M_f = 270$ g/mole, $\phi_f = 1$ (unassociated liquid-fuel molecules), $V_f = 32.5$ cm³/mole¹⁻¹⁸, and $\mu_f (T_{\text{melt}} = 3043 \text{ K}) = 4.51$ cp¹⁻¹⁹ gives

$$D_o(3043 \text{ K}) = 1.0 \times 10^{-8} \text{ m}^2/\text{s} \quad (1.4)$$

This result seems reasonable if compared to the following sources:

- a. The self-diffusion coefficient at the melting temperature ranges for a great variety of crystal between 10^{-9} and 10^{-8} m²/s¹⁻²⁰
- b. Extrapolation of measured oxygen self-diffusion coefficients in solid UO₂ gives $D_o(3042 \text{ K}) = 0.5 \times 10^{-8}$ m²/s.¹⁻¹⁶

However, because the oxygen ions of the fuel oxide are migrating in a chemical potential gradient due to the reduction of MO₂ to MO_{2-x}, their movement is described by the chemical diffusion coefficient, \tilde{D} . Reference 1-16 shows that the relation to the above calculated self-diffusion coefficient D_o is given by

$$\tilde{D}_o = D_o \frac{(2+x)}{(2RT)} \frac{d}{dx} (\Delta G_{O_2}). \quad (1.5)$$

The gradient of $(\Delta G_{O_2})/dx$ can be estimated from existing theoretical models for $\Delta G_{O_2}(x,T)$. At a temperature of 3380 K (slightly above the fuel melting point), the result is:

$$\tilde{D}_o(3380 \text{ K}) = (8.1 \pm 4.0) (10^{-7} \text{ m}^2/\text{s}). \quad (1.6)$$

For this investigation, \tilde{D}_o can be regarded as independent of the stoichiometry deviation, x .

1.2.3.2.2 Diffusion Coefficient of Gaseous Oxygen -- Reference 1-21 presents the following equation for the diffusion coefficient for gas pairs of nonpolar molecules A and B:

$$D_{AB} = \frac{1.858 (10^{-3}) T^{3/2} \left(\frac{1}{M_A} + \frac{1}{M_B} \right)^{1/2}}{p \sigma_{AB}^2 \Omega_D} \quad (1.7)$$

where:

- D_{AB} = mass diffusivity of A diffusing through B in cm^2/s ;
- T = absolute temperature in K
- M_A, M_B = molecular weights of A and B, respectively
- p = absolute pressure in atmospheres
- σ_{AB} = "collision diameter" a Lennard-Jones parameter in Angstroms
- Ω_D = "collision integral" for molecular diffusion, a dimension-less function of the temperature and of the intermolecular potential-field for one molecule of A and one molecule of B.

Reference 1-17 lists Ω_D as a function of $\kappa T/\epsilon_{AB}$; κ is the Boltzmann constant, which is 1.38×10^{-16} ergs/K; and ϵ_{AB} , a Lennard-Jones parameter, in ergs. The collision diameter σ_{AB} may be estimated from empirical relations when no experimental values are available,¹⁻²¹ as

$$\sigma_{AB} = \sigma_A + \sigma_B \quad (1.8)$$

where: $\sigma = 1.18 v^{1/3}_b$ or $\sigma = 0.841 v^{1/3}_c$ or $\sigma = 2.44 (T_c/P_c)^{1/3}$. ϵ_{AB} may be calculated from

$$\epsilon_{AB} = (\epsilon_A \cdot \epsilon_B) \quad (1.9)$$

where: $\epsilon/\kappa = 0.77 T_C$ or $\epsilon/\kappa = 1.15 T_B$ or $\epsilon/\kappa = 1.92 T_m$.

The gaseous oxygen diffusion coefficient (D_o^{gas}) depends on the total pressure (P) and the second gas components (B).

For the actual diffusion calculations, the following atmospheres are considered:

- a. In the case of fresh-fuel, oxygen diffusion is investigated for a pure fuel-vapor atmosphere (UO_2 -vapor). The diffusion coefficients resulting from Eq (1.7) are given in Table 1-3.
- b. For irradiated fuel, the diffusion atmosphere is assumed to consist of Xe and fuel vapor: the Xe is dominant at low temperatures and the fuel vapor at high temperatures. Since $D_o^{UO_2}$ is very similar to D_o^{Xe} for the same temperature and pressure, the diffusion coefficient of oxygen in the UO_2 -Xe-atmosphere is given with sufficient accuracy by

$$D_o^{UO_2-Xe} = D_o^{UO_2} \frac{P_{UO_2}}{P_{UO_2} + P_{Xe}}$$

Table 1-4 shows the fission-gas pressures P_{Xe} as estimated for a typical SPR-III experiment, the total capsule pressure ($P_{UO_2} + P_{Xe}$) and the resulting oxygen diffusion coefficient.

Table 1-3

Oxygen Diffusion Coefficients for Fresh-Fuel Experiments
($D_o^{UO_2}$ is strongly reduced with increasing temperature due to the increasing fuel-vapor pressure.)

T (K)	P_{fuel} (bar)	$D_o^{UO_2}$ (10^4 m ² /s)
3000	$3 \cdot 10^{-2}$	261
4000	8	1.57
5000	100	.18

Table 1-4

Oxygen Diffusion Coefficients for Irradiated-Fuel Experiments

T (K)	P_{Xe} (bar)	$P_{UO_2} + P_{Xe}$ (bar)	$D_o^{Xe-UO_2}$ (10^4 m ² /s)
3000	23.2	23.23	.450
4000	31.0	35	.431
5000	38.7	138.7	.130

Since the calculation procedure required estimation of some data, the oxygen diffusion coefficients were calculated for the $O-O_2$ system and compared with values given in Ref 1-22. The agreement in the temperature region from 3000 to 5000 K is within 7%. The calculated oxygen diffusion coefficients were used to calculate oxygen fluxes within typical SPR-III-capsule designs.

1.2.3.3 Estimated Oxygen Fluxes Within SPR-III Capsules

1.2.3.3.1 Liquid-Oxide Slab Geometry

- a. Gaseous Oxygen Diffusion. In one-dimensional geometry, the diffusion flux of oxygen from the

oxide surface across the full volume to the opposite container wall is given by

$$j_o = \frac{D_{o,gas} P_{o,surf}}{RT \Delta Z} \quad (1.11)$$

The resulting CO pressure as a function of time is then given by

$$P_{CO} = j_o \cdot F \cdot t \cdot RT/V_{free}, \text{ or}$$

$$P_{CO} = \frac{D_{o,gas} \cdot P_{o,surf} \cdot F \cdot t}{\Delta Z \cdot V_{free}} \quad (1.12)$$

$P_{o,surf}$ is the oxygen partial pressure at the liquid-oxide surface. The CO-pressure buildup according to Eq (1.12) is shown in Figure 1.2-4. Curve parameters are system temperature (3000, 4000, or 5000 K) and diffusion atmosphere (pure UO_2 -vapor for fresh-fuel experiments; Xe- UO_2 -atmosphere for irradiated-fuel experiments).

- b. Oxygen Diffusion in the Condensed Phase. At the interface between liquid fuel and carbon, CO may be generated by direct diffusion of oxygen ions to the carbon surface, thereby creating an oxygen-depleted zone within the oxide (Figure 1.2-5). The maximum oxygen depletion that can occur at the oxygen-graphite interface is given by the metallurgical-phase boundary in the (U,Pu)-O system. The phase boundary can be estimated from existing phase diagrams to be about $(O/M)_{ph.b.} = 1.5$ at temperatures slightly above the melting point.

In semi-infinite geometry, the solution of this diffusion problem gives for the total number of oxygen moles n_o diffused out of the liquid-oxide slab after the contact time, t :

$$n_o(t) = c_m \left(\frac{\bar{D}_o t}{\pi} \right)^{1/2} \frac{\text{moles}}{m^2} \quad (1.13)$$

The CO-pressure generation as calculated from Eq (1.13) ($P_{CO} = F \cdot n_o \cdot RT/V_{free}$) is very rapid (Figure 1.2-4, curve 6). However, in deriving

Eq (1.13) the assumption of undisturbed contact between the liquid oxide and the carbon surface is unrealistic due to the CO gas generated between them. More likely, a CO-film will spread between the liquid oxide and the graphite surface as oxygen diffusion proceeds (Figure 1.2-6). Because of the spreading of the CO film, the contact area, the oxygen flux into the carbon, and consequently the CO-generation will decrease with time. When the CO film is established, virtually no more CO is generated and the liquid layer collapses back onto the carbon. As the liquid layer collapses, the CO is released to the free volume above the oxide layer.

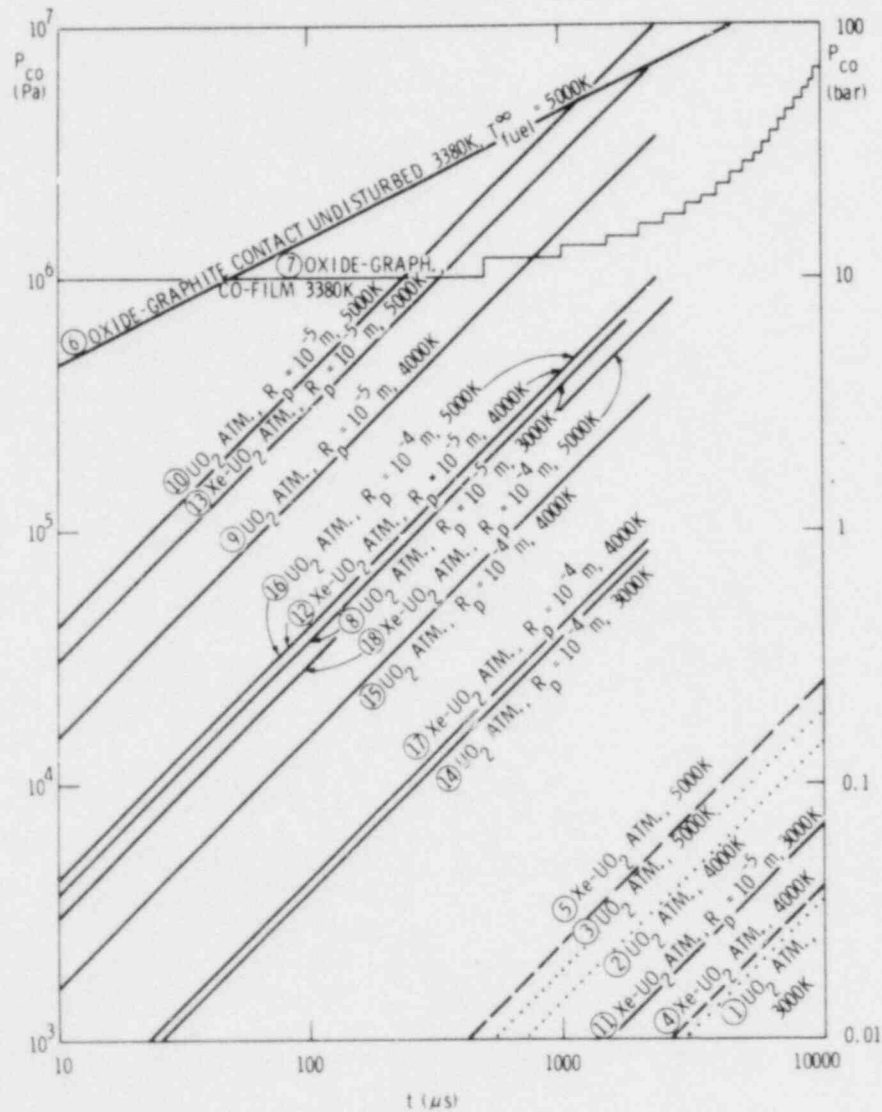


Figure 1.2-4 Calculated Maximum CO-Partial Pressure vs Time for Different Capsule Conditions and Fuel Geometries

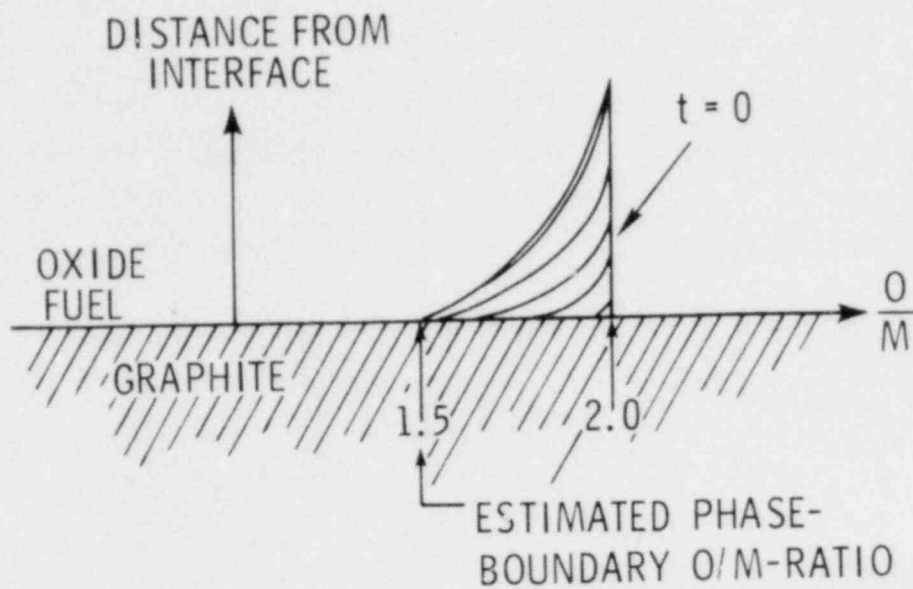


Figure 1.2-5 Oxygen Diffusion in the Condensed Phase

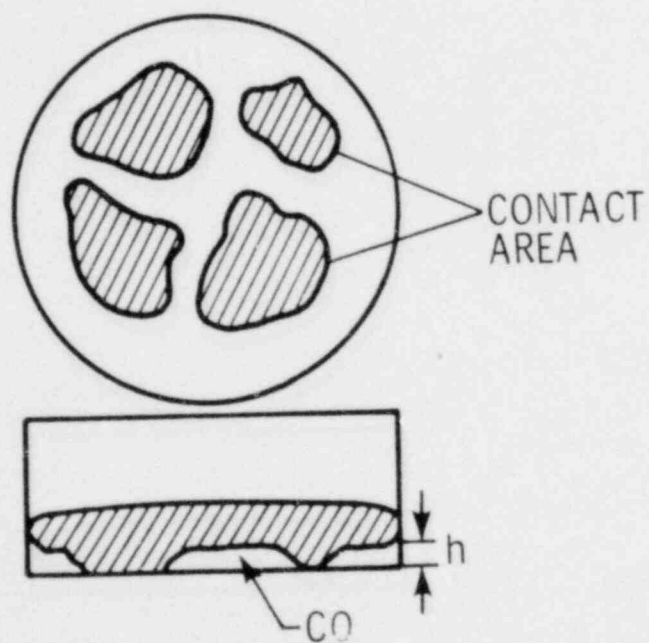


Figure 1.2-6 CO Film Formed as Oxygen Diffusion Proceeds

If the oxygen transfer to the carbon is assumed to be proportional to the instantaneous contact area, the following equation results for the relative contact area as a function of time:

$$\beta = \frac{\text{contact area betw. oxide and graph}}{\text{total container bottom area}} = \exp \left[- \frac{c_m RT}{p_{\text{tot}} h} \left(\frac{\tilde{D}_o t}{\pi} \right)^{1/2} \right] \quad (1.14)$$

Introduction of the appropriate numbers shows that the CO film could be completely formed ($p \approx 0$) in times shorter than 1 μ s, due to the high oxygen fluxes that are required for the film to collapse, because the forces acting on the liquid fuel are not well known at present. If gravity were the dominant force on the liquid layer, a 0.1-mm-thick CO film would collapse in about 4 ms. In this case the film-oscillation time would be about 4 ms. If additional forces are acting on the oscillating liquid-fuel layer (for instance, vapor-recoil forces due to rapid fuel evaporation), the oscillation frequency would be higher. Since the total capsule pressure after n oscillations would be

$$p_{\text{tot},n}(t) = p_o \left(1 + \frac{V_{\text{film}}}{V_{\text{free}}} \right)^{n(t)}, \quad (1.15)$$

the CO pressure is governed by the number of oscillations $n(t)$ and hence, indirectly, by the mean-collapse time of the CO film. In Eq (1.15), p_o is the initial gas pressure of 10 to 15 bar, and $V_{\text{film}}/V_{\text{free}}$ is the ratio of CO-film volume to total free volume in the capsule ($V_{\text{film}}/V_{\text{free}}$ probably ranges between 0.03 and 0.3). If the film-collapse times are considerably less than 1 ms, an appreciable CO pressure could be generated during the measuring times, in spite of CO-film formation.

As an example, the CO-pressure generation due to an oscillating liquid-fuel layer is given in Figure 1.2-4 for the not unreasonable figures of $p_o = 10$ bar, $V_{\text{film}}/V_{\text{free}} = 0.1$ and $\Delta t_{\text{oscillation}} = 0.5$ ms (curve 7).

1.2.3.3.2 Liquid-Oxide Droplet Geometry

a. Introduction. A number of mechanisms may cause dispersal of the test fuel into droplets, most of them related to the nonuniform energy deposition. For fresh fuel, they include:

- (1) Differential thermal expansion
- (2) Nonuniform vapor-recoil forces at the evaporating-liquid surface
- (3) Nonuniform vapor pressures due to inhomogeneities in the fissile distribution.

Irradiated fuel may be dispersed also by expanding-grain-boundary fission gas or by other fission products with high vapor pressures and nonuniform distribution such as Cs.

In fuel dispersal, the droplet geometry will last only for a period of milliseconds but, because of the larger fuel-surface area, a potential for rapid oxygen transfer exists. Therefore gaseous diffusion fluxes were estimated for the liquid-droplet geometry.

Stability criteria show that fuel droplets of the anticipated sizes (similar to grain sizes in experiment FD-1.6) will not be reflected elastically from the container walls, but instead will coat the container walls with a layer of liquid oxide. The maximum possible CO generation during this later phase of the experiment can be estimated from curve 6 of Figure 1.2-4, the respective curve for slab geometry.

b. Gaseous Diffusion. In a system of homogeneously distributed liquid-fuel droplets, the oxygen partial pressure is essentially homogeneous inside the system (Figure 1.2-7). A significant zero-partial-pressure gradient will exist only between the outer-most droplet layer and the graphite surface. Therefore the linear geometry solution as given in Eq (1.12) may be used.

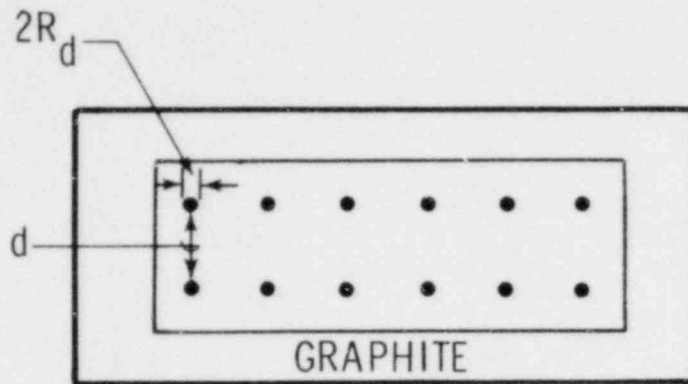


Figure 1.2-7 System of Homogeneously Distributed Liquid-Fuel Droplets of Uniform Radius R_d

The following modifications of Eq (1.12) are made:

- (1) Diffusion distance ΔZ is equal to the mean-droplet distance (d) in the system.

$$d = 2R_d (\alpha^{-1/3} - 1) \quad (1.16)$$

with

R_d = droplet radius

$$\alpha = \text{fuel volume fraction} = \frac{V_{\text{fuel}}}{V_{\text{total}}}$$

- (2) The effective surface for diffusion (F_D) is the sum of all droplet half-sphere areas ($2\pi R_d^2$) within the outermost layer of droplets:

$$F_D = O_{\text{cr}} \cdot \alpha^{2/3} \quad (1.17)$$

with O_{cr} = crucible surface area.

- (3) The free volume is expressed as $V_{\text{free}} = V_{\text{tot}} (1 - \alpha)$. The following equation then results for the CO-pressure buildup due to gaseous-oxygen diffusion:

$$P_{CO} = \frac{D_{O,gas} \cdot P_{O,surf} \cdot t}{2R_d} \cdot \frac{O_{cr}}{V_{tot}} \cdot \frac{\alpha^{2/3}}{(1-\alpha)(\alpha^{-1/3}-1)} \quad (1.18)$$

The CO pressure according to Eq (1.18) was calculated for a typical graphite container (height 5 mm, diameter 4.9 mm) with the following parameters:

- Droplet radius 10^{-5} m (grain size) and 10^{-4} m
- UO_2 -atmosphere (fresh-fuel experiments) and UO_2 -Xe-atm (irradiated-fuel experiment)
- Temperature 3000, 4000, and 5000 K
- Fuel volume ratio $\alpha = 1/3$

In Table 1-5 the different parameter combinations are related to the curve numbers of Figure 1.2-4. Increase of the fuel-volume ratio to 1/2 increases all CO pressures (curves 8 to 19) by a factor of 3. Decrease of α to 1/4 reduces all pressures by a factor of 1.7.

1.2.3.4 Conclusions. From Figure 1.2-4, a number of conclusions can be drawn about the important oxygen-transfer mechanisms and resulting maximum CO-generation rates.

1.2.3.4.1 Slab Geometry

- a. Diffusion of gaseous oxygen from the surface of the liquid-oxide via the above gas phase to graphite is too slow to cause measurable CO-pressures within times less than 10 ms (curves 1 to 5).
- b. Oxygen diffusing out of liquid-oxide contacting graphite is, in principle, rapid enough to create significant CO pressures if the bulk fuel is about 5000 K and if no additional resistances are present at the oxide-graphite interface (curve 6). For oxygen diffusion, even the development of a spreading and collapsing CO-gas film between oxide and graphite may not prevent appreciable CO formation in the capsule. This is because less than 1 μ s is needed for the complete formation of a CO film (vertical lines of curve 7) and the CO

pressure generation is therefore determined by the film-collapse time (horizontal lines of curve 7). Collapse times of less than 0.5 ms, as assumed for curve 7, can result in rapid CO pressure generation.

Table 1-5

Summary of the Investigated Oxygen Diffusion Problems

Geometrical Configuration of Liquid Fuel	Oxygen Diffusion Path	Diffusion Atmosphere	Temperature (K)	Curve Number in Fig. 1.2-4	
Slab Geometry	Diffusion via gas phase	UO ₂ vapor (fresh fuel)	3000	1	
			4000	2	
			5000	3	
		Xe-UO ₂ mixture (irr. fuel)	4000	4	
			5000	5	
	Fuel-graphite interface undisturbed	Diffusion out of liquid-oxide fuel to graphite surface	—	Bulk fuel 5000 interface 3380	6
	Spreading CO-film		—	Bulk fuel 5000 Interface 3380	7
Droplet Geometry (Fig. 1.2-2)	Droplet radius R _d = 10 ⁻⁵ m (grain size)	UO ₂ vapor	3000	8	
			4000	9	
			5000	10	
		Xe-UO ₂ vapor	3000	11	
			4000	12	
			5000	13	
	Droplet radius R _d = 10 ⁻⁴ m (1000 grain)	UO ₂ vapor	3000	14	
			4000	15	
			5000	16	
		Xe-UO ₂ vapor	3000	Too small	
			4000	17	
			5000	18	

However, mechanisms exist that are likely to create additional resistances against oxygen transfer:

- a. Limited C-O-reaction kinetics
- b. Poor oxide-graphite contact due to nonwetting and to the porous microstructure of graphite.

Experimental results are needed to clarify the inhibiting capability of these two mechanisms.

1.2.3.4.2 Droplet Geometry

- a. Droplet geometry is estimated to exist in the capsule only for a period of milliseconds after fuel dispersal occurred.
- b. If the liquid fuel is dispersed in droplets with a mean radius larger than about 10^{-4} m, CO pressures less than 10 bars due to oxygen diffusion via the gas phase are expected during-the-period of milliseconds after fuel dispersal (curves 14 to 18).
- c. If the liquid fuel is dispersed in grain-sized droplets (about 10^{-5} m) or even less, CO pressures significantly above 10 bars could be possible in the ideal droplet geometry if the outermost layer experiences temperatures between 4000 and 5000 K for several milliseconds (curves 9, 10, 13). However, in reality, not only oxygen will be transported to the container walls but also a several-fold amount of fuel vapor that has a high probability of condensing on the cold walls. Such a fuel-vapor-deposition layer, which was detected in posttest examinations, is likely to suppress oxygen transfer drastically. Therefore gaseous oxygen diffusion is not expected to lead to considerable CO generation.
- d. Some milliseconds after fuel dispersal, a significant part of the liquid fuel may coat the container walls due to the internal-pressure generation. As in the case of undisturbed slab geometry, the CO formation is determined by the time for which the interface temperature is above the fuel-melting point. Curve 6 shows that only 0.1 ms at 3380 K would be necessary to create CO pressures above 10 bars, if additional transfer resistances are again neglected.

In summary, with and without fuel dispersal the highest potential for appreciable CO formation comes from liquid fuel that is

- Contacting graphite for more than 0.1 ms
- Maintaining a temperature of 5000 K or above
- A layer thickness of at least 0.1 mm.

To finally clarify the actual CO generation during in-pile experiments the following additional information will be gathered:

- Experimental results about C-O-reaction kinetics
- Energy deposition and transfer as a function of time to determine whether and how long contacting bulk fuel is at critical temperatures of 5000 K or above.

1.2.4 Disassembly - Timescale Fuel-Dispersal Analysis

Under prompt-burst conditions, the work potential of expanding fuel vapor is a sensitive function of initial fuel temperature and thus of the ability of fission-product gases to cause fuel dispersal milliseconds before dispersal would occur from fuel-vapor pressure alone. A fuel-disruption experiment in the FD-1 series exhibited rapid disruption probably below but near the fuel-melting temperature. This experiment (FD-1.6) consisted of heating a single fuel pellet (including original cladding), previously irradiated in EBR-II to 4.9 atom percent burnup, in the ACPR with two short-power pulses. The first pulse raised the hottest parts of the pellet to a calculated temperature of 1800 K. This temperature was maintained within ± 200 K for 0.45 s before another, larger, pulse with a FWHM of 11 ms drove the fuel through melting. The disruption was recorded on high-speed motion-picture film and was seen to occur 3.5 ± 0.5 ms before the peak of the pulse. At disruption the heating rate was 133 K/ms (1.33×10^5 K/s) in the hottest part of the fuel.

According to calculations, at the time of disruption an axial temperature gradient at a given radius exists with a peak-to-minimum ratio of

1.22. The highest temperatures were at the ends of the pellet. The disrupted fuel appeared to come from these regions, squirting out between the still-intact cladding and the spring-loaded end restraints. Calculations show that the highest temperatures at the axial ends occurred at a fractional radius of 0.6 to 0.7 with radial temperatures decreasing by about 300 K both toward the centerline and toward the surface.

Photographic-radiometric measurements of the maximum temperature at the surface of the expanding cloud of disrupted fuel yield, on extrapolation back to disruption time, a temperature of 2700 K. Calculations using the two-dimensional time-dependent heat-transfer program (TAC 2D) yield a temperature of 2600 K for the hottest node at disruption time. Uncertainties in measured and calculated temperatures amount to no more than ± 200 K for each. Both determinations of the disruption temperature, therefore, support the hypothesis that fuel disruption below but close to the fuel melting point is caused by fission gas.

Throughout the period before disruption, maximum fuel temperatures were more than 1000 K below those necessary to produce even 1 bar of fuel-vapor pressure. The disruption was, therefore, induced by pressures arising from retained fission products. The film record suggests that the breakup produced very small particles of fuel, possibly on a granular-size scale.

The heating transient in FD-1.6, unlike that of other experiments in the FD-1 series, resembled a prompt burst and was not prototypic of LOF heating conditions. Further experiments with similar heating rates are planned for the third quarter of 1979. These experiments will explore the sensitivity of the disruption behavior to (a) pretreatment (i.e., temperature and duration before fast heating begins), (b) heating rate after pretreatment, and (c) maximum temperatures attained.

To assist in planning experiments and to gain some insight into the behavior demonstrated in FD-1.6, a fission gas-release code has been programmed to model transient behavior of intragranular fission gas. The

calculation is based on the Harwell NEFIG¹⁻²³ model with some improvements. The additional assumption is made that random migration of small bubbles contributes to coalescence and single-gas-atom sweeping.

The model has not yet been built into a whole-pin calculation but has been used to calculate the transient gas release in the FGR 39 experiment.¹⁻²⁴ In this experiment, in that part of the fuel where the retained fission-gas concentration was both high and approximately constant, a reasonably uniform heating rate and temperature gradient were maintained throughout the transient. Therefore, a calculation of the gas release based on a single typical grain can represent fairly accurately the overall response.

Assuming that the early release of about 10% of the retained gas at low temperature (about 1673 K) was unrelated to intragranular-gas behavior, the comparison between experiment and calculation shows close agreement (Figure 1-2.8). Considering the approximate treatment of experimental conditions, this is very satisfactory and gives confidence in applying the model to the FD-series transients.

Application of the model to the FD-1.6 experiment shows that by the time of disruption only about 1% of the intragranular gas reaches grain boundaries by biased migration of bubbles in a temperature gradient. Although gas release by random migration is not included in the calculation, it will probably add no more than 1% to the above value. Under these circumstances, it is difficult to see how the disruption behavior can be accounted for by freshly released intergranular gas, even assuming there is no mechanical equilibration of bubble pressure on grain boundaries during such a fast transient. Grain-boundary-vacancy-diffusion calculations similar to those performed by Hull and Rimmer¹⁻²⁵ and by Speight and Harris¹⁻²⁶ suggest grain-bubble-equilibration times of the same order as the FD-1.6 transient time (i.e., 1 to a few milliseconds).

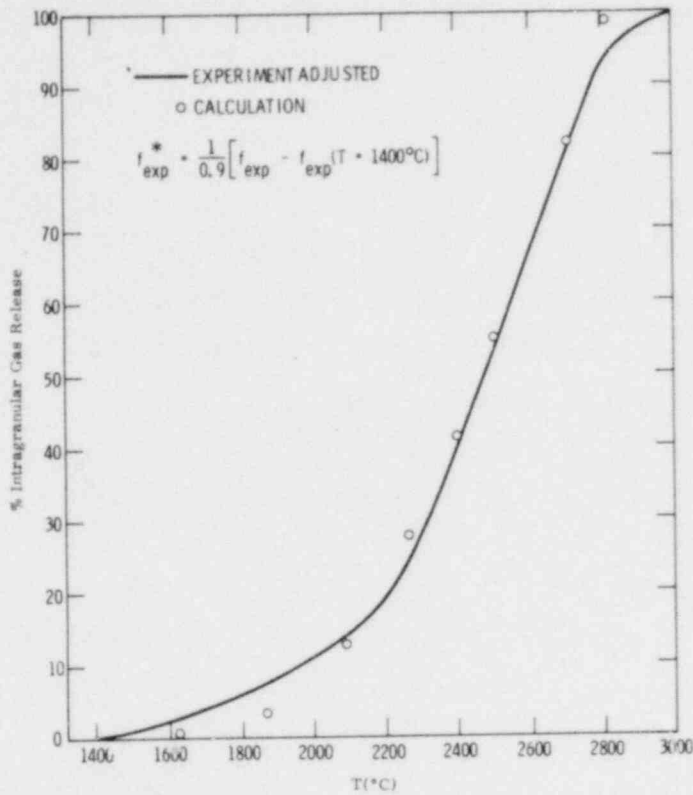


Figure 1.2-8 FGR39* Adjusted to Exclude Early Gas Release

Preexisting grain-boundary gas, if there is any, is not likely to be responsible for disruption by overpressure during the transient since heating from 1800 through 2700 K will only increase the bubble pressure by 50%. Two possibilities for disruption remain: intragranular pressures may disrupt grains, and/or inter- and intragranular gases may produce rapid plastic deformation close to the melting point.

At least two criteria must be satisfied before local stresses within grains can lead to transgranular fracture. The stresses must first exceed the brittle fracture strength and, secondly, enough energy must be available to create crack surfaces. There are large uncertainties in both of these criteria. The brittle fracture stress of single crystal, but very impure (4.9% burnup) UO_2 is not known. However, fracture surfaces in polycrystalline UO_2 exhibit a mixture of intergranular and transgranular fractures; perhaps the single-grain brittle-fracture stresses in

irradiated UO_2 are not far from the polycrystalline value of about 1.4×10^5 kN/m² (1400 bars). These stresses are easily exceeded during fast transients in the vicinity of small intragranular bubbles, sometimes by more than an order of magnitude.

In calculating energy requirements for transgranular fracture, some geometric configuration of bubbles must be envisaged. The simplest configuration is to consider each bubble in a volume, C_b^{-1} , where C_b is the volume concentration of bubbles. The surface area of a disk-shaped crack around a bubble of radius (a) is then $2\pi(R^2 - a^2)$ with R given by about $(1/4 C_b)^{1/3}$ if the crack from one bubble is to join that from its nearest neighbor. A comparison of this energy requirement with the work done by gas loading is shown in Figure 1.2-9, using the calculations for FD-1.6 for different crack height openings. Although the criterion is not met, under favorable circumstances the gas loading is able to propagate cracks 30 to 50% of the distance required for them to join up. The elastic strain energy in the lattice, based on values of Young's Modulus between 1.4×10^{11} N/m² to 0.5×10^{11} N/m² over the range of temperature of interest, is more than an order of magnitude smaller than energy from gas loading and cannot contribute significantly. Therefore, it appears that some potential exists for intragranular breakup. However, the same can be said of the other transients in the FD-1 series that did not exhibit disruption. The heating rate in these other FD-1 experiments was about one order of magnitude slower than in FD-1.6 (about 10 K/ms rather than 100 K/ms).

Investigation is continuing on rapid plastic deformation near the melting point and on the possibility of frothing or foaming once melting has occurred. In addition, an intergranular gas model is being prepared that will allow a proper examination of intergranular-bubble conditions to be made.

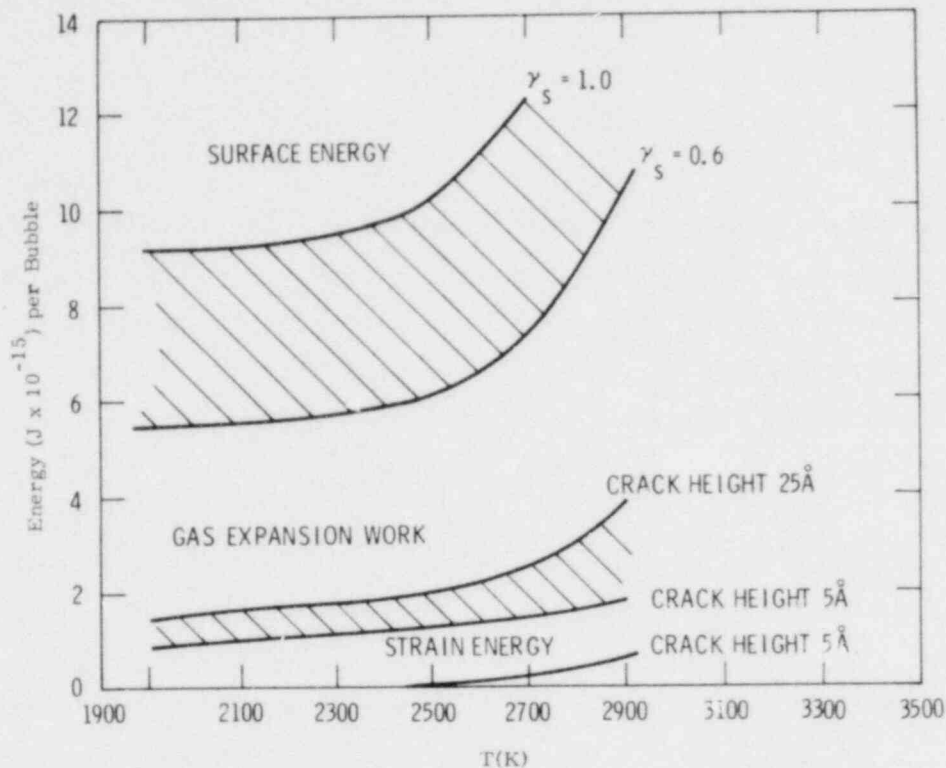


Figure 1.2-9 Comparison of Energy Required and Energy Available for Crack Propagation Between Intragranular Bubbles in FD 1.6.

1.2.5 ACRR Disassembly Timescale EEOS Experiments

Because of the marginal deposition capabilities in SPR-III with respect to both dose and profile, the irradiated-fuels EEOS experiments are being moved to the ACRR. This shift has several advantages:

- A much better profile can be obtained
- Larger samples can be irradiated
- The timescale (90% of deposition is about 20 ms) is typical of disassemblies and of the companion fuel-dispersal studies discussed in 1.2.6, below.

A program of ACRR pressure measurements is thus currently planned for FY80. Probably four to six experiments will be used in the first series.

1.2.6 ACRR Disassembly Visualization Experiments

In conjunction with the FD-2 experiments, a series of high-ramp rate disassembly visualization experiments will be performed in the ACRR. The rationale for these experiments has been given in paragraphs 1.2.1 (Introduction) and in 1.2.4. Note that the heating modes will closely resemble those of the related pressure experiments described above. In addition, the fuel used in the two sets of experiments will be closely matched. The FD-2 canister design can be used, once necessary changes have been made.

1.2.7 LOF-Timescale Fuel-Disruption Phenomenology

1.2.7.1 FD-1 Experiments and Analysis

During this period, FD-1 work has moved in three directions. These included presentation of a paper at the Brussels Conference on Nuclear Power Reactor Safety. The paper was well received and the experiments were referenced in the summary session as benchmark; the results of these experiments raise potential unresolved questions about the safety of advanced reactors in an LOF accident. Interested attendees at the Brussels Conference called for additional, improved experiments that more closely simulate prototypical conditions.

The second and third areas of FD-1 work have been the continued writing, as time allows, of the experiment's topical report and the LASL postmortem of the FD-1.4, -1.7, and -1.8 fuel. The status of the LOM post-test examination by LASL is that the project has been set aside due to other DOE priorities. Thus, essentially nothing more has been done in this reporting period. LASL now has all the equipment necessary to proceed. Only manpower and hot-cell logistics are lacking.

1.2.7.2 FD-2 Experiments and Analysis

Planning of the forthcoming fuel-disruption experiment series, FD-2, has continued. Design of the experiment double chamber and the

internal parts of the composite apparatus has been finalized. Machine drawings are being done for fabrication of the required 16 dual chambers. All the compound parts and diagnostic equipment to be obtained from outside Sandia are now on order, including the fresh UO_2 fuel.

The method for sampling the gases that emanate from the fuel has been established; because of limited space two spirals of stainless-steel tubing with remotely actuated valves will be used in place of bottles. One spiral will be redundant.

A functional laboratory-prototype inner canister and interior components have been assembled for design purposes and improvement efforts. Figure 1.2-10 shows views of the can, internal parts, and a single-frame image of the front and back of a simulated fuel rod. The new geometry allows for simultaneous photography of the entire fuel segment (front and rear) on one frame. Thus, with one camera the total clad and fuel disruption sequence will be as illustrated in Figure 1.2-10e, at up to 10 000 frames/s. Figure 1.2-10a shows the inner can, a thermocouple gage, a hand-controlled valve for chamber evaluation, two remotely controlled valves, and a centrally located window. The gas-sample "grab bottles" will be affixed to these two valves. Attached to these valves (immediately on the under side of the can lid) are two additional valves identical to the upper ones and to which are connected "sniffer probes" that reach into the fuel region. These inside valves and probes appear in Figures 1.2-10b and e. Two fused-silica lamps seen in Figure 1.2-10d backlight (through diffusers, not shown) the fuel element seen in Figures 1.2-10b and c. The optics include two calibrated half-silvered prism mirrors, two 100%-reflecting mirrors, and a fully reflecting, front-surface, right-angle cylindrical prism (Figure 1.2-10c). Each canister also includes a half-inch-thick, high-quality uprasil window. The fuel-mounting arrangement (Figures 1.2-10b and c) applies axial loading to any given pellet, due to the weight of the pellets above and the spring within the pins (PNL 9, 10, and 11).

POOR ORIGINAL

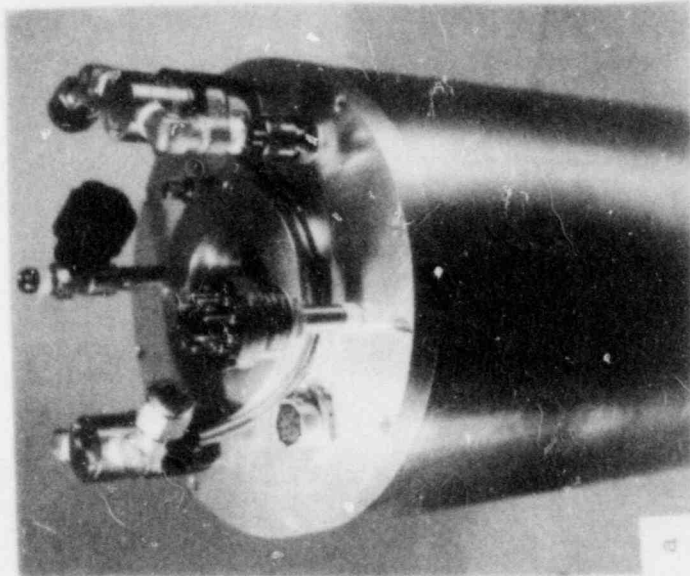
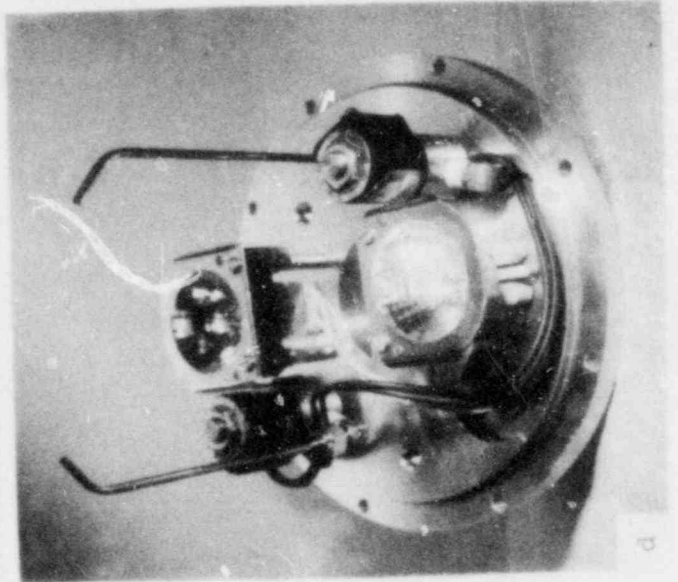
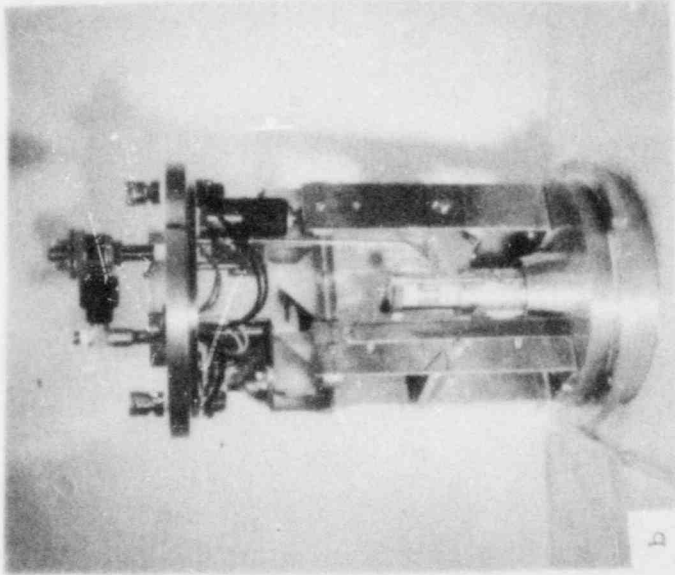
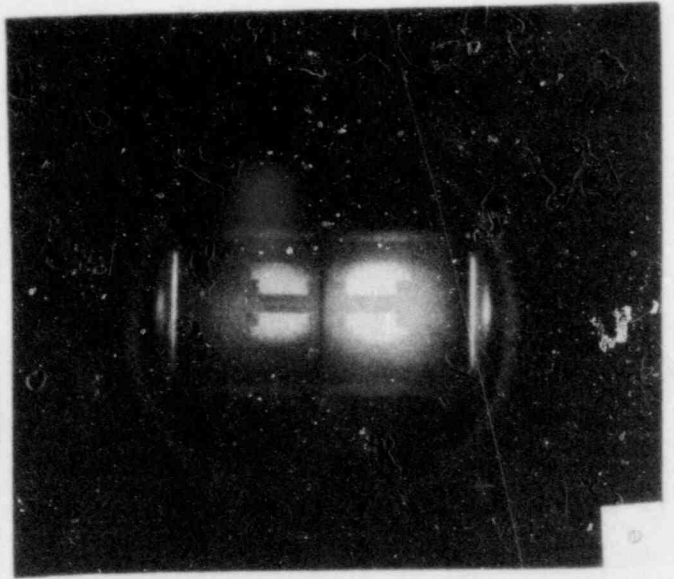
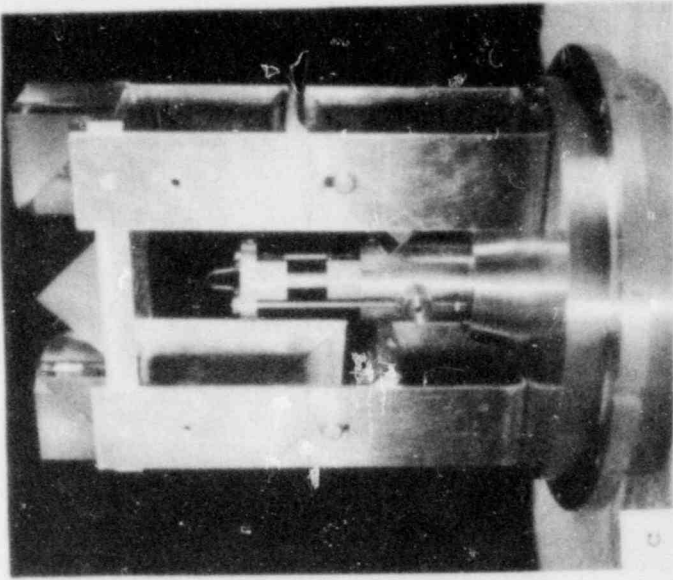


Figure 1.2-10
Views of Inner Can, Internal Parts,
Image of Fuel (front and rear).

After final assembly and mechanical and vacuum testing, the can (illustrated in Figure 1.2-10a), with the addition of tubing spirals, is inserted into the outer canister (not shown). This insertion completes the double-chamber assembly required for plutonium-bearing tests.

The neutronic and heat-transfer calculations, which have aided in the fuel geometry determination, indicate the fuel temperature profile and history will be nearly prototypic of an LOF-heating sequence. Those calculations are complete for the 70%-fissile atom-enriched fuel, and are underway for the 40% enriched fuel. For an ACRR output of 200 MW, a power factor of 75 W/cm^3 of 70%-enriched test fuel per MW of reactor output will be used to produce fuel melting into the unrestructured fuel. The surface temperature will be about 600 K less and the clad will melt at less than halfway through the neutronic pulse. A cadmium filter will attenuate the thermal-neutron flux to produce this power factor. For the 40%-enriched fuel, it now appears a power factor of about $125 \text{ W/cm}^3/\text{MW}$ will be necessary to produce the fuel temperatures, profiles, and histories desired. These calculations are proceeding.

The question of gap-conductivity value for use in the heat-transfer calculations, and the question of fuel contamination by H_2 , CO , and N_2 continue to be unresolved. Perhaps both questions will be answered in FD-2: the first, by comparison of calculation to experimental results; and the second, by cutting the fuel pins in a contaminant-free environment and then exposing one or two fuel sections to well-characterized contaminated gas. Comparison tests of fuel response to a known transient can then be run. Note clearly, however, that these fuels are sintered at the time of manufacture in a 92%-Ar plus 8%- H_2 atmosphere. The binder material is a hydrocarbon. The fuel-pin assembly takes place in an N_2 atmosphere, and the fuel has up to 50 ppm of carbon impurities. Because of these facts, the contamination "problem" may not be a critical one. However, until it is checked out the problem must be treated as potentially serious.

1.2.8 FISGAS Development

The FISGAS code has been used to calculate the fission-gas-release rates for HEDL test FGR 39.¹⁻²⁴ The FGR (fission-gas-release) test series is designed to provide data on the release rate of fission gas from irradiated mixed-oxide fuel heated by a transient. In these tests, short segments of irradiated fuel are heated externally by an electrically heated tungsten tube surrounding the fuel. The released gas is contaminated with impurities such as nitrogen. In later experiments in the FGR series, an on-line mass spectrometer is used to separate out the amount of fission gas from the released gas. Thus, the FGR 39 test provides accurate data on the gas-release rate. Earlier data from test FGR 15, for example, is not reliable because of the large amount of indistinguishable contaminants.

The FISGAS calculation assumed a xenon-gas concentration of 1.7×10^{20} atoms/cm³ in the unrestructured fuel from a radius of 0.1675 cm to the fuel surface. The remainder of the fuel was assumed to be devoid of gas. This distribution is an approximation to the recommendation of Randklev.¹⁻²⁷

The calculations are compared to the data in Figure 1.2-11; clearly there is a substantial discrepancy. The results of FRAS2-type modeling is also shown in the figure. Even without gas holdup on the grain boundaries there is a serious discrepancy with the gas-release data. While the large gas release in FGR 39 at 1673 K may be questioned, the higher temperature data shows no anomalous sudden release. Between 1673 and 2273 K an additional 10% of the gas is released in the experiment. However, the FRAS2-type calculation yields only 2% release. For gas releases of up to 75% in the experiment, FRAS2 underpredicts release by a factor of 5 or more. Since FISGAS provides an additional gas hold-up region (the grain boundary), it must predict less gas release than FRAS2. The source of the discrepancy in gas release between FISGAS and the experiment is the treatment of intragranular gas migration and release. Perhaps the difficulty lies in the rate constants for gas migration, or it may be the incorrect modeling of the intragranular gas-release mechanism.

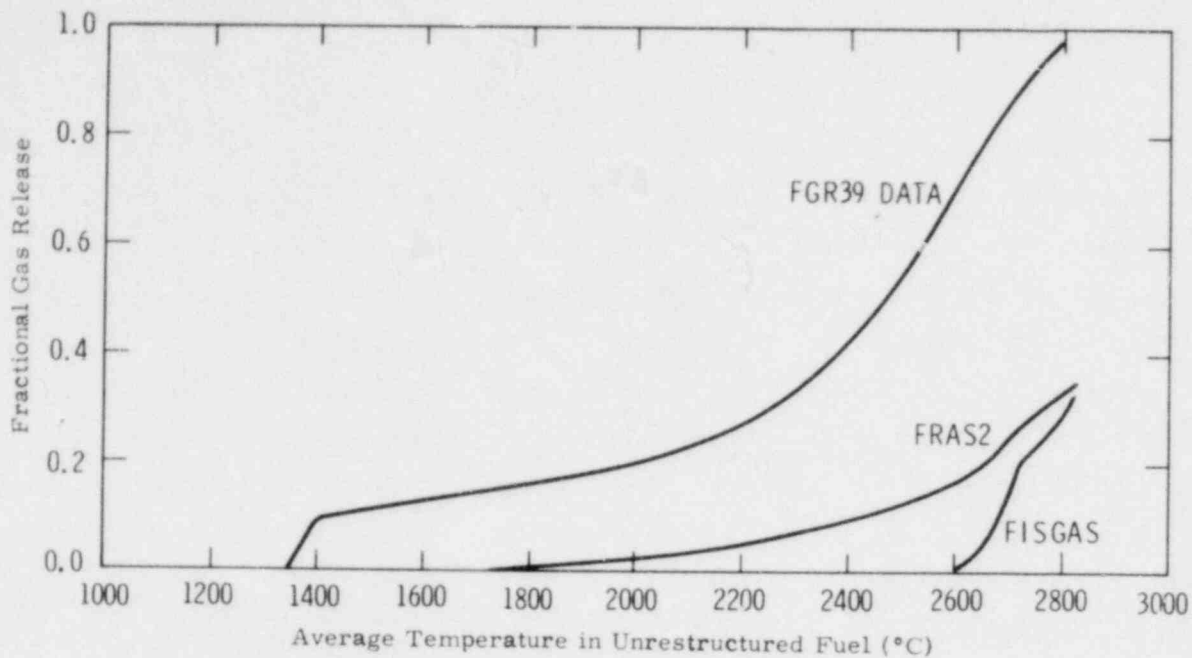


Figure 1.2-11 Comparison of FIGSAS Prediction of Gas Release to FGR 39 Test Data

References for Section 1

- 1-1 K.D. Lathrop, DTF-IV, A Fortran IV Program for Solving the Multi-group Transport Equation With Anisotropic Scattering LA-3373, (Los Alamos, NM: Los Alamos Scientific Laboratory, 1966).
- 1-2 K.D. Lathrop and F.W. Brinkley, TWOTRAN II: An Interfaced Exportable Version of the TWOTRAN Code for Two-Dimensional Transport, LA-4848-MS, (Los Alamos, NM: Los Alamos Scientific Laboratory, 1973).
- 1-3 S.L. Thompson and H.S. Lawson, Improvements in the CHARTD Radiation - Hydrodynamic Code II: A Revised Program, SC-RR-710713, (Albuquerque, NM: Sandia Laboratories, 1977).
- 1-4 S.L. Thompson, CKE052 - An Equation-of-State Test Program for the CHARTD/CS₂ EOS Package, SAND76-0175, (Albuquerque, NM: Sandia Laboratories, 1976).
- 1-5 S.L. Leibowitz et al, Properties for LMFBR Safety Analysis, ANL-CEN-RSD-76-1, (Argonne, IL: Argonne National Laboratory, 1976).
- 1-6 Advanced Reactor Safety Research Quarterly Report, July-September, 1978, Advanced Reactor Research Department, SAND78-2002, NUREG/CR-0470, (Albuquerque, NM: Sandia Laboratories, 1979).
- 1-7 K.O. Reil, M.F. Young, and T.R. Schmidt, Prompt Burst Energetics Experiments: Fresh Oxide/Sodium Series, SAND78-1561, (Albuquerque, NM: Sandia Laboratories, 1978).

- 1-8 P.A. Pizzica and P.B. Abramson, "EPIC-FCI: A Numerical Model of Fuel and Coolant Motions Following Pin Failure", NSE 64, 465, 1977.
- 1-9 H. Wider, "An Improved Analysis of Fuel Motion During an Overpower Excursion," Ph.D. Thesis, Northwestern University, IL, 1974.
- 1-10 H. Jacobs, "Computational Analysis of Fuel-Sodium Interactions With an Improved Method," Int. Mtg on Fast Reactor Safety and Related Physics, CONF-761001, Chicago, IL, 1976.
- 1-11 L.L. Smith et al, SIMMER-II: A Computer Program for LMFBR Disrupted Core Analysis, LA-7515 M, (Los Alamos, NM: Los Alamos Scientific Laboratory, 1978).
- 1-12 K.O. Reil and A.W. Cronenberg, "Effective Equation-of-State Measurements on Uranium Dioxide," Trans Am Nuc Soc, 27, 576, 1977.
- 1-13 D.A. Benson, Application of Pulsed Electron Beam Vaporization to Studies of UO₂, SAND77-0429, (Albuquerque, NM: Sandia Laboratories, 1977).
- 1-14 Advanced Reactor Safety Research Quarterly Report, April-June 1978, SAND78-2001, NUREG/CR-0469, (Albuquerque, NM: Sandia Laboratories, 1979).
- 1-15 H.S. Carslaw and J.C. Jaeger, Conduction of Heat in Solids, Oxford University Press, 1959.
- 1-16 W. Breitung, "Oxygen Self- and Chemical Diffusion in UO_{2+x}," J. Nuc. Mat., 74, 10, 1978.
- 1-17 J.R. Wilby, C.E. Wickes, and R.E. Wilson, Fundamentals of Momentum, Heat, and Mass Transfer, (New York, NY: John Wiley and Sons Inc., 1976) p 489 and p 483.
- 1-18 P.E. Potter, and P. Browning, "A Summary of Equation-of-State Studies and Results in the United Kingdom," IWFR Meeting on Equation-of-State of Materials of Relevance to the Analysis of Hypothetical Fast Breeder Reactor Accidents, AERE Harwell, England, 19 to 23 June 1978.
- 1-19 L. Leibowitz et al, Properties for LMFBR Safety Analysis, ANL-CEN-RSD-76-1, March 1976.
- 1-20 Kohler, "The Liquid State."
- 1-21 R.B. Bird, J.O. Hirschfelder, and C.F. Curtiss, "The Equation-of-State and Transport Properties of Gases and Liquid," Handbook of Physics, E.U. Cond (ed), (New York, NY: McGraw-Hill Book Co., Inc., 1958) Ch. 4-5.

- 1-22 K.S. Yun, S. Weissman, and E.A. Mason, "High-Temperature Transport Properties of Dissociating Nitrogen and Oxygen," Physics of Fluids, 5, 6, p 672, 1962.
- 1-23 J.R. Matthews and M.H. Wood, "Modelling the Transient Behavior of Fission Gas," Jour Nucl Mat, 84, 125, 1979.
- 1-24 C.A. Hinman and O.D. Slagle, Ex-Reactor Transient Fission Gas Release Studies, Fuel Pin, PNL-2-4, HEDL TME 77-83, 1977.
- 1-25 D. Hull and D.E. Rimmer, Phil Mag, 4, 673, 1959.
- 1-26 M.V. Speight and J.E. Harris, J Metal Sci, 1, 83, 1967.
- 1-27 E.H. Randklev, "Radial Distribution of Retained Fission Gas in Irradiated Mixed-Oxide Fuel," Trans Am Nuc Soc, 28, 234, June 1978.

2. FUEL DYNAMICS

- 2.1 TRANSITION PHASE (S. W. Eisenhower, 4422; D. O. Lee, 4721; M. L. Corradini, 5511; F. Gonzalez, 4422)

2.1.1 Introduction

Following the loss of initial geometry in a core-disruptive accident, and assuming that neither early shutdown nor rapid hydrodynamic disassembly takes place, the accident enters the transition phase. At this point, one or a number of subassemblies have melted down and radial propagation takes place as subassembly hexcans are melted through. The progression of the transition phase may strongly affect the severity of the accident, and it is therefore important to understand in detail the phenomena associated with this accident stage. In particular, several key questions need to be answered. First, in the early stages of the accident is the fuel dispersive; that is, how far can the molten-core material and fission-gas mixture move axially before it freezes? Secondly, if blockages form and the core is bottled up, what is its configuration--does it remain boiled up, or does the pool collapse followed by the occurrence of a recriticality? Answers to these questions depend upon resolving the uncertainties in transition-phase phenomenology. Work at Sandia is directed toward the mechanics of fuel-blockage formation and boiling-pool behavior. Both analytic and experimental studies are included in this effort. Activities during the reporting period were concentrated in two areas: continuation of the liquid-liquid ablation experiments using Refrigerant-11 (R-11) and ice, and an initial attempt to model the heat-transfer mechanism observed in these tests.

2.1.2 Liquid-Liquid Ablation - Experimental Work

Fuel penetration into the upper axial blanket and fission-gas-plenum regions of the reactor is controlled by the energy-exchange process between the flowing fuel and the solid steel-cladding and subassembly

walls. The heat-transfer rates can be affected by four distinct phenomena: (1) fuel freezing and subsequent crust behavior; (2) solid steel melting and possible entrainment into the fuel, referred to here as liquid-liquid ablation; (3) slurry freezing of the fuel; and (4) liquid fuel-sodium coolant interaction effects on the fuel freezing process. A detailed discussion of these four aspects of the streaming and freezing sequence and their relative importance was given in an earlier quarterly report.²⁻¹ The experiments currently in progress are designed to investigate the physics associated with the second phenomenon of solid wall melting and possible entrainment. This particular heat-transfer mechanism is postulated to occur during fuel streaming after the removal of the initial frozen-fuel crust, and assuming negligible fuel-crust renewal.

As noted above, the experiments use R-11 flowing through an ice pipe to study the heat transfer between a melting wall and a turbulently flowing liquid. This refrigerant was chosen so that it would not freeze upon contact with the ice, thereby eliminating the freezing process and isolating the behavior of the melting wall. The R-11 and H₂O are immiscible and have a similar density ratio ($P_R/P_W = 1.47$) as the fuel-steel system (1.3). The experiment is conducted at Reynold's numbers representative of the fuel-streaming sequence ($2 \times 10^4 < Re < 10^5$). Note that R-11 and water are not intended to simulate directly the UO₂/stainless-steel pair. The approach has been to include (to the extent possible) the important properties of the system while concentrating upon the underlying phenomenology.

2.1.2.1 Experimental Apparatus and Procedure

Figure 2.1-1 shows a schematic of the test rig. A detailed description of the apparatus has been given in an earlier quarterly;²⁻² only a brief review is given here. The principal components are the system pressurizer and accumulator, supply reservoir, ice pipe, control valves, and associated instrumentation.

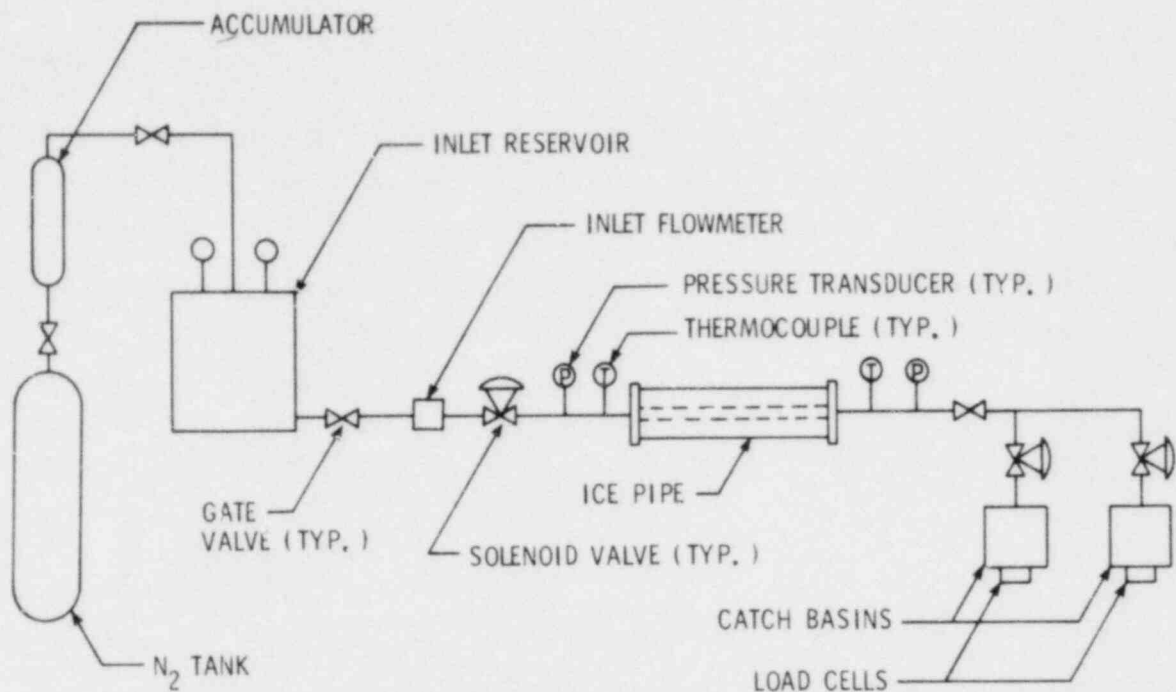


Figure 2.1-1 Schematic of Liquid-Liquid Ablation Experiment Apparatus

During operation, the system is pressurized using a high-pressure nitrogen tank. This tank is connected to a 12-L accumulator used to ensure constant flow during a test. The supply reservoir and all of the critical system piping is made of stainless steel. This allows for the future use of high-temperature or corrosive materials. The reservoir has a useful capacity of approximately 30-L and is currently pressure rated at 6.8 atm (100 psi or 0.68 MPa). The supply reservoir and the inlet section are equipped with heat tape for operation at elevated temperatures.

The ice pipe (Figure 2.1-2) has an outer diameter of 10.2 cm and a nominal internal diameter of 0.6 or 1.3 cm. Two different lengths (31 and 85 cm) have been used in the present tests. The pipe is formed by pouring distilled water into a plexiglas mold. Cold ethylene glycol

(233 K, -40°C) flows in a copper tube that passes through the center of the mold and is removed after freezing to form the internal channel. In some cases, high-speed motion pictures are taken during the experiments. For this reason every effort is made to produce ice pipes that are optically clear. In addition, to improve visual observation of the two fluids, the refrigerant is dyed red and the melting ice dyed blue. The water-soluble blue dye is inserted at axial points along the ice-pipe length by means of dye sticks frozen in place. Single frames from the high-speed motion pictures (taken at 200 frames/s) will be shown and discussed below.

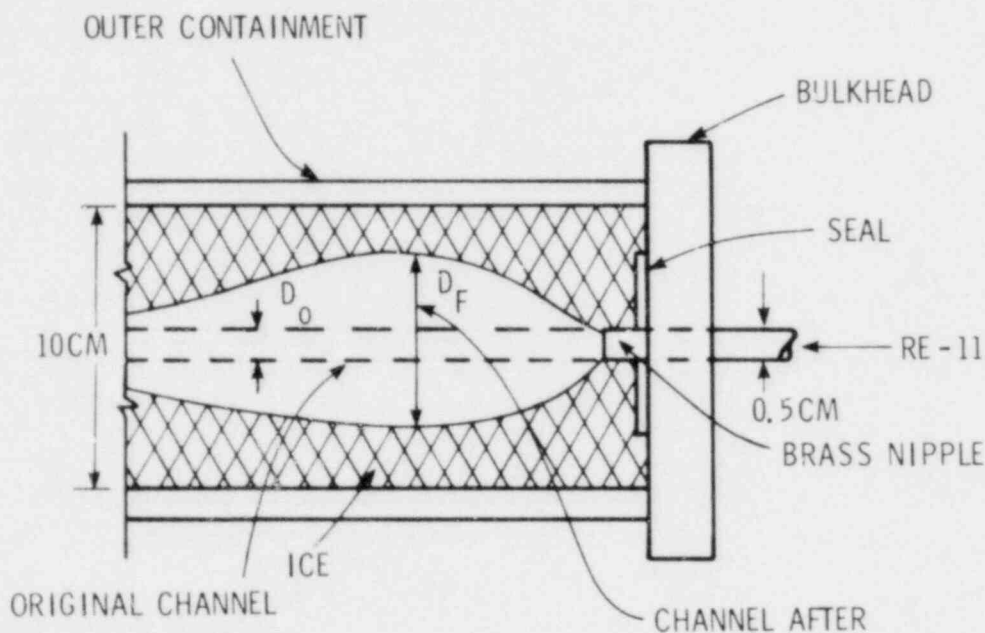


Figure 2.1-2 Observed Melting Pattern During Liquid-Liquid Ablation Experiments

In operation, flow through the ice pipe is controlled by three solenoid valves: one upstream and two downstream from the ice pipe. Sequencing of the valves is determined by operation of two timers. At the start of a test run, following a 5-s delay to allow recording of the pre-test conditions, the inlet and one of the outlet valves opens. During this period the outlet flow goes into catch basin No. 1. Following a

preset interval, the two outlet valves re-sequence and flow passes into the second basin. The experiment continues until a second timer limit is exceeded and the inlet valve closes.

Instrumentation consists of thermocouples, pressure transducers, an inlet flowmeter, and load cells on the outlet catch basins. The thermocouples (Type K) are located in the supply reservoir, at the inlet and outlet of the ice pipe, and in the ice pipe itself. The thermocouples in the ice pipe are passed through fittings in the plexiglas pipe and are positioned at various depths in the ice. Several of the thermocouples at different axial locations are positioned so that they are in immediate contact with the flowing refrigerant; these are used to measure the axial temperature distribution. Pressure transducers are located at the inlet and outlet of the test section.

The inlet flowmeter (Brooks Model 4021B) is a positive-displacement flowmeter designed for operation at low-flow rates. This flowmeter is very accurate and, in conjunction with the two load cells mounted on the catch basin, permits a precise determination of the inlet refrigerant flow rate and the total flow rate. For all tests conducted, the mass flow rate is kept constant by using a high-driving pressure and throttling at the test-section outlet. This result is verified by the flowmeter output and the constant slope of the load-cell output voltages throughout a test. In addition, the amount of ice melted is determined by measuring the amount of water collected in the downstream basins at the end of each test.

Following appropriate amplification and filtering, the transducer signals are recorded on two 14-track FM tape recorders. At a later time the signals are reproduced on a strip chart recorder and analyzed. A system is also available to digitize the data for further analysis on the Sandia computing system.

2.1.2.2 Visual Observation of the Melting Process

In the previous quarterly²⁻³ a discussion of the phenomena observed visually during the melting process was given. That discussion is continued here. In addition, single frames from the high-speed motion pictures will now be presented. The test parameters for the experiments discussed below are given in Table 2-1.

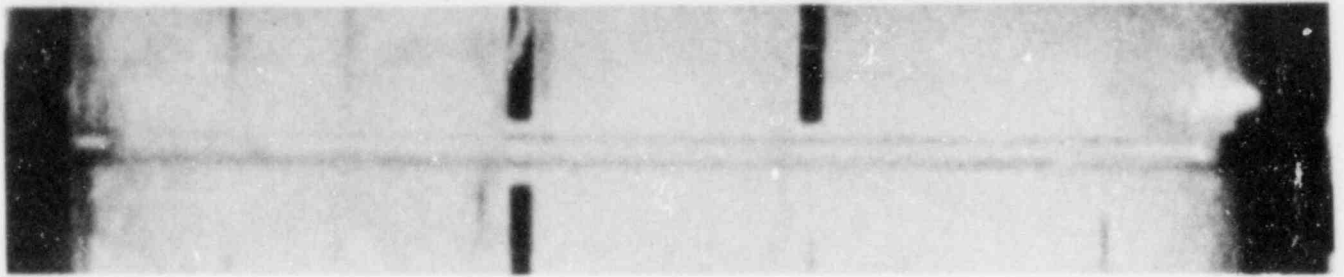
Table 2-1

TEST DATA FOR EXPERIMENTS DESCRIBED IN THIS QUARTERLY

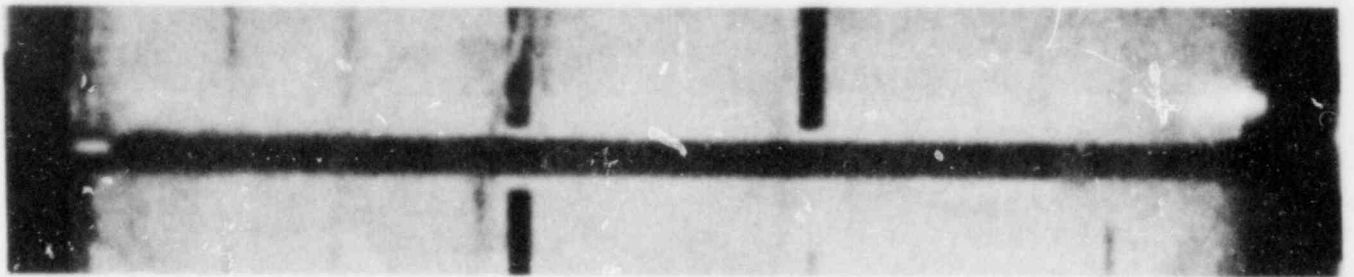
Test No.	Orientation	Length (mm)	Diameter (mm)	Temperature - °C		R-11 Mass Flow (kgs)
				Inlet	Ice	
31VD-004-1/4	Vertical, Downflow	310	6.4	25	-3	0.087
31VU-005-1/4	Vertical, Upflow	310	6.4	24.5	-6	0.062
31HO-006-1/4	Horizontal	310	6.4	25	-7	0.088
85VU-001-1/4	Vertical, Upflow	850	6.4	21.5	-6	0.097

The flow development is shown in three stages in Figure 2.1-3. Figure 2.1-3a shows the ice pipe just before the flow begins. The 0.6-cm internal channel is clearly visible as are the dye sticks and thermocouples. Figure 2.1-3b shows the situation 2.15 s after flow initiation. The R-11, dyed red as previously noted, is flowing horizontally, left to right. A slight bulge is visible at the brass inlet nipple which extends approximately 1 cm into the ice pipe. Also visible are irregularities at the upper edge of the flow channel. These irregularities are interfacial waves formed at the interface between the R-11 and a layer of water at the channel wall. The existence of this water film strongly affects the heat transfer and will be discussed in detail below. The behavior of the interfacial waves will also be examined. Figure 2.1-3c is taken from the motion picture 1 min after the flow begins. The inlet section now exhibits the characteristic bell shape seen in all the tests. Beyond this region, which extends approximately 10 cm, the variation of diameter with axial position is seen to be quite small. This effect arises from the presence of the water film at the wall.

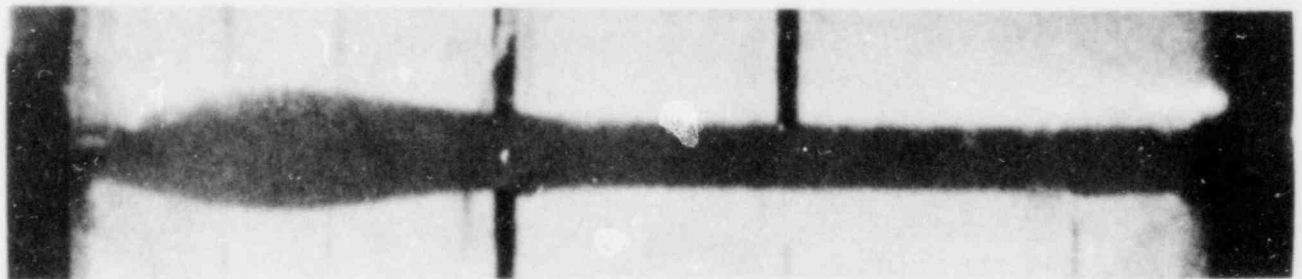
POOR ORIGINAL



a. Before Flow Initiation



b. $t = 2.15$ s

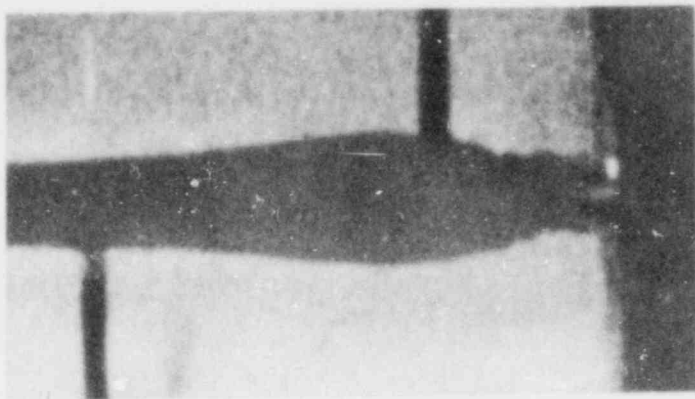


c. $t = 60$ s

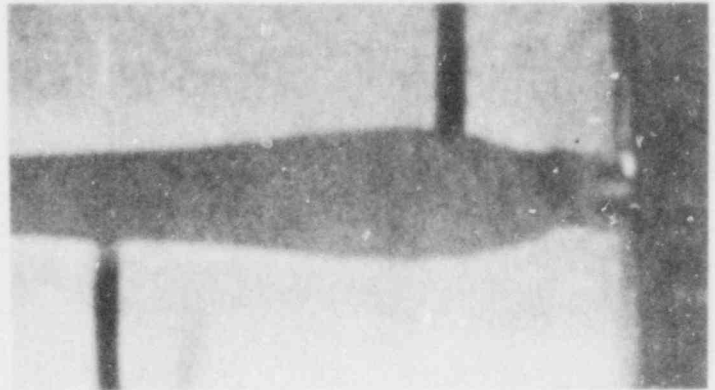
Figure 2.1-3 Development of Flow Channel in Ice Pipe

POOR ORIGINAL

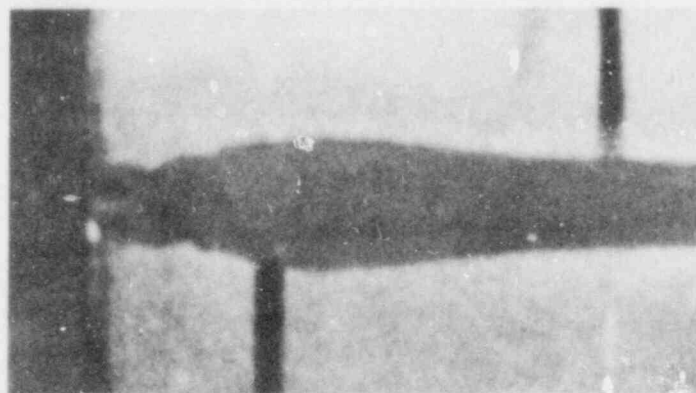
Figure 2.1-4 is a series of closeups of the inlet section for TEST 31VU-005-1/4 in vertical upward flow. The interval between frames is 20 ms. Large waves can be clearly seen at the interface between the R-11 and the water at the wall. The actual wall itself is smooth. The quality of the black and white photograph is not sufficient to show the blue bands upstream of the dye stick near the inlet. In the motion picture, the recirculation behind the inlet nozzle can be clearly seen with entrainment of water from the interfacial waves. The only entrainment apparent in the films is in this recirculation region and does not seem to occur downstream.



a.



b.



c.

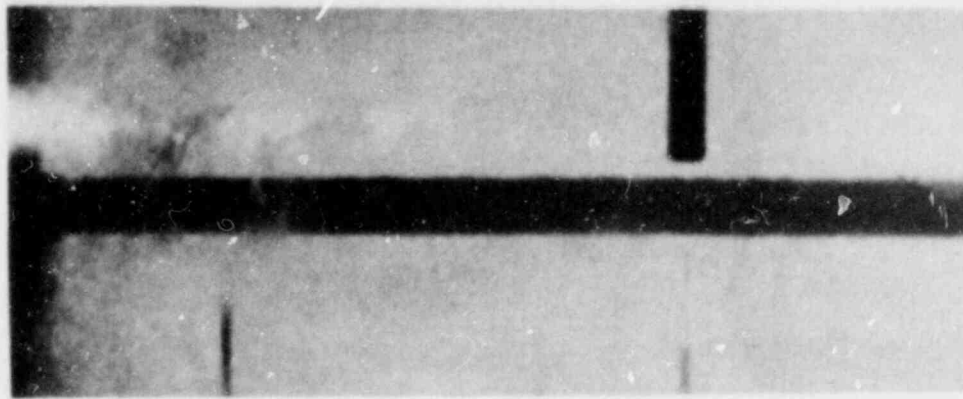
Figure 2.1-4 Closeup of Inlet Section: Test 31VU-005-1/4
(Time Between Frames is 20 ms)

A primary concern in the early experiments has been to identify the effect of flow orientation on the behavior of the interfacial waves and the heat transfer to the wall. This concern stems from the fact that in a multicomponent or multiphase flow, the gravitational or buoyant force can be very important. That is, in the R-11/H₂O system, the difference in density affects both the radial distribution of the water film and the net force exerted on it.

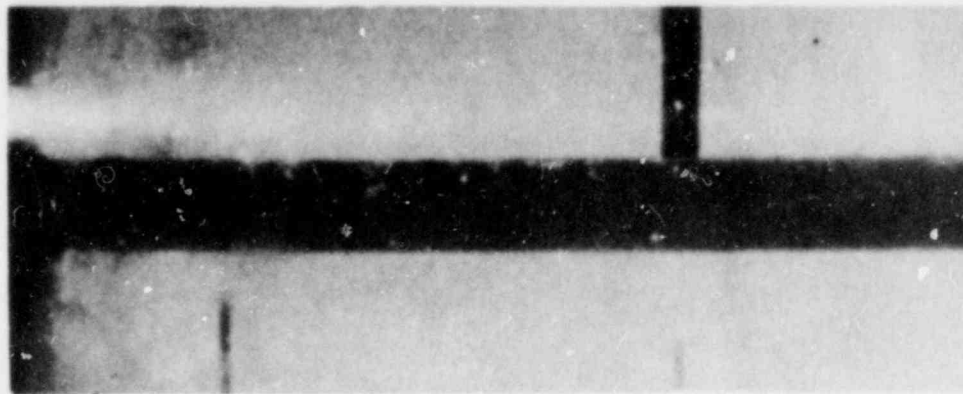
The variation of film thickness in horizontal flow as a result of the net-buoyant force on the water is visible in Figure 2.1-5. These frames show the flow near the outlet in TEST 31HO-006-1/4. At the top of the flow channel and in Figure 2.1-5b the actual film thickness is visible. The film also exists at the bottom; however, it is much thinner. For this reason, the melting process occurs preferentially in the downward direction. This effect can be seen in Figure 2.1-3c. The motion pictures indicate that the water in the film has a vertical velocity component that produces a net transport of mass within the film to the top of the channel.

The total net force on the film in the direction of flow is a major factor affecting the film thickness and interfacial phenomena. The film thickness depends upon two processes discussed in detail in Section 2.1.3. However, a brief qualitative description is given here in conjunction with the visual observations. The first of the two processes is the rate at which ice melts and enters the film. This rate is inversely proportional to the film thickness. On the other hand, the axial transport of water depends upon the net force exerted in the film. The components of this force are the interfacial shear in the direction of flow, the wall shear opposing the flow, and the body force arising from the difference in density between R-11 and water. This force is always directed upward.

POOR ORIGINAL



a. Early Time



b. After Approximately 60 s

Figure 2.1-5 Flow at the Ice-Pipe Outlet:
Test 31HO-006-1/4, Horizontal Flow

In vertical downward flow, the interfacial shear and body force are in opposite directions. It is thus possible for the film to flow either with or against the flow in the turbulent core. This condition leads to the production of very large waves near the point of flow reversal (upward film flow). This situation is a direct analog of gas-liquid annular flow except that in the case of gas-liquid annular flow the same behavior arises in upward flow.

Symbols for the following development appear in Table 2-2. In the ice pipe experiments the R-11 flow rate (M_R) is very nearly constant. Hence, as the channel diameter (D) increases, the velocity decreases as

$$V_R = \frac{4 \dot{M}_R}{\rho_R \pi D^2} \quad (2.1)$$

where ρ_R is the R-11 density. The interfacial shear stress is roughly

$$\tau_i = f \frac{\rho_R V_R^2}{2} \quad (2.2)$$

where the friction factor, f , can be quite large due to interfacial waves (see Section 2.1.3). Accordingly, the interfacial shear drops ($\tau_i \propto D^{-4}$ at constant f) and, for a particular flow rate, the buoyant force may equal or exceed the shear force.

The onset of this condition is shown in Figure 2.1-6 (TEST 31VD-004-1/4). Very large waves can be seen at the core-film interface. The direction of flow in the film is still downward; however, the velocity is quite low. The amplitude of the large waves is on the order of $0.2D$. It can also be seen that the large waves tend to overtake the smaller ones. This behavior is consistent with that seen in gas-liquid annular flow. Although not shown here, flow reversal could be easily initiated at this point by decreasing slightly the R-11 flow rate.

2.1.2.3 Experimental Heat-Transfer Measurements

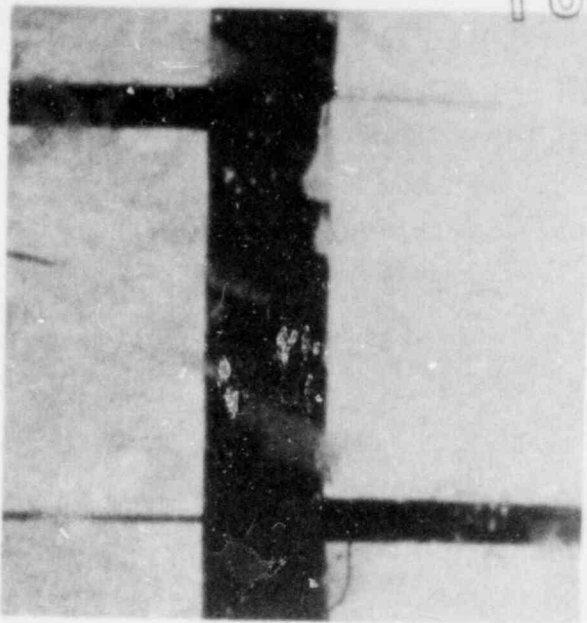
Quantitative results from the experiments include refrigerant and ice-pipe temperatures, refrigerant-mass-flow rate, and the ice pipe diameters as functions of the axial distances and times measured from the motion pictures. Although inlet- and outlet-pressure measurements were taken during the tests, no attempt was made to deduce the interfacial shear stress (τ_i) between the water and refrigerant. Future experiments will attempt to implant pressure taps at the inlet and outlet in the ice pipe itself to accurately measure τ_i .

Table 2-2

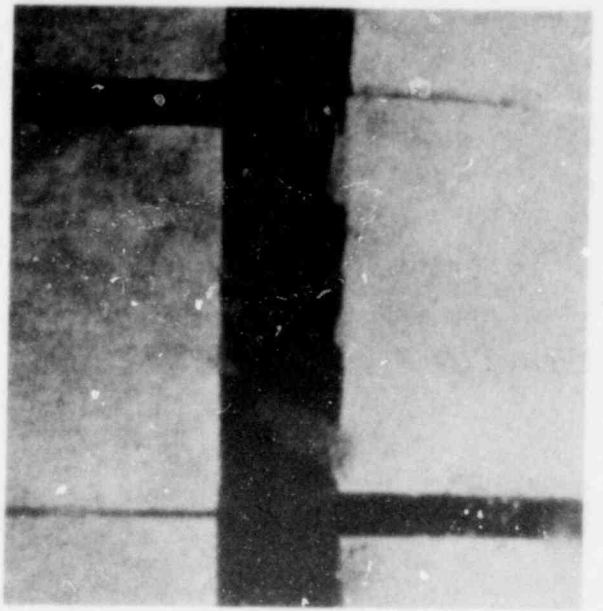
Nomenclature for Section 2.1-2

<u>Symbol</u>	<u>Description</u>
C_p	Specific heat
D	Diameter of ice pipe
D_o	Initial diameter of ice pipe
g	Acceleration of gravity
h	Heat-transfer coefficient
k	Thermal conductivity
L	Length of ice pipe
L_s	Heat of fusion of ice
\dot{M}	Mass-flow rate
P	Pressure
R_e	Reynolds number
T	Temperature
t	Time
V	Velocity
W_e	Weber number
x	Radial dimension
z	Axial dimension
δ	Water-film thickness
Γ	Flow of water per unit width
λ	Wavelength
λ_c	Taylor instability critical wavelength
μ	Viscosity
ρ	Density
τ_L	Interfacial shear stress
σ	Surface tension
e	Experimental value
I	Ice value
i	Inlet value
m	Melting value
o	Outlet value
R	Refrigerant value
W	Water value
$\langle \rangle$	Spatial average

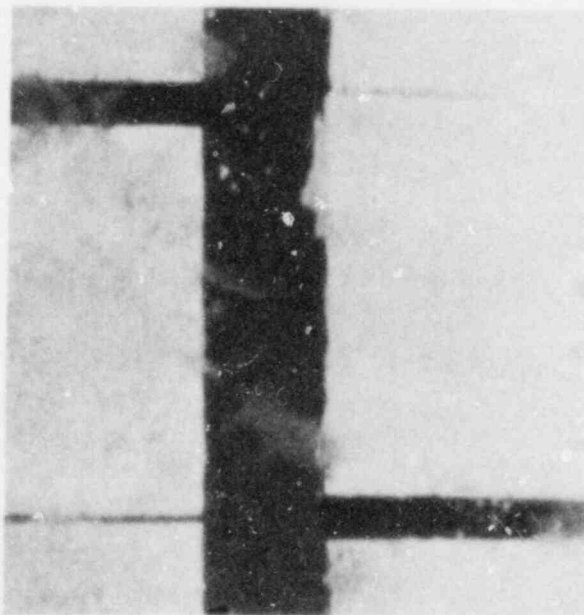
POOR ORIGINAL



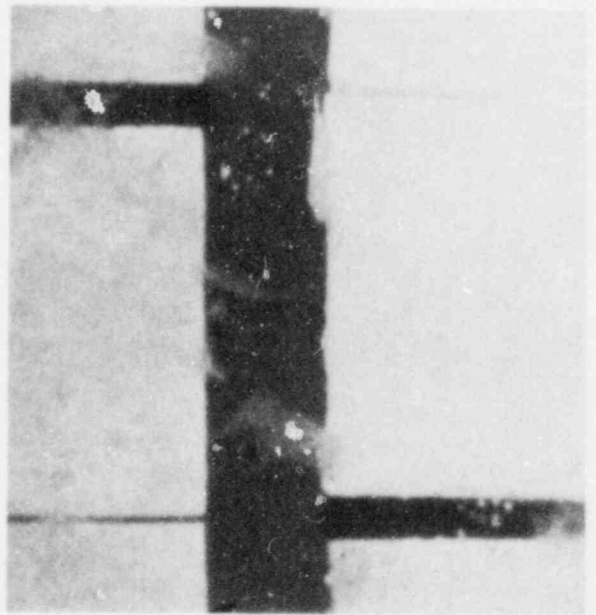
a.



c.



b.



d.

Figure 2.1-6 Interfacial Waves in Downward Flow Near the Flooding Limit: Test 31VD-004-1/4. Time between frames is 5 ms

Figure 2.1-7 illustrates a typical temperature trace for an experiment. The most interesting result is that the refrigerant temperature difference is essentially constant throughout the transient tests. This behavior is seen at the outlet and with thermocouples that were imbedded in the ice pipe and entered the refrigerant flow as the pipe melted. To understand the implication of this unexpected result, consider a simple macroscopic energy balance on the ice pipe,

$$\dot{M}_R C_{PR} (T_{R_i} - T_{R_{out}}) = \langle h \rangle \pi DL (T_{R_{avg}} - T_M), \quad (2.3)$$

where:

- C_{PR} = Specific heat of R-11
- T_R = R-11 temperature
- L = ice-pipe length
- T_M = melting point of ice,

the subscripts "i", "out", and "avg" denote inlet, outlet, and average conditions, and where the brackets on the heat transfer coefficient (h) denote a spatial average. The average refrigerant temperature can be given by

$$T_{R_{avg}} = \frac{T_{R_i} + T_{R_{out}}}{2} \quad (2.4)$$

where:

- sub i = inlet
- sub out = outlet
- sub avg = average conditions
- h = heat-transfer coefficient
- $\langle \rangle$ = a spatial average on h

A Nusselt number defined as

$$\text{Nu}_e \equiv \frac{\langle h \rangle D}{K_R} \quad , \quad (2.5)$$

can be solved for in Eq (2.3). The result is,

$$\text{Nu}_e = \frac{\dot{M}_R C_{P_R} (T_{R_i} - T_{R_{out}})}{K_R \pi L \frac{T_{R_i} - T_{R_{out}}}{2} - T_M} \quad . \quad (2.6)$$

So far a constant inlet refrigerant temperature, refrigerant flow rate, and for the observed constant differential temperature, this Nusselt number is essentially constant throughout the test. Another useful way of looking at this is to write the equation for the temperature distribution in the refrigerant. That is,

$$T_R(L) - T_m = (T_R(0) - T_M) \exp \left(\frac{-\langle h \rangle \pi D L}{\dot{M}_R C_{P_R}} \right) \quad (2.7)$$

which can be rearranged to yield

$$\langle \text{Nu} \rangle = \frac{\dot{M}_R C_{P_R}}{\pi L K_R} \ln \left[\frac{T_R(L) - T_M}{T_R(0) - T_M} \right] \quad . \quad (2.8)$$

Hence, the Nusselt number can be readily determined from a semilog plot of temperature versus distance. Figure 2.1-8 shows such a plot for a test in upward vertical flow. The slope of the line in such a plot varies only slightly with time. These results are further indications that the laminar water-film flow controls the energy-exchange process. If the heat-transfer rate were governed by the turbulent refrigerant flow, then the Nusselt number (Nu_e) would be a strong function of the Reynolds number (Re_R) ($\text{Nu} \propto \text{Re}^{.8}$). Thus, as the pipe melts, the diameter increases and

for a constant mass flow rate, the Reynolds number decreases inversely. Typically, a factor of 3 increase in the diameter decreases Re_R by 3 and would suggest a decrease in Nu_e by 2.5. This was not experimentally observed. Observe that in both of the methods of determining Nu_e outlined above, it is unnecessary to know the actual diameter at any time. This is particularly useful in tests such as these where the flow geometry is time-dependent.

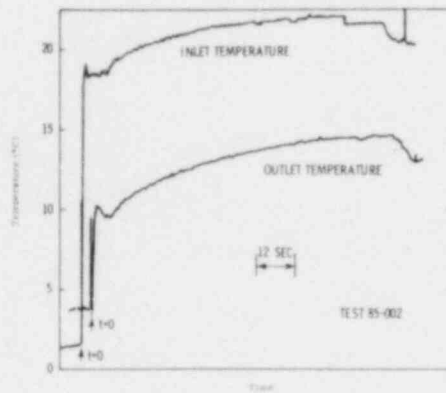


Figure 2.1-7 Typical Temperature Trace for an Experiment

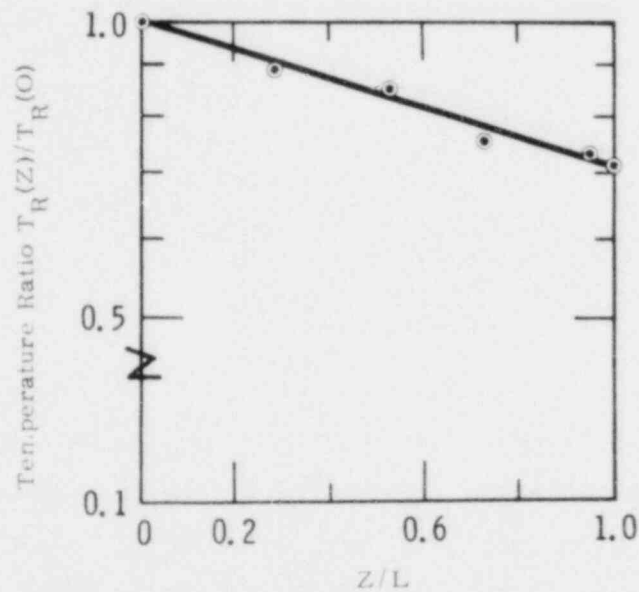


Figure 2.1-8 Semilog Plot of Temperature vs Distance for a Test in Upward Vertical Flow

The Nusselt number is dependent upon the length of the pipe as Eq (2.4) indicates. For the short pipe (31 cm), the Nusselt numbers lie in the range $215 < Nu_e < 260$, and for the long pipe $120 < Nu_e < 160$. There can be two possible reasons for this result:

- a. The fractional length of the ice pipe in the entrance region is decreased as the total length is increased; therefore, the enhanced heat transfer in this zone has less of an effect on the overall Nusselt number.
- b. As the pipe length increases the temperature difference in the new length is lower and the driving potential for energy transfer is lower; thus, the overall Nusselt number for the longer length decreases.

To reiterate, there are two main observations to make about the test results: (a) the rate of ice-pipe meltout is quite slow at any fixed axial distance, slightly more than doubling its original size during the test; and (b) for any fixed time, the difference of the ice pipe's diameter change at different axial distances is small. The first experimental observation indicates a quasi-steady melting process and the second indicates the ice pipe meltout rate is a weak function of the axial distance.

During the next quarter an extensive series of tests in upward vertical flow is planned. The purpose of this series is to investigate the functional dependence of the Nusselt number on the flow conditions and to compare the experimental data with the heat-transfer model outlined in the next section.

2.1.3 Preliminary Analysis of the Ice-Melting Experiment

The two-fluid melting experiment has exhibited two significant characteristics that were not expected: (a) there is no water-film entrainment into the turbulent flow of the refrigerant; (b) the refrigerant temperature difference across the ice pipe remains essentially constant throughout the test for a constant mass-flow rate, giving a nearly constant Nusselt number. Preliminary calculations indicate that past

annular gas-liquid correlations do not predict this lack of entrainment and thus future isothermal liquid-liquid annular flow experiments are planned to understand the phenomenon of liquid entrainment. There are two characteristics of the melting process that were analytically dealt with: (a) given this lack of water entrainment and the inlet refrigerant conditions, prediction of the temperature distribution of the refrigerant flow in the ice pipe is desirable; and (b) it is necessary to predict the melting rate of the ice pipe.

To predict the refrigerant's temperature distribution and the melting rate of the ice pipe, a simple heat-transfer model was developed assuming that the water film controls the energy-exchange process. The refrigerant flow is turbulent and is characterized by an average velocity and temperature at every axial distance (z) and time (t). In addition to this physical characterization, the following assumptions are made:

- a. The flowing water film is not entrained in the refrigerant flow and is assumed to be fully developed both hydrodynamically and thermally. This assumption essentially neglects the entrance region effect.
- b. The water film thickness (δ) has been visually observed as small compared to the ice pipe diameter, and, therefore, curvature effects are neglected.
- c. The thermophysical properties of the refrigerant and water are assumed constant. This approximation is valid because the temperature differences are small in these tests.
- d. The ice pipe melting phenomenon is assumed to be quasi-steady. In other words, the melting rate of the ice pipe is much slower than the transit time of the refrigerant through the ice pipe. Therefore, a temperature distribution in the refrigerant can be determined based on a steady-state analysis for a given time; then the ice-pipe diameter change is evaluated separately.

2.1.3.1 Quasi-Steady Refrigerant Temperature Distribution

The physical picture of the water-refrigerant system is given in Figure 2.1-9.

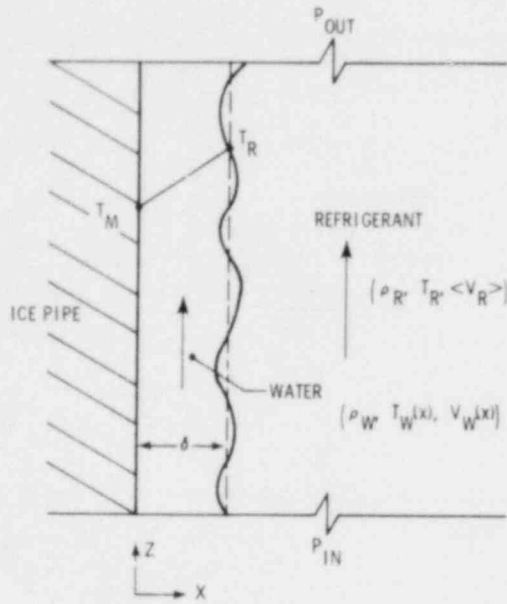


Figure 2.1-9 Physical Picture of the Water-Refrigerant System

The axial-momentum equation for the water film is expressed as,

$$\mu \frac{d^2 V}{dx^2} = \frac{dp}{dz} + (\rho_R - \rho_W)g, \quad (2.9)$$

where for the case of horizontal flow, the term $(\rho_R - \rho_W)g$ is zero. Additional nomenclature for equations presented in 2.1.3 appears in Table 2-2. The boundary conditions are:

$$p = p_{out} \text{ @ } z = L \quad (2.10a)$$

$$p = p_{in} \text{ @ } z = 0 \quad (2.10b)$$

$$V_z = 0 \text{ @ } x = 0 \quad (2.10c)$$

$$\tau_i = +\mu \frac{dV}{dx} \text{ @ } x = \delta \quad (2.10d)$$

The shear stress at the interface, τ_i , is not known a priori; therefore, two models are used in the analysis as suggested by Collier²⁻⁴ for annular flow,

$$\tau_i = 0.005 \left(1 + 300 \frac{\delta}{4}\right) \frac{R \langle v_R \rangle^2}{2} \quad (2.11a)$$

$$= 0.005 \left(1 + 300 \frac{\delta}{D}\right) \left(\frac{4}{\pi}\right)^2 \frac{\dot{M}_R^2}{D^4 R}$$

or

$$\tau_i = 0.005 \frac{\rho_R \langle v_R \rangle^2}{2} = \frac{0.005}{2} \left(\frac{4}{\pi}\right)^2 \frac{\dot{M}_R^2}{D^4 R} \quad (2.11b)$$

The first model was originally developed by Wallis²⁻⁵ for air-water annular flow where the interface is very wavy. Collier suggests that it is valid for $Re_w \geq 500$. The second model is used for annular flow when the interface is nearly smooth. Collier suggests its applicability to be $Re_w < 100$. The water-film Reynolds number in Sandia's experiments are between these Reynolds number limits; thus both models are applied separately. If the differential equation is integrated twice and the constants solved for, the velocity is given by

$$v_z = \left[\frac{p_{out} - p_{in}}{L} + (\rho_R - \rho_W)g \right] \frac{\delta^2}{2} \left[\left(\frac{x}{\delta}\right)^2 - \frac{2x}{\delta} \right] + \frac{\tau_i \delta}{\mu} \left(\frac{x}{\delta}\right) \quad (2.12)$$

and the average velocity is

$$\langle v_z \rangle = 1/3 \frac{p_{out} - p_{in}}{L} + (\rho_R - \rho_W)g \frac{\delta^2}{\mu} + \frac{\tau_i \delta}{2\mu} \quad (2.13)$$

Now the term $(\Delta P/L)$ can be related to the shear stress by an overall force balance on the ice pipe,

$$\frac{\Delta P}{L} = \frac{4\tau_i}{D} \quad (2.14)$$

and thus $\langle V_z \rangle$ is

$$\langle V_z \rangle = (\rho_R - \rho_W) \frac{g\delta}{3\mu} + \frac{\tau_i}{2\mu} \left(\delta + \frac{4}{3} \delta \left(\frac{\delta}{D} \right) \right) \quad (2.15)$$

This expression can be approximated by

$$\langle V_z \rangle = (\rho_R - \rho_W) \frac{g\delta^2}{3\mu} + \frac{\tau_i}{2\mu} \quad (2.16)$$

because $\delta/D \leq 0.1$ and thus the third term is negligible. One further approximation is to neglect the buoyant force in Eq (2.16) for high-refrigerant velocities giving

$$\langle V_z \rangle = \frac{\tau_i}{2\mu} \quad (2.17)$$

Depending on the model for τ_i , the total water-mass flow rate per unit width (Γ) is

$$\Gamma = \rho_W \delta \langle V_z \rangle = \frac{\rho_W \delta^2}{2\mu} \left[0.005 \left(1 + 300 \frac{\delta}{D} \right) \frac{\rho_R \langle V_R \rangle^2}{2} \right] \quad (2.18a)$$

$$\approx \frac{\rho_W \delta^2}{2\mu} \left[1.5 \frac{\delta}{D} \frac{\rho_R \langle V_R \rangle^2}{2} \right]$$

for Eq (2.11a) or

$$\Gamma = \frac{\rho_W \delta^2}{2\mu} \left[\frac{0.005 \rho_R \langle V_R \rangle^2}{2} \right] \quad (2.18b)$$

for Eq (2.11b),

A simple energy balance for the water film can be made, like that of Nusselt,²⁻⁶ equating the energy transferred across the interface in an increment (dz) to the energy required to raise the ice mass (dΓ) to its melting temperature, melt it, and raise it to bulk temperature of the flowing water film. This is expressed by,

$$k_W \frac{dT}{dx} \Big|_{x=\delta} dz = d\Gamma \left[L + 1/3 C_p (T_R - T_M) + C_p (T_M - T_I) \right] \quad (2.19)$$

where the term, $1/3 (T_R - T_M)$ presents the bulk temperature difference of the water ($T_{Wb} - T_M$). This is found by assuming a linear water-film temperature profile

$$T_W = T_M + (T_R - T_M) \frac{x}{\delta} \quad (2.20)$$

and solving for the bulk temperature

$$(T_{Wb} - T_M) = \frac{1}{\langle V_z \rangle} \int_0^{\delta} dx V_z(x) (T_W - T_M)(x) \quad (2.21)$$

The temperature gradient (dT/dx) at the film interference in Eq (2.19) is found by differentiating Eq (2.20) and substituting it into Eq (2.19). Finally, the term dΓ is found by differentiating Eq (2.19) and substituting into Eq (2.19). The unknown quantity in Eq (2.19) is now the water-film thickness (δ) and can be solved for by integrating from the entrance of the ice pipe (z = 0 where δ = 0) to any distance (z). If it is assumed that the variance of the refrigerant temperature with the axial distance is not large, the differential equation can be integrated giving

$$\delta(z) = \left[\frac{4k_W (T_R - T_M) z}{3 \rho_W L \frac{1.5 \langle V_R \rangle^2 \rho_R}{2\mu D}} \right]^{1/4} \quad (2.22a)$$

for τ_{wi} given by Eq (2.11a) and

$$\delta(z) = \left[\frac{3K_W (T_R - T_M) z}{2 \rho_W L^1 \frac{0.005 \rho_R \langle V_R \rangle^2}{2\mu}} \right]^{1/3} \quad (2.22b)$$

for τ_{wi} given by Eq (2.11b)

where

$$L = L + 1/3 C_P (T_R - T_M) + C_{P_I} (T_M - T_I) \quad (2.23)$$

The local heat-transfer coefficient ($h(z)$) is defined as

$$h(z) = K_W / \delta \quad (2.24)$$

and the overall heat-transfer coefficient is given as

$$\langle h \rangle = \frac{1}{L} \int_0^L dz h(z) \quad (2.25)$$

Given these expressions for the heat-transfer coefficient, the temperature distribution in the refrigerant can be found by an energy balance on the refrigerant flow,

$$-M_R C_{P_R} dT_R = h(z) \pi D (T_R(z) - T_M) dz \quad (2.26)$$

To a first approximation: if the diameter is not a strong function of the axial distance (z) and $h(z)$ is approximated by $\langle h \rangle$, this expression can be analytically integrated from the inlet to any z , giving

$$T_R(z) - T_M = [T_R(z=0) - T_M] \exp\left(-\frac{\langle h \rangle \pi D z}{M_R C_{P_R}}\right) \quad (2.27)$$

A more accurate temperature profile can be found if $h(z)$ is used but the result is not significantly changed.

2.1.3.2 Ice-Pipe Melting Rate and Diameter Change

The melting rate of the ice pipe and the associated diameter change can be found by forming a mass balance on the ice pipe,

$$\rho_{W_I} \pi D dz \frac{d(D/2)}{dt} = \rho_W \pi D \langle V_z \rangle d\delta \quad (2.28)$$

Rearranging,

$$1/2 \frac{dD}{dt} = \frac{\rho_W}{\rho_{W_I}} \langle V_z \rangle \frac{d\delta}{dz} \quad (2.29)$$

Now $d\delta/dz$ can be found by differentiating Eq (2.22a) or (2.22b) and substituting into Eq (2.29). If the approximation is made that the temperature at the interface does not change substantially with time, then the equation can be analytically integrated to give,

$$D^{9/4} - D_o^{9/4} = \frac{9t}{8z^{1/4}} \left[\frac{4k_W(T_R - T_M)}{3\rho_W L^1} \right]^{3/4} \frac{\rho_W}{\rho_{W_I}} \left[\frac{0.005 \left(\frac{4}{\pi}\right)^2 M_R^2}{\rho_R \mu_W} \right]^{1/4} \quad (2.30a)$$

for τ_i given by Eq (2.11a) and

$$D^{7/3} - D_o^{7/3} = \frac{14t}{9z^{1/3}} \left[\frac{3k_W(T_R - T_M)}{2\rho_W L^1} \right]^{2/3} \frac{\rho_W}{\rho_{W_I}} \left[\frac{0.005 \left(\frac{4}{\pi}\right)^2 M_R^2}{\rho_R \mu_W} \right]^{1/3} \quad (2.30b)$$

for τ_i given by Eq (2.11b).

Equation (2-22) through (2-25), (2-27) and (2-30) are used to predict the temperature distribution in the refrigerant, the heat-transfer coefficient, and ice-pipe diameter as a function of the axial distance and time. Because they are decoupled, the heat-transfer coefficient and temperature distribution can be solved separately from the diameter change. Finally, two points should be noted about the approximations made:

- a. The diameter's dependence on the axial distance is slight ($D \sim z^{1/9}$ or $z^{1/7}$); therefore, its effect on the heat-transfer coefficient will be small as time progresses.
- b. The heat-transfer coefficient is a function of the local temperature difference ($T_R(z) - T_M$) to the 1/4 or 1/3 power; thus a reasonable approximation is provided by assuming that the heat-transfer coefficient is independent of the axial distance.

2.1.3.3 Discussion

The simple model described in the previous section was used to predict the experimental results. Some of the results are given in Figures 2.1-10, 2.1-11, and 2.1-12. The parameter that has the major impact on the results is the model for the interfacial shear stress (τ_i). If the model for the shear stress overestimates the experimental value, this increases the force driving the water-film flow, and decreases the thickness of the film (δ) at any given axial distance. This, in turn, would increase the heat-transfer rate to the ice pipe, lowering the temperature of the refrigerant above experimental values and overestimating the melt rate of the ice pipe. The opposite effect occurs if the shear stress underestimates the interfacial shear in the experiment. The shear-stress model of Wallis²⁻⁵ given by Eq (2.11a) seems to overestimate the shear stress as Figures 2.1-10 and 2.1-11 indicate. The refrigerant-temperature distribution is below that measured in the experiments, indicating the predicted film thickness is small ($\delta/D \sim 0.01$). Also, because the heat rate is predicted to be higher than in the experiment, the ice-pipe-diameter change is overestimated.

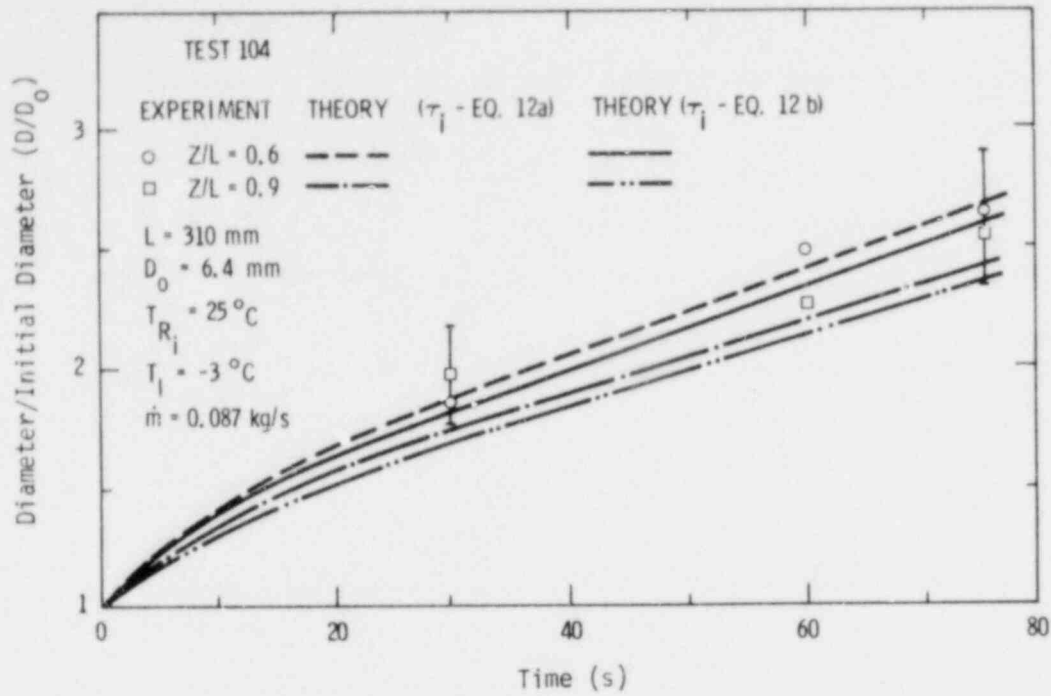


Figure 2.1-10 Model Agreement With Experimental Results (1)

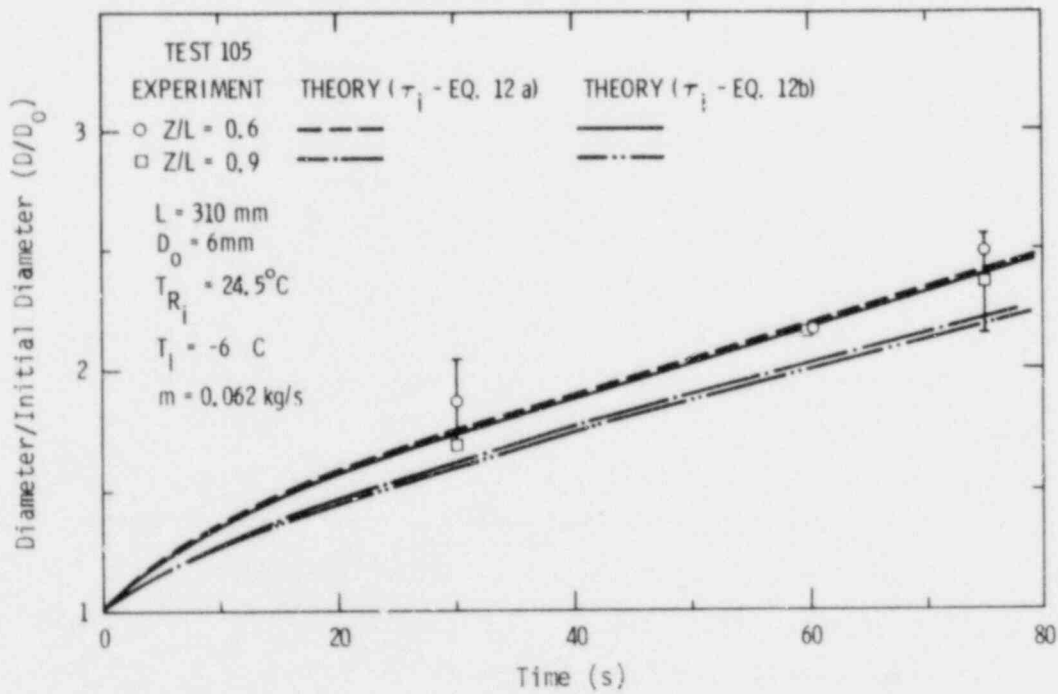


Figure 2.1-11 Model Agreement With Experimental Results (2)

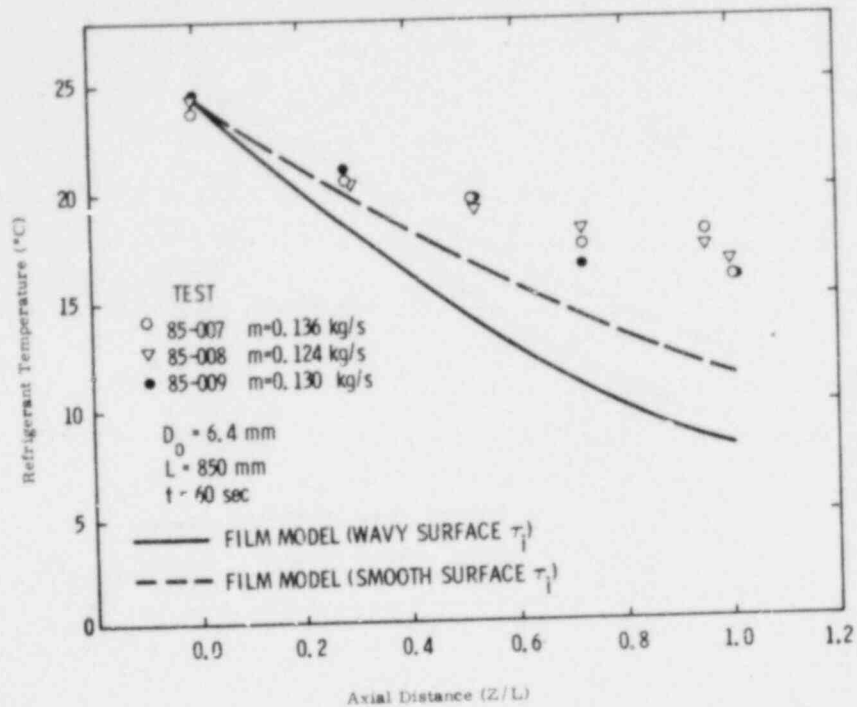


Figure 2.1-12 Model Agreement With Experimental Results (3)

If the model for τ_i given by Eq (2.11b) is used, the agreement with all the experimental results is much better as Figures 2.1-10, 2.1-11, and 2.1-12 indicate. Even though the agreement is superior to the previous model, the tendency of the analysis is still to overpredict the heat-transfer rate and, thereby, slightly overestimate the refrigerant's temperature difference across the pipe and pipe's diameter change.

The disagreement may be due to two possible effects: (a) the constant-temperature boundary condition at the water-refrigerant interface may be unrealistically optimistic; and (b) the models used for interfacial shear stress in a gas-liquid system may not be applicable in the liquid-liquid system. Correction of the first possible source of error requires that the turbulent-refrigerant flow field be coupled to the flowing laminar water film. This has been done by Boley²⁻⁷ for a hot fluid flowing into a solid pipe made up of the same material in laminar flow. However, it may prove quite difficult for a two-fluid system, and may not

be the dominant error. This second possible error may be another reason for the observed lack of agreement. When Wallis' model for τ_i is used, temperature-distribution and diameter-change profiles as a function of time are closer to the observed experimental behavior although the magnitude of the results indicates an overestimate of the heat-transfer rate. Conversely, when the other τ_i model is used, the magnitude of the temperature distribution and diameter change are closer to the experiment, although the profiles of these quantities as a function of time are not in as good agreement. This would suggest that a different functional relationship for τ_i in a liquid-liquid system is appropriate. To examine this possibility, experiments are being planned to measure the interfacial shear stress in a liquid-liquid system. Past work in this area^{2-8,9,10} has not indicated a useful model for τ_i .

The final observation is that the heat-transfer model exhibits the same general trend as the experiment; the overall Nusselt number defined by Eq (2.3) is constant with time. This can be seen by forming the product $\langle h \rangle D$. For example, the overall heat-transfer coefficient using τ_i in Eq (2.11a) indicates that $\langle h \rangle \propto D^{-5/4}$. Therefore, the product $(\langle h \rangle D)$ is a weak function of the diameter ($D^{-1/4}$) and thus a doubling of the diameter, which occurs during the experiment, only changes the Nusselt number by 18%, which is small.

2.2 Initial and Extended Fuel Motion (IEFM) (L.M. Choate, 4423; R.S. Howard, 1136; R.W. Ostensen, 4425; J.L. Portugal, 4425; K.O. Reil, 4423; D.J. Sasmor, 4453; W.H. Sullivan, 4426; S.A. Wright, 4426; M.F. Young, 4425)

2.2.1 Introduction

Phenomenological investigations are being conducted in transient overpower (TOP), loss-of-flow (LOF), and LOF-driven-TOP advanced reactor-accident sequences. To support accident analysis, detailed phenomena associated with core disruption must be identified and modeled. These phenomena include fuel motion inside the clad prior to failure, axial fuel-failure location, mode of cladding-failure, fuel-disruption modes, rate of

dispersal, fuel plateout, and extended fuel motion into the blanket (potential for blockage).

Current activities in the program are directed toward planning for up to 19-pin preirradiated fuel tests in the ACRR and participation in the NRC international-exchange program on CABRI through preanalysis of A and B series tests (TOP and LOF-driven TOP, respectively) with single-pin geometries and fresh fuel. Some reactor safety tests may be required that involve larger bundle sizes and full-length pins. Facilities in which to conduct these tests are therefore being evaluated on a continuous basis. Work on LOF and TOP accidents has been done in the DOE program at TREAT and will continue in the TREAT Upgrade. This program will be coordinated with the DOE program in order to take the maximum advantage of the available data.

The test planned for the ACRR will require an in-pile flowing-sodium system, high-power operating modes in the reactor, preirradiated fuel, hot-fuel handling facilities, and a high-resolution fuel-motion-diagnostics system. The fuel-motion system has been completed and will be installed in the ACRR tank early in 1979. The capability of the ACRR to operate in high-power modes has been established and will be available late in 1979. Work on the design and development of a flowing-sodium system has begun and will continue through 1979. The availability of the loop is the item that determines the pace of the IEFM-program work.

2.2.2 In-Pile Flowing-Sodium System for ACRR

The conceptual design of the interim in-pile flowing-sodium loop is continuing. This loop will be used in TOP, LOF, and PBE type tests of up to seven fresh UO_2 pins and possibly one preirradiated mixed-oxide pin, and will serve as a forerunner of a more advanced loop to be used in similar preirradiated fuel tests of up to 19 pins. Emphasis thus far has been directed at reviewing the scope of the experimental program with related test requirements as well as assessing various design criteria relating to those requirements.

Closely coupled to the design of the sodium loop are the constraints imposed upon the sodium environment relative to conducting "prototypic" experiments. The sodium-flow volumes necessary to provide a rate of flow sufficient to accommodate the test of interest are particularly important to loop design. An analysis was performed to estimate these requirements relative to the classes of experiments to be performed within the IEFM program and the number of test pins involved.

Flow areas can be found by enclosing the pin bundle in an hexagonal can, introducing flutes, and rounding the hex corners to reduce the excess flow area on the periphery. Table 2-3 lists the relevant flow areas. These areas are based on a CRBR core with 0.23-in. OD pins and 0.056-in. OD wire wraps. Fluting reduces the flow area by about 15% for a 19-pin bundle. Going from a 7-pin bundle to a 19-pin bundle raises the flow area, and thus the ultimate sodium-supply requirements, by a factor of 2.4.

Table 2-3
Flow Areas for In-Pile Tests (cm²)

<u>No. Pins</u>	<u>Hex</u>	<u>Fluted</u>	<u>CRBR</u>	<u>Fluted/CRBR</u>
1	--	0.309	0.173	1.79
7	1.930	1.593	1.212	1.31
19	4.529	3.915	3.288	1.19

To determine the volume of sodium needed for the tests, the areas in Table 2-3 are multiplied by the flow rates (610 cm/s for TOP conditions, full flow; 122 cm/s for LOF conditions, 20% flow) and the flow times. Flow times are listed in Table 2-4. Here, 5 s are allowed for the flow to be brought up to speed and stabilized prior to reactor start (this time is highly speculative). Because the tests are so short, allowing much more than 5 s for flow startup can force the needed sodium volume to much higher amounts. For all tests, a 2-s posttest-flow reserve is provided. This reserve can also be used to check the test section for the

degree of posttest blockage. Because their sodium requirements are relatively small, the test-flow times for LOF and LOF-driven-TOPS are somewhat generous. The total flow times in Table 2-4 appear to be reasonable minimum-flow-time requirements for the specified in-pile tests.

Table 2-4
Flow Times for In-Pile Tests (s)

	<u>Flow Stabilize</u>	<u>Test</u>	<u>Reserve or Posttest</u>	<u>Total</u>
LOF	5	13	2	20
LOF-driven-TOP	5	8	2	15
PBE (LOF)	5	5	2	12
PBE (TOP)	5	5	2	12
TOP-1	5	5	2	12
TOP-2	5	9	2	16

By combining the flow velocities, areas and times, the sodium volumes in Table 2-5 are found. If a tank-to-tank transfer system is used with one or both tanks in the ACRR glory hole, then the tanks are limited to about 6 in. diameter. The tank heights needed to hold the required sodium volumes are given in Table 2-6.

Table 2-5
Total Sodium-Flow Volume for In-Pile Tests (liters) (fluted area)

	<u>1-pin</u>	<u>7-pin</u>	<u>19-pin</u>
LOF	0.75	3.89	9.55
LOF-driven-TOP	0.57	2.92	7.16
PBE (LOF)	0.45	2.33	5.73
PBE (TOP)	2.26	11.66	28.66
TOP-1	3.02	15.55	38.21
TOP-2			

Table 2-6

Tank Height (ft) to Hold Sodium in the Glory Hole (fluted area)

	<u>1-pin</u>	<u>7-pin</u>	<u>19-pin</u>
LOF	0.14	0.70	1.7
LOF-driven-TOP	0.10	0.53	1.3
PBE (LOF)	0.08	0.42	1.0
PBE (TOP)	0.41	2.1	5.2
TOP-1	0.41	2.1	5.2
TOP-2	0.54	2.8	6.9

For LOF flow rates, 19-pin tests can be easily performed with a tank-to-tank sodium-transfer system fitting in an integral package in the ACRR glory hole. However, TOP flow rates (i.e., full flow) bring this approach into question for a 19-pin bundle. For a TOP-2 test, with both supply and receiver tanks in the test package, total tank height is 14 ft. Add 6 ft for test length and 5 ft for gas supply, valve, and miscellaneous. This gives a 25-ft high package. This is clearly near the limit of feasibility and may exceed it if the test package height is limited by hot-cell geometry. In conclusion, the 19-pin test requirement may seriously impact the sodium-loop design.

Partly because of the previously noted constraints, the interim loop will be fabricated for use with only a 7-pin maximum. This loop is envisioned as a gas-driven, single-pass, tank-to-tank, U-shaped system packaged in an appropriate container, and capable of accommodation entirely within the ACRR's vertical loading tube. The fuel-train and dump-tank sections can also be handled as an integral package within the existing hot-cell facility. The requirement for handling within the hot-cell facility is one of many constraints on loop design caused by the limitations imposed by the need for compatibility with existing facilities. The U-shaped design is being considered over the concentric design because it is fundamentally simpler and has less impact on the designs of other loop components. Next quarter, calculations to be performed with MORSE will

confirm compatibility of the U-shaped design with the slotted core necessary for the coded-aperture-imaging system. If these calculations should predict severe asymmetric heating, modifications to the U-shaped design will be required or a shift to the concentric design may be indicated.

Figure 2.2-1 schematically shows the conceptual design of the interim in-pile flowing-sodium loop. The test articles indicated on the figure would be located within the ACRR flux distribution and the coded-aperture-imaging fuel-motion diagnostic system. The figure represents only a conceptual design and some of the components and features of the loop, as discussed below, will likely change as more requirements are quantified. Further component design changes are likely once the stress and safety-analysis studies are initiated during the preliminary and final loop designs.

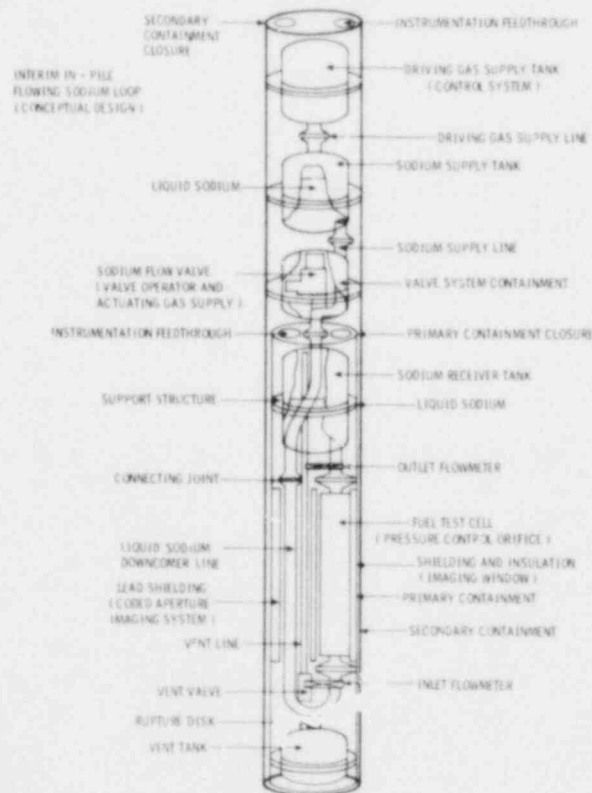


Figure 2.2-1 Interim In-Pile Sodium-Loop Conceptual Design

The flow channel for sodium coolant, which contains the test fuel pin, will be designed to model power-reactor conditions. In operation, the steady-state flow of sodium will be established and the reactor will be operated to produce the pin failure being studied. Fuel motion will be recorded by the coded-aperture-imaging system, while pressures and coolant flow will be monitored to record the details of the fuel-pin failure. Sodium flow in the system will be blocked with a valve closure when the excursion has passed. The system will be allowed to cool for subsequent evaluation within the hot cell.

More important features of the flowing sodium system are:

- a. Test cell - One fuel pin or seven fuel pins can be accommodated at full flow. For shorter flow times or at a reduced flow rate (LOF) the loop could support a 19-pin bundle. Fresh fuel would be no problem, but tests of preirradiated fuel are probably facility-limited at present. At least one single-pin PBE test with preirradiated fuel is considered as a design requirement for the interim loop.
- b. Sodium-Receiver (Dump) Tank - This tank is immediately above the test cell. Fuel debris is assumed to enter the inventory in the receiver and therefore the receiver is located within the primary containment. Three conduits through the length of the receiver tank will reduce its storage capacity. They are the sodium downcomer, an instrumentation conduit, and a vent line. The primary containment closure is now planned to be integral with the top of the receiver tank.
- c. Sodium-Valve Assembly - This will be a normally (failure mode) closed, remotely actuated, bellows-sealed valve that opens or closes the path between the supply and receiver tanks through the test cell. A gas reservoir inside the valve containment will permit several operations of the valve. Exhaust from the actuator will be contained in the volume of the valve containment. Operation will be by electrical signals that penetrate the upper section of the valve containment.
- d. Sodium-Supply Tank - This tank is above the valve. It can be pressurized to a preset value to produce the desired flow when the valve is opened. Heaters

will heat the sodium inventory to the desired temperature before flow is started.

- e. Gas-Supply Tank - This tank is above the sodium-supply tank. It contains the argon (or helium) driving gas reserve, with controlling hardware located inside the secondary containment vessel. Capability will exist to limit the available gas pressure to a specified maximum value.
- f. Vent System - A vent tank allows the pressure in the receiver to be held nearly constant as flow progresses. This permits more flexibility in the absolute pressure on the test article as flow proceeds. A rupture disk connects the vent tank to the sodium downcomer piping as a safety precaution.
- g. Containment System - Containment of sodium in the flowing channel may be breached at the time of the reactor excursion. The primary containment is defined as the vessel into which leakage of coolant (possibly including fuel and fission products) could occur during such a breach. Only small pressures would prevail. Secondary containment is yet another vessel that packages all the loop components. All sodium is contained in structurally-sound vessels inside the secondary containment. Penetrations of the containment barriers are reduced where possible and are limited to electrical feed throughs.
- h. Sodium Piping - Piping for sodium flow is connected with proven joints. The system will be proof-tested and leak-tested. All piping will serve as a containment barrier but will not be counted as such.

Provisions are planned for monitoring and controlling the thermal preheating system so that it can safely interface with the reactor. Nontrivial precautions are required during handling, preparation, and posttest evaluation, especially if preirradiated test fuel is involved. These precautions are not obvious and may become a weak point in the program if facility restrictions continue.

Upon completion of a test on the ACRR, the sodium will be allowed to freeze in place. Afterwards, the pipe joint just above the primary-containment vessel and below the sodium valve-enclosure tank will be broken so that the primary containment vessel (containing the failed-fuel

section) may be accommodated within the existing hot cell for disassembly and postmortem examination. The remainder of the uncontaminated portion of the loop hardware will be cleaned in preparation for further use.

Because the sodium-environment requirements are so very important to loop-hardware design, the evolution of these requirements continues. In particular, inertial length and internal-pressure conditions will be investigated and reported next quarter. Fuel-train design considerations will also be reported.

2.2.3 Advanced Operating Modes for the ACRR

The designs of the two prototype rod-drive programmers for interfacing with the ACRR control console have been completed. One system is based on hard-wired logic components and provides a maximum of eight program intervals. The second system is a microprocessor-based device. This system provides up to 62 program intervals. Final selection will be based upon laboratory evaluation of the two systems.

Parts procurement for both programmers is approximately 80% completed. Fabrication of the hard-wired logic system was started on December 1, 1978 and was completed in early March. Programming for the microprocessor-based system was begun and is approximately 50% completed.

A new motor and translator power supply were selected and are now available for evaluation. Design of the required mechanical modifications to the rod drives has been started.

2.2.4 Energy-Deposition Measurement in the CABRI Test Pin

Accurate energy-deposition measurements within the fuel pin of the CABRI sodium loop are needed to correctly model the LOF and prompt-burst accidents simulated in the A and B series experiments. Present techniques are only capable of measuring the energy deposition to within 10%. Such large uncertainties can lead to large errors when predicting the fuel-melt fractions, time of clad failure, fuel-vapor pressures, and other phenomena

of interest. Therefore, the objective of this program is to provide a series of diagnostic tools which, when integrated with the French Calorimeter,²⁻¹¹ can measure the time and spatially-dependent energy depositions in the test pin to within 3 to 5%. Several types of detectors will be used to perform this task and, in addition, an unfolding algorithm will be provided which, when given the detector responses, can determine the energy deposition within the fuel pin. Both the detectors and the unfolding algorithm will use techniques originally developed for the Sandia In-Core Fuel-Motion-Detection Program.

To accurately monitor the energy deposition within the fuel pins, the detectors must be close to the fuel. For this reason, the detectors will be placed at different axial locations within the sodium by-pass loop and approximately 23 mm away from the fuel-pin centerline. The detectors will consist of ten neutron detectors and five gamma detectors. Five of the neutron detectors will be commercially purchased fission chambers that are specially designed to be linear in the flux-range of interest. The remaining five neutron detectors will be fission-couples fabricated at Sandia. The five gamma-sensitive detectors will be identical to the fission couples except that tungsten will be used as a heat source instead of depleted uranium.

This quarter the fission chambers were ordered from Reuter-Stokes at a cost of \$3200 per detector. These detectors are designed to operate in the flux range of 2×10^{14} - 2×10^{17} nV and have a neutron-to-gamma sensitivity of 20. The detectors will be 25.5 mm long, 6.35 mm OD, and will have a cable length of 12 m with a 3.1-mm OD. The detector will be sodium-compatible at 573K (300°C) for one week and will probably be attached to the inner wall of the sodium bypass loop.

The package designs for the thin-film fission-couple and gamma-couple detectors were completed this quarter. Figure 2.2-2 illustrates the fission-couple design. A few prototype detectors are being assembled to determine their ease of fabrication and assembly. The detectors will

be tested for sodium compatibility next quarter and will be subjected to several SPR pulses next quarter.

FISSION COUPLE SUBSTRATE - 18 JUNCTIONS / SUBSTRATE, 12 USED - 6
 SPARE, 4 SUBSTRATE (2 BACK TO BACK) USED YIELDING 48 JUNCTIONS - 24
 URANIUM, 24 TUNGSTEN .010" THK

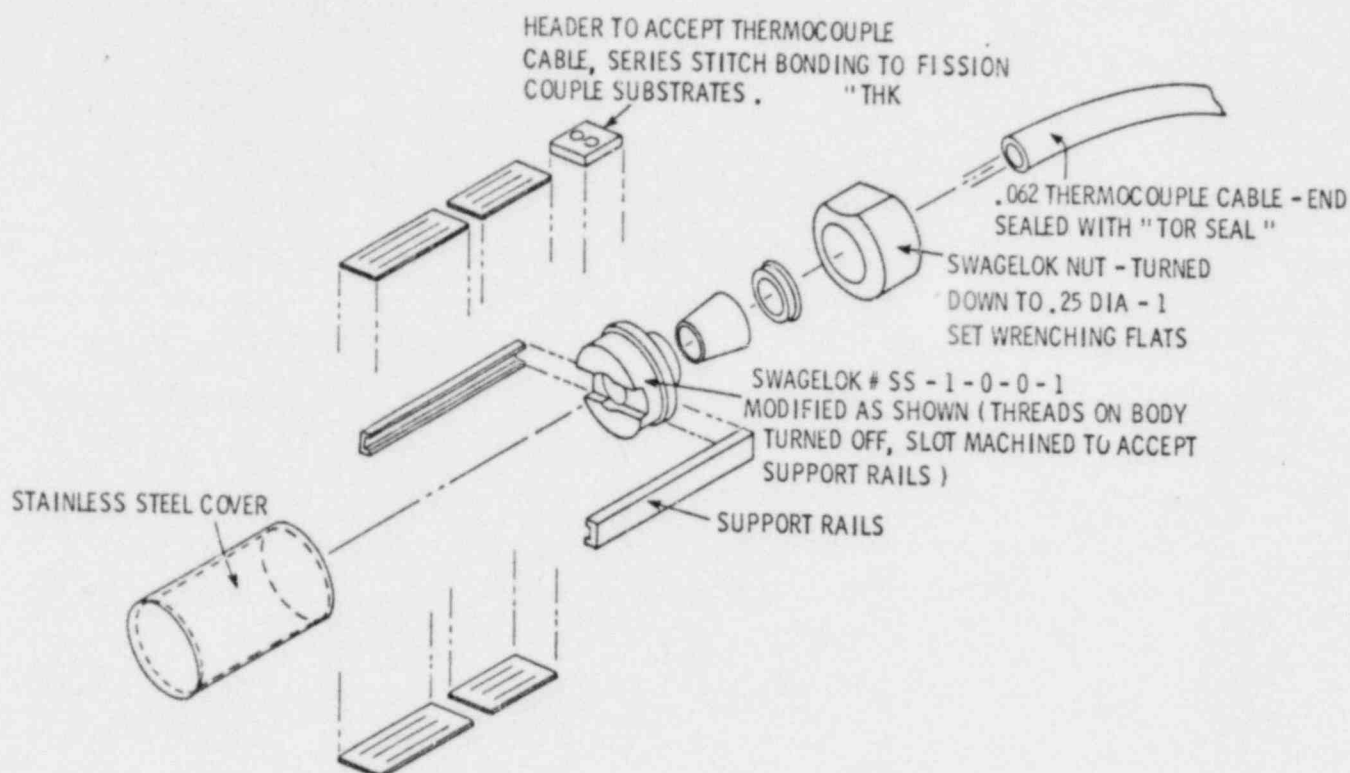


Figure 2.2-2 Fission Couple Detector - CABRI

Reactor experiments with fission-couples were performed this quarter to determine the heat losses and rise-time of the tested detector. For this detector (which differs from the CABRI fission-couple), the 90% rise-time was 2.0 ms and the heat losses were on the order of 40% of the maximum temperature rise after the reactor pulse. These data will be used to help develop algorithms that can correct for heat losses over time periods of 2 s. Once the heat-loss algorithms are generated, it will be

possible (given the detector responses) to modify the in-core fuel-motion-detection-kernel generation techniques²⁻¹² and the unfolding techniques.²⁻¹³ These modifications will allow investigators to determine the energy deposition in the fuel pins.

2.2.5 CABRI Tests Calculations With the EXPAND Code

As part of the multinational CABRI program, Sandia is providing pretest calculations of A-series (TOP), single-pin, fresh-fuel tests. These calculations, using the EXPAND code, are aimed at predicting fuel-pin failure. Exchange of technical information between Sandia and the other partners of the CABRI program (France, West Germany, United Kingdom, and Japan) continues to improve such that the program is evolving, as intended, into a much needed and useful technical-exchange program in reactor safety.

During this period, an active program has been conducted to perform the precalculations of the CABRI tests of the A-series which have been scheduled for the near future. These precalculations were related to A2, A3, and A1R tests; a postcalculation was done for the A1 test. Each of those analyses will be examined in chronological order.

2.2.5.1 A2 First Precalculation -- As A1 had already been performed in July 1978, the first precalculation for A2 was accomplished in September 1978. The major results have been documented in a rough draft of a CABRI Note²⁻¹⁴ written and released on January 29, 1979. For the first set of precalculations, the main results can be summarized.

In the steady-state condition, the center and surface temperatures of the fuel were 2692 K (2419°C) and 1353 K (1080°C), respectively, with a gap width of 66.5 μm at the peak-power node. The axial-fuel expansion was 1.55 cm. During the transient, the maximum molten-fuel areal fraction of 59.6% was attained after 130 ms. A clad failure was expected at 330 ms according to the Larson-Miller life-fraction rule. At the same time, the onset of sodium boiling was foreseen at the top of the coolant channel without interfering with the prediction of clad failure in

the single-phase zone. For the time being, EXPAND is not able to deal with two-phase sodium. The energy deposition during the transient at peak-power node was 0.38 kJ/g.

2.2.5.2 A2 Second Precalculation -- Since there were some differences among the calculations made by the other CABRI-project partners, all the data and EXPAND itself were investigated with the purpose of interpreting these differences. Two corrections were made in the application of the Larson-Miller life-fraction rule (correction of unit and shift from natural to decimal logarithms); the negative heat transfer from sodium to structure was also corrected.

At the same time, some of the data were improved (specific power of 117 W/g instead of 106 W/g at the peak-power node and a slightly changed-axial power shape).

While running this new calculation, the sensitivity of results with regard to the coupling factor was studied. Before the test, the uncertainty of the coupling factor (as calculated) is in the range of +10 to +15%. The main results are presented in Table 2-7. The conclusions inferred from the new results are different from the previous conclusions. No clad failure is expected in the nominal case (but an energy deposition 10% higher would result in a clad failure at 220 ms).

At steady state, the inner- and surface-fuel temperatures were 2751 K (2478°C) and 1354 K (1081°C), respectively. The increase in the fuel-center temperature is due in this case to a higher specific power. For the surface temperature, the result of higher specific power has been compensated for by a decrease in sodium temperature after correction of the model for heat transfer between sodium and structure.

Table 2-7

A2 Test Sensitivity Study

Power	$P_o - 10\%$	P_o	$P_o + 10\%$
Specific Power in Steady State (W/g) at peak-power node.	105.3	117	128.7
<u>Steady State</u>			
<u>At Peak-Power Node</u>			
Inner-fuel temperature ($^{\circ}\text{C}$)	2316	2478	2624
Outer-fuel temperature ($^{\circ}\text{C}$)	1037	1081	1122
Inner-clad temperature ($^{\circ}\text{C}$)	527	541	556
Outer-clad temperature ($^{\circ}\text{C}$)	497	508	519
Gap width (μm)	68	64	60
Gap conductance ($\text{W}/\text{cm}^2\text{C}$)	0.525	0.563	0.602
Axial-fuel expansion (cm)	1.46	1.57	1.68
Average-energy deposition (kJ/g)	1.474	1.638	1.802
Na inlet/outlet temperature ($^{\circ}\text{C}$)	400/511	400/523	400/535
<u>Transient State</u>			
<u>At Peak-Power Node</u>			
Onset of fuel melting (ms)	50	42	42
Max. melt fraction (%)	45.5	69.5	79
Time of max. melt fraction (ms)	130	130	130
Gap closure/open (ms)	No	42-50/74-130	42-50/74-130
Max. axial-fuel expansion (cm)	2.98	3.27	3.57
Cladding deformation	Plastic	Plastic	Plastic
Max. temperature rise of Na at top of fissile length	307	343	288 at pin failure
Time of max. Na temperature (ms)	530	530	220
Life fraction at 6.130 s	6.85×10^{-4}	3.6×10^{-3}	1.144 at 220 ms (pin failure)
The average energy deposition at SCRAM (kJ/g)	2.198	2.443	2.687
Transient energy deposition in fuel power-peak node (kJ/g)	0.527	1.030	1.333

The gap size of 64 μm (which is larger than those found by the other partners) comes from EXPAND having a fuel-cracking model that allows for complete porosity release (generally not considered in other codes). The axial-fuel expansion remained almost unchanged at 1.57 cm. The maximum molten-fuel fraction was increased to 69.5% for an energy deposition at SCRAM at the peak power node of 0.805 kJ/g.

All these results (which are final) will have to be recalculated because the enrichment of the test pin has been changed from 12 to 20% for all the fresh-fuel tests of the CABRI program. This change was made to permit a higher energy deposition. Moreover, the driver-core configuration has been changed to withdraw the excess of reactivity. Although the A2 precalculation has been performed with a symmetrical axial-power shape (control rods in upper position), the new precalculation should take into account the new axial-power profile (control rods slightly inserted).

2.2.5.3 A1 Postcalculation -- After the A2 calculation, the decision was made to postcalculate the A1 test without knowing very accurately the results of the test except that the clad did not fail.

Several calculations have been performed on A1; the last one indicated no clad failure and an energy deposition at SCRAM of 0.556 kJ/g (at axial peak-power node). The data of the A1 calculation should be reviewed and determined more accurately. For instance, the axial-power profile was considered as symmetrical with respect to the core mid-plane. In fact, the power profile was very asymmetrical due to the large insertion of the control rods in the driver core. As soon as the exact conditions of the experiment are shown, a new calculation for A1 will be performed.

2.2.5.4 A3 Precalculation -- Concurrent with receipt of the calculational results for A1, the A3 test was precalculated according to the data available at that time. The A3 precalculation yielded a double-clad failure at 188 ms after initiation of the transient with an energy deposition at the peak power node of 0.770 kJ/g at failure.

This calculation exemplifies the work done for the CABRI test precalculations but, like the preceding A1 calculation, it should be considered as a benchmark problem rather than an actual prediction of the experimental results. As previously stated, the test-pin enrichment will be changed along with other important parameters. Further, the model for heat transfer between sodium and structure was not corrected at that time.

Since knowledge of the A3 conditions is dependent upon the performance of the A1R and A2 tests, information from these tests must be obtained before a rigorous predictive calculation for A3 is initiated.

2.2.5.5 A1R Precalculation -- The A1R test, designed as a repetition of A1 but with improved experimental conditions, is expected to be performed very shortly. The A1R experimental conditions were fairly well known and a complete set of calculations, including reactivity studies, have been performed. All the results are documented in Table 2-8 and will become the subject of a CABRI Note to be published on A1R precalculations.

The main results are:

- a. At steady state, the center fuel temperature is 2731 K (2485°C) (at axial-peak-power node) and the fuel-surface temperature is 1400 K (1127°C) with a gap width of 66 μm . The axial-fuel expansion is 1.56 cm.
- b. If these steady-state results are compared with the results obtained by the other CABRI partners, the gap-size value calculated by EXPAND is larger than the other values (between 50 and 57 μm). This disparity is caused by a fuel-cracking model in EXPAND resulting in porosity release and more space between fuel and clad. Concerning the radial-temperature profile, the maximum fuel temperature is very close to the others, but the fuel-surface temperature is more than 100 K higher. This is the consequence of a larger gap in EXPAND analysis.

Table 2-8

AIR Test Sensitivity Study

Power	$P_o-20\%$	$P_o-10\%$	P_o	$P_o+10\%$	$P_o+20\%$
Specific Power in Steady State (W/g) at peak-power node.	118.08	132.83	147.59	162.35	177.16
<u>Steady State</u>					
<u>At Peak-Power Node</u>					
Inner fuel temperature (°C)	2118	2297	2458	2604	2739
Fuel surface temperature (°C)	1028	1073	1127	1172	1215
Gap width (μm)	74	70	66	62	59
Gap conductance (W/cm ² -C)	0.46	0.49	0.53	0.56	0.59
Axial-fuel expansion (cm)	1.33	1.45	1.56	1.66	1.76
Na inlet/outlet temperature (°C)	400/544	400/563	400/581	400/600	400/618
<u>Transient State</u>					
<u>At Peak-Power Node</u>					
Onset of fuel melting (ms)	--	130	80	70	60
Time of minimum gap width (ms)	100	100	100	100	100
Minimum gap width (μm)	37.6	32.2	27.2	20.6	12.6
Gap conductance (W/cm ² -°C)	1.03	1.19	1.38	1.71	2.36
Time of max melt fraction (ms)	--	500	500	500	250
Liquidus radius (mm)	0	0	0	2.253	2.258
Solidus radius (mm)	0	1.856	2.240	2.623	3.000
Molten fuel fraction (%)	0	8.53	30.25	51.09	63.00
Max temperature rise of Na (°C) at top of finite length	241	273	306	33.8	371
Time of max Na temperature (s)	1	1	1	1	1
Max fuel temperature (°C)	2800	2847	2847	3012	3247
Max clad temperature (°C); time (ms)	686(500)	723(500)	763(500)	804(500)	857(250)
Max axial-fuel expansion (cm)	2.26	2.43	2.62	2.82	3.03
Life fraction at 5 s.	5.45	8.99	1.6	6.68	2.39
	x 10 ⁻⁷	x 10 ⁻⁶	x 10 ⁻⁴	x 10 ⁻⁴	x 10 ⁻³
Average energy deposition at SCRAM (kJ/g)	0.523	0.588	0.653	0.719	0.785

For transient conditions, the onset of fuel melting is at 80 ms after initiation of the transient (between 71 and 92 for the others). The minimum gap size is 27 μm which is higher than the other results which predict a gap closure during the transient. The maximum molten-fuel fraction should be 30.25% at 500 ms. The other codes find values between 22 and 52%. The EXPAND result seems to be quite reasonable since, as shown in Table 2-8, there is a very high sensitivity of the maximum molten-fuel fraction to the energy deposition. For the nominal case, the liquidus threshold has not been reached (the fuel temperature never passed the melting point of 3120 K (2847°C)) and this result agrees with the others. The main conclusion (similar to the others) is that no clad failure is expected in this experiment. EXPAND predicts a clad-life fraction of only 1.6×10^{-6} after 5 s. The clad deformation is still in elastic regime and the energy deposition at peak mode at SCRAM in the test pin is 0.653 kJ/g which is close to the German figure of 0.67 kJ/g but somewhat higher than the French value of 0.52 kJ/g. The gamma heating of the Niobium tube, 4% of the test-pin power, is not taken into accounts therefore, the specific power of 147.59 W/g, which equals a peak linear rating of 480 W/cm, should have been increased by 4%.

- c. Two additional points which should be emphasized are:
- (1) The maximum fuel-column expansion (finite lengths only) is 2.62 cm with EXPAND as compared to 2.76 cm for the French code. Since neither the clad expansion nor the upper and lower fertile zone dilatation are calculated, it is not possible to predict accurately the telescope displacement.
 - (2) The maximum clad temperature reached during the transient is in acceptable agreement with the others (1036 K for EXPAND and 1018 to 1053 K for the other codes), but the time at which the maximum is attained is much earlier than the others (0.5 s against 1.3 to 1.5 s for the others). No clear explanation for the discrepancy is available at the present time.

Besides the correction that was made, the model of heat transfer between sodium and structure has been significantly improved. Instead of

describing one structure-region representing the different regions between the coolant channel and the bypass channel with average thermal properties, EXPAND is now able to describe explicitly the Niobium tube. The gap and the Zircalloy tube are taken into account by a coefficient of heat transfer for the sodium bypass channel. This coefficient is now an input in EXPAND. This more precise description has improved the sodium temperature in the coolant channel which was somewhat low (according to the reference conditions) despite a correct mass flow rate especially for the A2 calculations.

2.2.6 Conclusion

The calculations for the A1, A1R, A2, and A3 CABRI tests have been performed with different levels of sophistication. For the upcoming tests, the most extensive precalculations pertained to A2 and A1R. EXPAND has demonstrated its capability to deal with A2 and A1R transients that occurred over a much longer period of time than the transients of tests previously performed in the ACPR.

The experimental results will allow for determining whether the physical models in EXPAND are definitively appropriate for this kind of experiment. The postcalculation for A1 will be reconsidered with respect to actual experimental conditions as soon as these conditions are available, probably in the next reporting period.

The experimental conditions of the A2 and A3 tests will depend on the results of A1 and A1R. Updated precalculations will be performed when accurate information related to A1 and A1R is received.

2.3 Fuel-Motion Detection (FMD) (S.A. Wright, 4423; P.J. McDaniel, 4231; D.A. McArthur, 4423)

2.3.1 In-Core Fuel-Motion Detection

Fuel-motion experiments were performed in the SPR-III to test the feasibility of in-core FMD. The experiments performed this quarter are part of a series of experiments to determine the effects that fuel-bundle

size, and detector type and location have on the resolution capabilities of the detector method. To accomplish this task, two types of detectors (gamma-sensitive Pt-self-powered detectors and fast-neutron-sensitive fission-couple detectors) will be used to monitor fuel motion in 7-, 19-, and 37-pin bundles. In addition, these experiments will also be used to develop and test unfolding techniques that are necessary if fuel motion is to be accurately determined, given the detector responses. In this report a brief description of the progress achieved in the experiments, the detector development and testing, and the unfolding techniques will be given.

2.2.1.1 SPR-III Fuel-Motion Experiment -- The experimental plan and safety-analysis report for the 7-pin FMD experiment was presented to the Reactor Safeguards Committee. The committee accepted the experiment with no modifications and also delegated authority to the SPR Committee to approve the larger 19- and 37-pin experiments. The major limitations placed on the experiment by the safety-analysis report are that the minimum reactor pulse be limited to 573 K (300°C) and the first experiments be limited to reactor pulses less than 423 K (150°C). This last restriction will be removed when dosimetry shows that the energy deposition in the test pins are within 20% of the values presented in the safety-analysis report.

The experiment test stand was assembled with seven fuel pins arranged in a hexagonal lattice and with 30 Pt-self-powered detectors (Pt-SPD's) placed in and around the fuel bundle. Each detector has a sensitive region 25.4 mm long; consequently, 12 of the detectors were placed axially 25.4 mm apart between the first and second row of pins. Five more detectors were placed still further from the bundle and are used as gross-motion monitors. The last detector is a normalization detector and is far enough away from the fuel bundle to be insensitive to fuel motion. After assembly the test stand was tested in the laboratory to assure that the fuel pins move freely and that the fuel-pin locking device operates correctly.

During the experiments the data from the detectors were recorded using a data-acquisition system capable of sampling at 5- μ s intervals. This system can store 1024 10-bit data points per channel. A total of 64 channels are available. Figure 2.3-1 shows a typical voltage output of a Pt-SPD when the output was shunted through a 2-k Ω resistor. After each reactor pulse, the data is recorded on a floppy disk and then analyzed with an LSI-11 minicomputer to extract from the detector signals the pertinent information such as peak value or area under the pulse. This reduced data is then sent to the Sandia CDC computers via the NOS time-share system.

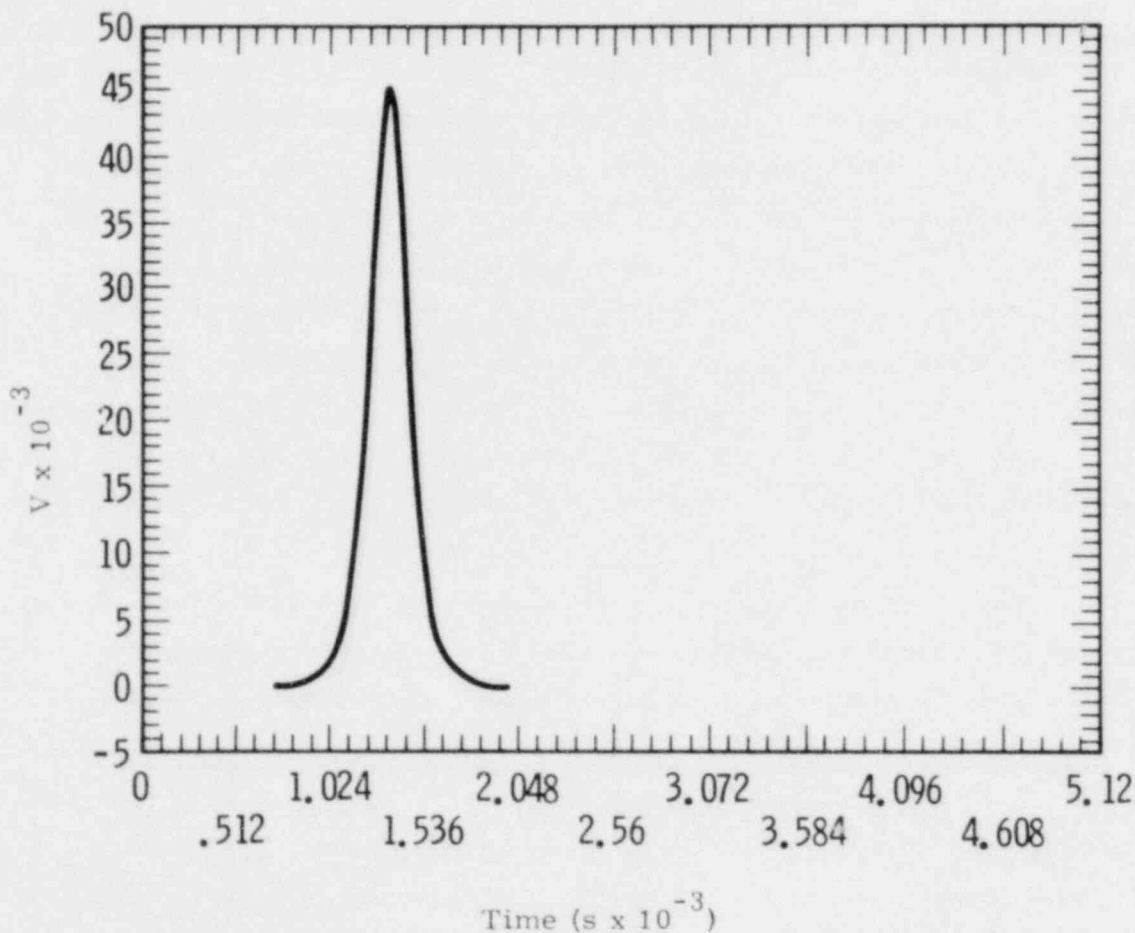


Figure 2.3-1 Typical Output Voltage of a Pt-SPD When the Voltage is Shunted Through a 2k Ω Resistor in the In-Core FMD Experiments.

The first fuel-motion experiments were performed in January 1979. In these experiments, two reactor pulses were performed with the fuel pins fully inserted; two other pulses were performed with seven of the fuel pins withdrawn 15.2 cm (see Fast Reactor Safety Quarterly for an illustration of the experimental assembly).

Unfortunately, of the 30 detectors placed in the experiment, only 23 gave usable signals. Nevertheless, signals attributable to fuel motion were clearly observed. The signals from detectors near regions where the fuel was removed were observed to decrease by 15 to 20% of the background signal. In regions toward which fuel was moved, the signals increased by 18 to 22% of the background signal. This result is extremely encouraging because these signals are twice as large as expected for this type of detectors.

2.3.1.2 Detector Design Development and Testing -- In addition to the last fuel-motion experiments, experiments were performed to measure the neutron and gamma sensitivities of the fission-couple detectors and the Pt-SPD's to the SPR-III spectrum. The results of these experiments will be used to assess the sensitivity of various detectors to fuel motion. They will also be used to improve the techniques for generating detector-response kernels. The neutron and gamma sensitivities were measured by perturbing the neutron-to-gamma flux ratios observed by the detectors in two separate reactor pulses. Neutron-sensitive foils and gamma-sensitive thermal-luminescent diodes (TLD's) were used to measure the neutron and gamma fluxes. The neutron and gamma sensitivities of the two detectors are shown in Table 2-9. The Pt-SPD is seen as almost entirely sensitive to gammas while the fission-couple detector is sensitive to both neutrons and gammas. The fission-couple used in these experiments has a high gamma sensitivity because it was made without a gamma-compensating tungsten chip. If it becomes necessary to lower the gamma sensitivity of the detector to improve the fuel-motion sensitivity, the gamma-compensating chip can be included in the detector fabrication.

Table 2-9

Fission-Couple and Pt-SPD Sensitivities

	<u>Neutron Sensitivity</u>	<u>Gamma Sensitivity</u>
Fission-Couple*	3.2×10^{18} V/nvt	3.9×10^{-18} V/F δ [†]
Pt-SPD**	4.1×10^{-24} A/ms	3.2×10^{-23} A/ $\phi\delta$

[†]F is the gamma fluence = $\int \phi_{\delta} dt$

*The fission-couple is a ^{238}U thin-film thermocouple heated by four depleted uranium chips. No tungsten chips were used for gamma compensation

**The Pt-SPD has a platinum emitter length of 25.4 mm with an OD of 0.48 mm. The Inconel sheath is 1.59 mm OD and 1.02 mm ID

2.3.1.3 Unfolding Calculations -- During this report period a series of one-dimensional forward-transport calculations were run to analyze the effects of fuel removal on the Pt-SPD's signals. These calculations were performed with the XSDRN transport code using the BUGLE cross-section library. This library is a coupled neutron-gamma set of cross sections that is required when calculating the responses of the gamma-sensitive Pt-SPD's. Three general conclusions can be drawn from these calculations. First, the detector signals, due to removal of fuel from a region, appear to be linear for fuel-density reductions up to 95%. For density reductions greater than 95%, the detector signals are nonlinear. Second, the sensitivity of a Pt-SPD to fuel motion appears to be about one-half as strong as the ^{238}U fission-couple. Typical signal levels for the Pt-SPD, when all the fuel is removed from a region near the detector, are approximately 7% of background; for the ^{238}U fission-couple, the signal levels were 15%. Comparing these calculational results to those of the SPR experiments, it is clear that the observed signed responses are approximately twice as large as predicted. This difference will be investigated next quarter.

In addition to the one-dimensional forward-transport calculations, the MORSE code was run to determine the adjoint fluxes for each detector and the forward flux in the test assembly. The adjoint calculations take about 10 min each and the forward calculation takes about 1 hr. These fluxes were then combined in the code RHOPER to determine the detector-response kernel for each detector. Some errors were made in generating these detector-response kernels but they are good enough to use in the unfolding of the experimental data. When these kernels are used to calculate detector responses, the results agree very well with the one-dimensional forward results. However, when they are compared with the experimental results, the calculations almost always underpredict the signal changes. During the next quarter the kernels will be recalculated to correct the known errors and some unfolding of the experimental data will begin.

2.3.2 Coded-Aperture-Imaging Fuel-Motion Detection

2.3.2.1 Introduction -- The Coded-Aperture-Imaging task is concerned with the imaging problem that will arise in large LMFBR safety test experiments (those with more than seven LMFBR fuel pins). Imaging in these large tests is expected to differ significantly from one-to-seven-pin tests because of the greater scattering and absorption of the imaging radiation within the large bundles of test fuel pins, and because of the greater complexity of the image itself. Coded-aperture imaging of both gamma rays and neutrons is being studied.

In gamma-ray imaging studies, a 37-pin bundle has been chosen as a representative case of a larger test. As reported in previous quarterly reports, realistic Monte Carlo transport calculations have been performed to estimate the signal changes to be expected from voiding of various amounts of test fuel, sodium, and steel. Parameters of the coded-aperture system were also varied in these calculations to improve the system's sensitivity to changes in the test-fuel geometry. The focus of present Sandia work in gamma-ray imaging is to check these calculational results with imaging experiments on a 37-pin bundle, using the PARKA reactor at

Los Alamos Scientific Laboratory.²⁻¹⁵ In these experiments the image changes caused by removal of varying amounts of fuel from the 37-pin bundle will be measured. These experiments will test not only the calculations, but will also investigate the effects of reactor-background radiation, the images produced by various possible codes in the coded aperture, and the problems encountered in reconstructing images of larger objects such as the 37-pin bundle. Successful completion of this program is expected to result in an optimized gamma-ray coded-aperture system for high-resolution imaging in large-bundle tests.

During this reporting period, major elements of the apparatus for the PARKA experiments were designed, and some fabrication work was begun. In order to choose candidate-coded apertures for the PARKA experiments, "mockup" optical experiments were also performed. In these optical experiments, complex objects analogous to fuel-pin arrays were imaged, using various candidate-coded apertures and analog-reconstruction methods (the only methods routinely available at present). Image quality varies widely and extensive optimization of the analog-reconstruction procedures will be necessary to obtain consistently good results. However, these experiments showed that imaging of objects up to seven-fuel-pins wide is feasible with off-axis Fresnel codes.

Imaging of fast neutrons is desirable in large-bundle tests because fission neutrons have a somewhat greater scattering length than fission-gamma rays, and because fast-neutron emission is more directly characteristic of the fuel geometry. The goal of the neutron-imaging portion of this program is to image fast neutrons with minimal backgrounds from slow neutrons or gamma rays, by making use of the greater sensitivity of the coded-aperture technique.

Work in previous quarters has shown that tungsten-coded apertures designed for high-resolution imaging can produce good static images of a small ^{252}Cf source, using only the fast neutrons ($E_n \geq 1.5$ MeV) emitted by the spontaneous fission source. Therefore, present work is concentrated on developing a practical fast-neutron-detector system for transient

imaging, and on measuring the limiting resolution that can be obtained with Sandia's recently developed static fast-neutron-imaging methods.

During this reporting period, it was necessary to emphasize the design of the PARKA gamma-ray experiment, so relatively little neutron-imaging work was performed. However, experiments performed on the ^{252}Cf source with neutron-sensitive scintillators indicated that an image-intensifier system would be required for further transient detector-development work. The dominant source of the spurious background in the Lexan images was also clearly identified and corrected by a relatively simple procedure.

2.3.2.2 Gamma-Ray Imaging

2.3.2.2.1 Gamma-Ray Imaging Experiments at PARKA -- The PARKA reactor facility at LASL includes a heavily-shielded room adjacent to the reactor, a hodoscope collimator, and an apparatus for manipulating a 37-pin test-fuel bundle to present voids of various sizes to the imaging system under test. The PARKA is a very low-power reactor without cooling that can produce a test-fuel power of $\sim 5 \text{ mW/g } ^{235}\text{U}$ under steady-state conditions. Steady-state runs of about 3-h duration should be required to record an image of the test-fuel bundle with $\sim 1\%$ statistics (this calculation neglects reactor backgrounds and reconstruction noise, but includes the effects of noise caused by the large number of resolution elements in the image).

For the coded-aperture experiments, the hodoscope collimator will be replaced by a somewhat shorter coded-aperture collimator made of steel. Additional shielding will be provided on either end of the coded-aperture collimator to reduce leakage. The new collimator is designed to accommodate coded apertures ranging in width from ~ 1.2 to ~ 3.2 cm, with vane thicknesses up to 2.54 cm. For these experiments, S_1 (source-to-aperture distance) $\cong S_2$ (coded aperture-to-scintillator distance) $\cong 1.375$ m, so that thick coded apertures can be used. For some aperture

designs a small amount of vignetting may occur on one side of image, somewhat reducing resolution.

Because of the low-reactor power level, it will be necessary to use an image intensifier in the recording system. An EMI four-stage image intensifier similar to the ones in the ACRR Coded-Aperture-Imaging System will be used to record the data. DuPont Hi-Plus/NDT has been tentatively chosen as the scintillator based on the extensive experiments of Stalker and Kelly.

Three coded-aperture designs and a rectangular pinhole have been chosen for evaluation during these experiments (Figure 2.3-2). All provide transverse spatial resolution of 2 mm and longitudinal spatial resolution of 2 cm, corresponding to the resolution requirements suggested for 37-pin bundle experiments.²⁻¹⁶ Of the coded apertures, the on-axis Fresnel code has been used extensively by Kelly;²⁻¹⁷ the off-axis Fresnel code was used in the recent successful neutron-imaging experiments. The uniformly-redundant array (URA) has been suggested by Chu²⁻¹⁸ as a preferable alternative to the on-axis Fresnel code for broad objects. The pinhole will allow a direct comparison between coded apertures and pinholes for reactor-imaging situations in which large constant backgrounds are likely to be present. Calculations by Chu²⁻¹⁸ have indicated that a significant noise advantage may exist for coded apertures in such cases, even for imaging of broad objects.

2.3.2.2.2 Coded-Aperture and Image-Reconstruction Studies -- In choosing an aperture, the relative shapes of aperture and object, and the ease of reconstructing the image must be considered in addition to statistical noise.

The shape question and the image-reconstruction process can both be studied and optimized with pure optical experiments, independent of the particular radiation type being imaged. Therefore, optical experiments have been performed with photographic mockups of various coded apertures and photographic objects similar to fuel-pin arrays.

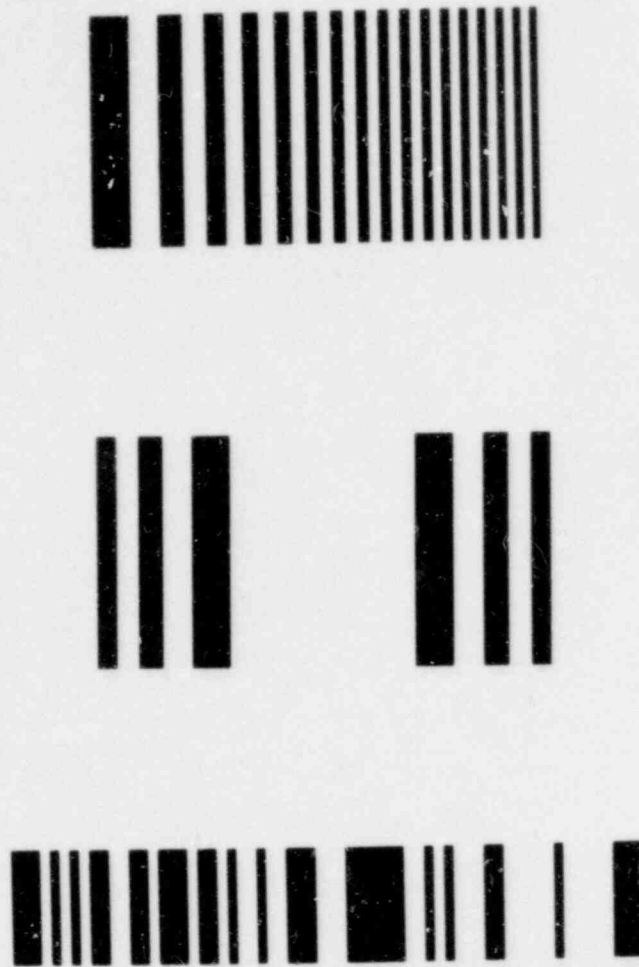


Figure 2.3-2 Candidate-Coded Apertures

Figure 2.3-3 shows a typical arrangement used to record the shadowgram produced by an arbitrary object and an arbitrary coded aperture. The object and apertures were drawn very accurately on an expanded scale using a Gerber plotter, then photoreduced onto Kodak Minicard II film to fit the 35-mm frame size of the camera used to record the shadowgram. The shadowgram was then back-illuminated and further photoreduced, yielding a pseudohologram of the same size as would have been obtained if actual LMFBR fuel pins and actual coded apertures had been used. Images were reconstructed from the pseudohologram in the usual fashion.

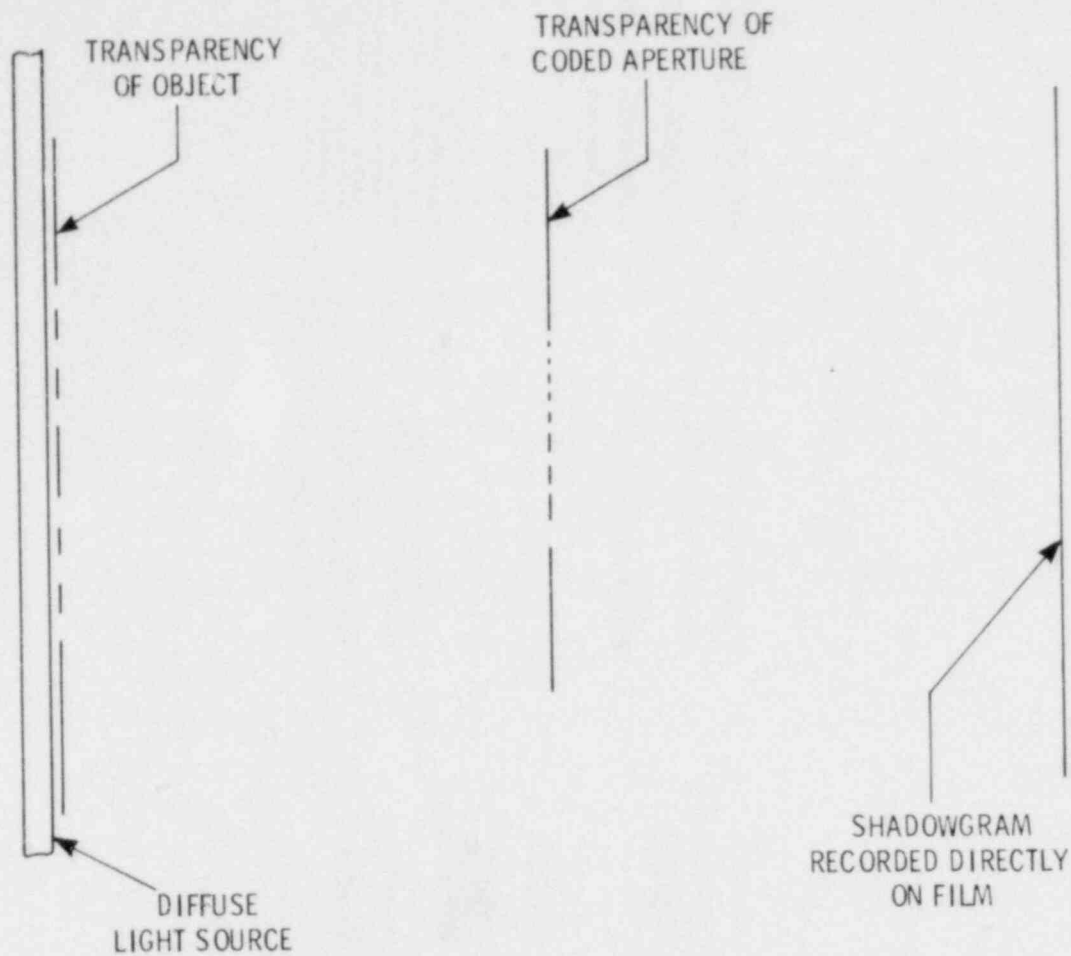


Figure 2.3-3 Typical Arrangement Used to Record the Shadowgram Produced by an Arbitrary Object and an Arbitrary Coded Aperture.

Images of "fuel-pin" arrays ranging from one to seven "fuel pins" in width have been made, using three off-axis Fresnel-coded apertures of slightly different resolutions. The widths of the reconstructed images agree with theory to about 10%, and gaps between the "fuel pins" are resolved for the two coded apertures with higher resolution. The background in the reconstructed image is typically much more uniform than that observed for on-axis Fresnel-coded apertures (presumably because an iris diaphragm is used to block the dc light and the out-of-focus "+1" image). Although adjustment of the iris position is critical, its position need not be changed in going from an object one "fuel pin" wide to an object seven "fuel pins" wide, in agreement with theory.

The reconstruction procedure was also improved during these experiments by use of a lens with very low aberrations to yield the smallest possible dc spot, and by routine bleaching of the pseudoholograms to increase the brightness of the image by about a factor of 50.

Analog reconstruction is the fastest and simplest reconstruction method available for survey work of this kind. However, it is clear from these purely optical experiments that the image quality is limited primarily by poor control of parameters during analog reconstruction. Large variations in image brightness and clarity occur; it is not known whether these variations are caused by exposure variations, chemical variations during development and bleaching, film quality variation, or poor focus during photoreduction. Careful optimization of exposure has dramatically improved image quality in earlier work with point sources; in future work greater attention will be paid to exposure optimization during formation of the shadowgram and the pseudohologram. Methods of predicting the optimum exposure will also be investigated.

2.3.2.2.3 Fast-Neutron Imaging -- A previous report described the spurious background that appeared on Lexan used in fast-neutron detection. During this reporting period, the cause of this background was discovered to be a light-induced chemical modification of the glue on the protective backing paper applied by the manufacturer. This background has been greatly reduced by simply keeping the Lexan sheets in a light-tight covering until the backing paper is removed and the Lexan is prepared for exposure to fission fragments. Because of the emphasis on the PARKA experiments, no further work with the improved Lexan exposure technique was performed during this period.

In developing a transient fast-neutron detector, scoping experiments on light-emission intensity from a neutron-sensitive scintillator (NE-102) were performed at the ^{252}Cf spontaneous-fission source. These experiments showed that an image intensifier will be needed for further experimentation, even though very weak light emission could be observed

with ordinary photographic film placed in contact with the scintillator. Orders have been placed for an image-intensifier system, and an interim image intensifier has been located for preliminary work.

References for Section 2

- 2-1 Advanced Reactor Safety Research Quarterly Report, October-December 1977, SAND78-0611, NUREG/CR-0323, (Albuquerque, NM: Sandia Laboratories, 1978).
- 2-2 Advanced Reactor Safety Research Quarterly Report, April-June 1978, SAND78-2001, NUREG/CR-0469, (Albuquerque, NM: Sandia Laboratories, 1979).
- 2-3 Advanced Reactor Safety Research Quarterly Report, July-September 1978, SAND78-2002, NUREG/CR-0470, (Albuquerque, NM: Sandia Laboratories, 1979).
- 2-4 J.G. Collier, Convective Boiling and Condensation, (New York, NY: McGraw-Hill, 1972).
- 2-5 G.B. Wallis, One-Dimensional Two-Phase Flow, (New York, NY: McGraw-Hill, 1968).
- 2-6 W. Nusselt, VDI Zeitschrift, 60, 541, 1916.
- 2-7 W.W. Boley, "Two-Dimensional Melting in a Channel," Ph.D. Thesis, University of Connecticut, 1965.
- 2-8 G.C. Gardner and J. Kubie, "Flow of Two Liquids in Sloping Tubes: An Analogue of High Pressure Steam and Water," Int. Multiphase Flow, 2, 435-541, 1976.
- 2-9 J. Kubie and G.C. Gardner, "Flow of Two Liquids in a Helix: An Analogue of High-Pressure Helical Boilers," Int. Multiphase Flow, 2, 353-366, 1977.
- 2-10 D. Hasson et al, "Annular Flow of Two Immiscible Liquid I and II," Canadian Jnl of Chem. Eng., 48, 514-526, 1970.
- 2-11 D. Freund and M. Schwarz, "CABRI Startup Experiments: Thermal Energy Measurements During TOP," CABRI Note 137/77.
- 2-12 "Sensitivity Analysis Applied to the Calculation of Detector-Response Kernels," Proceedings of the Theory and Application of Sensitivity and Uncertainty Analysis, Oak Ridge, TN, August 22-24, 1978.

- 2-13 P.J. McDaniel et al, "Fuel Motion Unfolding Based on Point Detector Responses," Proceedings of the Theory and Application of Sensitivity and Uncertainty Analysis, Oak Ridge, TN, August 22-24, 1978.
- 2-14 J.L. Portugal and M.F. Young, "Predictive Calculation for CABRI A2 Test," CABRI Note US 1/79, January 29, 1979.
- 2-15 A.E. Evans, J.D. Orndoff, and W.L. Talber, STF Diagnostic Instrumentation Evaluation With PARKA, Report LA-UR-77-7212, Los Alamos Scientific Laboratory, 1977.
- 2-16 H.V. Wider, M.G. Stevenson, and D.A. McArthur, "Material Diagnostic Requirements for STF," Specialists Meeting on Fuel and Cladding Motion Diagnostics for Fast Reactor Safety Test Facilities, Los Alamos Scientific Laboratory, Los Alamos, NM, December 5-6, 1977.
- 2-17 J.G. Kelly and K.T. Stalker "Coded Aperture Imaging of Reactor-Illuminated LMFBR Fuel Pins," Trans Ameri Nucl Soc, 27, pp 521-3, November-December 1977.
- 2-18 K.W. Chu, Coded Aperture Imaging - A Comparison Between Fresnel Zone Apertures and Uniformly Redundant Array Apertures, Report SAND78-1625 (Albuquerque, NM: Sandia Laboratories, 1978).

3. CORE DEBRIS BEHAVIOR - INHERENT RETENTION

3.1 Molten-Core Containment (D.A. Powers, 4422; A.W. Mullendore, 5834)

3.1.1 Introduction

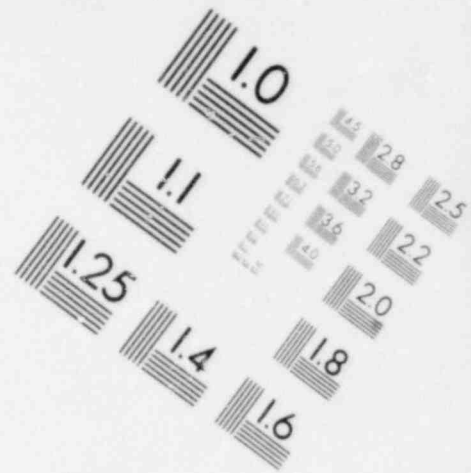
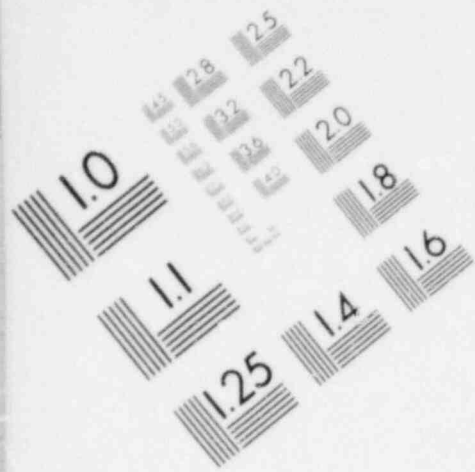
The aggressive behavior of molten materials has been the focus of the study of core materials interaction with concrete. However, a phase arises in any core-meltdown accident at which the internal-heat generation by fission products is insufficient to maintain the core materials in the molten state. The convenient assumption is often made that significant core-debris/concrete interactions cease when this state is reached. Such an assumption ignores the observed temperature ranges of concrete melting which are less than the solidification temperatures of core-melt constituents. The Molten-Core Containment program involves the performance of appropriate experiments and accurate experiment modeling. These activities will permit prediction of future hypothesized interaction situations.

3.1.2 Code-Comparison Tests

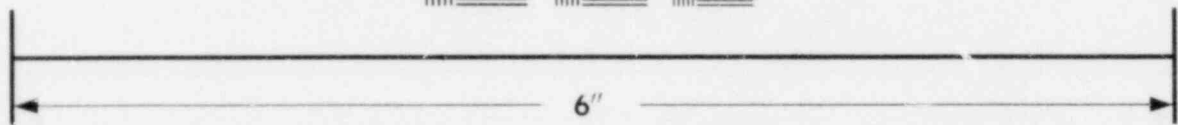
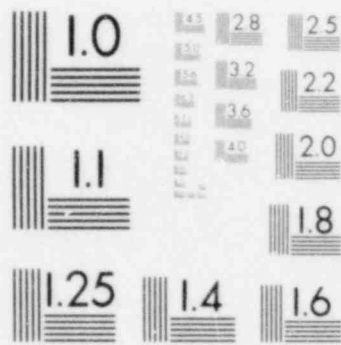
Sandia Laboratories and Project Nukleare Sicherheit of Kernforschungszentrum, Karlsruhe, have agreed to perform two standard tests. Data from these will be used to evaluate predictions made by computer models of the melt/concrete interactions. To date the prediction codes are:

- WECHSEL - developed at KfK by W. Murfin and M. Reimann
- CORCON - developed at Sandia by J.F. Muir
- CAVERN - developed at the Kraftwerke Union by K. Hassman et al

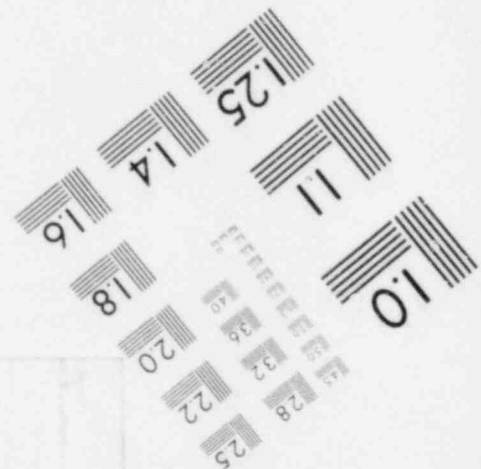
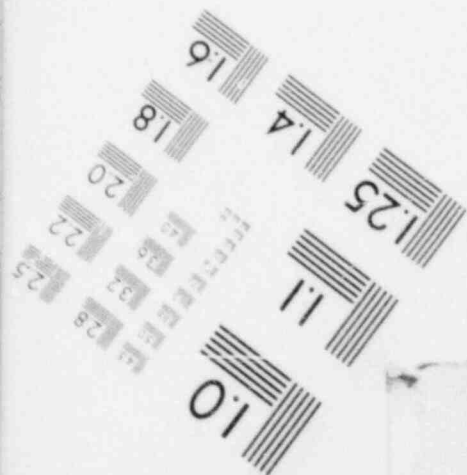
Developers of the GROWS code (ANL and UCLA) will be invited to participate in this activity.



**IMAGE EVALUATION
TEST TARGET (MT-3)**



MICROCOPY RESOLUTION TEST CHART



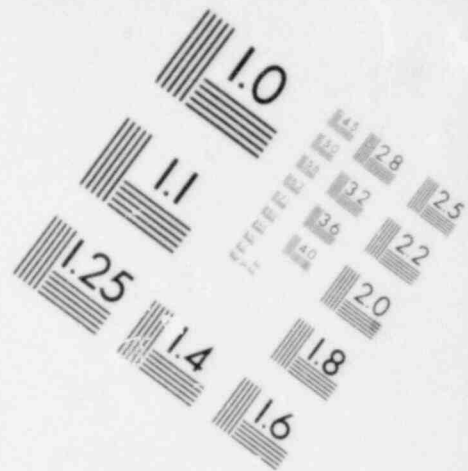
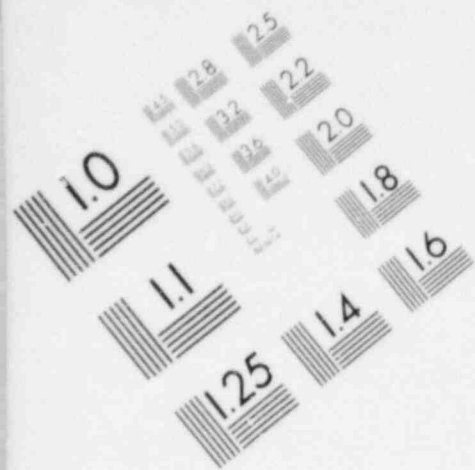
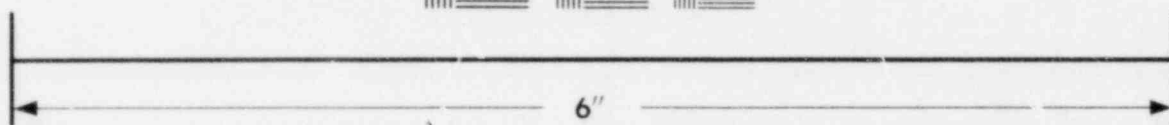
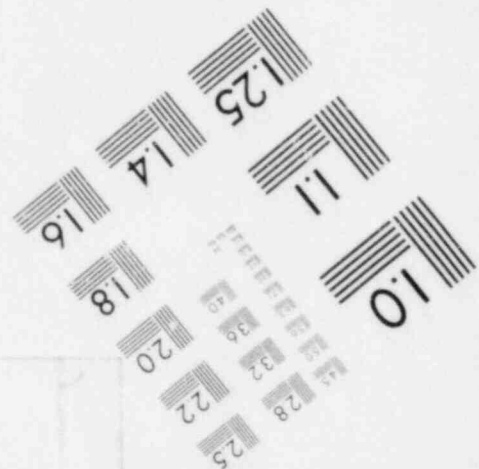
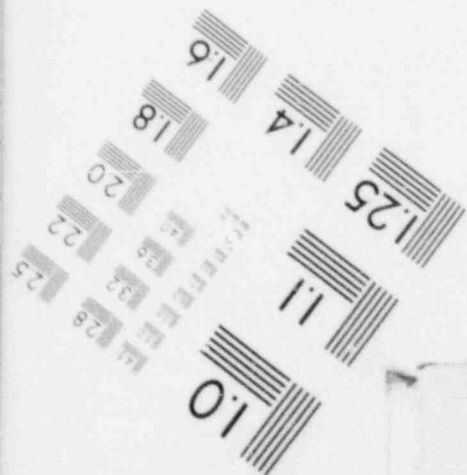


**IMAGE EVALUATION
TEST TARGET (MT-3)**



MICROCOPY RESOLUTION TEST CHART



21

The comparison between experimental data and computer predictions will be performed to compare the codes rather than to attempt to verify the computer models. The comparisons are expected to point to areas where improvements in the code should be made.

The two standard tests will be

- a. Sandia performing a test (COIL series) in which about 200 kg of molten stainless steel will be deposited on the so-called CRBR or generic southeastern US (GSEUS) limestone concrete.
- b. KfK performing a test (called "Super-thermit") in which about 1000 kg of thermitite will react with a siliceous concrete.

Only geometry data and other data necessary to make the model predictions will be supplied to the model developers. Some of these data for the COIL test are given in the following subsection. Actual experimental results will be made available only after the model predictions have been provided to the experimental groups.

Data that will be used in the comparison of the codes are:

- a. Posttest profile of the crucible cavity.
- b. Velocity of melt penetration.
- c. Temperature distributions (both spatial and temporal) in the concrete.
- d. Posttest weight of the metallic phase of the melt.
- e. The time at which solidification of the melt begins.

The last item on this list is fairly subjective data to collect. However, the models have shown this to be a very sensitive quantity to predict. Differences of a factor of 10 can arise in this prediction. Experimenters will have to keep detailed records on this process. The modelers will then have to select the data they want to use.

3.1.3 Specifications for Standard Test Problem - COIL Series

All basic procedures for the standard-test problem will be similar to those described in Reference 3-1. The discussion presented below repeats many of the points expressed in the reference and expands upon those where experimental procedure has improved since that document was released.

3.1.3.1 Test Arrangement

- a. Melt. Type 304 stainless steel weighing about 200 kg. Melt will be teemed at a temperature of 1973 K.
- b. Crucible. Cylindrical block with a coaxial cylindrical cavity identical to that described in Reference 3-1.
- c. Top Hat. A top hat will be lowered over the crucible once the melt is in place so that gases and aerosols produced in the test can be measured.

3.1.3.2 COIL Test Instrumentation

3.1.3.2.1 Test Procedure

- a. Time zero will be indicated by thermocouples within the cavity that fail on impact of first portion of melt.
- b. Duration of the pour will be indicated by motion-picture and television coverage of test.
- c. Top hat closure will be indicated by motion-picture coverage and by gas-flow meters.

3.1.3.2.2 Diagnostics

- a. Response of concrete
 - (1) Embedded thermocouples in concrete will provide temperature profiles and erosion rates.
 - (2) Fracturing of the concrete will be indicated by displacement gages mounted horizontally

on the exterior wall, 25 cm and 43 cm below the top of the crucible.

(3) Moisture migration in concrete will be monitored by electrical conductivity and pressure-transducer probes located on centerline of crucible. Locations of these sensors will be 2.5, 5.0, and 10 cm below the original bottom of the crucible cavity.

(4) Concrete:

Type: Clinch River Limestone Concrete

Composition (weight %)

Fe ₂ O ₃	1.2
Cr ₂ O ₃	0.004
MnO	0.01
TiO ₂	0.12
K ₂ O	0.68
Na ₂ O	0.078
CaO	45.4
SiO ₂	3.6
Al ₂ O ₃	1.6
CO ₂	35.7
SO ₂	Not detected
Evaporable H ₂ O	2.3
Chemical H ₂ O	1.8
MgO	5.67

Melting Range: 1703 to 1873 K

Aggregate Size: Per ACI specifications; maximum size is 2 cm. Fine aggregate made of crushed limestone.

b. Effluent

(1) Upward heat flux will be indicated by two gages: one mounted parallel to the surface of the melt; the other located perpendicular

to the surface of the melt. The active portion of the gage is about 50 cm above the surface of molten pool. The two gages should allow separation of upward heat transfer into terms of convective-mass transfer and radiation.

- (2) Gas-phase temperature will be monitored by shielded thermocouples at the heat-flux gage and at the gas-sampling port.
- (3) Aerosol concentration will be monitored optically at the gas-sampling port with a laser system and an incandescent system. Both forward and right-angle scattering will be sensed.
- (4) Gas flow will be measured by a pitot tube, a pressure drop, and a turbine flowmeter.
- (5) Gas composition will be monitored by grab samples. Real-time, continuous composition data for H_2O , CO , CH_4 , and CO_2 will also be provided.
- (6) Aerosol will be collected with initial cascade impactors.

c. Melt Temperature

- (1) As is feasible, melt temperature will be taken by immersion thermocouples. To do this, the top hat will be raised.
- (2) When the top hat is raised, a pyrometer will be used to measure surface temperatures. This will also afford an opportunity to detect crust formation.

d. Power Input

- (1) Waterflow to the cooling coil will be measured.
- (2) The ΔT of water will be measured.

3.1.3.2.3 Posttest Measurements

- a. An x-ray of the crucible will be taken to determine the erosion profile.
- b. Chemical analysis of the slag and steel will be provided as a measure of melt oxidation.

3.1.4 Concrete compositions for the Computer Model CORCON

The computer program CORCON will be used to predict the nature of melt/concrete interactions during a hypothetical reactor accident involving fuel melting. The model will allow variable concrete compositions as input. However, default concrete compositions will be built into the model. The default compositions will make the model more useful for generic, as opposed to site-specific, investigations.

One especially important use of CORCON will be for sensitivity analyses; concrete composition will clearly be a variable in such analyses. Because the impact of concrete composition on the nature of melt/concrete interactions should be well-understood, use of a single default concrete composition would be unwise.

Criteria for selecting default concrete compositions include:

- a. Concretes should be representative of those found in a significant number of existing reactors or representative of concretes of particular interest to a substantial number of potential users of CORCON.
- b. The properties of the default concretes should vary over a substantial range.
- c. The selected concretes should have been subjected to experimental study of their interactions with high-temperature prototypic melts.

The Molten Core/Concrete Interactions Study and the Molten Core Technology program at Sandia have involved three types of concrete:

- Basaltic-aggregate concrete
- Limestone-aggregate - common-sand concrete

- Generic SE US concrete (the so-called CRBR concrete)

The first two of these concrete types are representative of concrete in a large number of light-water power reactors. The first type is also quite similar to concrete found in the Fast-Flux Test Facility. The third concrete type is of particular interest since this concrete would be used in the Clinch River Breeder Reactor should it be built.

Properties of concrete that are currently believed to have the most direct influence on melt/concrete interactions are:

- a. Melting temperature range of solid concrete decomposition products.
- b. Quantities of materials such as hydrates and carbonates in the concrete that may be thermally decomposed to yield volatile products.
- c. The ratio of hydrates to carbonates in the concrete.

Basaltic-aggregate and limestone-aggregate - common-sand concretes both begin to melt about 1373 K. The liquidus temperatures for these concretes are 1623 to 1673 K. Consequently, both of the first two types of concrete are completely molten at temperatures below the solidification temperature of metallic phases of a hypothetical core melt. The Generic SE US concrete begins to melt at about 1723 K and is not fully molten until temperatures in excess of 1873 K are reached. The melting-temperature range of this concrete includes the solidification temperature expected for metallic phases of a hypothetical core melt.

Decomposition reactions of concrete typically occur in three temperature ranges and may be broadly categorized as:

- The loss of evaporable water (343-523 K)
- The loss of chemically constituted water (623-823 K)
- The loss of carbon dioxide from calcite and dolomite in the concrete (853-1323 K)

Weight losses associated with each of these reactions for the three concrete types are listed in Table 3-1. These data show

- a. Weight losses from the concrete due to the thermal-decomposition reactions may be ordered as: basaltic-aggregate concrete < limestone-aggregate - common-sand concrete < SE US concrete.
- b. Weight losses from basaltic-aggregate concrete are almost entirely due to dehydration reactions.
- c. Weight losses due to dehydration are similar for all three concrete types.
- d. Weight losses from limestone-aggregate - common-sand concrete are due to both dehydration and decarboxylation reactions which yield nearly equal volumes of volatile decomposition products.
- e. Volatile decomposition products of generic SE US concrete are predominantly carbon dioxide.

Table 3-1
Weight Losses for Three Concrete Types

	<u>Evaporable Water Loss</u>	<u>Chemically Constituted Water</u>	<u>Carbon Dioxide</u>
Basaltic-Aggregate Concrete	3 w/o (0.038 L/g)	2 w/o (0.025 L/g)	1.5 w/o (0.008 L/g)
Limestone-Aggregate - Common-Sand Concrete	2.7 w/o (0.034 L/g)	2 w/o (0.025 L/g)	22 w/o (0.112 L/g)
Generic SE US Concrete	2.3 w/o (0.029 L/g)	2 w/o (0.025 L/g)	35.7 w/o (0.182 L/g)

Gas volumes in liters/gram concrete at standard temperature and pressure.

It is apparent that the three concrete types used in the Sandia experimental program satisfy the criteria of default concretes for CORCON. Compositions for these concretes may be expressed in a variety of ways.

The oxide basis for concrete compositions is shown in Table 3-2. Choices for the oxides of iron and manganese are quite arbitrary since these elements are polyvalent. At elevated temperatures, manganese and iron are best treated as mono-oxides. Water contents of the concretes have been differentiated into evaporable and chemically constituted water to be consistent with the needs of CORCON.

Table 3-2
Chemical Composition of Default Concretes

	<u>Basaltic- Aggregate Concrete</u>	<u>Limestone Aggregate- Common-Sand Concrete</u>	<u>Generic SE US Concrete*</u>
Fe ₂ O ₃	6.25	1.44	1.20
Cr ₂ O ₃	ND	0.014	0.004
MnO	ND	0.03	0.01
TiO ₂	1.05	0.18	0.12
K ₂ O	5.38	1.22	0.68
Na ₂ O	1.80	0.082	0.078
CaO	8.80	31.2	45.4
MgO	6.15	0.48	5.67
SiO ₂	54.73	35.7	3.6
Al ₂ O ₃	8.30	3.6	1.6
CO ₂	1.5	22.0	35.7
SO ₂	0.2	0.2	--
Evaporable H ₂ O	3.0	2.7	2.3
Chemical H ₂ O	2.0	2.0	1.8

*Sometimes called CRBR concrete or GSEUS concrete

Alternative descriptions of concrete in terms of the mix used to make the concretes are shown in Table 3-3. Such descriptions are not especially accurate. Water used to make the concrete bears no simple relationship to the two types of water present in cured concrete. The mix description together with the chemical descriptions of concrete in Table 3-2

and chemical description of the concrete constituents in Table 3-4 should assist in the formulation of chemical descriptions of concrete where chemical data are not available. Caution is definitely urged when this procedure must be used.

Table 3-3
Engineering Composition of Default Concrete

	<u>Limestone- Aggregate - Common-Sand Concrete (lb)</u>	<u>Basaltic- Aggregate Concrete (lb)</u>	<u>Generic SE US Concrete (lb)</u>
Coarse Aggregate	187	205	364
Fine Aggregate	93	---	260
Sand	205	230	---
Fly Ash	---	---	3.2
Cement	94	94	94
Water	42	45	53-59

Table 3-4
Chemical Compositions of Concrete Constituents

<u>Oxide</u>	<u>Type 1&2 Cement</u>	<u>Limestone Aggregate from Generic SE US Concrete</u>	<u>Basaltic Aggregate</u>	<u>Sand</u>	<u>Fly Ash</u>	<u>Limestone Aggregate from Limestone Sand Concrete</u>
Fe ₂ O ₃	4.11	0.38	7.78	2.15	11.7	0.33
Cr ₂ O ₃	0.011	0.012	0.063	0.042	0.022	ND
MnO	0.08	0.04	0.08	0.02	0.02	ND
TiO ₂	0.20	0.04	1.82	0.18	2.24	0.05
K ₂ O	0.54	0.36	7.20	2.70	3.50	0.30
Na ₂ O	0.27	0.16	1.85	1.74	0.34	0.15
CaO	63.5	47.2	6.54	1.52	1.30	45.56
MgO	1.53	0.60	9.70	0.34	1.14	0.80
SiO ₂	20.1	8.0	54.9	82.8	51.2	12.98
Al ₂ O ₃	4.2	1.2	9.51	7.24	24.5	1.25
CO ₂	ND	38.0	ND	ND	ND	40.0

ND = Not determined

Melting ranges for the default concretes are:

<u>Concrete</u>	<u>Solidus</u>	<u>Liquidus</u>
Basaltic	1353 K	1653 K
Limestone	1473 K	1673 K
Common Sand	--	--
CRBR Limestone	1723 K	1873 K

Heats of melting are not adequately known, but should be about 100 cal/g.

Thermal effects involved in the decomposition of concrete have been incompletely studied. Until more reliable data are available, the values in Table 3-5 are recommended.

Table 3-5

Thermal Effects Values for Concrete Decomposition

<u>Concrete</u>	<u>Heat of Decomposition or Phase Change (cal/g concrete)</u>			
	<u>Loss of Evaporable Water</u>	<u>Loss of Chemical Water</u>	<u>$\alpha \rightarrow \beta$ Phase Change in SiO</u>	<u>Decarboxylation</u>
Basaltic	18.3	28	1.3	13.6
Limestone	16.5	28	0.3	200
Generic	14.0	28		324
SE US	--	--	--	--

Heat capacity of concrete is a poorly defined quantity because of time and mass dependence of the decomposition reactions. Heat capacity may be defined for the solid decomposition products of concrete. This heat capacity has again not been well investigated. In the absence of quality experimental data, the equations below are recommended:

a. Basaltic Concrete:

$$C_p = 0.2245 + 0.0001332 T - \frac{4698.7}{T^2}$$

b. Limestone-Aggregate - Common-Sand Concrete:

$$C_p = 0.1697 + 0.0001031 T - \frac{3276.5}{T^2}$$

c. Generic Southeastern United States Concrete:

$$C_p = 0.1085 + 0.0000497 T - \frac{1433.23}{T^2}$$

T = absolute temperature (K)

To correct for the volatile species, add the following factors:

a. For $0 < T < 373$ K

$$C_p (1) = \frac{W_e}{100} (0.6222 + 0.000428 T)$$

b. For $0 < T < 658$ K

$$C_p (2) = \frac{W_{CH}}{100} (0.5244 + 0.401 \times 10^{-3} T)$$

c. For $0 < T < 873$ K

$$C_p = \frac{W_{CO}}{100} (0.175 + 0.00012 T - 0.189 \times 10^{-6} T^2)$$

where

W_e = weight percent evaporable water

W_{CH} = weight percent chemical water

W_{CO} = weight percent carbon dioxide

A formula for the "heat capacity" of concrete that takes into account both mass-loss and heats of decomposition may be written as:

$$\begin{aligned}
C_p &= (\text{cal/K} - \text{g concrete}) \\
&= C_p(\text{res}) + C_p(1) \text{ g (393)} + C_p(2) \text{ g (693)} + C_p(3) \text{ g (993)} \\
&\quad + W(1) f(333, 453) + W(2) f(663, 713) + W(3) f(843, 863) \\
&\quad + W(4) f(999, 1123)
\end{aligned}$$

where

$$g(T_0) = \text{erfc} \left[5(T - T_0)/T_0 \right]$$

$$f(T_r, T_u) = \frac{1}{\sqrt{2\pi}\sigma} \exp \left(-1/2 \left(\frac{T - \mu}{\sigma} \right)^2 \right)$$

$$\mu = \frac{(T_r + T_u)}{2}$$

$$\sigma = \frac{1}{2} (T_r - T_u)$$

T = absolute temperature (K)

$C_p(i)$ = residue heat capacity and correction terms defined above

$W(j)$ = decomposition energies from Table 3-5

(j=1) heat of evaporable water loss

(j=2) heat of chemical water loss

(j=3) heat of $\text{SiO}_2 \alpha \rightarrow \beta$ phase change

(j=4) heat of decarboxylation

Plots of this heat-capacity function for the various default concretes are shown in Figures 3.1-1 and 3.1-2. The shapes of the curves in the vicinities of decomposition reactions are designed to account, in an approximate way, for the kinetic nature of the decomposition reaction. The adjustable parameters in the $g(T_0)$ and $f(T_r, T_u)$ functions may be varied to give even better agreement with the kinetic behavior of the decomposition reactions. A more sophisticated treatment of this aspect of heat capacity is definitely possible. Because of these heat effects, the above formula is applicable only when concrete is first heated. After concrete has been completely decomposed, the residual heat capacity ($C_p(\text{res})$) functions describe heat capacity, again in units of cal/K-g virgin concrete.

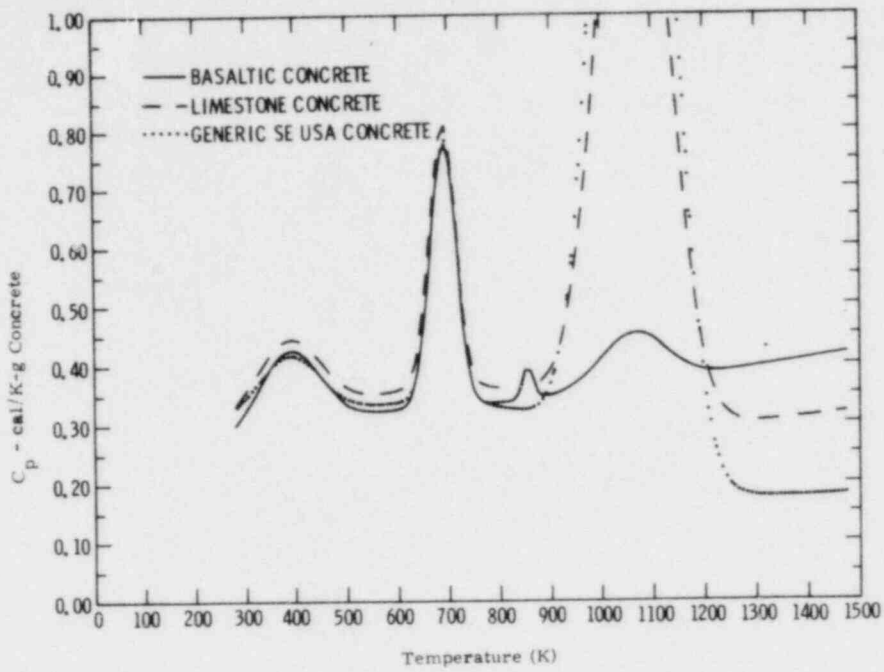


Figure 3.1-1 Heat Capacity vs Temperature With Heat Effects

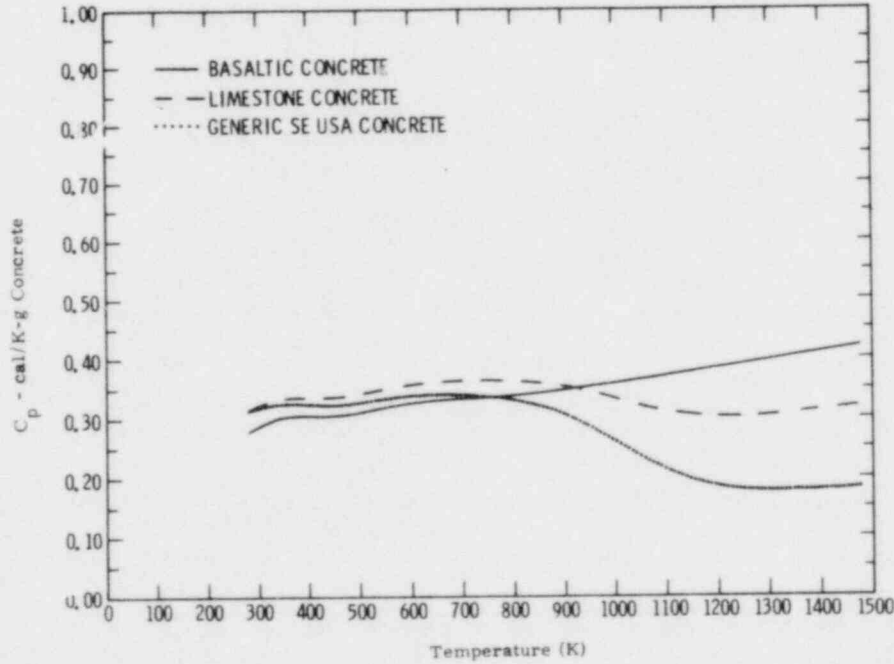


Figure 3.1-2 Heat Capacity vs Temperature Without Heat Effects but Including Mass-Loss Effects.

3.1.5 Comparison of Heat-Capacity Model to Other Models and Experimental Data

Harmathy³⁻² has described a model for estimating the thermophysical properties on concrete, including its heat capacity. He used his model to predict heat capacity of a silaceous concrete he labeled "#2". A comparison of Harmathy's estimates and those made with the model described here is shown in Figure 3.1-3.

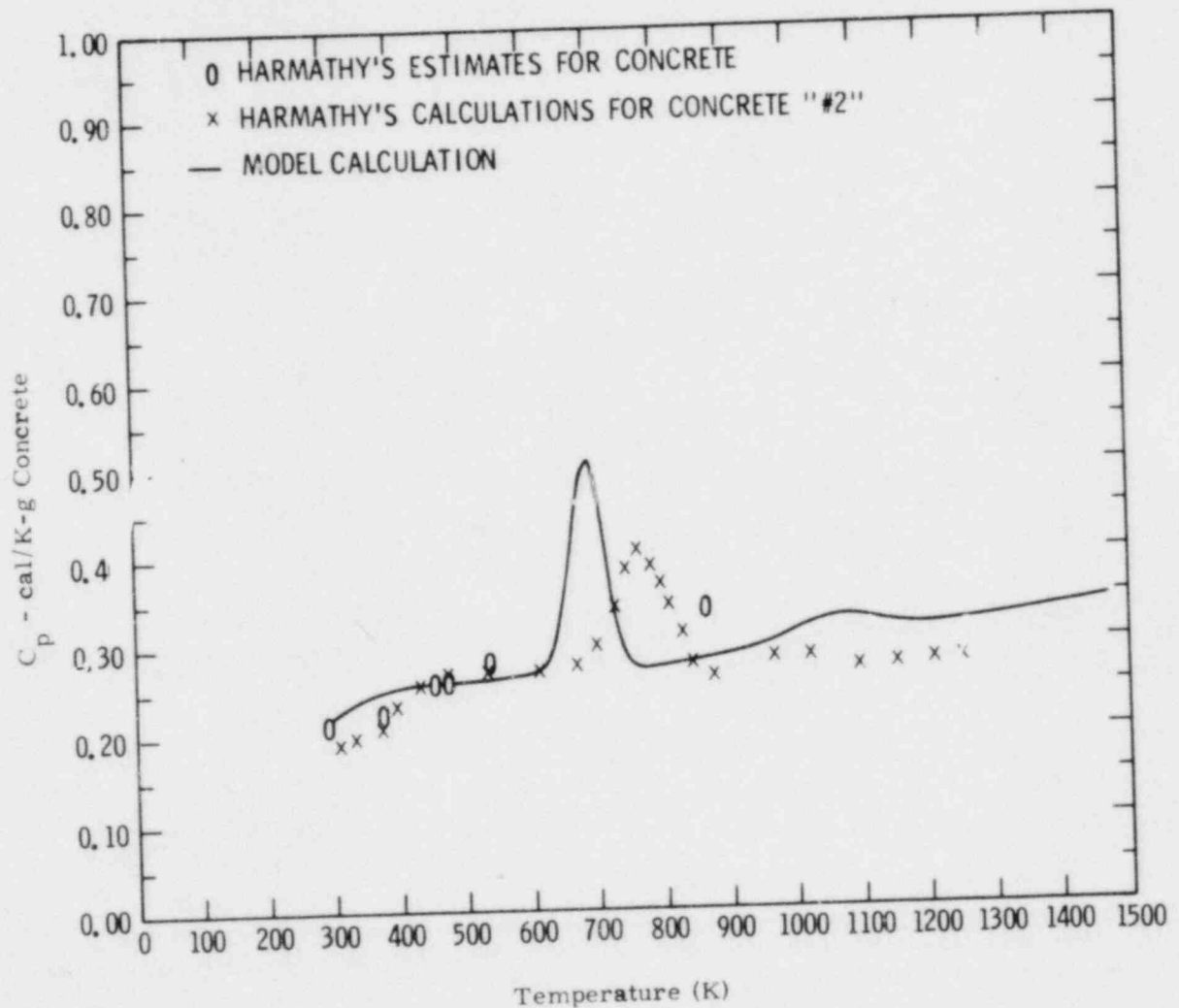


Figure 3.1-3 Comparison of Harmathy's Estimates and Results of Modeling.

Harmathy's characterization of concrete #2 was not suited for the requirements of the model described here. The necessary changes required some reinterpretation of the data. The most important changes were:

- a. Cement binder was assumed to be a fully cured mixture of $(\text{CaO})_{1.62}$, SiO_2 , $1.5 \text{ H}_2\text{O}$, and $\text{Ca}(\text{OH})_2$.
- b. Weight-loss in the thermogram of Harmathy's cement binder #2 was assumed due to loss of CO_2 at temperatures above 873 K.

The composition of cement #2 was then found to be:

Na_2O	4.00 w%
CaO	19.28 w%
Al_2O_3	25.18 w%
SiO_2	48.92 w%
free H_2O	0.79 w%
bound H_2O	1.06 w%
CO_2	0.46 w%

All of the silica in the concrete was assumed to be bound so that no $\alpha \rightarrow \beta$ phase-transition occurred.

The residual heat capacity of the material was determined to be:

$$C_p(\text{res}) = 0.2003 + 0.9772 \times 10^{-4}T - \frac{4364}{T^2}$$

The general trends of Harmathy's calculation and the calculation produced from the present model are quite similar. Up to 600 K, agreement between the two models is good. Any discrepancies are because the present model allows easier removal (lower temperature removal) of free water than does the Harmathy model. Consequently, Harmathy predicts a more abrupt change in heat capacity in the vicinity of 370 K.

The present model predicts that the bound-water loss influences heat capacity at lower temperatures than predicted by Harmathy's model.

This is a fine example of the difficulties in understanding the heat capacity of chemically reacting substances. Because these reactions are kinetic in nature, the heat effects they produce arise at temperatures that are functions of the heating rate. In the model presented here the heat-effect terms are characterized by a parameter that determines the location and a parameter that determines the magnitude and breadth of the heat effect. Some arbitrary values of these parameters have been used in this mode. Simply adjusting these parameters would bring the present model into good agreement with the Harmathy model in the region of bound-water loss. A similar rationale could be used to adjust the rise in heat capacity due to decarboxylation at about 1050 K.

The physical justification for varying the parameters for the endothermic reactions is a question. These parameters relate to the kinetic-rate expressions for the concrete reactions developed by Powers.

Elsewhere, Harmathy has presented heat-capacity data for several varieties of concrete.³⁻³ Again, his characterizations of these concretes were not suitable for the needs of the present model. To compare the experimental data to the calculated estimates, it was assumed that:

- a. The autoclaved siliceous concrete "SL" was similar to Harmathy's concrete "#2".
- b. The siliceous concrete "S" was similar to the balsaltic concrete described above.
- c. The calcareous concrete "C" was similar to the limestone - common-sand concrete described above.

Comparison between the experimental and calculated heat capacity are made in Figures 3.1-3, 3.1-4, and 3.1-5.

Peeh has also presented heat-capacity data for a siliceous concrete. These data, which agree well with Harmathy's data for concrete "S", are compared with calculated results in Figure 3.1-4.

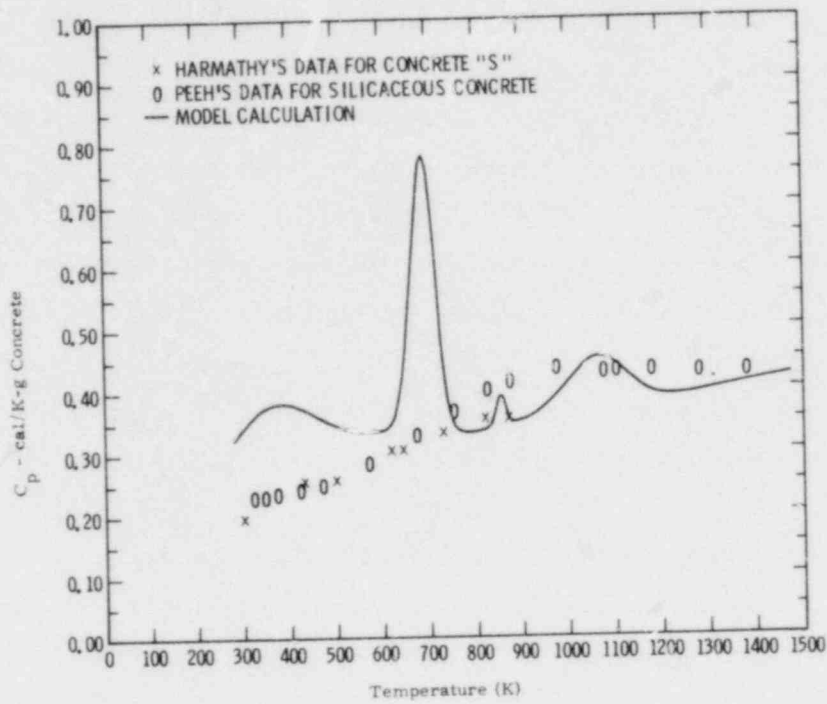


Figure 3.1-4 Comparison of Model Calculations With Harmathy's and Peeh's Data.

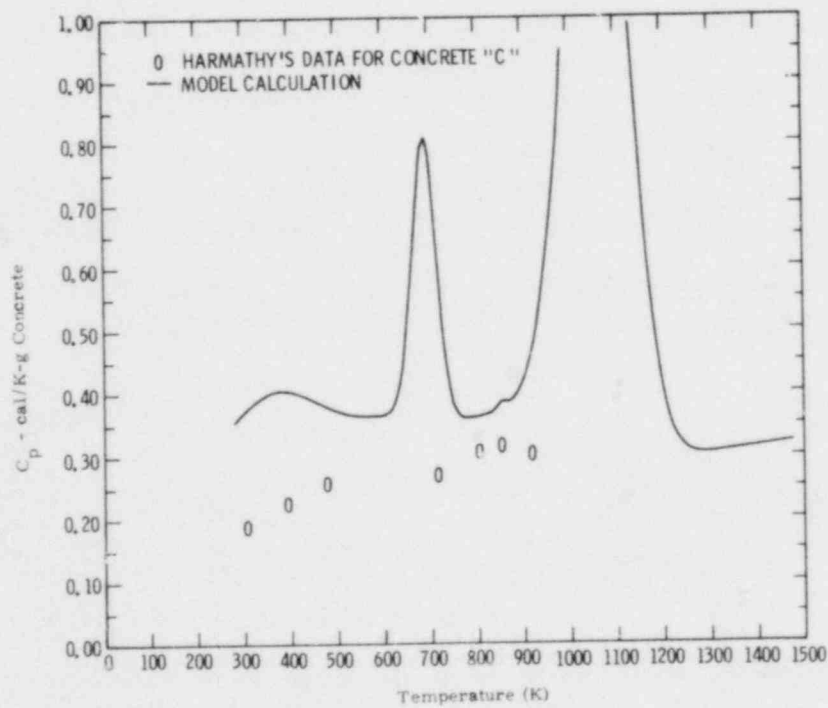


Figure 3.1-5 Comparison of Model Calculations With Harmathy's Data

There is very strong disagreement between the model predictions and the experimental data for Harmathy's concrete "C". No explanations for this disagreement can be offered at this time. Characterization of concrete "C" was not suitable for this model and data for the limestone - common-sand default concrete were used. This might be a source of the discrepancies.

3.1.6 Steel Oxidation During Melt/Concrete Interactions

Table 3-6 lists the chemical composition of various steel samples taken during the COIL tests.

Table 3-6
COIL Test-Steel Compositions

<u>Sample Description</u>	<u>*Composition (w%)</u>			
	<u>Cr</u>	<u>Fe</u>	<u>Ni</u>	<u>Mn</u>
Stainless steel prior to melt formation.	18.4	69.6	8.72	1.85
Stainless-steel melt just prior to teem into concrete crucible.	18.8	68.0	8.61	1.76
Steel after transient test with generic SE US concrete.	17.5	66.0	8.37	1.94
Stainless steel after a test with generic SE US concrete sustained for 9.5 min.	15.3	70.8	9.26	6.35

*Compositions do not necessarily total 100% because of included nonmetallic material in the samples.

The percentage data shown in Table 3-6 are not suitable for determining the absolute extent of melt oxidation because the total metal weight at the conclusion of the test could not be measured. The data are

suitable for determining the relative extents to which constituents of the melt are oxidized. In doing this, analytic errors and sampling errors are important since the relative determinations involved small differences in large numbers.

If nickel oxidation is assumed to have a relative value of 1, then the extent of chromium oxidation is 1.35 and iron oxidation is 2.08 in the transient tests. Similar relative values for oxidation during a sustained test of molten stainless steel with generic SE US concrete are:

Ni 1.00
Mn 1.49
Fe 4.15
Cr 5.14

These results do not recognize the varying concentrations of constituents in the melt. When the sustained tests are normalized for metal atom concentration, they become:

Ni 1.00
Mn 6.57
Fe 0.50
Cr 2.16

These results are still not in good agreement with thermodynamic estimates and obviously more sophisticated analysis and more extensive chemical-composition data are needed.

3.1.7 Posttest Analysis of the Crucible Used in Test BURN 0

The experimental details and objectives of Test BURN 0 have been described elsewhere.³⁻⁴ One objective of this test was to observe the interaction of molten corium with the refractory materials of calcia-stabilized zirconia, hafnium carbide, tungsten carbide, and yttrium oxide. Posttest inspection of the crucible described here was intended to confirm the observations made from x-rays of the crucible described in Reference 3-4. Dissection of the crucible showed that the solidified melt consisted

of an upper layer of slag and metal droplets and a lower layer of stainless steel. Figure 3.1-6 is a photograph of the top surface of the steel layer. Notice that eruptions occur in this layer at positions above the refractory test specimens in the concrete.

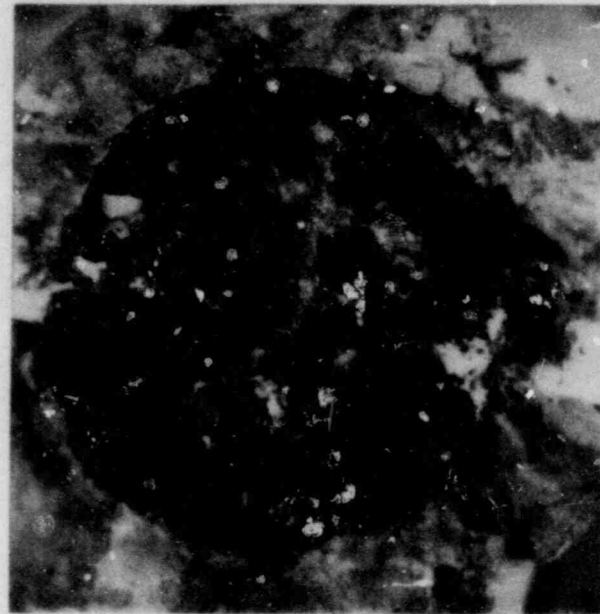


Figure 3.1-6 Top Surface of Solidified Steel in Test BURN No. 0

The steel had flowed into crevices created by the specimens in the concrete. The steel was removed with some difficulty. The surface below the steel is shown in Figure 3.1-7. Refractory specimens are marked in this figure.

The impact of the melt on the specimens may be summarized as:

- a. W_2B - badly eroded and powderized
- b. HfC - powderized on surface
- c. Y_2O_3 - fractured internally; powderized on surface
- d. ZrO_2 (CaO stabilized) fractured internally; powderized on surface.

POOR ORIGINAL



Figure 3.1-7 Concrete/Steel Interface in Test BURN No. 0

Figure 3.1-8 is a photograph of the under surface of the steel.

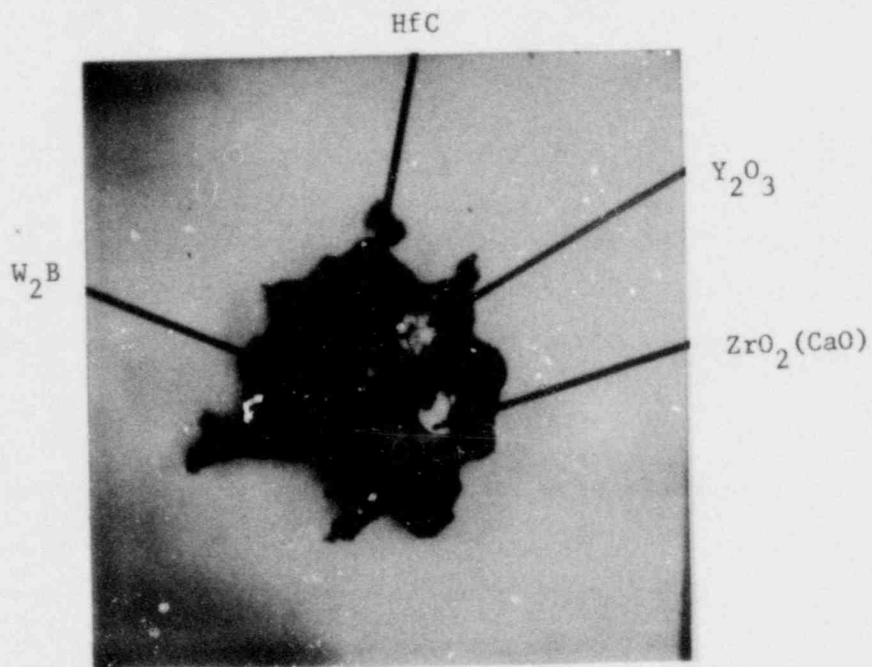


Figure 3.1-8 Under-Surface of Steel Showing Included Refractory Material

POOR ORIGINAL

None of the materials considered in BURN 0 appeared suitable for prolonged exposure to the melt. Yttrium oxide was the best behaved of the samples, but it too suffered from thermal shock.

Posttest dissection of the crucible showed that at their tips, the tungsten electrodes used to sustain the melt had alloyed with steel (see Figure 3.1-9). Some melting of this alloy occurred but the electrodes were not shorted together by metal.



Figure 3.1-9 Alloyed Electrodes Used in Test BURN No. 0

3.1.8 Further Analysis of Data From Test BURN 1

Details of Test BURN 1 have been described elsewhere.³⁻⁵ One of the most important pieces of data that came from this test was the motion picture record of the x-ray image of the melt during the test. Frame-by-frame analysis of this record has been undertaken to determine the time of contact between the melt and the concrete and the swelling of the melt produced by gas evolved during melt/concrete interaction.

Sketches of the mostly-metallic pool of Test BURN 1 were made at 1-s intervals. The depth of the pool was measured at 30 or more locations on each of these sketches. The mean and maximum pool depths were computed from the measurements. The time dependencies of the mean and maximum pool depths are shown in Figure 3.1-10 and 3.1-11, respectively. Pool depths are normalized by dividing by the calculated depth of a 100% dense-steel melt weighting 832 g.

As these figures show, the pool is substantially swelled by gases. For the small pool used in Test BURN 1, the swelling can be as much as 250% of the gas-free pool depth.

The relationship between pool swelling and the rate of gas evolution is of interest. Gas-generation data from test BURN 1 are shown in Figure 3.1-11. The regression of mean-pool-level swell against the rate of gas generation is shown in Figure 3.1-12. At the highest generation rates, level swell appears to be roughly independent of gas-generation rate. At gas-generation rates below about 150 L/min, level swell is approximately a linear function of gas-generation rate. At very low gas-generation rates, data become very noisy; low gas-generation rates developed in Test BURN 1 when the melt was beginning to freeze. The viscous, two-phase melt present at this time was elevated and deformed as a body by single gas bubbles.

The quantitative aspects of the relationship between gas-generation rate and pool swelling observed in Test BURN 1 may not be applicable to a much thicker melt. This is especially true for the magnitude of pool swelling. The general shape of the relationship (that is, a region at high gas-generation rates during which swell is independent of gas-generation rate and a region where swell is strongly dependent on gas-generate rate) would be expected for any melt. Confirmation of this point will be considered in the XR test series.

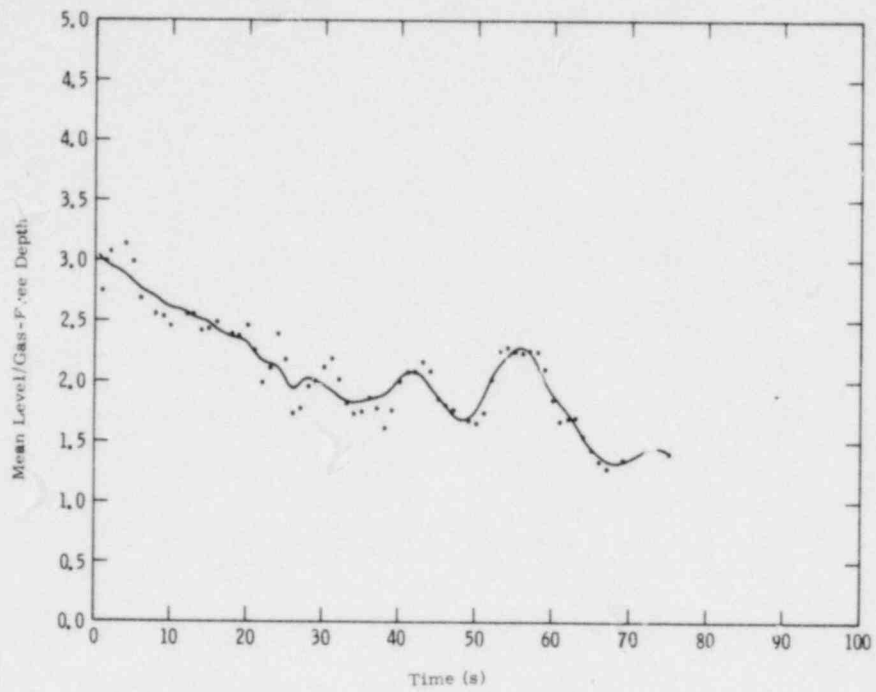


Figure 3.1-10 Level Swell in Test BURN No. 1, Mean Pool Depth

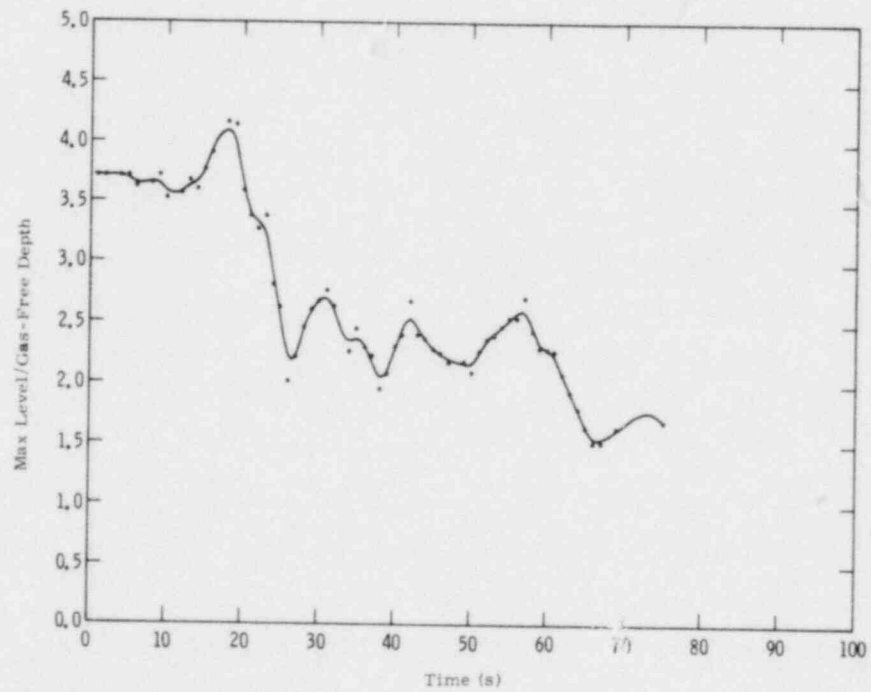


Figure 3.1-11 Level Swell in Test BURN No. 1, Maximum Pool Depth

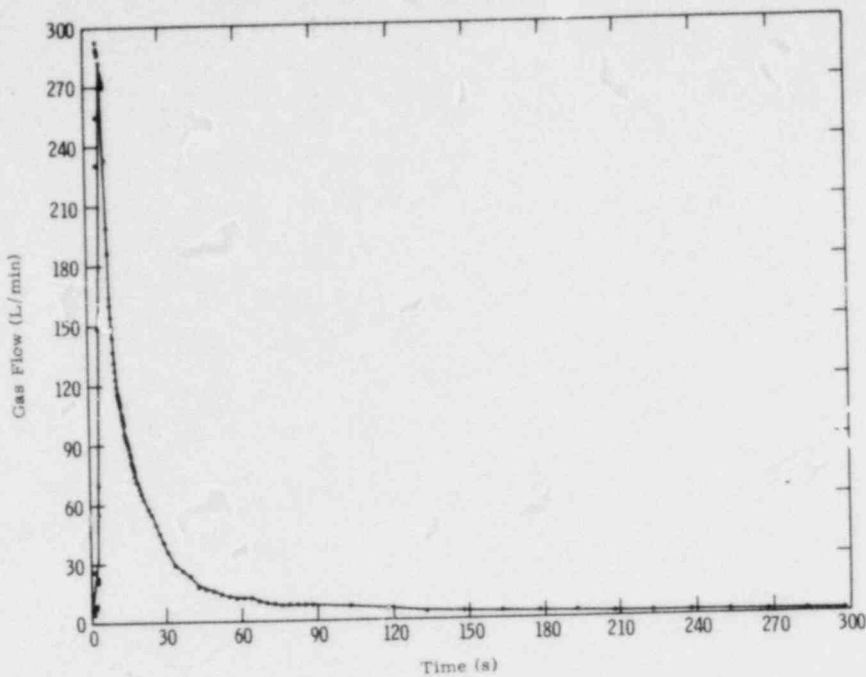


Figure 3.1-12 Gas Flow Data for Test BURN No. 1

For each frame of the x-ray image (about 0.04-s intervals) melt contact with the concrete was noted for the nine locations defined in Figure 3.1-13. Subjective decisions concerning contact were necessary especially for points near the centerline of the crucible cavity, since the melt is truly three-dimensional but the image is only two-dimensional. Resolution with the x-ray technique is limited to about ± 0.3 cm. Further, a light "halo" developed about the perimeter of the very x-ray-dense melt where it was adjacent to the much less dense concrete. Contact between melt and concrete could not be defined closer than ± 0.3 cm. These limitations on the x-ray technique prevent positive determination if a gas-film separates the melt and concrete, and if that film is less than 0.3 cm thick.

Observations of melt contact were averaged over 1-s intervals; mean contact times and standard deviations of these means were calculated. These results are present in Table 3-7 and Figures 3.1-14 through 3.1-22. A piece-wise least squares, smoothing polynomial line has been drawn through the data in figures. These smoothing, polynomial lines are compared for 5 through 9 in Figure 3.1-23.

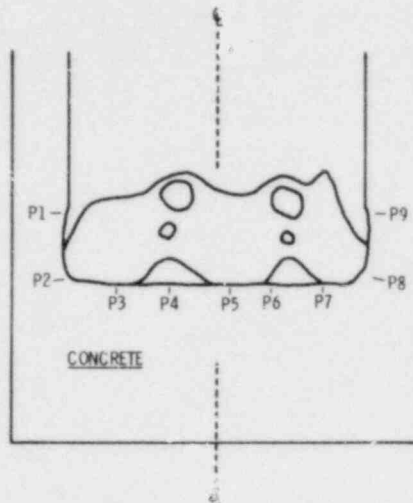


Figure 3.1-13 Schematic Diagram of Gas Evolution at a High-Temperature Melt/Concrete Interface.

Table 3-7

Percent of Time Melt in Contact With Concrete at Various Locations and During Various Time Intervals.

Location**	Time Interval (s)*							
	0-9	10-19	20-29	30-39	40-49	50-59	60-67	0-67
P1	31(6)	56(5)	46(4)	48(3)	51(5)	33(4)	4(7)	40(20)
P2	59(9)	87(6)	92(1)	93(1)	89(2)	88(1)	91(4)	86(16)
P3	66(10)	89(6)	97(1)	96(2)	84(3)	68(6)	42(9)	79(20)
P4	19(5)	29(13)	33(6)	31(3)	12(2)	13(2)	3(3)	21(18)
P5	59(5)	74(4)	89(4)	95(2)	94(3)	83(7)	66(4)	80(16)
P6	64(15)	48(7)	29(4)	30(2)	17(3)	9(3)	7(1)	30(23)
P7	40(3)	48(6)	79(14)	91(2)	79(5)	73(2)	62(1)	68(22)
P8	84(3)	92(2)	94(1)	97(1)	95(1)	91(4)	90(2)	92(9)
P9	25(5)	40(4)	44(4)	48(1)	46(3)	41(3)	68(16)	45(22)

* Mean % of time that melts contact concrete is outside the parentheses. The standard error of the mean is inside the parentheses.

** Locations depicted in Figure 3.1-13.

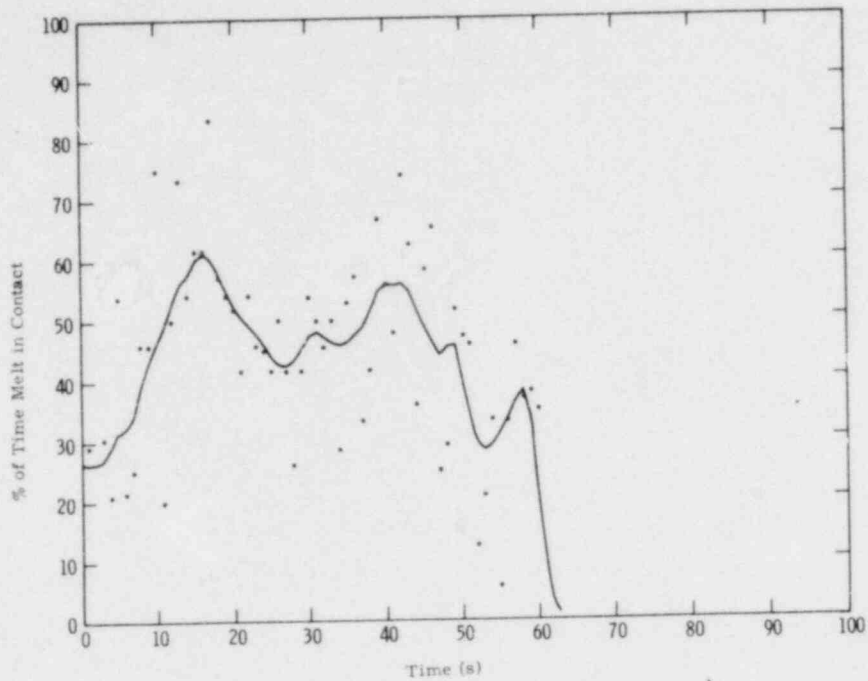


Figure 3.1-14 Contact Times-Test BURN 1, Position 1

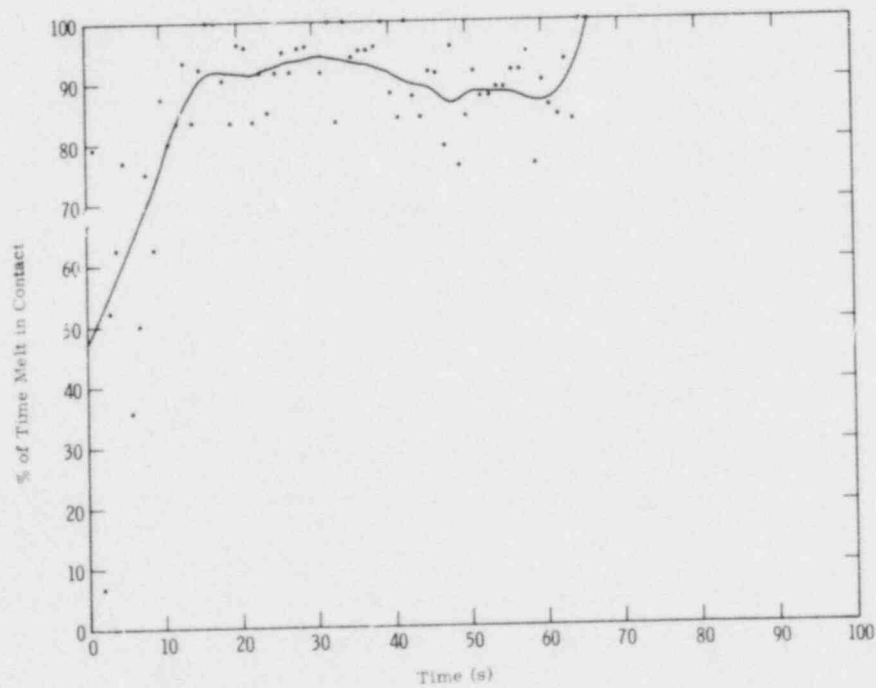


Figure 3.1-15 Contact Times-Test BURN 1, Position 2

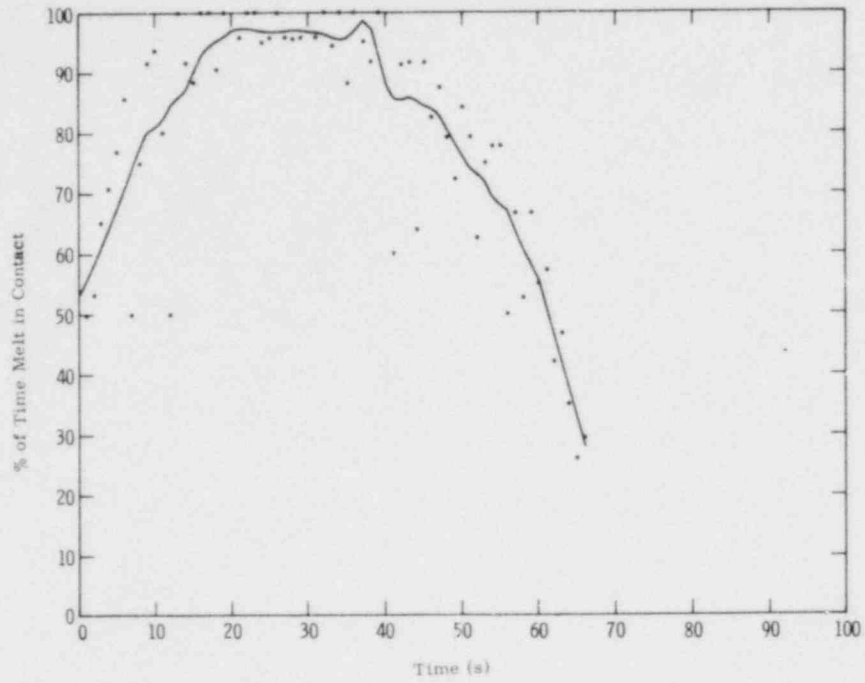


Figure 3.1-16 Contact Times-Test BURN 1, Position 3

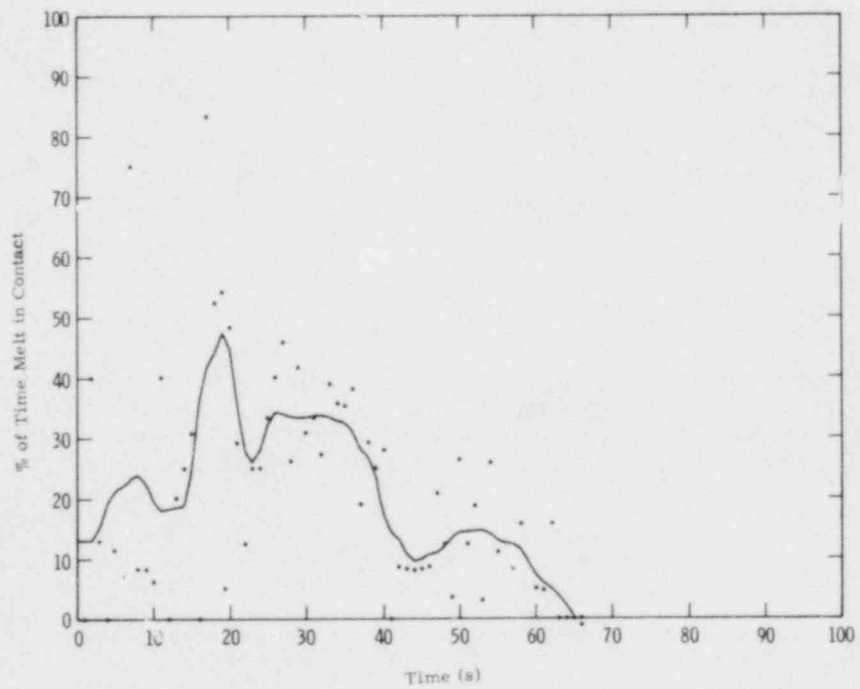


Figure 3.1-17 Contact Times-Test BURN 1, Position 4

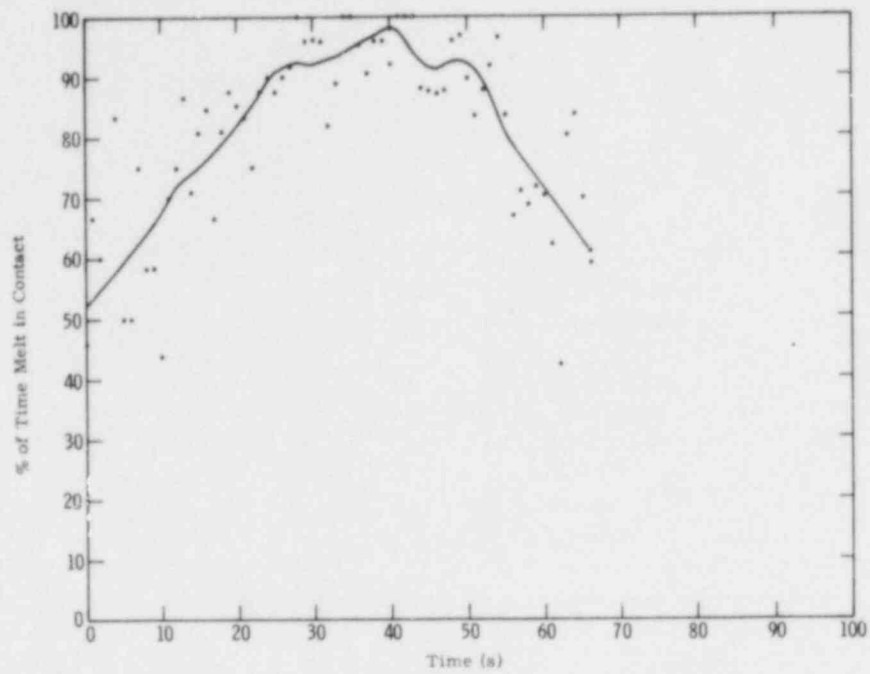


Figure 3.1-18 Contact Times-Test BURN 1, Position 5

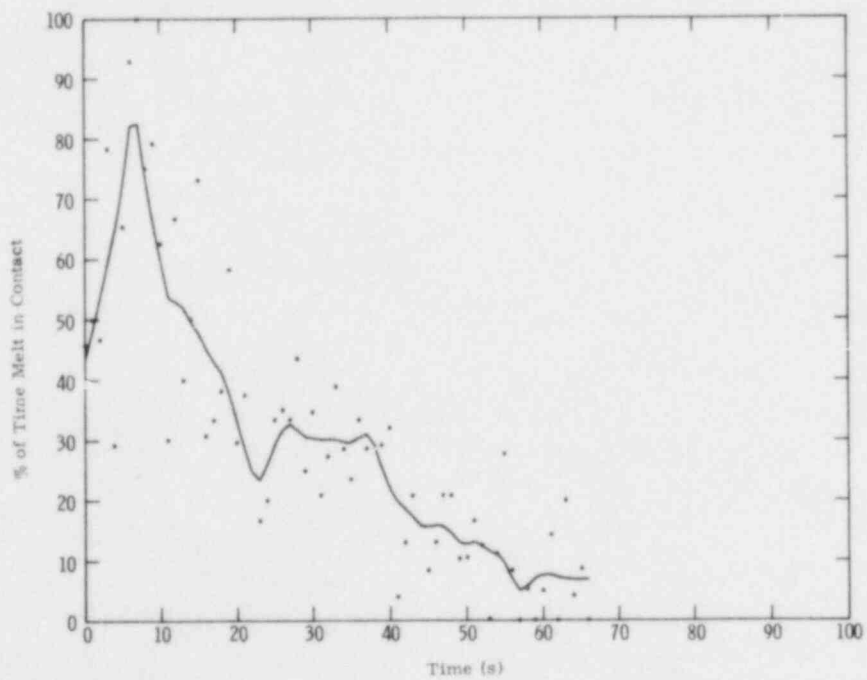


Figure 3.1-19 Contact Times-Test BURN 1, Position 6

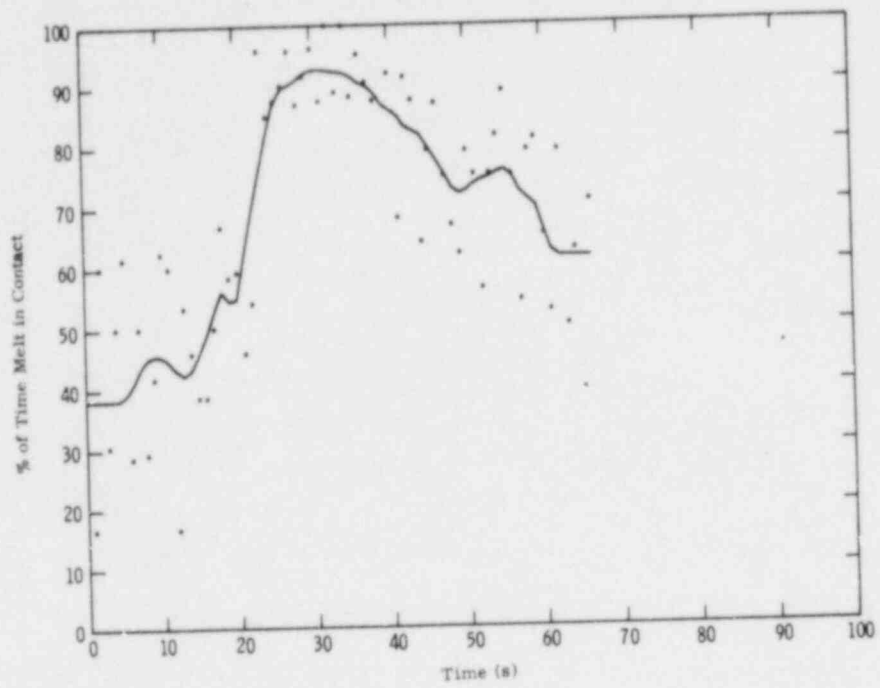


Figure 3.1-20 Contact Times-Test BURN 1, Position 7

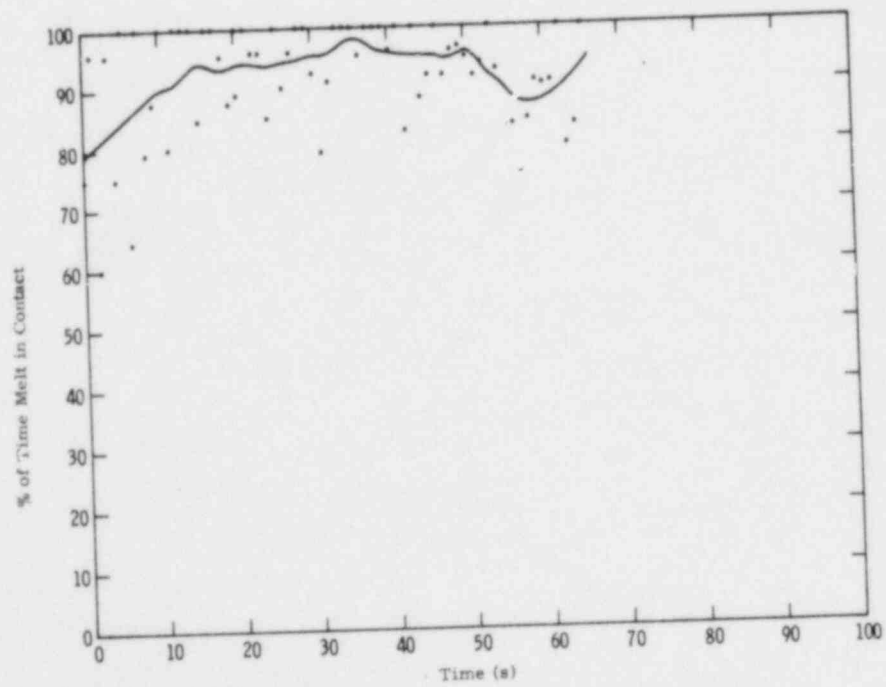


Figure 3.1-21 Contact Times-Test BURN 1, Position 8

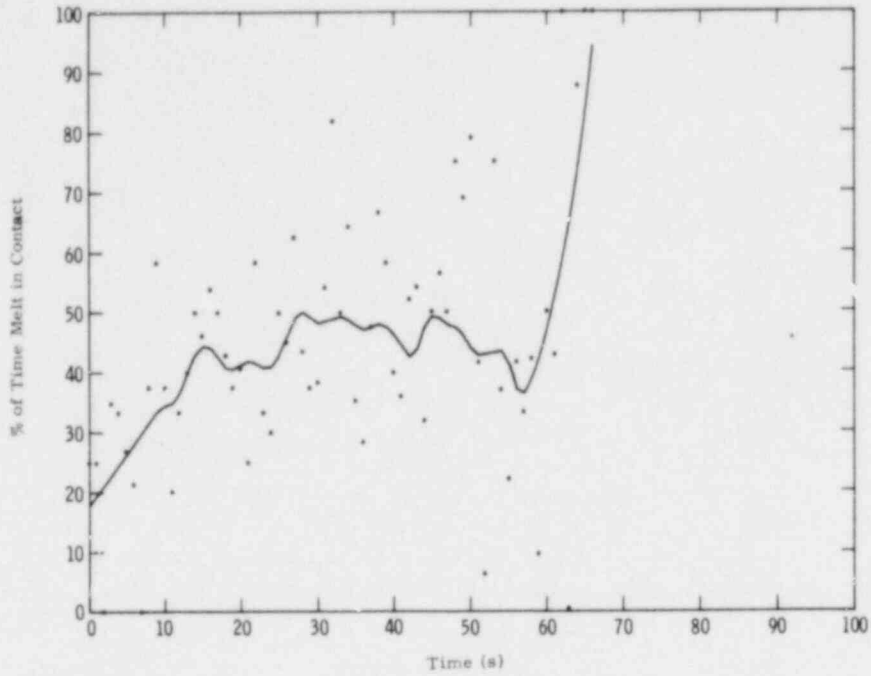


Figure 3.1-22 Contact Times-Test BUPN 1, Position 9

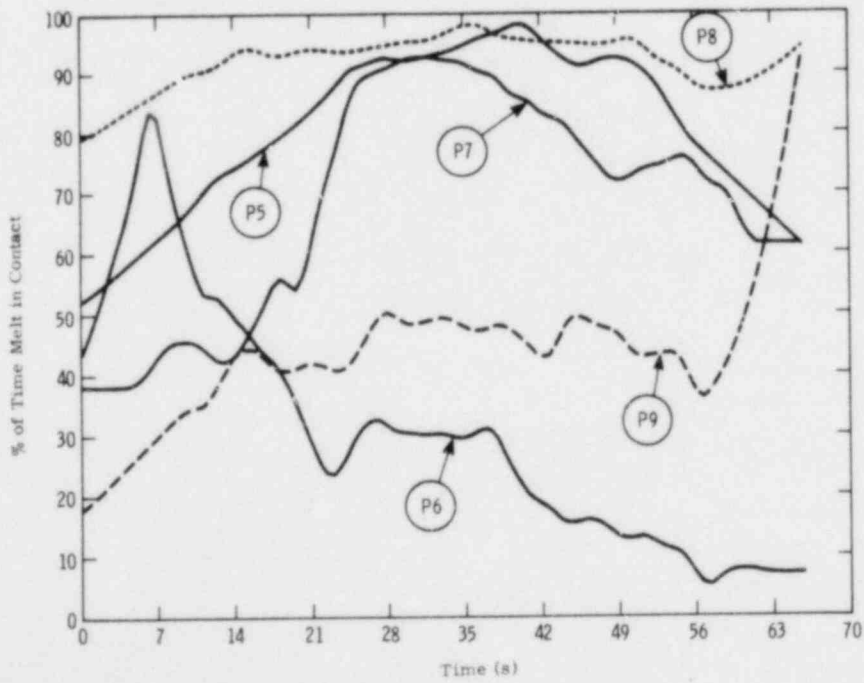


Figure 3.1-23 Contact Times-Test BURN 1

The quantitative data again reflect the qualitative observations made above concerning pool behavior. The melt has approximate symmetry about Point 5. Points on the cavity walls near the top of the pool (P1 and P9) are contacted by the melt only 40 to 50% of the time. Metal froze in contact with P9 and away from P1 at the end of the test. Points near the corners created by intersection of the cavity walls with the cavity bottom (P2 and P8) are apparently contacted by the melt 80 to 90% of the time during the so-called "steady-state" portion of the interaction. This is also true for points P3 and P7 on the bottom of the cavity near the walls. Melt contacts these points less often toward the end of the test when the melt is viscous and individual gas bubbles at the interface cause more global disturbances in the melt.

P6 and P4 are at the sites of localized gas emissions described above. Melt is in contact with these points only 20 to 30% of the time. Interestingly, these points also correspond to the sites of maximum concrete erosion.

P5, nearest the centerline, is in contact with the melt about 70% of the time. This point corresponds to the point of least concrete erosion at the base of the cavity.

Efforts to measure bubble sizes and residence times from the x-ray image were largely unsuccessful. During the period of violent melt agitation, distinct bubbles did not develop. During the steady-state period, gas bubbles formed and broke free of the interface within single frames. The melt depth was too small to monitor bubble travel through the melt. Transit times were less than 0.04 s during the first 30 s of the test. Transit times were about 0.08 s during the last 20 s of the test. Bubble sizes were about 0.5 to 2 cm in diameter. These sizes were somewhat larger than the sizes of crevices formed by gas bubbles entrapped in the solidified melt.

3.1.9 High-Temperature Melt Interactions With Core-Retention Materials

Available alternatives to concrete-structural (core-retention) materials that do not generate substantial volumes of gas when they interact with high-temperature melts may be categorized as follows:

- a. Refractory Materials - The thermal and chemical inertness of these materials are expected to allow the materials to withstand the interaction with high-temperature core melts. These materials would then be expected to retain the melt until it solidifies.
- b. Sacrificial Materials - By melting and dissolving melt materials, the sacrificial materials extract heat from a core melt and dilute the melt source to the point that the melt can be retained by conventional materials.
- c. Intermediate Materials - These materials possess, to various degrees, qualities of both the preceding categories of materials. They are still free of constituents that thermally decompose to yield volatile products.

Examples of materials falling into these three categories are listed in Table 3-8.

Table 3-8

Examples of Core Retention Materials

<u>Material Types</u>	<u>Specific Examples</u>
Refractory	MgO* UO ₂ ThO ₂ Graphite
Sacrificial	Borox* Sodium Metaborate Basalt Hematite Lead ZnCl ₂
Intermediate	High alumina cement* Firebrick*

*Materials used in scoping experiments

Scoping experiments to examine the real behavior of these materials have been conducted. Melts of stainless steel weighing about 200 kg and heated to 1973 K (1700°C) have been teemed into crucibles of:

- Borax
- High alumina cement
- Firebrick
- MgO

In the case of the latter three crucible materials, induction coils were embedded in the crucible material to sustain the melts after teeming. Experimental techniques were similar to those used in large-scale melt/concrete interaction tests and are described in Reference 3-6 and 3-1.

The test with firebrick was done with a firebrick layer over basaltic concrete. A 1.59-cm (5/8-in)-thick steel liner coated the firebrick. The arrangement is shown schematically in Figure 3.1-24. The arrangement is intended to mimic the design of the reactor cavity in the Fast Flux Test Facility.

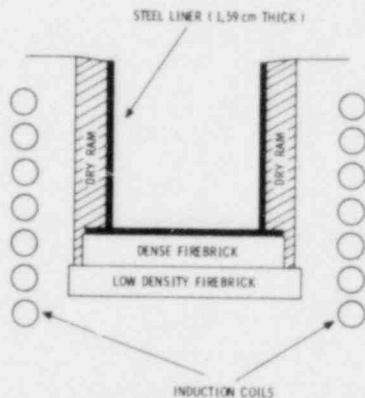


Figure 3.1-24 Schematic of Lined Basaltic Concrete Crucible

A complete report of the melt-interaction tests with these core-retention materials will soon be issued. Only a brief account of the more significant highlights of the tests will be presented here.

Results of the tests are summarized in Table 3-9. This table presents only the events observed during the tests.

Table 3-9

Qualitative Results of Melt/Core-Retention Material Interactions Tests

No.	Melt [†]	Crucible	Duration	Remarks
1	200-kg stainless steel	Borox	Transient* test	During the teem, a tremendous cloud of aerosol formed. This dissipated immediately, once molten metal was no longer flowing into the crucible. Erosion was about 6 cm.
2	200-kg stainless steel	High alumina cement	Melt sustained for 7 min after teem	Modest amounts of gas were evolved that proved to be hydrogen. Little aerosol formed. Virtually no erosion occurred.
3	200-kg stainless steel	Fire-brick coated basalt	Melt sustained for 2 h	Teem of the metal was completely uneventful. For 2 h little occurred aside from modest gas evolution. At the end of 2 h, the melt contacted concrete and the test was abruptly terminated.
4	122-kg stainless steel	MgO	Test was continued for sometime, but coupling was so poor that melt could not be sustained.	Only limited amounts of slag-line attack on the MgO lines was obscured. The melt could not be sustained.

*After teeming, the melt cooled naturally.

†Melt initially 1700°C

The teem of steel into borax produced a significant cloud of aerosol material. Aerosol formation ended immediately after teeming of the melt stopped. Some gas bubbles, probably from gas entrained in the borax casting, continued to percolate through the melt. Convection cells developed and could be clearly seen in the molten pool of borax that quickly submerged the metallic melt. Probes inserted into the metallic melt suggested that the melt was quickly quenched about its boundary. Liquid steel could still be detected inside the solidified shell for 7 to 12 min after the conclusion of the teem. Figure 3.1-25 shows that very little of the borax was eroded.

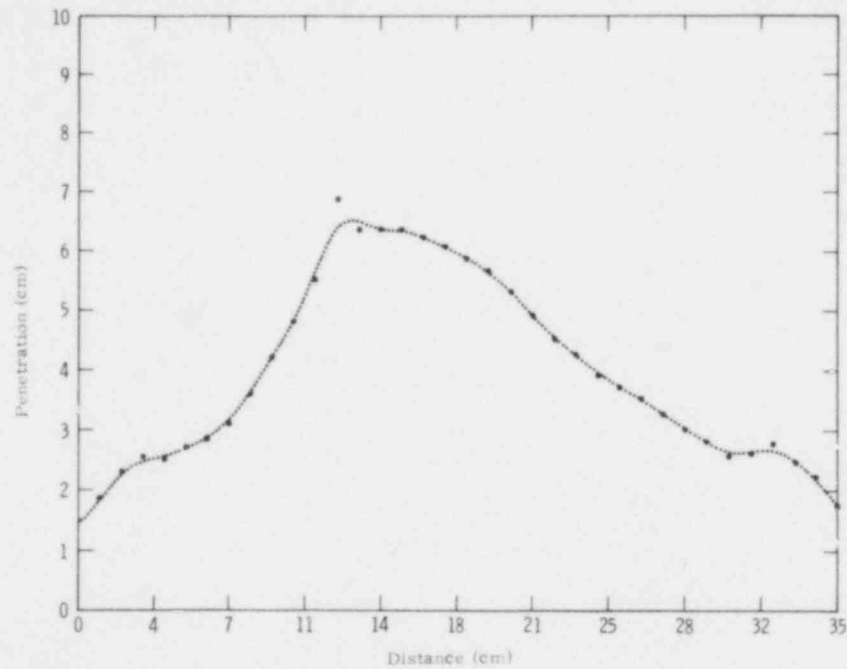


Figure 3.1-25 Borax Test Penetration Data, 0 Degrees

The erosion of borax seemed a completely thermal process. Near the centerline of the crucible cavity, where the melt stream formed during the teem of the steel, erosion was at least 50% greater than at surrounding surfaces of the cavity. This would reasonably be expected in view of the much higher melt-to-borax heat fluxes that develop in teemed melt than in quiescent pools of melt.

The resistance of borax to erosion by a melt may be rationalized in terms of the high-heat capacity of solid borax and the good heat-transfer properties of liquid borax. The perimeter of the steel was quickly quenched causing a pool of liquid borax to form. The liquid borax transferred heat quickly to the pool surface and to the solid borax. Melting borax kept the pool temperature quite low.

The rate of borax erosion is clearly a function of the heat flux from the steel. Once the core-melt materials solidify, the erosion rate would be a function only of the internal heat-generation rate.

The melt teem into high-alumina cement was similar to, though much less violent, than teems into concrete; only modest gas evolution occurred. During the test the outputs of Type K thermocouples embedded in the crucible were monitored. Failure of these sensors, often used in concrete/melt-interaction tests to monitor concrete erosion, suggest there was substantial erosion of the high-alumina cement. Posttest x-rays of the crucible, however, indicated that very little, if any, erosion occurred. The test was terminated after only 7 min when cooling water to the embedded induction power supply was interrupted.

High-alumina cement is a very attractive alternative to concrete. Its refractory properties are not well-known. Evidence from this test suggests that the melting point must be greater than 1973 K. The one concern with high-alumina cement is that it does contain some hydrates which decompose to yield water that may be reduced to H_2 by the melt. A thermogravimetric curve for high-alumina cement is shown in Figure 3.1-26. It may be possible to dry high-alumina cement and improve its core-retention capabilities without seriously degrading its structural properties.

The interaction test with firebrick was, in reality, a test of a composite material (firebrick over basaltic concrete). The third layer (a steel liner over the firebrick) was undoubtedly quickly penetrated by the melt as shown in previous tests in this program.³⁻⁷ The firebrick

admirably restrained the melt. The steel did not "wick up" into the brick as has been observed in the case of sodium melts. Erosion was probably by a melting mechanism. It required 2 h to penetrate 6.35 cm (2-1/2 in.) of the first layer of brick. Once this brick was penetrated, the melt came into contact with basaltic concrete and a very nearly explosive interaction occurred; the test was terminated.

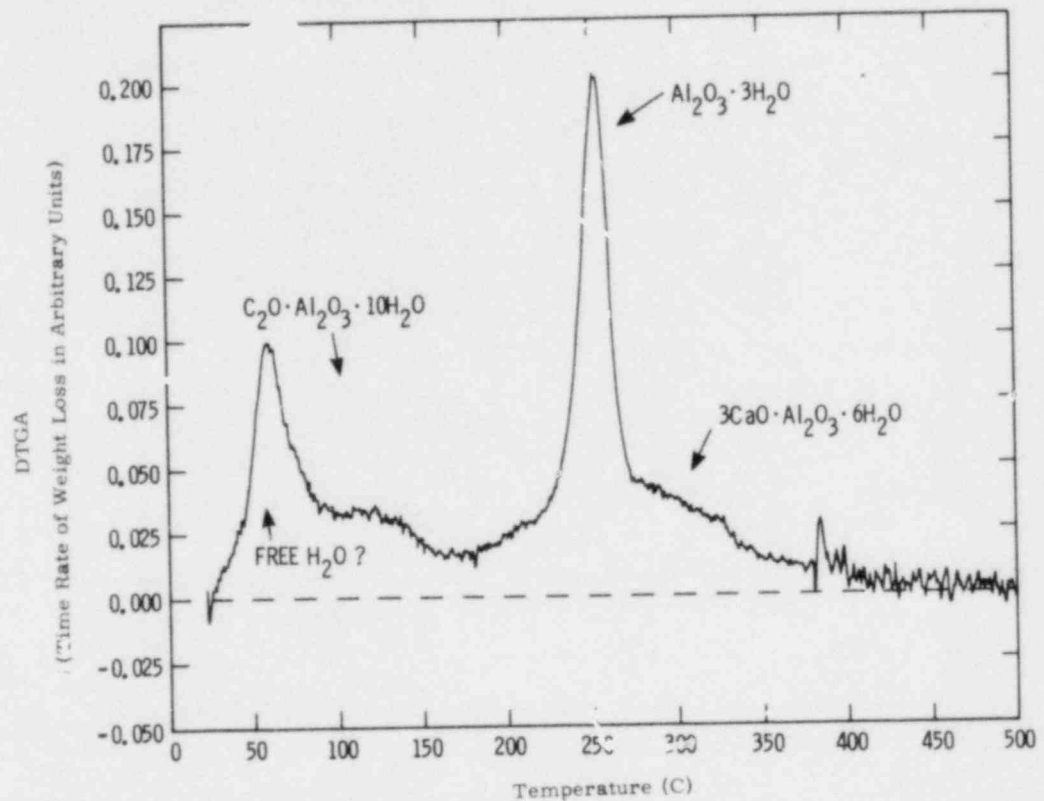


Figure 3.1-26 Survey TGA High-Alumina Cement

Prior to the vigorous eruptions associated with melt/concrete interactions, gases were liberated from the crucible. This gas came from heating concrete under the firebrick. Forty minutes after start of the test, gas evolution was sufficient to produce a self-sustaining flame at the top of the instrumentation tower covering the crucible.

The MgO crucible used in the final test in this series is shown in Figure 3.1-27. It consisted of a 1.27-cm(1/2-in.)-thick MgO liner

POOR ORIGINAL

surrounded by 98% pure MgO bricks. Unfortunately, coupling between the melt and the induction coil surrounding the melt was too poor to sustain the melt. Only modest slagline attack was observed.

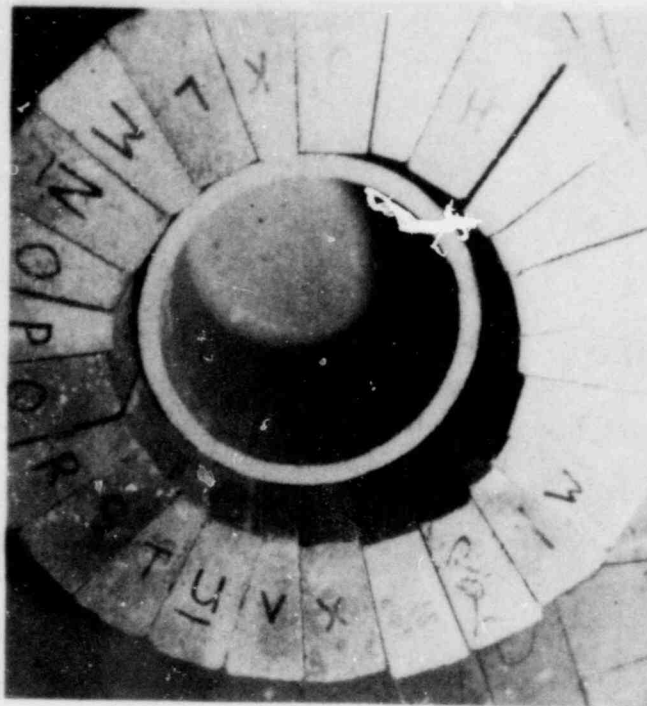


Figure 3.1-27 MgO Crucible Used in Final Test

The tests described above are only the first part of a program to survey interactions between core materials and the selected core-retention materials. Future tests will include small-scale interactions between the materials and both molten stainless steel and mixtures of UO_2 and stainless steel.

The poor results, due to equipment failure, observed in tests with high-alumina cement and MgO argue for repeating these tests. The test with high alumina can easily be repeated. The test with MgO, on the other hand, will have to be completely reevaluated. It is unlikely that this test will be repeated in this fiscal year. Small-scale tests with MgO will be conducted.

3.1.10 Other Large-Scale Tests

Three other large-scale tests were run during the report period:

- NAILS - 1
- NAILS - 2
- COIL 6L and COIL 6L reheat

Data reduction has not begun for these tests. Only a brief account of the tests and qualitative observations made during the tests are reported here.

The two NAILS tests were conducted to investigate the behavior of heated core debris in contact with concrete. Philosophically these tests were quite similar to the BURN 2 and BURN 3 tests. However, in these tests large crucibles identical with those of the COIL-series tests were used. Induction coils embedded in the concrete crucibles heated simulated, metallic core debris. The simulated core debris was about 75 kg of common 16-penny nails. The concrete in both NAILS 1 and NAILS 2 was the FFTF basaltic concrete; test NAILS 1 ran for 20 min and test NAILS 2 ran for 40 min.

The data collected in the two NAILS tests included:

- Concrete erosion
- Gas flow rate
- Gas composition
- Concrete temperatures
- Upward heat flux.

Qualitative behavior during the tests was quite similar to that observed in tests BURN 2 and BURN 3. Once the nails were heated to temperatures above the concrete solidus, the concrete began to erode. Gas evolution began at fairly low temperatures and continued throughout the test.

Posttest x-rays of the crucibles suggest that some of the nails did melt, whereas in the BURN-series tests with concrete melting in the

range of 1373-1623 K (1100-1350°C) no melting of the metal was observed. This suggestion has not yet been confirmed by posttest dissection of the crucibles. Crucible inspection to date has shown that the nails slumped substantially during the test. Many unmelted nails could be seen entrained in the slag.

Another point of interest observed during the test was that slag at the top of the pool remained fairly molten, though quite viscous throughout the test. Solidification of a crust over the melt did not occur until several minutes after power to the induction coils was turned off. This observation is especially surprising since, in the case of test NAILS 2, an air void 27.94 cm (11 in.) deep separated the upper crust of the melt from the main body of the melt.

Test COIL 6L repeated Test COIL 3 which was supposed to involve sustaining the melt for about 1 h. A power-supply failure during the teem of the 200-kg stainless-steel melt caused this test to be aborted. Post-test x-rays of the crucible showed that little erosion of the concrete occurred during the teeming and natural cooling of the melt. This suggests that erosion observed in the earlier COIL tests came about mostly during the sustained portion of the test. It had been previously suggested that much of this erosion occurred when the melt was first poured, since the sustaining temperature of the melt (~ 1773 K) was much lower than the melt temperature during the teem (~ 1973 K).

After the melt used in test COIL 6L had cooled, three Type-S thermocouples were located in holes drilled in the metal slug. Power was applied to the metal and the temperatures monitored in an effort to determine the coupling efficiency between the metal and the induction coils in the concrete. The temperature data were quite complex (perhaps too complex to analyze satisfactorily). They did suggest that at 120-kW electrical power a minimum of 30 kW of thermal power was deposited in the metal. This technique for calibrating the power input to the melt does not appear to be satisfactory.

3.2 PAHR Debris Bed (J.B. Rivard, 4422; R.J. Lipinski, 4425;
J.E. Gronager, 4422)

3.2.1 Introduction

The objective of the experimental studies of debris beds is to provide information on the behavior of fragmented reactor materials following a core disruptive accident in a fast reactor. Because fuel debris will continue to generate power due to the decay of contained fission products, high temperatures and resultant melting could threaten containment if the generated heat is not removed. Initially, it is desirable to ascertain the cooling capability which debris may possess due simply to natural processes (i.e., cooling that is not aided by forced circulation or other imposed measures).

3.2.2 Debris-Bed Analysis

3.2.2.1 Hardee-Nilson Model Extension -- The Hardee-Nilson formulation for debris beds³⁻⁸ was extended to one spatial dimension. A bed consisting exclusively of sodium at the saturation temperature was considered, since it was shown previously that subcooling can be modeled by an overlying conduction zone.³⁻⁹ The momentum, energy, and mass conservation equations were similar to those in Reference 3-8:

$$S = -\rho_{\ell} H \frac{d}{dz} (\gamma v_{\ell}) \quad (3.1)$$

$$v_{\ell} = -\frac{\kappa}{\mu_{\ell}} \left(\frac{dP}{dz} + \rho_{\ell} g \right) \quad (3.2)$$

$$v_v = -\frac{\kappa}{\mu_v} \left(\frac{dP}{dz} \right) \quad (3.3)$$

$$\frac{d}{dz} \left(\rho_v (1-\gamma) v_v + \rho_{\ell} \gamma v_{\ell} \right) = 0 \quad (3.4)$$

where

- z = distance above the bottom of the bed
- S = source per bed volume
- ρ = density
- H = heat of vaporization
- Y = fraction of sodium which is liquid at height z
- v = velocity
- κ = permeability
- μ = dynamic viscosity
- g = gravitational acceleration
- P = pressure
- v_{ℓ}, v_v = liquid and vapor sodium, respectively.

The equations may be reduced to:

$$S = \rho_{\ell} H \frac{d}{dz} \left(\frac{Y g \kappa}{v_{\ell} + \frac{Y}{1-Y} v_v} \right) \quad (3.5)$$

For a uniform source, a closed form for Y is obtained:

$$Y = \beta \pm \sqrt{\beta^2 - S v_{\ell} z / (\rho_{\ell} g k H)} \quad (3.6)$$

where

$$\beta = \frac{1}{2} - \left(\frac{v_v}{v_{\ell}} - 1 \right) S v_{\ell} z / (2 \rho_{\ell} g k H) \quad (3.7)$$

The superficial velocities (average microscopic velocity times sodium volume fraction in the bed) are found to be:

$$v_{\ell} = \frac{-g \kappa}{\left(\frac{Y}{1-Y} \right) v_v + v_{\ell}} \quad (3.8)$$

$$v_v = \frac{g \kappa \rho_l}{v_v \rho_v} \left(1 - \frac{v_l}{\left(\frac{\gamma}{1-\gamma} \right) v_v + v_l} \right) \quad (3.9)$$

where γ is given in Equation (3.6).

The heat-removal rate at the top of the bed ($z = L$) may be obtained by multiplying the vapor velocity by the density, the heat of vaporization, and the vapor fraction. This then reduces to:

$$q_L = \frac{g \rho_l \kappa H}{v_l} \frac{\gamma_L}{1 + \left(\frac{\gamma_L}{1-\gamma_L} \right) \frac{v_v}{v_l}} \quad (3.10)$$

where γ_L is the liquid fraction at the top of the bed. As the source (S), the bed depth (L), or the permeability (κ) is varied, Eq (3.6) predicts γ_L varies; this variation produces a different value of heat removal according to Eq (3.10). Using γ_L as an index of the bed state, as γ_L increases from zero to one, q_L increased to a maximum and then decreases back to zero as Figure 3.2-1 shows.

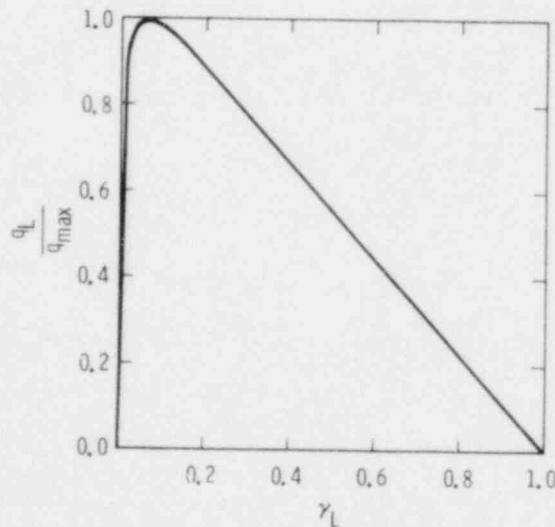


Figure 3.2-1 Liquid Fraction vs Dimensionless Heat Flux, Both at the Top of the Bed (Na-UO₂ bed)

Differentiating q_L with respect to γ_L ,³⁻⁸ the result is the same as that obtained by Hardee and Nilson for a bed with no subcooling:

$$q_{\max} = \frac{g \rho_l \kappa H}{v_l} \frac{1}{(1 + \sqrt{v_v/v_l})^2} \quad (3.11)$$

Thus, the one-dimensional extension of the Hardee-Nilson formulation does not yield a new equation for the dryout heat flux of a nonsubcooled bed.

The double solution of Eq (3.6) may now be interpreted. Figure 3.2-2 shows the liquid fraction (γ) as a function of height for various values of S . For a given S , there are two solutions. The first solution (with $\gamma(0) = 1$) has a large liquid fraction and a small space for vapor flow. Thus it is vapor-flow limited. The second solution has a very small liquid fraction and is liquid-flow limited. The two solutions have different γ_L 's corresponding (in Figure 3.2-1) to the two γ_L possible for a given q_L . If a flow perturbation in the first solution causes a decrease in γ , Figure 3.2-1 predicts a state of enhanced heat removal that will cool the system and allow a restoration of γ to its previous state. Thus the first solution is thermally stable. Similar logic indicates thermal instability for the second solution.

The equations may be easily changed to model a heat source that is in the liquid only (e.g., microwave heating of water or Joule heating of molten UO_2 out-of-core). In this case, S is still defined as the source per bed volume, but is proportional to the liquid fraction γ . Equation (3.5) then becomes:

$$S = \rho_l g H \frac{d}{dz} \frac{\gamma \kappa}{\gamma_l + \frac{\gamma}{1-\gamma} \gamma_v} \quad (3.12)$$

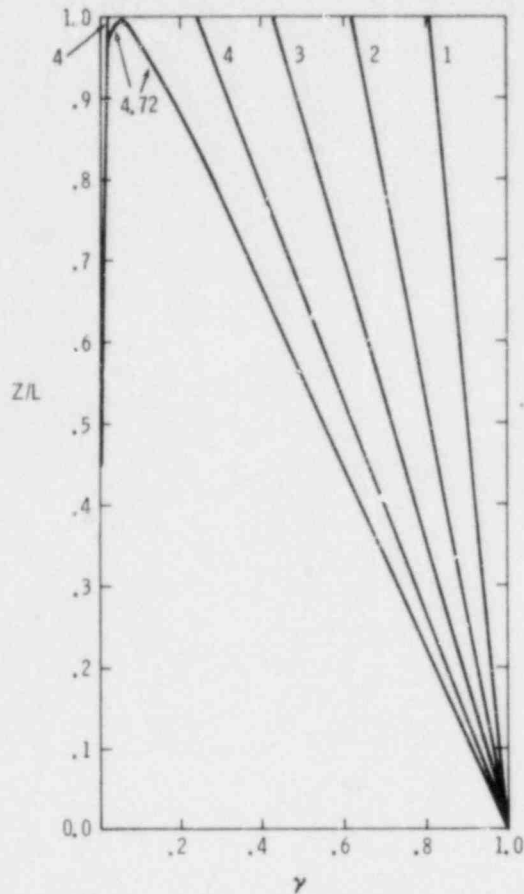


Figure 3.2-2 Liquid Fraction vs Dimensionless Height With Heat Source in the Particles (bed depth is 10 mm; permeability is 10^{-10}m^2 ; system is Na-UO₂). Numbers by the curves are bed power (MW/m^3).

This equation is not soluble in closed form; however, a computer-generated solution appears in Figure 3.2-3. The shape of the stable solution is not radically different from the uniform source case, although the power density in the liquid must be higher to compensate for the powerless vapor regions. The unstable solution vanishes since, without liquid, zero-power generation is balanced by zero heat removal. The velocity Eq (3.8) and (3.9) are unchanged. The dryout heat flux is found to be the same as that given by Eq (3.11), dependent only on liquid-material properties and permeability. However, determination of the liquid region source strength and bed depth that generates that heat flux is not simple since it depends on integrating the liquid fraction.

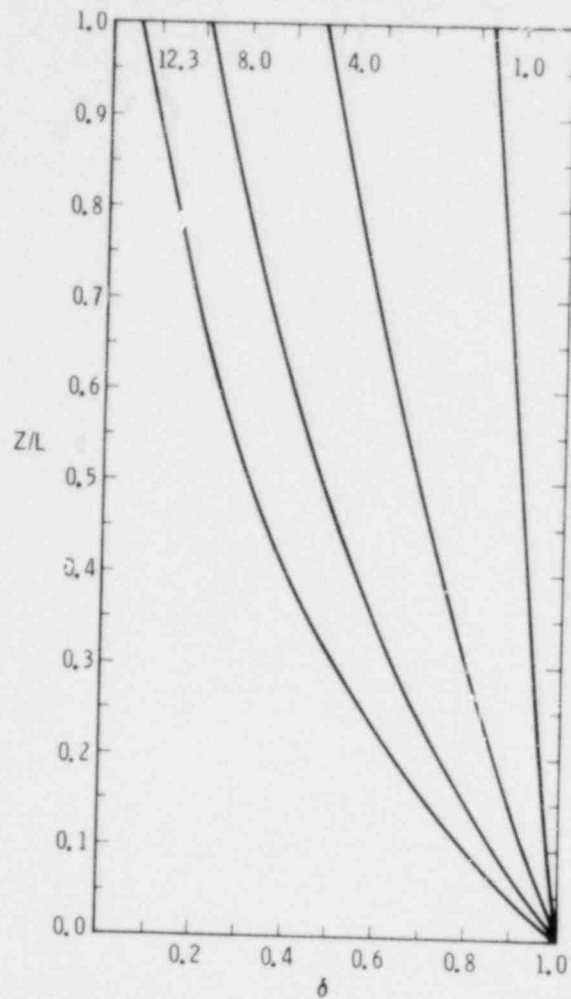


Figure 3.2-3 Liquid Fraction vs Dimensionless Height With Heat Source in the Liquid Only. Numbers by the curves are bed power (MW/m^3).

The vapor velocity is maximum for the stable solution at the bottom of the bed (where $\gamma = 1$), as Eq (3.9) shows. Using the bed-fluidization criterion from Wallis,³⁻¹⁰ the requirement to fluidize the bottom of the bed reduces to:

$$\rho_S (1-\epsilon) < \rho_L \quad (3.13)$$

where ρ_S is the solid density and ϵ is the sodium volume fraction in the bed. This is simply a statement that the fluidized particles be supported by the weight of the liquid. At the top of the bed at incipient dryout,

the vapor velocity is at its maximum, but is not much reduced; the requirement is

$$\rho_s (1-\epsilon) (1 + \sqrt{v_l/v_v}) < \rho_l \quad (3.14)$$

Neither of these conditions is met with UO_2 particles and sodium (for typical sodium fractions of approximately one-half), nor are they met with UO_2 and water. Nevertheless, experimental observations indicate channels void of particles forming in such beds.³⁻¹¹ Although the formation of a channel is subject to further investigation, the maintenance and possible growth within an existing channel may be explained. The pressure drop per length within the channel must equal that of the surrounding liquid: $dP/dz = \rho_l g$. The vapor velocity in the channel must be sufficient to establish this pressure gradient. Scoping calculations indicate that such velocities are in the laminar regime so that the Hagen-Poiseuille law for pressure drop in a pipe may be used.³⁻¹² Combining this with the single-particle terminal-velocity equation³⁻¹¹ yields the following criteria for levitation of a single particle of diameter d_p in a channel of diameter d_c :

$$d_c > \frac{4}{3} \sqrt{\rho_s/\rho_l} d_p \quad (3.15)$$

For Na- UO_2 systems, the critical size for channel maintenance is five particle diameters. (Another way to visualize this criterion is to consider a single particle in a channel as a "bed" with a very large void fraction and use Eq (3.14).)

3.2.2.2 Empirical Post-Dryout Model -- The one-dimensional extension of the Hardee-Nilsen model predicts a dryout heat flux for a debris bed with overlying saturated sodium that is independent of bed depth. If such a bed is at incipient dryout and the power is increased slightly, the bed will generate more heat than can be removed by the two-phase mode and dryout will begin. As the two-phase region shrinks, it will receive heat from the dry zone below it via conduction. Thus, the two-phase zone will

still have to permit passage of a heat flux greater than the Hardee-Nilson-predicted maximum. Since heat removal with a uniformly distributed source is easier than removal with a source skewed toward the bottom (since the heat must travel a greater average distance), the bed will still be unable to remove all the generated heat. Thus, the depth-independent dryout heat-flux prediction implies that, for powers slightly above incipient dryout, the entire two-phase zone will vanish and the bed will heat and melt because of the low dry-bed conductivity.

Fortunately (for reactor safety), experimental evidence refutes these predicted consequences. In the Sandia Na-UO₂ fission-heated debris-bed experiment (D-3),³⁻⁹ a bed was brought beyond the state of incipient dryout to a state with a stable two-phase zone overlying a stable dry zone. This condition was held for 99 min until shutdown. In light of this evidence, a new model which could predict this behavior was developed.

Experimental data on dryout heat flux vs bed depth has been obtained at UCLA³⁻¹³ and ANL.^{3-11,14} For nonsubcooled beds, the data indicate a dryout heat flux independent of bed depth for deep beds only. As the bed depth is decreased, a point is reached where the dryout heat flux increases linearly with decreasing depth. Beds thinner than this are called shallow beds. This effect is seen both for volume-heated beds and bottom-heated beds, although the dryout flux for a bottom-heated bed is less than that for a volume-heated bed of the same depth. These observations suggest a way to explain the D-3 behavior. When the source within a shallow bed at dryout is increased, the two-phase zone may decrease slightly in size leaving a conducting dry zone below. In the narrower state, the two-phase zone may pass more heat through it than before, although some of that heat is now applied directly at the bottom rather than being uniformly dispersed. As long as the increased heat-removal capability of the thinner state is greater than the decreased capability from shifting slightly toward a bottom-heated state, the two-phase zone

will be able to handle the increased load and will be stable with a dry zone below it.

These concepts were incorporated into an empirical model. First, the dryout behavior of nonsubcooled beds was parameterized:

$$q_{d,v} = \begin{cases} a_v - b_v L & L < (a_v - q_{v,\min})/b_v \\ q_{v,\min} & L > (a_v - q_{v,\min})/b_v \end{cases} \quad (3.16)$$

$$(3.17)$$

$$q_{d,b} = \begin{cases} a_b - b_b L & L < (a_b - q_{b,\min})/b_b \\ q_{b,\min} & L > (a_b - q_{b,\min})/b_b \end{cases} \quad (3.18)$$

$$(3.19)$$

where $q_{d,v}$ and $q_{d,b}$ are the dryout-heat fluxes for volume-heated and bottom-heated shallow beds of length L , $q_{v,\min}$ and $q_{b,\min}$ are the dryout fluxes for deep beds, and a_v , b_v , a_b , and b_b are slopes and intercepts in the shallow-bed correlations. Second, the assumption is made that the dryout heat flux could be determined by linearly combining the volume-heated and bottom-heated relationships in proportion to the boiling and dry zone thicknesses, respectively:

$$\frac{L_{tp} (a_v - b_v L_{tp}) + L_d (a_b - b_b L_{tp})}{L_{tp} + L_d} = S(L_{tp} + L_d) \quad (3.20)$$

where S is the volumetric heat source in the bed.

The dry-zone length (for nonsubcooled beds) may then be determined to be

$$L_d = L_T - \lambda_{ns} \pm \sqrt{\lambda_{ns}^2 + \beta_{ns}} \quad (3.21)$$

where

$$\lambda_{ns} = (a_v - a_b - b_b L_T) / (2(b_v - b_b)) \quad (3.22)$$

$$\beta_{ns} = (a_b L_T - S L_T^2) / (b_v - b_b) \quad (3.23)$$

and where L_T is the total bed depth.

The first solution (with the positive root) is thermally unstable, while the second is stable.

Values for a_v , b_v , $q_{v,min}$, a_b , b_b , $q_{b,min}$ may be obtained from Reference 3-71 for Na-UO₂ systems:

$$a_v = 2.04 \times 10^6 \text{ W/m}^2$$

$$b_v = 11.3 \times 10^6 \text{ W/m}^3$$

$$q_{v,min} \cong 0.15 \times 10^6 \text{ W/m}^2$$

$$a_b = 1.12 \times 10^6 \text{ W/m}^2$$

$$b_b = 10.2 \times 10^6 \text{ W/m}^3$$

$$q_{b,min} \cong 0.15 \times 10^6 \text{ W/m}^2$$

These values predict shallow-deep transition depths of 0.167 m and 0.095 m for volume- and bottom-heated systems, respectively. Thus, Eq (3.21) will be valid as long as the two-phase zone is kept less than 95 mm.

A zone-thickness plot for a 60-mm-thick Na-UO₂ bed is shown in Figure 3.2-4. The thermally unstable solution for the dry two-phase interface is marked with a dashed line. At 3.335 W/g-UO₂, the two solutions meet and any further increase in power causes the two-phase zone to vanish, similar to the original deep-bed predictions. This is the point where bottom-heating inefficiencies overcome reduced thickness efficiencies.

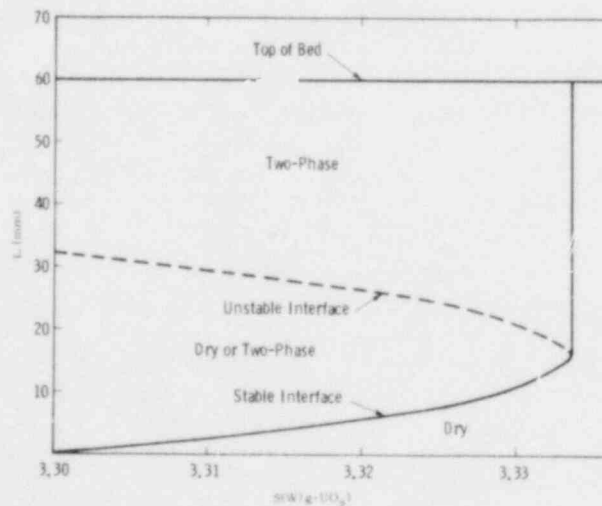


Figure 3.2-4 Bottom-Insulated Bed With Saturated Sodium Above

For a top-subcooled bed, the series conduction model³⁻⁹ may be folded in. Then the dry zone length is

$$L_d = L_T - \lambda_{ts} + \sqrt{\lambda_{ts}^2 + \beta_{ts}} \quad (3.24)$$

where

$$\lambda_{ts} = (a_v - a_b - b_b L_T - b_v L_{ts}) / (2(b_v - b_b)) \quad (3.25)$$

$$\beta_{ts} = (a_b L_T - a_v L_{ts} - S(L_T - L_{ts})^2) / (b_v - b_b) \quad (3.26)$$

$$L_{ts} = L_T - \sqrt{L_T^2 - 2k_e (T_s - T_t) / S} \quad (3.27)$$

and where k_e is the effective conductivity at the top of the bed, and T_s and T_t are the temperatures of sodium saturation and the top of the bed, respectively.

Bottom-cooling may also be added to the model by assuming conduction dominates downward heat flow.³⁻⁹ However, the foregoing equations have assumed an insulated bottom. Therefore, with downward heat flow, the dry zone must be split into upward and downward heat-flow regions by a plane of zero heat flow. The lower region then will be the same thickness by symmetry. There might also be a zone of subcooled debris below the dry region. The zone thickness may be redefined as follows: L_{wu} , L_{tpdu} , L_{du} , L_{dd} , and L_{wd} are the wet upward conduction, two-phase plus dry upward, dry upward, dry downward, and wet downward conduction zone thicknesses, respectively. L_t is the total bed thickness. The following equation results:

$$L_t = \sqrt{L_{tpdu}^2 + \frac{2k_w (T_s - T_t)}{S}} + \sqrt{L_{du}^2 + \frac{2k_w (T_s - T_b)}{2}} \quad (3.28)$$

where

$$L_{tpdu} = \frac{a_v + (2b_v - b_b)L_{du}}{2(S + b_v)} + \quad (3.29)$$

$$\sqrt{\left(\frac{a_v + (2b_v - b_b)L_{du}}{2(S + b_v)}\right)^2 - \frac{(a_v - a_b + (b_v - b_b)L_{du})L_{du}}{S + b_v}}$$

and T_b is the temperature at the bottom of the bed. The equation is solved iteratively for L_{du} , from which the other thicknesses are easily obtained as follows:

$$L_{dd} = L_{du}, \text{ and} \quad (3.30)$$

$$L_{wd} = \sqrt{L_{dd}^2 + \frac{2k_w (T_s - T_b)}{S}} - L_{dd} \quad (3.31)$$

The behavior of a top-cooled and bottom-cooled bed from low powers up to incipient fuel melt may now be described using the conduction model and postdryout models. A plot of zone thicknesses for a 100-mm-thick bed with fixed top and bottom temperatures of 500 and 300 K, respectively, below saturation is shown in Figure 3.2-5. Clearly, a relatively small percent increase in power beyond dryout causes significant dry zone thicknesses. Due to the low thermal conductivity of dry debris, fuel melt would occur with a total dry zone thickness of about 20 mm. Thus, while the postdryout model predicts the existence of a stable dry zone beyond incipient dryout, it also predicts that the amount of power increase needed to reach fuel melt is not significant. Therefore, it is important to understand the effect of various parameters on incipient dryout since the power increase allowed by postdryout states may not be very large.

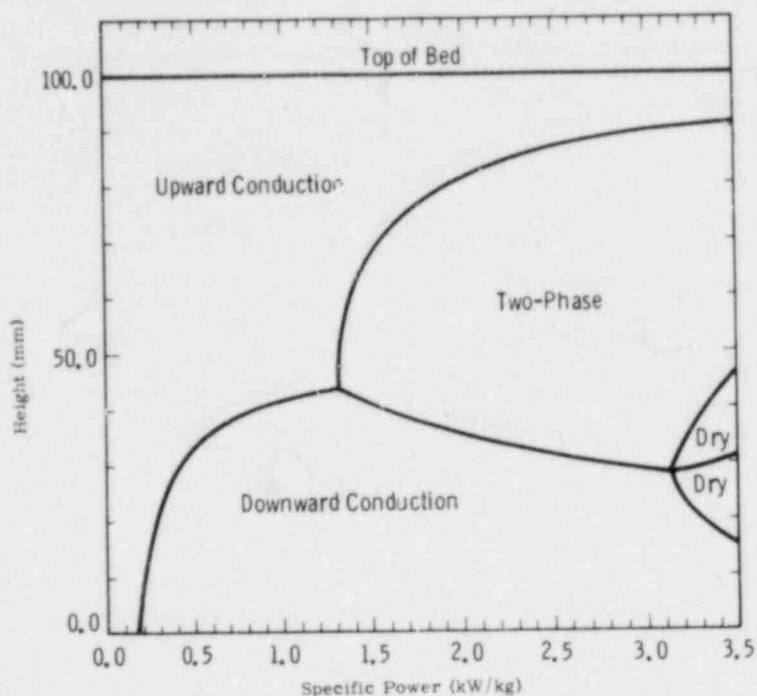


Figure 3.2-5 Model Predictions of Zone Thicknesses for a 100-mm-Thick Bed Cooled Above and Below by Sodium 500 and 300 K Below Saturation, Respectively (the dry zone is divided by a line dividing upward from downward heat flow).

One parameter affecting incipient dryout is bottom cooling, which was reported in a previous quarterly.³⁻¹⁵ In that analysis the predicted effects were based on the assumption that the two-phase region behaved similarly to a deep bed, with a depth-independent dryout heat flux. Alternatively, the two-phase zone may be assumed to follow shallow-bed behavior. This has significant effects in bottom-cooled cases because heat removal from the bottom may cause a deep bed to have a very shallow two-phase zone. The equation given in Reference 3-15 is easily modified to

$$L_t = \sqrt{q_{tp}^2 + \frac{2k_w (T_s - T_t)}{S}} + \sqrt{\frac{2k_w (T_s - T_b)}{S}} \quad (3.32)$$

where

$$q_{tp} \begin{cases} \frac{a_v}{S+b_v} & \text{for } S > \frac{a_v}{q_{b,min}} - b_v \end{cases} \quad (3.33)$$

$$\begin{cases} q_{b,min} & \text{for } S < \frac{a_v}{q_{b,min}} - b_b \end{cases} \quad (3.34)$$

Figure 3.2-6 shows the dryout condition for a bed cooled above with sodium 400 K below saturation and cooled below by various amounts. Curves from assumption of both deep and shallow behavior are shown for comparison (where the extended Hardee-Nilson model uses deep-bed behavior and the empirical model uses shallow-bed behavior merging into deep-bed behavior at the transition thickness). As the figure shows, use of the shallow-bed condition in the comparison model substantially increases dryout-bed thicknesses over the strictly deep-bed correlation in the extended Hardee-Nilson model.

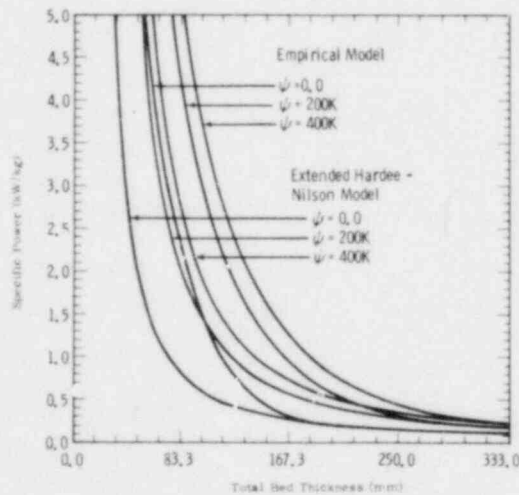


Figure 3.2-6 Specific Power at Incipient Dryout for Beds Cooled Above by Sodium 400 K Below Saturation and Cooled Below by Various Amounts (ψ is the temperature drop that exists across the bottom conduction zone).

3.2.2.3 Bottom-Cooled Debris-Bed Experiment

The empirical model previously described was incorporated in the General Electric TAC 2D heat-transfer code³⁻¹⁶ and was used to model thermally a proposed design for a debris-bed experiment capable of reaching incipient fuel melt. The proposed design included a 100-mm-deep Na-UO₂ bed of 100 mm diameter contained in a molybdenum-encased thoria crucible. The system was cooled by sodium at the top 350 K below saturation and at the bottom 50 K below saturation. A power of 3.0 W/g-UO₂ produced incipient melt in a stable dry zone 20 mm thick. Figure 3.2-7 shows the computer simulation. Although the crucible had sufficient side-cooling to keep the molten region away from the wall, the whole bed was still fairly close to one-dimensional. Only 11% of the generated heat was lost radially. The peak temperature in the molybdenum encasement was 1348 K, well below its melting point of 2883 K.

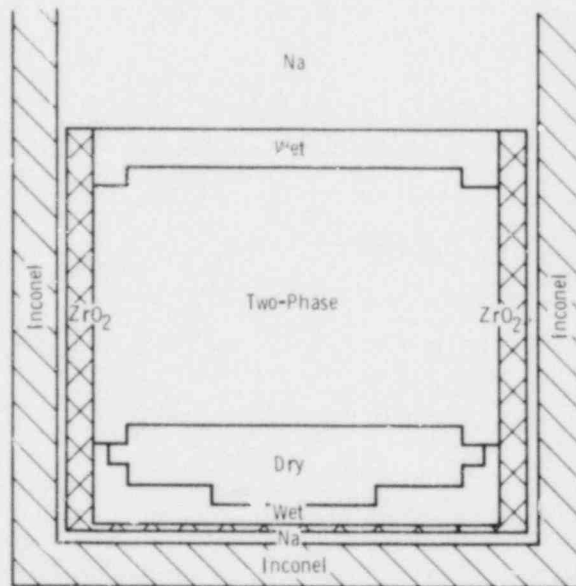


Figure 3.2-7 Computer Simulation of a Steady-State Debris-Bed Design. Source strength is 3.0 kW/kg-UO₂. The "wet" zone is liquid sodium and debris; the "two-phase" zone is two-phase sodium and debris; and the "dry" zone is sodium vapor and debris. The bed is at incipient fuel melt at the center of the dry zone. (The rectangular outlines of the zones shown correspond to the grid spacing used in TAC 2D and do not reflect the smooth contours which exist.)

3.2.3 Ultrasonic Sensor Development

3.2.3.1 Objective

The objective of the ultrasonic sensor-development program as it relates to the debris-bed experimental program is to provide information on the behavior of debris beds formed following an HCDA. Earlier debris-bed experiments D-1, D-2, and D-3 provided initial data characterizing debris beds at various bed loadings, D-3 also provided data on bed-dryout conditions which will be further investigated in the upcoming D-4 experiment. Presently, preparations are being made for the D-4 experiment that is intended to provide extended dryout characteristics of debris beds. This data will enable investigators to make comparisons with the current dryout model discussed earlier. This report section will emphasize the preparations for the D-4 experiment and will comment on the development of the new instrumentation to be employed in the experiment.

3.2.3.2 Preparation for the Experiment -- The D-4 debris-bed experiment is currently scheduled to run from July 16 through July 23, 1979. The components previously ordered are arriving as scheduled and fabrication of the experiment vessel is continuing. X-ray photography and component testing are being performed to assure the integrity of the equipment. The safety analysis report for the experiment is approaching completion and the ACRR Safety Committee review is expected in mid-April.

Based upon past experience, modification to the existing helium loop was necessary to measure low-helium flow rates more accurately. A new helium-heater/flow-rate measurement section has been designed for insertion between the portable helium-cooling loop and the piping connecting it to the experiment package. The new addition physically replaces the previous heater section used to melt the sodium within the canister prior to the actual experiment. (The new section includes a 18-kVA electric heater to replace the old heater section.) The flow-rate-measurement components consist of two sections: a 2.54-cm section to measure low-flow rates (9.1 to 34.1 kg/h) and a 5.08-cm section to measure

high-flow rates (31.8 to 100 kg/h). The new equipment will be tested and operating procedures formulated during OPST (Out-of-Pile System Tests).

Two preliminary experiments are being scheduled to test various functions of the experiment-support equipment. The first test is the OPST (to be conducted in late May) in which the actual debris-bed experiment canister is replaced by an electrically heated canister. The experiment is conducted with all the supporting equipment including diagnostics. The OPST objectives are:

- a. Shakedown of the new heater/flow-rate measurement section
- b. Measure the experiment capsule-heat-exchanger characteristics
- c. Testing the electronic systems
- d. Training of personnel

The second test is the Reactor Compatibility Experiment (RCE) to be performed in late June. The RCE consists of placing the experiment package, without supporting-equipment connections, into the ACRR. The objectives of the second test are:

- a. Confirm neutronic worth calculations for the new ACRR configuration.
- b. Determine the physical compatibility of the experiment package with the ACRR (size and position).

The results of the two experiments will be discussed in the next quarterly.

3.3 PAHR Molten Pool (D.W. Varela, 4422; R.J. Lipinski, 4425; D.J. Sasmor, 4453; J.E. Gronager, 4422; W. Drotning, 5824)

3.3.1 Introduction

The in-core molten-fuel-pool program provides for investigating the heat-flux distribution and containment-ablation potential of molten LMFBR

debris materials under typical temperature and heating conditions. Additionally, the molten-pool technology is being combined with that of the debris-bed experiment program to study the heat-transfer characteristics of sodium-filled debris beds from incipient boiling through dryout to molten-pool formation.

The major activities during this period included the preparation for microscopic posttest analysis of a series of high-temperature furnace experiments, the initiation of a feasibility study to perform thermal-conductivity measurements of UO_2 powder beds at high temperatures, the thermal analysis of the MP-1 and MP-2 in-core experiments, and the continued development of ultrasonic thermometry.

3.3.2 High-Temperature Furnace Experiments

Three series of high-temperature furnace experiments were completed this reporting period and materials interactions were examined under possible PAHR conditions following a hypothetical core disruptive accident. The first series was intended to address the general question of sintering of the debris bed; it consisted of simply heating UO_2 powders of various particle sizes and observing densification and consolidation. The second set of experiments was designed to assess the way in which a bed of UO_2 and steel might resegment above the melting point of steel. The third set of experiments involved reactions between UO_2 powders and MgO disks. Results of these samples, as obtained from visual examinations, have been reported in previous quarterly reports.^{3-4,3-15}

During this period, the furnace experiment samples were potted, sectioned, and polished and are now ready for optical microscopy, scanning electron microscopy (SEM), and electron microprobe examination. The extent of neck growth between grains in UO_2 , and the extent to which second-phase material (steel) is involved in the sintering will be investigated. The possibility of steel wetting UO_2 at high temperatures will also be investigated. For the UO_2 -MgO experiments, the diffusion of UO_2 into grain boundaries and the possible decomposition of MgO at very high temperatures will be addressed.

3.3.3 Thermal-Conductivity Measurements (Feasibility Study)

The thermal conductivity must be known with accuracy in order to model the transition from debris-bed dryout to a molten pool. Unfortunately, there is no experimental information for the thermal conductivity of UO_2 -packed beds in the temperature range of interest (1273 K - 3123 K).

A feasibility study has very recently been initiated to investigate the technology available to perform such measurements. The activity during this period has been limited to a literature search for possible experimental designs and methods of measurement. During next quarter, the feasibility of using these designs and methods at high temperatures will be evaluated. If necessary, new concepts will be investigated. The effects of sintering and radiation which become relevant at high temperatures will be important considerations. Also, the possibility of having a second phase (steel) will be considered.

3.3.4 Thermal Modeling of MP-1 and MP-2

With the TAC 2D heat-transfer code,³⁻¹⁶ thermal conditions in molten pool tests MP-1 and MP-2 were modeled using only the conduction equation. Most of the temperature-dependent thermal conductivities and specific heats were nominal values taken from Reference 3-17. The thermal conductivities of powdered urania and powdered zirconia were determined with the formula of Godbee and Ziegler.³⁻¹⁸ Thermal radiation between and through the particles was considered;^{3-19,3-4} however, good agreement with the experiment could only be obtained without the radiation terms. Apparently grain boundaries within the particles greatly reduced their transparency and small particles distributed between the larger ones reduced interparticle transmission.

The calculated temperatures for MP-2 with nominal material properties and without radiative heat transfer within the urania are shown in Figures 3.3-1, 3.3-2, and 3.3-3. Temperatures both within the urania and

in the surrounding insulation are followed fairly well from startup to beyond shutdown. Only 0.2% of the urania is predicted to be molten using the nominal values. However, with the 7% increased power and a 10% reduction in the conductivity of the powdered urania, the shape and quantity of molten urania at shutdown matches that determined by x-radiography. These changes are within the range of uncertainty in the experiment.

3.3.5 Ultrasonic Thermometers-Instrumentation Development

During the D-2 debris-bed experiment, a "disturbance" or rapid change in the bed characteristics was identified. Investigations postulated that the bed may have raised or erupted in some manner. To properly characterize a possible disturbance, and also to determine the size of the two-phase heat-transfer zone within the bed, a sodium-level detector will be incorporated into experiment D-4. A new sodium-level detector that meets the physical requirements of the experiment capsule is under development. The new sodium-level sensor uses technology similar to that of ultrasonic thermometers. The sensor has been successful in detecting levels of mercury. A prototype is being constructed for hot sodium testing. A detailed description of the sensor as well as the results of the sodium experiments will be reported in the near future.

During this reporting period, ultrasonic thermometers (UTs) have been evaluated for use in the debris-bed program. A favorable review of the UTs ability to provide several temperature-sensitive regions along a single thin (~ 20 mil) sensor has led to the incorporation of a UT into the D-4 experiment with the primary objective of evaluating its performance for future high-temperature debris-bed experiments.

Several advances have been made in the construction of UT sensors and the performance of the electronic equipment. Techniques have been developed to produce uniform notching of the UT sensor, improving the axial resolution from 10 to 6 mm. Low-temperature experiments have given excellent results; further testing is expected to confirm these same excellent results at high-temperatures.

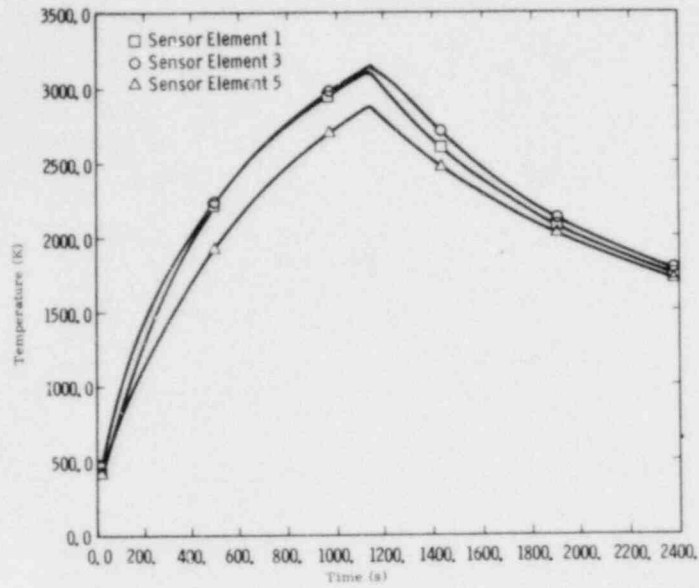


Figure 3.3-1 Model Predictions of Ultrasonic Thermometer Readings for the Top, Middle, and Bottom of the Bed for MP-2 (the experimental data follows the predictions but is too noisy for a close comparison in this form).

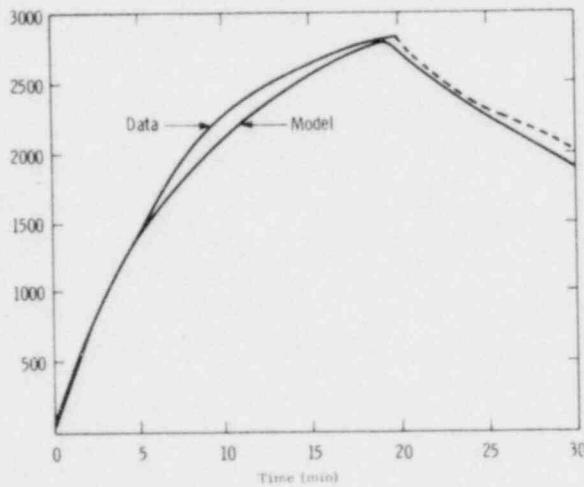


Figure 3.3-2 Model Predictions and Experimental Data for the Average of the Five Elements of One Ultrasonic Sensor in the MP-2 Bed (the dashed line is a "best-guess" combination of the two sensors).

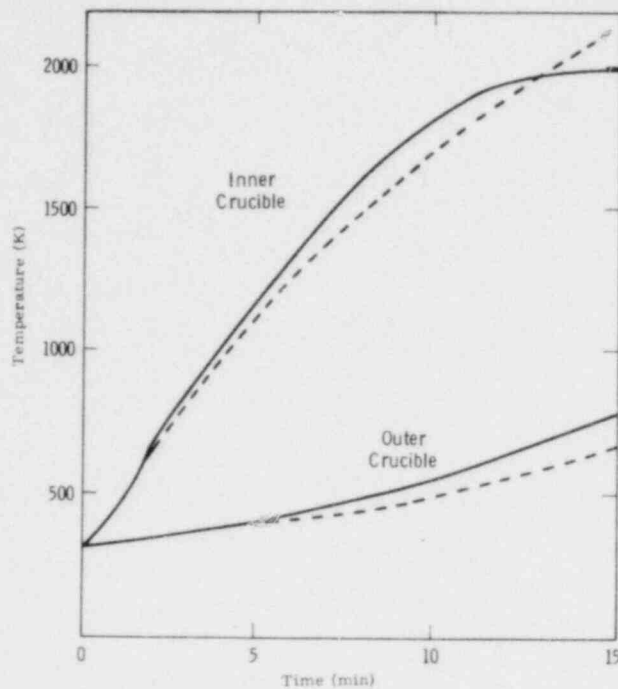


Figure 3.3-3 Experimental Data (solid lines) and Model Predictions (dashed lines) for Temperatures at the Side Midpoints of the Inner and Outer Crucibles in MP-2. (The inner thermocouple began failing near 1900 K. The model used nominal experiment values, but the fit would be improved with slightly higher power.)

Additional UT electronic components have been constructed. Currently four units are being fabricated to service four more UT sensors. The electronic units are modular to cut costs and to provide for easy maintenance and repair.

An HP-9845 minicomputer will soon be interfaced with UT electronics to accomplish the following:

- a. Improve the sample rate or data for a UT measurement. This will improve the mean-temperature measurement due to the statistical nature of the UT data.
- b. Provide system monitoring. The minicomputer would provide constant monitoring of the UT signals and would reveal a loss of data immediately.
- c. Provide data reduction of UT signals on-line and off-line. Internal graphics would provide easy analysis of data.

The minicomputer improves the accuracy and reliability of the UTs, making them attractive to the experimenter.

3.3.6 Future Activities

Posttest microscopic analysis of the high-temperature furnace experiments will be conducted. Various experiment concepts for measuring an effective thermal conductivity of UO_2 -packed beds at high temperatures will be evaluated. Work will continue in developing and adapting an ultrasonic-thermometry system for use in debris-bed experiments.

3.4 Containment Analysis (P.S. Pickard, 4424; J. Odom, 4424)

3.4.1 CONTAIN Code Development

The development of the advanced reactor-containment code (CONTAIN) continued during this period. The major effort has been devoted to either evaluation or development of specific models for subsequent incorporation into CONTAIN. Development of some models has progressed to the stage where integration of selected models into the overall code structure is ready to begin.

CONTAIN development has proceeded in three basic submodules:

- a. The control module, which controls logic flow, cell interaction, and system balances.
- b. The compartment atmosphere module, CAM, which involves Na-burning aerosol behavior, gas flow, and heat transfer.
- c. SINTER, which includes Na and debris-pool models, material interactions (Na, melt-concrete, etc.), fission-product distribution, and heat transfer.

A schematic block diagram of the basic functions of CONTAIN is shown in Figure 3.4-1; legends for the figure appear on the facing page. CONTAIN will be based on a reference cell concept. Logic (and fast-core memory) is provided for only one cell or compartment. Each cell is

computed sequentially by the same set of models. Cell data are stored at the end of each time step, providing a restart for the next time step. When all cells have been updated, mass and energy flow among interacting cells is computed. Interaction quantities are then retained as sources/sinks for each cell on the next time step. In this manner a significant reduction in core-memory requirements can be achieved since only limited data from all cells are required at any one time. Considerably more detailed phenomenological models may then be considered for future incorporation into CONTAIN.

3.4.2 Cavity Debris-Pool Model - SINTER

A preliminary version of the cavity debris-pool model has been compiled. This version of SINTER models a one-dimensional sodium pool in an arbitrary structural configuration. The sodium pool may contain a fuel/steel-debris bed. Further, sodium may be allowed to boil or leak from the pool with time. Preliminary models for water release from concrete and the sodium/concrete reaction are included and are currently being upgraded. Fission-product distribution routines are included in the preliminary version with initial fission products obtained from input. Initial efforts to interface SINTER with the overall code structure have begun in order to define data storage and transfer requirements.

3.4.3 Compartment Atmosphere Module (CAM)

The compartment atmosphere module basically performs mass and energy balances for the cell atmospheres and includes heat-transfer, sodium-burning, and aerosol-behavior models. The current version operates as a single-cell atmosphere with only a simple debris-pool model incorporated to help define data-transfer requirements. Heat transfer from atmosphere to surrounding walls or structure is accomplished sequentially. An aerosol-behavior module is being developed for CONTAIN, incorporating both a HAARM-3 log-normal particle-size distribution and a more general option that allows a general description of the particle-size distribution.

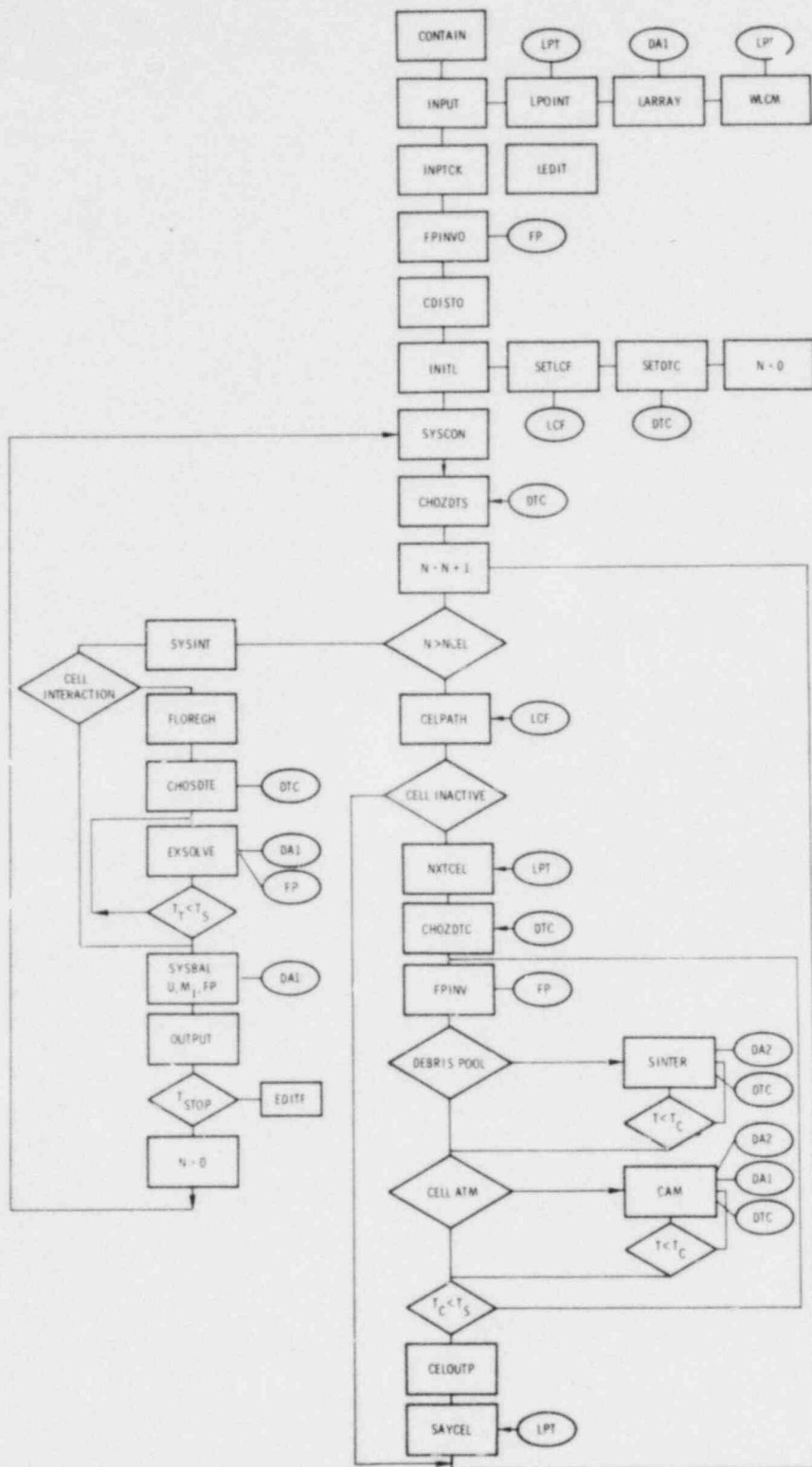


Figure 3.4-1 Schematic Logic Flow for CONTAIN

NOTES FOR FIGURE 3.4-1

Time Definitions

T_S = System time

T_C = Cell time T_E = Cell interaction time

Control Data Blocks

LCF = Control flag data

LPT = Data storage pointer

DTC = Time-step control data

Datlocks

DA1 = System interaction data

DA2 = Cell data

FP = Fission-product data

Routine Functions

FPINVO - Initial fission product inventory

FPINV - Fission product inventory for cell

CHOZDT(X) - Choose time step

S = Sys

C = Cell

E = Cell interaction

NXTCEL - Bring in cell data from storage

SAVCEL - Store cell data

FLOREGM - Determine gas flow regime for cell exchange

EXSOLVE - Solve mass, energy, and momentum balances for cell exchange

SYSBAL - System balances

SINTER - Cavity debris-pool model

CAM - Cell atmosphere model

3.4.4 Cell-Interaction Module

The atmospheres of cell volumes interact based on pressure and energy gradients between cells. In each cell the state variables must be determined, while mass and energy exchanges between cells are accounted for. The method of solution generally employed is to treat the cell-state variables quasi-statically, using "frozen" flow conditions as boundary sources. The flow conditions are then recomputed based on stagnant cell properties.

For reactor-containment analysis, the transients occur over relatively long times, requiring a transient solution that is stable for very long time steps. Semi-implicit techniques, which solve simultaneously for cell and flow parameters, are being examined in an attempt to attain high stability for long time steps. The set of equations describing mass energy, and momentum balances for interacting-cell volumes is now being programmed for computer solution. Techniques will be examined to establish an optional approach for stability with long time steps. System balance routines for mass and energy will be included in the cell-interaction module.

3.5 Fragmentation (T. . Chu, 1537)

3.5.1 Overall Program Progress

The test apparatus for the forward (melt into sodium) experiments was modified to accommodate dual ranges of transducers. Two experiments were performed. The test apparatus for the reverse (sodium into melt) experiments is being assembled in preparation for the first such experiment. For the combined interaction (sodium and melt into concrete crucible) experiments, the test apparatus was fabricated and three crucibles were cast.

3.5.2 Results of Forward Experiments

The planned forward series was concluded during this reporting period with the performance of two additional fragmentation experiments.

Each experiment used 20 kg of corium-producing metallothermic mixture and 23 kg sodium; one of the experiments used a sodium temperature of 523 K (250°C) and the other, a sodium temperature of 963 K (690°C). The test conditions for all the experiments are summarized Table 3-10. While data are still being analyzed, sufficient information is available to arrive at some general conclusions.

Table 3-10

Test Conditions for FRAG Experiments

	<u>FRAG 1</u>	<u>FRAG 2</u>	<u>FRAG 4</u>	<u>FRAG 5</u>	<u>FRAG 6</u>
Stream Size (mm)	13	51	51	51	51
Melt	Fe	Fe	UO ₂ -ZrO ₂ (70%)	UO ₂ -ZrO ₂ (70%)	UO ₂ -ZrO ₂ (70%)
	Al ₂ O ₃ (44%)	Al ₂ O ₃ (44%)	Stainless steel	Stainless steel	Stainless steel
Melt Mass (kg)	12	13	20	20	
Sodium Mass (kg)	23				23
Sodium Temperature (°C)	520	480	420	250	690
Max Observed Pressure Bar	2	20	---	4	3
Mechanical Damage	No	Yes	No	No	No

No test exhibited a single coherent energetic event; rather, the interactions were all characterized by a series of pressure events occurring throughout the time period corresponding to the draining of the melt crucible. For all of the experiments performed, the corium melt (approximately 70% O, 30% stainless steel) consistently resulted in milder interactions than the steel melts (approximately 44% Al₂O₃, 56% Fe).

POOR ORIGINAL

In the first four fragmentation experiments (FRAG 1, 2, 4, and 5), the MgO inner-reaction vessel was always cracked but no damage from melt attack was indicated. In FRAG 6, however, the crucible bottom showed evidence of melt attack. Relative to a crucible diameter of 34 cm and a melt stream diameter of 5 cm, a region of the crucible bottom with a diameter of approximately 18 cm showed a depth of attack up to 2 cm. Since the surface of the region attacked by the melt appears to be pitted rather than smooth, the attack is apparently at least partly caused by thermal stress. However, further analysis of the fragments is expected to provide more information concerning the method of the melt attack. Figure 3.5-1 compares the appearance of the attacked crucible and a new crucible. Apparently the higher sodium temperature (963 K) resulted in a more stable boiling around the melt, allowing it to maintain a more coherent mass upon reaching the bottom of the vessel. This behavior is also consistent with the fact that FRAG 6 was the only experiment of the present series in which fragments of several centimeters were found (Figure 3.5-2).

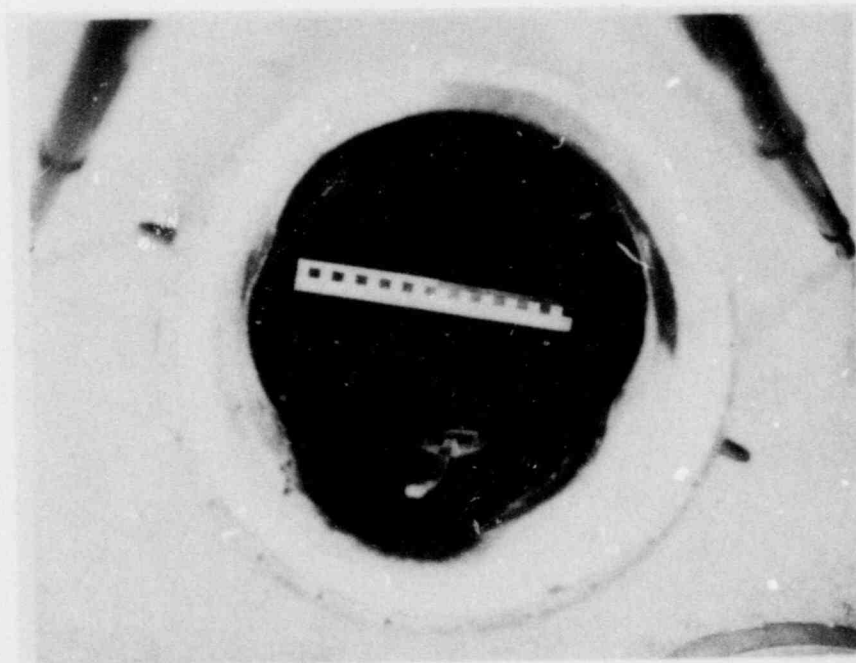


Figure 3.5-1 Comparison of a Melt-Attacked Crucible and a New Crucible (the new crucible is at right)

POOR ORIGINAL

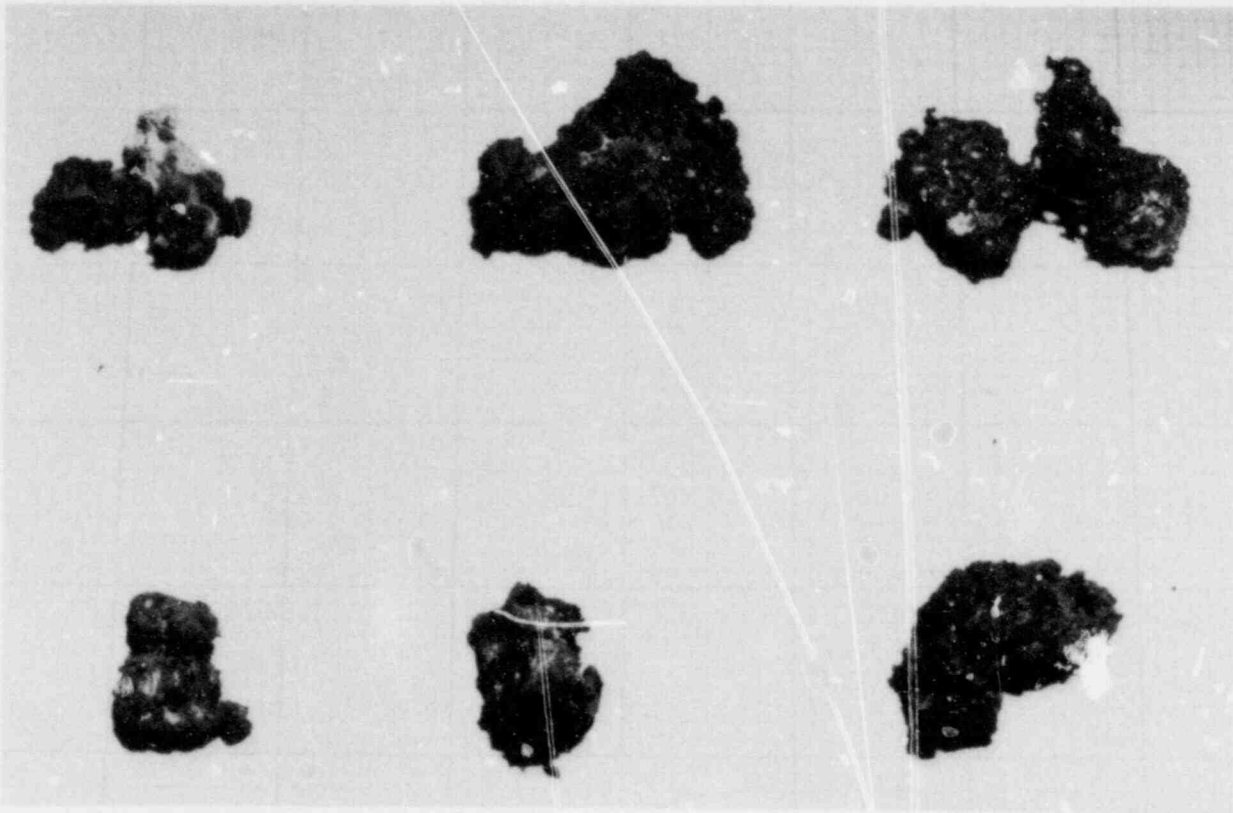


Figure 3.5-2 Large Fragments From Test FRAG 6

A procedure was established for measuring the apparent density of fragments; the density of the fragments from FRAG 4 was found to be 4.93 g/cm^3 , less than both the stainless steel and the oxides. This low value of apparent density is caused by the large number of fragments with internal voids, and is especially true for larger fragments. Figure 3.5-3 shows examples of internal voids. There is an ongoing effort to determine whether there is substantial differences in the apparent density of larger and smaller fragments. Previous measurements show that for the bottom part of the bed in FRAG 4, the weight fraction of the fragment is 0.8 using a fragment density of 4.93 g/cm^3 . The void fraction of the bed is calculated to be 0.57 or 56% of the bed volume is occupied by sodium.

The debris from FRAG 2 and FRAG 4 have been analyzed for particle sizes larger than $45 \mu\text{m}$. Figure 3.5-4 shows that size distributions for both FRAG 2 and FRAG 4 are approximately log-normal. Since the melts for

POOR ORIGINAL

the two tests are different, no direct comparison can be made, but FRAG 4 distribution does show good agreement with the data of the ANL M-Series tests.³⁻²⁰ The median-size particle is 320 μm .

In the future, data and fragment analysis will continue. The reverse experiments are expected to start next quarter.



Figure 3.5-3 Fragments From FRAG 4 Showing Internal Voids
25X BEI

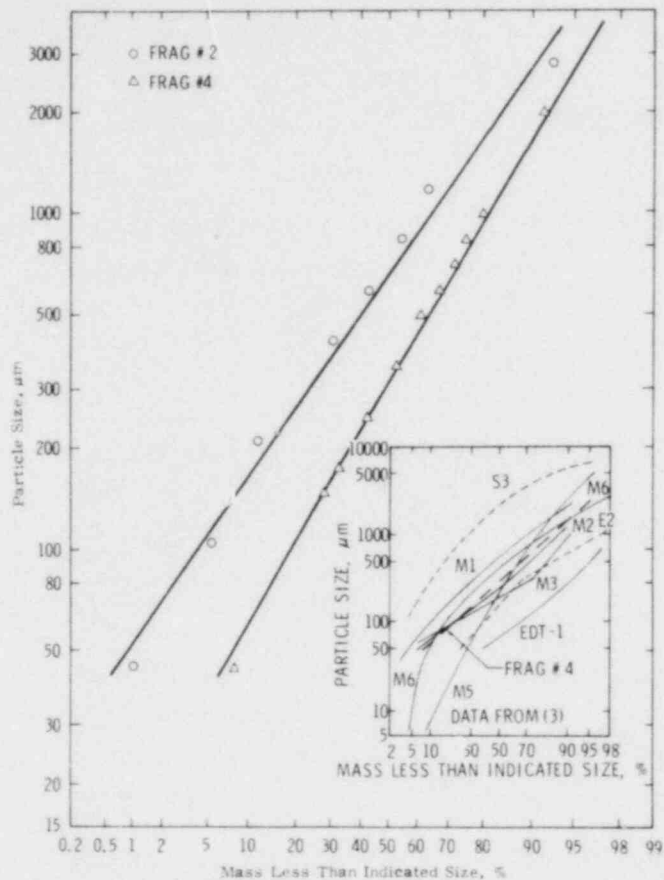


Figure 3.5-4 Fragment Size Distribution

3.6 Sodium Containment and Structural Integrity (R.U. Acton, 1537; J.V. Beck, 1537; R.L. Coats, 4422; N.R. Keltner, 1537; L. A. Kent, 1537; R.L. Knight, 4424; R.A. Sallach, 5846; J.E. Smaardyk, 5534; D.L. Wesenberg, 4431; C.M. Stone, 5521)

3.6.1 Introduction

Work on this program progressed in all areas during this reporting period. Two large-scale sodium-concrete interaction tests, 13 and 14, were conducted. However, only Test 13 is included in this report since Test 14 was run late in the reporting period. Both chemical and physical separate-effects experiments were accomplished. The physical tests explored the effect of initial sodium temperature on the sodium-concrete interaction. The chemical tests explored the addition of water to molten sodium. In the area of structural integrity, radiant-heat-flux tests were conducted on square steel plates. Finally, in computer simulation, a

simple heat-conduction model was found inadequate for describing the temperature history in concrete subject to sodium attack.

3.6.2 Large-Scale Test 13: Sodium-Basalt Concrete

In the two previous tests on basalt concrete, the geometry of the test article had been questioned as to its effect on concrete constraint (cracking) and upon the sodium-water reaction. Test 13 was designed to provide for as nearly a one-dimensional test as was possible with the existing concrete crucible. Figure 3.6-1 shows the test design that was developed. A steel insert was placed into the cylindrical cavity of the basalt-concrete crucible. The outside diameter of the liner was such that a 2.5-cm annulus existed between the liner and the cavity sidewall. This annulus was filled with MgO powder, which is inert to sodium and acts as thermal insulation and a physical barrier. In this way, the effects on the sidewalls of the concrete cavity were limited in the experiment. The bottom of the concrete cavity had a layer of insulating firebrick mortared in place; a layer of dense firebrick was mortared over the insulating firebrick. The firebricks are described in Table 3-11 and are reported to be the same as were used in the Fast Flux Test Facility. The dense firebricks were 7.6 cm thick and the insulating bricks were 6.4 cm. A bottom plate was tack-welded onto the insert just above the dense firebricks. This bottom plate contained a 15.2- by 0.6-cm slot to allow the molten sodium to contact the firebrick and react in a restricted geometry.

Two hundred thirty-nine kg of sodium at 973 K were dumped into the lined-crucible cavity. The mass of the steel insert cooled the sodium to about 698 K in 20 min. Immersion heaters returned to sodium-pool temperature to a set point of 873 K in 145 min. The sodium reacted with both layers of firebrick and the concrete crucible bottom. Embedded thermocouples monitored the progress of the reaction front through these materials (see Figure 3.6-2). For example, the thermocouples between the two layers of firebrick (labeled "Middle" in Figure 3.6-2) indicated 523 K at 90 min into the test and 1198 K at 132 min. The thermocouples between the insulating firebrick and the crucible-cavity bottom (labeled "Bottom" in

Figure 3.6-2) peaked at 1423 K at 170 min into the test. The immersion heater failed at 12 h, ending the test.

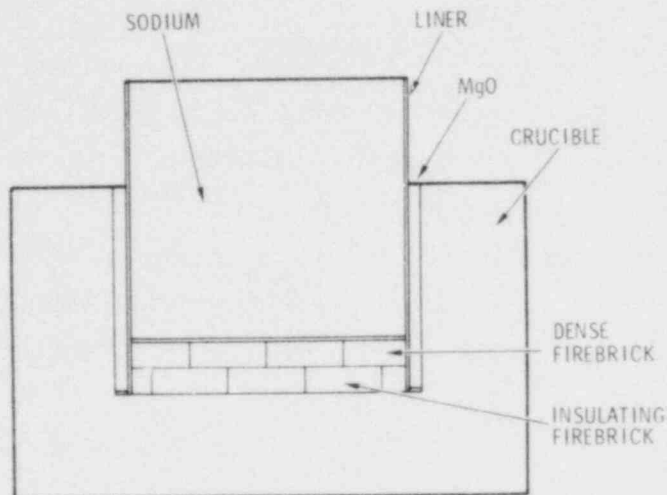


Figure 3.6-1 Test 13 Crucible

Table 3-11

Description of Firebrick

<u>Firebrick Material</u>	<u>Analysis of Firebrick (% Firebrick Material)</u>	
	<u>Insulating M-20</u>	<u>Dense Morex</u>
SiO ₂	57-60	56
Al ₂ O ₃	33-36	38
Fe ₂ O ₃	1-2	2
CaO	0.1-1.6	0.6
MgO	0.1-0.6	0.6
TiO ₂	1.5-2.5	1
Alkalies	1-2	1.6
<u>Bulk Density of Firebrick Mat'l</u>	<u>kg/m³</u>	
	600-700	2130-2190

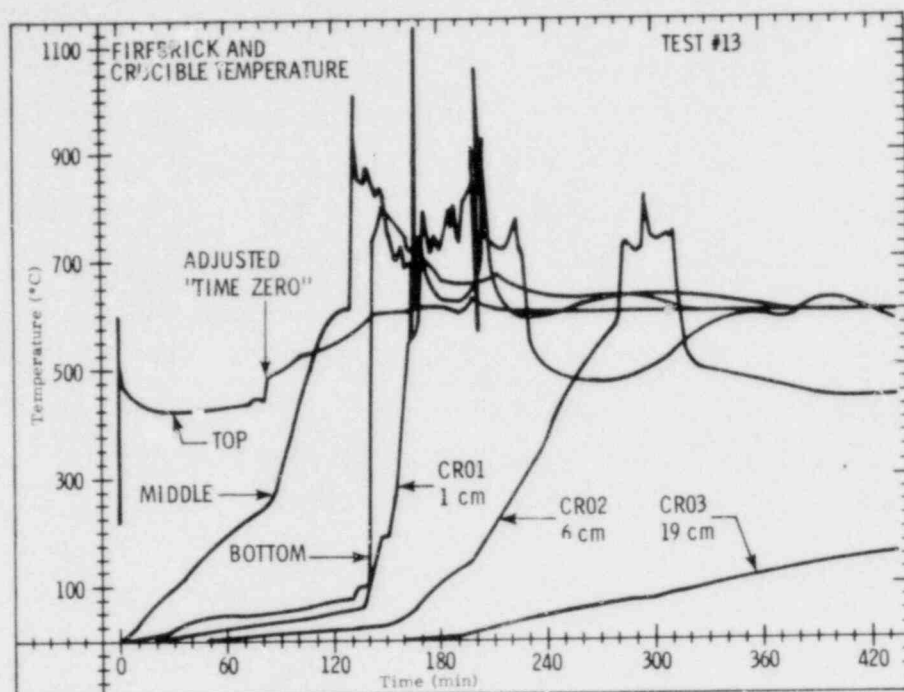


Figure 3.6-2 Progress of the Reaction Front Through Firebrick and Concrete

3.6.2.1 Test 13 - Results

Posttest examination revealed that the MgO powder was effective in isolating the sodium from the crucible-cavity sidewalls. The steel-insert bottom plate, which had been tack welded at four points around its circumference, had broken free and was pushed ~48 cm up into the insert by the reaction products. Five cm of reaction products were on top of the bottom plate of the insert (and 48 cm of reaction products were below the plate). All of the sodium had been consumed. Both layers of the firebrick had been consumed. The bottom of the concrete crucible had reacted to a depth of 25 cm, leaving a black, porous, cinder-like reaction product. The remaining 13 cm of concrete in the crucible bottom, although retaining the appearance of concrete, had little strength; it could be picked apart with a screw driver. In one area of the crucible bottom, reaction products were found on the floor of the test chamber under the crucible, indicating total penetration of the 38 cm of concrete. The last part of this total penetration was along a crack.

The thermocouple traces shown in Figure 3.6-2 allow an estimated rate of the reaction-front movement into the firebrick and concrete. An adjusted time-zero was established as the time of the first excursion of the thermocouple on top of the dense firebrick (between the firebrick and the insert bottom plate). This zero time is defined as that time when sodium-hydroxide saturation has taken place and NaOH begins to attack the firebrick. An explanation of the chemistry involved is in Section 3.6.2.2. The time lapse between the adjusted time-zero and the near-vertical trace on the "middle" thermocouple gives a measure of the time necessary for the reaction front to traverse the dense firebrick (7.6 cm thick). Figure 3.6-3 shows the reaction front-penetration rate developed from the above procedure.

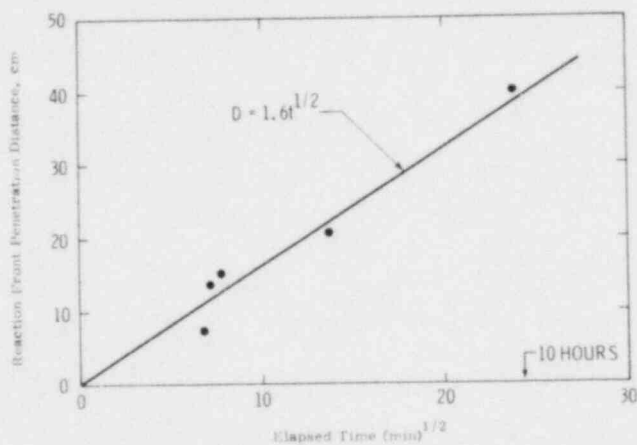


Figure 3.6-3 Penetration of the Sodium-Reaction Front into the Firebrick and Concrete of Test 13

The pressure built up by the reaction products was enormous, cracking the crucible horizontally at approximately the floor of the cavity and opening these cracks as wide as 15 cm. The half-inch reinforcing bars around the outer circumference of the crucible were broken. The concrete-crucible coupons tested on the day of the test gave a compression strength of 28.5 MPa (4139 lb/in²). All four chains that sealed the steel tophat to the crucible were broken. The sodium dump tank that sits on top of the test chamber was lifted 10 cm.

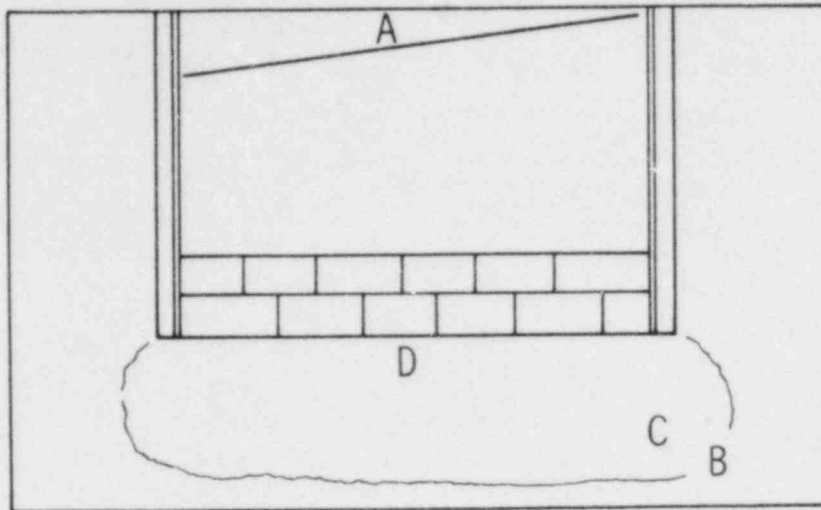
Four samples of reaction products from Test 13 were analyzed; they are described in Figure 3.6-4. X-ray diffraction patterns were made on ground-up samples of these products. Extractions were made with water; the water-soluble and the water-insoluble fractions were analyzed using standard techniques. The results of the analyses are shown in Table 3-12.

Table 3-12

Analysis of Reaction Products - Test 13

	SAMPLE			
	A	B	C	D
<u>% Water Soluble</u>	<u>58</u>	<u>76</u>	<u>47</u>	<u>44</u>
NaH	21	0	3	2
NaAlO ₂ *	3	4	3	3
Na ₂ SiO ₃	8	23	21	21
NaOH	19	40	--	--
Na ₂	--	--	20	21
Undetermined	7	9	0	(3)
<u>% Water Insoluble</u>	<u>42</u>	<u>24</u>	<u>53</u>	<u>56</u>
Al ₂ O ₃	12	2	5	6
SiO ₂	17	8	24	25
Fe ₂ O ₃	1	4	6	5
CaO	1	4	8	9
Na ₂ O	6	1	6	7
Undetermined	5	5	4	4

*Identified by x-ray diffraction



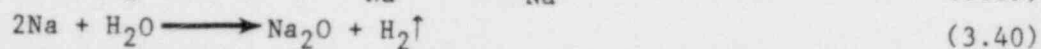
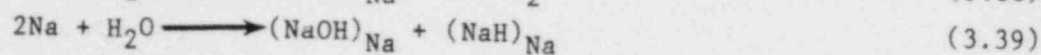
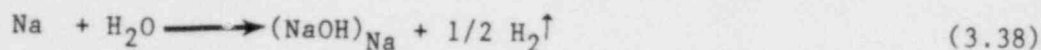
- Sample A: Slag-Like Matter Taken From Top of Flawed-Plate
- Sample B: Yellowish Matter (Attacking Phase) From Bottom Part of Crucible
- Sample C: Black Matter Immediately Above Sample B
- Sample D: Reacted Concrete Taken Just Below What Had Been Brick-Concrete Interface

Figure 3.6-4 Description of Test 13 Reaction Products Samples

3.6.2.2 Chemistry: Sodium-Basalt Concrete

A chemical reaction model has been postulated for the sodium/basalt concrete interaction. The model is derived mostly from observations of the reactions in the sodium/basalt concrete experiments. Three tests with basalt-concrete crucibles (two with firebrick included) have been performed. The model is consistent with the results.

3.6.2.2.1 Initial Reaction -- The initial contact of hot molten-sodium metal with concrete produces a thermal gradient in the concrete. The effect of this gradient is the thermal desorption of water from the concrete and the movement of this water, in part, to the sodium/concrete interface. There is then a reaction between the molten sodium and water. The reaction products vary, depending on temperature and whether the evolved gas escapes or builds up;



Equation (3.38) is probably the most favored reaction in terms of kinetics. It occurs in those cases where $T > 683 \text{ K}$ and the evolved gas is vented. Experimentally, it occurs when there is a sodium pool on a bare concrete surface. The evolved gas forms bubbles that rise through the sodium pool and aid in homogenizing the pool composition. Sodium hydroxide is not formed immediately as a separate phase since there is an appreciable solubility of NaOH in Na at temperatures above 673 K (a solubility which increases with increasing temperature).

Equation (3.39) is expected for $T > 683 \text{ K}$ when the evolution of H_2 gas is restricted. A local overpressure of H_2 gas develops and forces the formation of NaH. The degree of solubility of NaH is not known for these temperatures and saturation with respect to NaH may occur rapidly.

Equation (3.40) is expected for $T > 973 \text{ K}$. The coexistence of NaOH and Na requires only a moderate overpressure of H_2 ($\leq 1 \text{ atm.}$) for $T < 973 \text{ K}$. Above 973 K , H_2 pressures in excess of 1 atm are required. Thus in experiments where $T < 973 \text{ K}$ and gas evolution is not restricted, the formation of solid Na_2O is expected.

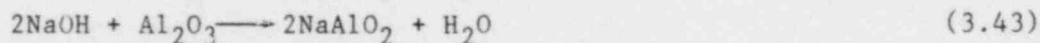
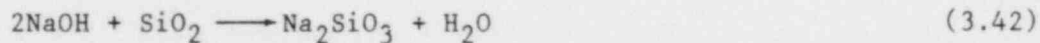
Equation (3.41) is expected when $T < 683 \text{ K}$ and describes the equilibrium products. It probably is not as favored kinetically as Eq (3.38) and thus may not be observed in dynamic situations.

The solubility of NaOH in Na can produce a time delay before the onset of further reactions. If the sodium pool is well-stirred, then the entire pool must be saturated with respect to NaOH before a separate NaOH phase can form. Estimates of the solubility limit are 10-20 mole-percent for temperatures of 673 to 773 K . Therefore, an appreciable amount of the total sodium must react before NaOH separation occurs. In

deep pools, hours may be needed. However, in situations where the sodium pool is quiescent or where movement is more restricted (such as in the penetration of the sodium behind a liner or within a debris bed), then saturation can occur quickly since only local quantities of sodium need be saturated.

3.6.2.2.2 Reactions of NaOH -- The formation of an NaOH phase permits a detrimental attack on the concrete. This attack is detrimental because NaOH is liquid and capable of dissolving within itself the reaction products formed from the concrete/NaOH reaction.

The appropriate equations are:



(Other sodium silicates are possible. However, only the metasilicate (Na_2SiO_3) has been identified in the reaction products.)

Some heat is liberated by these reactions, but even more is produced by the further reaction of the water from Eqs (3.42) and (3.43) with sodium metal (or equivalent chemical species). Inasmuch as the water is produced locally and the diffusion distance to the sodium is small, a hot spot or reaction zone can be produced. Such a zone is indicated by the thermocouple data and exhibits temperatures greater than the sodium-pool temperature. This reaction zone is observed to move into the concrete; it is particularly evident in Test 13.

3.6.3 Physical Separate-Effects Tests

The current effort in this area is to examine the effect of sodium-pool temperature on the sodium/limestone-concrete interaction. Thus far tests have involved the interaction of 4.5-kg charges of sodium introduced onto 0.09 m^2 limestone-concrete surfaces at sodium temperatures of 873, 923, 973 and 1023 K. At the 873-K temperature, the attack on the concrete was barely discernable. The attack was more pronounced as the temperature

increased; however, even at 1023 K the effect was minor and had the appearance of freeze-thaw damage to a concrete surface.

3.6.4 Chemical Separate-Effects Tests

A series of experiments was carried out in which various quantities of water were added to a molten-sodium pool. The reaction process was followed by monitoring the resultant hydrogen-pressure.

In these experiments water was added to the vapor space above the sodium pool. Hydrogen-pressure rose rapidly but not unreasonably, leading to the conclusion that the reaction was limited by the diffusion of water vapor to the sodium surface. The hydrogen pressure rose to a maximum value in 10 to 20 min, then declined over a period of hours to an equilibrium value.

Attempts were made to determine these equilibrium pressures as a function of composition and temperature. They did not vary greatly with composition, implying that the composition lay in two-phase or three-phase regions of the phase diagram. Determination of solubility limits from these data has not been possible.

By gradually heating the sodium pool, the relationship between hydrogen-pressure and temperature could be estimated. No reasonable data could be obtained during cooling. The reaction of hydrogen with the sodium pool was slow, although the desorption process apparently proceeds quickly when the pool is heated.

From the pressure/temperature relationship, a heat of reaction could be calculated and is equivalent to the heat of decomposition of sodium hydride. At any given temperature the observed hydrogen pressure is 80 to 85% of that expected from the decomposition of sodium hydride.

3.6.5 Structural Integrity

The first series of flat-plate radiant-heat-flux experiments has been completed. These tests subjected a 381- x 381-mm (15- x 15-in.) carbon-steel plate (9.75 mm thick) to a centrally distributed heat flux. The applied heat flux varied from 10 W/cm² to 150 W/cm² with most of the interest focused at the higher values. The experiments are designed to simulate the structural response of a steel, concrete-cell liner to a localized spill of molten sodium. The time-duration of interest is on the order of 30 s. These experiments serve to provide data for benchmarking analytical techniques and to provide a mechanism to evaluate the use of strain gages in a high-temperature environment. Of primary importance are the data taken at discrete points on the plates. These data will be compared with analytical results. Measurements such as temperature, displacement, and strains were made and comparison of these measured quantities with analytical results will serve to qualify the analytical procedures used in the analysis of cell liners. Some preliminary calculations were made before these experiments were performed in order to quantify the values of temperature, displacement, and strain that would occur during the test. This early model assumed one-dimensional heat transfer through the plate with temperature-dependent material properties. Agreement of centerline plate temperatures was excellent between the analysis and experiment for all of the flux levels. The early structural model used a bilinear stress-strain curve with a temperature-dependent Young's modulus and yield stress; Figure 3.6-5 shows these early results. The experimental data clearly show a more complex response pattern (see Figure 3.6-6). The model must be upgraded in two areas. First, the temperature distribution should reflect some spatial variation. Accordingly, a two-dimensional model was developed that modeled the spatial temperature distribution. The second area that required change was the structural-material mode. Apparently carbon steel has a widely varying work-hardening slope³⁻²¹ over the temperature range of interest. The material model was updated by the addition of a temperature-dependent work-hardening slope. Results incorporating these changes are shown in Figure 3.6-7; the agreement is qualitatively better than before. The displacement pattern is due to a complex interaction between the

temperature-dependent material properties and the thermal loading; computed and measured strains are shown in Figure 3.6-8. These strain measurements were the first ones to undergo the heating-rate compensation, and it is expected that further refinements in the procedure will be made in the future.

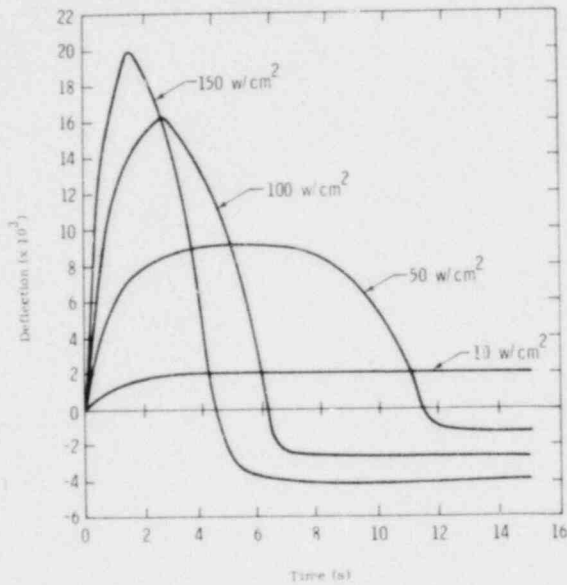


Figure 3.6-5 Pretest Estimates of Plate Centerline Deflection

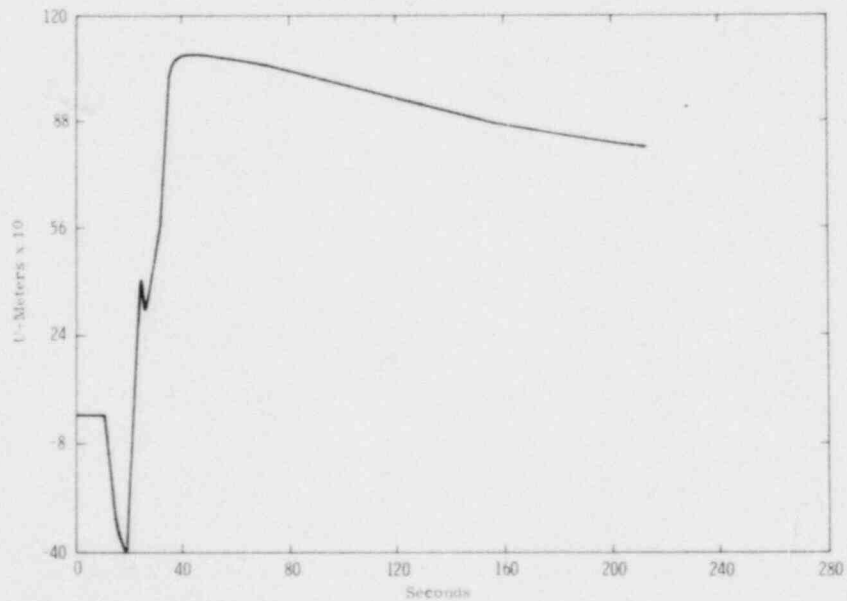


Figure 3.6-6 Experimental Centerline Deflection Data - 100 W/cm²

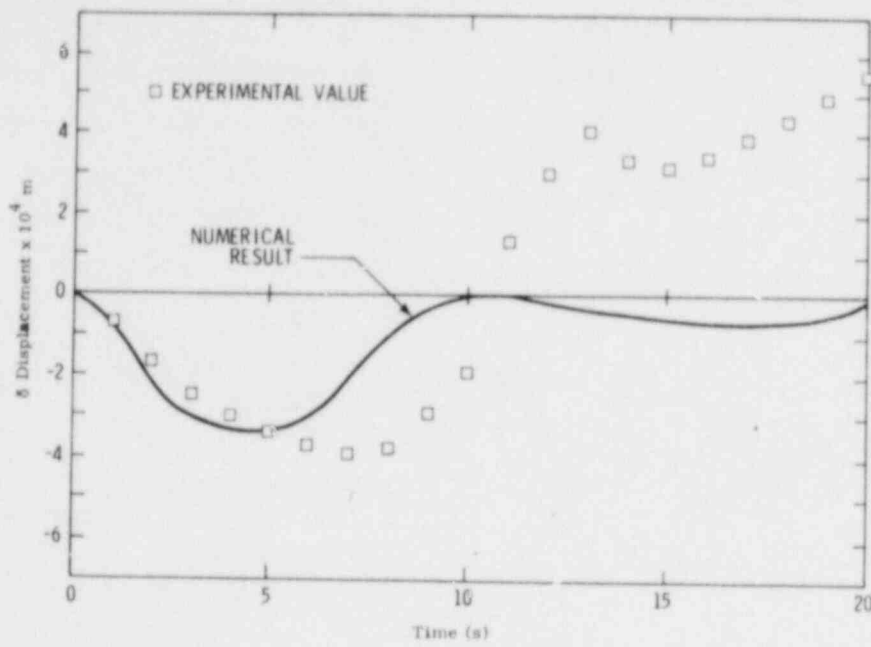


Figure 3.6-7 Comparison of Analytical and Experimental Plate Centerline Deflection - 100 W/cm^2

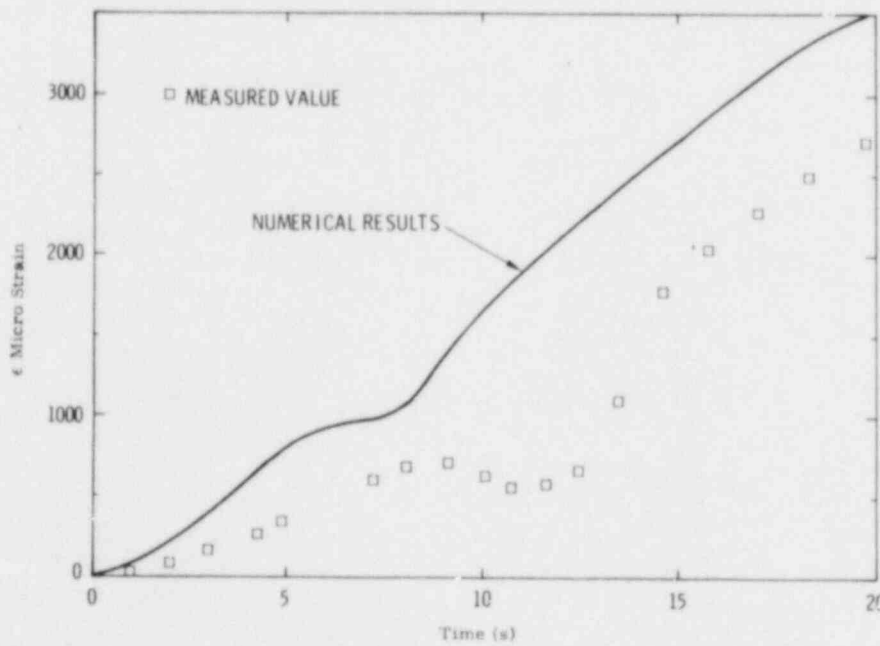


Figure 3.6-8 Comparison of Analytic and Measured Strain Near Plate Centerline - 100 W/cm^2

Work is underway on a new model for the structural calculations. It is hoped that this new model will provide better quantitative results. It is also expected that the second series of experiments will begin shortly to provide additional data for analytical comparison.

3.6.6 Computer Simulation

Transient-temperature data from large-scale Tests 4, 8, and 9 were used to find some pseudothermal properties of concrete. Concrete under high-thermal-flux conditions has heat and mass transfer occurring inside it. A satisfactory model would include mass transfer by the moving of vapor and liquid. At the time of this investigation, estimations of the properties for a simple transient heat-conduction model were undertaken because

- The variability of resulting properties was of interest
- The "best" average values were desired
- An indication of the adequacy of this simple model was needed
- A more adequate model was not programmed and available for use.

The properties estimated were thermal conductivity and the density-specific heat product. In general, these properties could not be found independently because the net heat flux was not known. Both thermal conductivity and density-specific heat were found as functions of temperature. Program PROPTY was used to estimate the properties. The analyses clearly indicated that the simple heat-conduction model is not adequate since the pseudo properties were rather variable.

3.7 Aerosol Source Normalization (R.M. Elrick, 4422)

During an energetic hypothetical core-disruptive accident, fuel vapor may be produced which subsequently condenses to form small very particulated debris (molten or solid) that can be transported to the upper vessel regions and through breaks that may have occurred in the vessel. The

possibility of transporting this material depends strongly on its initial character.

Aerosol produced from in-pile (ACRR) experiments is being characterized to determine the physical properties of fuel particles that result from the vaporization and melt breakup of fuel pins subjected to simulated overpower excursions. The characteristics of these particles will be compared with those produced by out-of-pile experiments at ORNL which are part of the NRC-sponsored Aerosol Release and Transport (ART) program. Subsequent in-pile studies will examine the interaction of particles with the supporting structure and with sodium.

During this period, preparation continued on the second series of in-pile aerosol sampling experiments at Sandia as well as on the first series of out-of-pile experiments at ORNL. Both series began in March.

3.7.1 Out-of-Pile Comparison Tests at ORNL

The out-of-pile comparison tests at ORNL were designed to characterize debris produced by resistively heating the fuel to vapor. In addition to sampling this fuel debris, fuel-temperature profiles will also be measured. These characteristics and temperature profiles will then be reproduced in fuel neutronically heated in the ACRR. Finally, fuel debris from these similar experiments will be compared. Techniques for sampling debris and photometrically measuring fuel radiance and temperature were verified in the first series of in-pile experiments.

In November, Sandia staff personnel visited ORNL to discuss specific design features of the out-of-pile experiments. These talks resulted in Sandia's agreement to prepare six sampling wheels and associated hardware (motor, motor mount, power supply and speed transducers). Also, Sandia would prepare instructions for positioning the wheels and would be responsible for the sampling. During the following months, the prepared items were sent to ORNL. All sampling wheels were certified at maximum speed of 24 000 rpm (2.5 ms/revolution). More of the vapor-like fuel debris reaches the sampling wheel as the mean free path of gas in the

chamber increases. ORNL demonstrated that the discharge of energy stored in capacitors is not affected when chamber pressure is reduced to about 100 μ m. This pressure is similar to the pressure used in the in-pile experiments.

Parties to the discussions at ORNL decided to measure fuel-temperature and radial-temperature profiles with the photometric techniques used at Sandia, provided a clear side view of the fuel could be obtained. Sandia will perform these measurements. Originally the stack of fuel pellets, compressed between heating electrodes, was enclosed in a quartz tube. The radial space between the pellets and the tube was filled with UO_2 microspheres ~ 0.038 cm in diameter. Two designs will be tried to give a photographic view of the fuel without adversely affecting energy discharge through the fuel or heat loss from the fuel. ORNL designed a quartz ring inside the tube; this ring displaced microspheres in a section between the fuel and the tube. Sandia designed a small alumina viewing port to displace the microspheres along the length of a fuel pellet and about 1/8 the circumference of the pellet. Viewing ports were fabricated and sent to ORNL for testing.

A series of five sampling experiments was conducted at ORNL during March. The fuel was resistively heating to vapor in three steps: a low preheat for several minutes to about 1800 K; a high preheat for about 30 s to about 300 K; and a capacitance discharge for several milliseconds. For this particular series; the last step deposited 18 to 28 kJ, until the quartz-retaining tube ruptured from internal pressure. Two Hycam cameras covered the event. One camera showed a closeup of an exposed fuel pellet with a radial hold drilled to the centerline of the pellet for observing centerline temperature. The other camera viewed the full length of the quartz tube. Both cameras ran at about 10 000 frames/s. Photographic conditions were set to record temperatures toward the end of the high preheat and during the capacitance discharge. The film is being processed for analysis. Debris from all five tests was sampled for wheel speeds of from ~ 4 to 2.5 ms/revolution and for wheel-cover aperture widths of from 0.0635 to 0.198 cm (similar to in-pile conditions). Quartz rings were

used to view fuel in three of the tests; an alumina viewing port was used in one test. In the fifth test, the original microsphere geometry was used.

3.7.2 In-Pile Sampling Experiments - Series II

In these experiments, the fission temperature of the fuel will be matched in space and time to temperature profiles measured in resistively-heated fuel at ORNL.

All fabricated and ordered parts have been received for the experimental canister, the optical train for photography and photometrics, and the in-pile vacuum system.

Changes in the design of the upper end of the optical train were completed as was the fitting of optical hardware to the ACRR. A new design was necessitated by structural changes in the offset-loading tube of the ACRR. This new design also allowed a greater depth of field for photography. This photographic system will be used to help validate the ACRR fuel-motion system, and will also be used in Fuel Dynamics and Aerosol Source experiments. For simultaneously viewing the side and end of the fuel in the ACRR aerosol experiments, a mirror system was designed and fabricated that equalizes the lengths of these two viewing paths.

The new drive mechanism for the sampling wheels, necessitated by sampling debris from a vertical fuel pin, was exercised successfully. This test confirmed that the motor would torque the additional inertia designed into the system, and that the O-ring would provide the driving friction.

During the next quarter, remaining tests for the ORNL series will be completed. These tests include measuring fuel-temperature profiles during the preheat stages and using a framing spectrograph to examine radiation emitted by the fuel during heating. All photographic film will be analyzed for fuel radiance and temperature; analysis of sampled fuel debris will begin for a selected run. A study will begin to establish

in-pile conditions that will reproduce temperature histories measured at ORNL. Development of hardware for the Series-II in-pile experiments will continue.

References for Section 3

- 3-1 D.A. Powers, Sustained Molten Steel/Concrete Interactions Test, SAND77-1423 (Albuquerque, NM: Sandia Laboratories, 1978).
- 3-2 T.Z. Harmathy, J. Materials, 5, 47, 1970.
- 3-3 T.Z. Harmathy, ACI Journal, p 132, February 1970.
- 3-4 Advanced Reactor Safety Research Quarterly Report, July-September 1978, SAND78-2002, NUREG/CR-0470 (Albuquerque, NM: Sandia Laboratories, 1979).
- 3-5 Light Water Reactor Safety Research Program Quarterly Report, April-June 1978, SAND78-1901, NUREG/CR-0422 (Albuquerque, NM: Sandia Laboratories, 1979).
- 3-6 D.A. Powers et al, Exploratory Study of Molten-Core Material/Concrete Interactions, SAND77-2042 (Albuquerque, NM: Sandia Laboratories, 1978).
- 3-7 Fast Reactor Safety Research Program Quarterly, October-December 1976, SAND77-0145, NUREG-0181-1 (Albuquerque, NM: Sandia Laboratories, 1977).
- 3-8 H.C. Hardee and R.H. Nilson, Nucl. Sci. and Eng., 63, 119-132, 1977.
- 3-9 J.B. Rivard, Post-Accident Heat Removal: Debris Bed Experiments D-2 and D-3, SAND78-1238, NUREG/CR-0421 (Albuquerque, NM: Sandia Laboratories, 1978).
- 3-10 G.B. Wallace, One-Dimensional Two-Phase Flow, p 64, (New York, NY: McGraw-Hill, 1969).
- 3-11 J.D. Gabor, E.S. Sowa, L. Baker, Jr., and J.C. Cassulo, ANS Fast Reactor Safety Meeting, Beverly Hills, CA, 1974, pp 823-844.
- 3-12 R.B. Bird, W.E. Stewart and E.N.L. Lightfoot, Transport Phenomena, (New York, NY: John Wiley and Sons, 1960) p 187.
- 3-13 V.K. Dhir, I. Catten, and W.E. Kastenberg, Study of Dryout Heat Fluxes in Beds of Inductively Heated Particles, NUREG-0262, NRC-7, 1977.

- 3-14 E.S. Sowa, S.D. Gabor, L. Baker, Jr., J.R. Pavlik, J.C. Cassulo, and W. Holloway, Meeting on Fast Reactor Safety and Related Physics, Chicago, IL, 1976, pp 2036-44.
- 3-15 Advanced Reactor Safety Research Quarterly Report, April-June 1978, SAND78-2001, NUREG/CR-0469 (Albuquerque, NM: Sandia Laboratories, 1979).
- 3-16 T.F. Petersen, TAC 2D - A General Purpose Two-Dimensional Heat-Transfer Computer Code -- Users's Manual, GA-8868, (San Diego, CA: Gulf General Atomics, 1969).
- 3-17 Properties for LMFBR Safety Analysis, ANL-CEN-RSK-76-1, L. Leibowitz, ed (Argonne, IL: Argonne National Laboratory, 1976).
- 3-18 H.W. Godbee and W.T. Ziegler, J. of Ap. Ph., 37, 1, p 40, 1966.
- 3-19 A.B. Hill and R.H. Wilhelm, A.I. Ch. E. Journal, 5, 4, p 486, 1959.
- 3-20 E.L. Gluekler and L. Baker, Jr., "Post-Accident Heat Removal in LMFBR's," ASME Winter Meeting November 27-December 2, 1977: Nuclear Reactor Safety Heat-Transfer Section, Atlanta, GA, pp 285-324.
- 3-21 W.J. Afee and W.K. Sartory, Evaluation of the Structural Integrity and LMFBR Equipment Cell Liners-Results of Preliminary Investigations, ORNL-TM-5145 (Oak Ridge, TN: Oak Ridge National Laboratory, 1976).

4. ELEVATED TEMPERATURE DESIGN ASSESSMENT

(W.A. Von Rieseemann, 4442; J.A. Van DenAvyle, 5835;
W.B. Jones, 5835; W.B. Gauster, 5111; S.W. Key, 5521;
D.W. Lobitz, 5521; C.M. Stone, 5521)

4.1 Uniaxial Creep-Fatigue Behavior Program

4.1.1 Creep Testing

No additional creep tests were conducted. Examination using positron annihilation (PA) of specimen 316-C-5 (593°C, 170 MPa, 1991 h, 5% strain) was completed and is discussed in Section 4.1.3b.

4.1.2 Creep-Fatigue Testing

Six additional creep-fatigue specimens of 316 stainless steel were sent to Mar-Test, Inc., to continue testing of specimens with long-term hold periods. The test matrix is given in Table 4-1.

Table 4-1

Creep-Fatigue Tests at Mar-Test, Inc.
(316 stainless steel; $\dot{\epsilon} = 4 \times 10^{-3} \text{ s}^{-1}$)

Specimen No.	$\Delta\epsilon_t$ (%)	Temp (°C)	Hold Time (min)		Number Cycles
			Tensile	Compressive	
316-MTF-17	0.5	593	0	10	4000
316-MTF-18	0.5	593	10	0	40
316-MTF-19	0.5	510	0	0	Failure
316-MTF-20	0.5	510	10	0	Failure
316-MTF-21	0.5	510	0	10	Failure
316-MTF-22	Reserve	---	--	--	---

The first test listed in Table 4-1 (316-MTF-17) is a duplicate of 316-MTF-12 with a 10-min compressive hold that had cracked significantly at an unexpectedly low number of cycles (3000). Specimen 316-MTF-17 was run to 4000 cycles (667 h) with no visual indication of cracking; it was subsequently removed from test and sent to Sandia for analysis. Specimens

316-MTF-18 and -19 were also completed and test 316-MTF-20 was initiated. Sample 316-MTF-18 with 40 cycles will provide information at about 2% of life, and the three tests at 783 K (510°C) will give samples damaged at a lower temperature that is more representative of advanced reactor operating conditions. In addition to providing mechanical properties data, these experiments will be used to generate samples for microstructural analysis and PA measurements.

Initial observations of surfaces of Type 316 stainless steel fatigued specimens were completed; these specimens were also used for sequential surface PA measurements. The goal is to follow the process of surface crack initiation by direct observation and PA measurements. Samples were observed by two methods: by making plastic replicas for viewing in the scanning electron microscope (SEM) and by direct viewing of the specimen in the SEM. Replica techniques attempted included standard acetate tapes, collodion solutions, and a silicon-based dental-impression material (Xantoprem Blue). These all failed to provide the necessary surface detail over a large enough area of the specimen, so observations were made by mounting the entire fatigue specimen in the SEM. Observations showed that an oxide layer $\sim 1 \mu\text{m}$ thick forms on samples tested in air at 866 K (593°C) for longer than a day. This oxide hides from observation the deformation and cracking of the metal surfaces and would likely affect PA readings; future iterations of these sequential tests will be carried out in vacuum.

4.1.3 Non-Destructive Examination

- a. Ultrasonic -- No ultrasonic testing was conducted during this period.
- b. Positron Annihilation -- A series of isochronal annealing measurements using the Doppler broadening PA technique was completed on 75% cold-worked Type 316 stainless steel. Results were in agreement with data given in the previous quarterly report on 25% cold-worked material (Figure 4.1-1); a large decrease in lineshape parameter began at approximately 473 K and continued to 873 K. Microhardness measurements on the 25 and 75% cold-worked samples indicate that dislocation annealing begins after 873 K (Figure

4.1-2). For Type 316 stainless steel this further confirms the hypothesis that vacancies contribute to a large fraction of the lineshape-parameter increase caused by room-temperature deformation. Further annealing studies are being made on samples fatigued at both room and elevated temperatures.

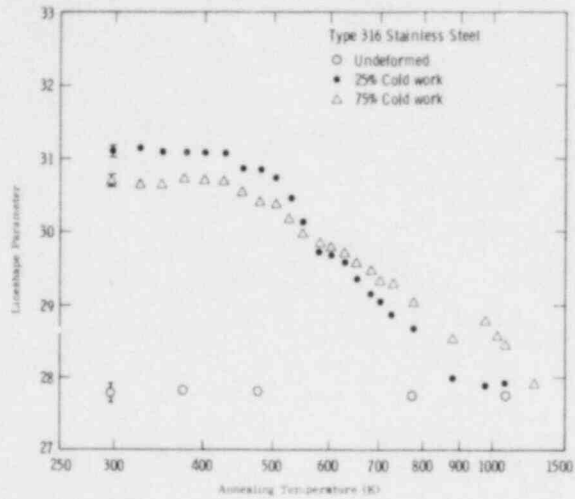


Figure 4.1-1 Lineshape Parameter vs Step-Annealing Temperature for 25% and 75% Cold-Worked Type 316 Stainless Steel

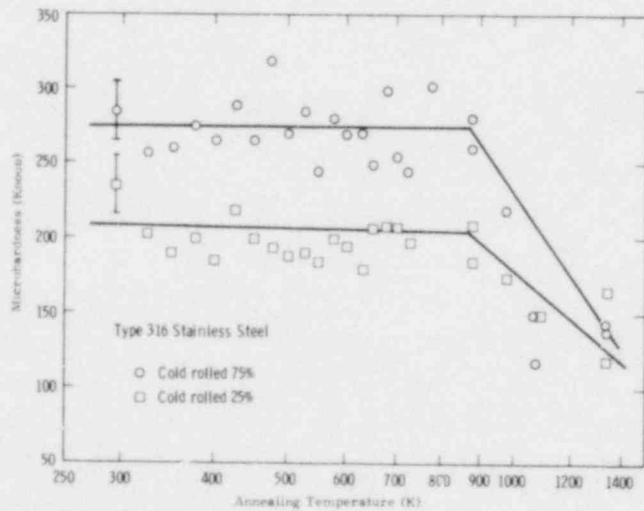


Figure 4.1-2 Microhardness vs Step-Annealing Temperature for 25% and 75% Cold-Worked Type 316 Stainless Steel

To better understand the individual roles of vacancies and dislocation in the PA response of metals, measurements were performed on isochronally annealed cold-worked pure nickel. Temperatures for vacancy and dislocation annealing have been extensively studied in the past using resistivity and internal-energy measurement techniques.^{4-1, 2} Results of an annealing run for 25% cold-worked nickel (99.995% purity level) are shown in Figure 4.1-3. Two annealing stages are evident: one beginning at 400 K (127°C), and corresponding to the previously observed temperature range for vacancy annealing; the other stage beginning at 600 K (327°C) caused by dislocation annealing. This interpretation has also been confirmed by transmission electron microscopy (TEM) observations made on samples annealed to the ends of the two annealing stages.

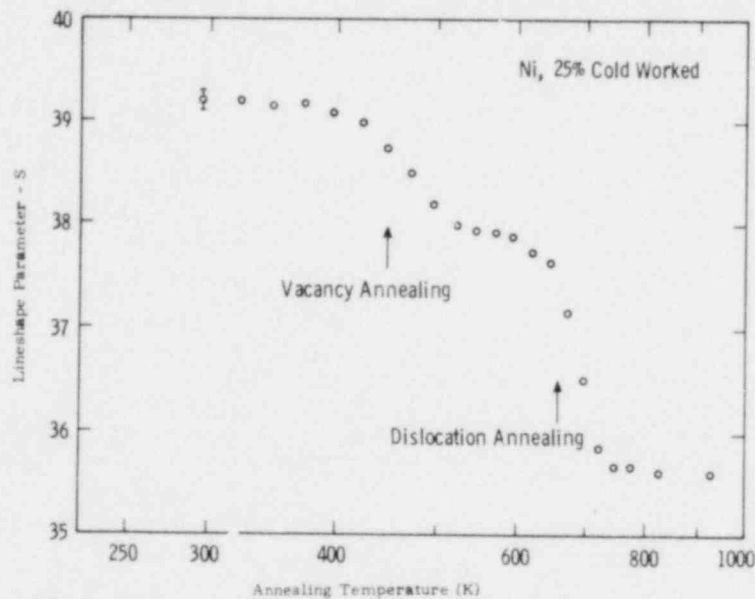


Figure 4.1-3 Isochronal Annealing Curve for Pure (99.995%) Nickel

The magnitude of the decrease due to vacancy annealing in nickel is approximately 36% for the total effect, while in Type 316 stainless steel vacancy annealing accounts for 80 to 90% of the total decrease. This difference implies that positrons are trapped much more effectively at dislocations in nickel than in the stainless steel.

Surface PA measurements using the angular-correlation technique were made on three Type 316 stainless-steel samples: an undeformed control specimen; a specimen (316-PAF-16) given 20 cycles at 866 K at a total strain range of 1.0%; and a specimen (316-PAF-15) run 2500 cycles to failure under the same conditions. Measured lineshape parameters are shown in Figure 4.1-4. These values measured by the angular-correlation technique cannot be directly compared to previously reported values determined by the Doppler broadening technique. While the lineshape parameter did increase with the number of fatigue cycles, there are two problems: duplicate measurements do not always fall within their respective statistical error bars; and the error bars are large (± 0.1) with respect to the total measured change ($\sim +0.9$). These results have poorer statistics than previous PA measurements by the Doppler broadening technique.

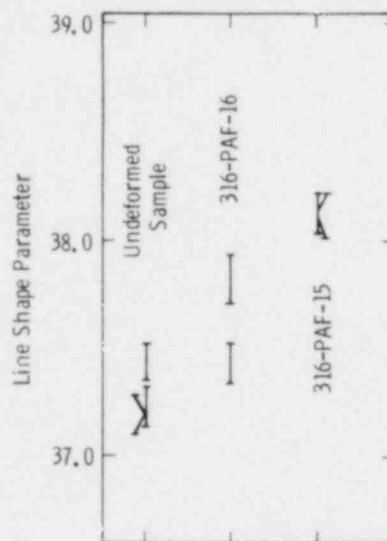


Figure 4.1-4 Surface Positron Annihilation Values of Deformed Samples Using the Angular-Correlation Technique

These two problems are related in that the statistics of the technique improve with the number of individual PA events counted (these can be increased by using a more active positron source or by using a longer counting time). The counting time used here was a relatively long 33 h, so further increases in accuracy would require a stronger positron source

(an expensive item). The long counting times also permit long-term electronic drifts in instrumentation that are a cause of the first problem. Sandia is currently assessing the possibility of obtaining a more active source.

Three additional PA measurements using the Doppler broadening technique were carried out on Type 316 stainless-steel samples fatigued at 866 K with various hold times. Figure 4.1-5 shows these data for specimens cycled with a 10-min compressive hold, combined 10-min tensile plus 2-min compressive hold, and a 10-min zero-stress hold. PA values for these samples are essentially equivalent to other data on the figure at the same number of cycles. PA measurements were not able to distinguish among specimens cycled without hold periods and with various combinations of hold periods.

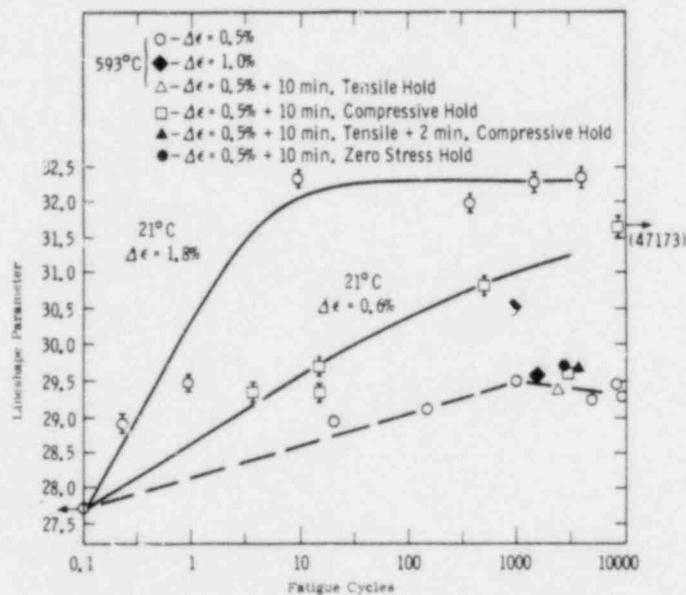


Figure 4.1-5 Lineshape Parameters vs Number of Fatigue Cycles for Type 316 Stainless Steel

4.1.4 Microstructural Analysis

No additional transmission-electron microscopy on deformed samples was carried out during this period.

4.1.5 Multiaxial Material Behavior

Set-up of the Multiaxial Test Facility continued with installation and checkout of the safety-interlock module and development of induction coil configurations for specimen heating. A three-axis micrometer platform was purchased to mount induction-heating coils and allow precise and reproducible alignment of the coils. This is necessary to provide a uniform temperature distribution over the specimen gage length. Specimen and grip alignment were checked using strain-gage-instrumented samples to insure that bending stresses were not introduced during specimen mounting and that stresses were equal around the specimen circumference during tensile or compressive loading. Preparation continued on the necessary safety-related documents for the high-pressure system to obtain internal Sandia approval to operate the facility.

4.2 Creep-Fatigue Damage Analysis

The analytical support for the creep-fatigue experiments continued to focus on the design and analysis of the biaxial specimen initiated last quarter. Emphasis was placed on the investigation of load limitations to assure the preclusion of buckling. To date two buckling analyses have been completed using the MARC general-purpose structural finite-element code. Figure 4.2-1 shows the finite-element model of the tubular specimen. The analysis procedure involves internally pressurizing the specimen and then incrementally imposing an axial compression at the grip end until an instability occurs. The axial-buckling load can then be obtained from the axial-reaction forces at either the grip end or the plane of symmetry at the test section center. Although in the analyses completed so far, room-temperature properties were used for the Type 316 stainless steel from which the specimens will be fabricated; plans include a similar set of buckling analyses using elevated-temperature properties. In order to eliminate heat-to-heat uncertainties, a uniaxial room-temperature test on a solid specimen made from the stock that will be used for biaxial specimens was run to establish an accurate room-temperature stress-strain relation for the specimens.

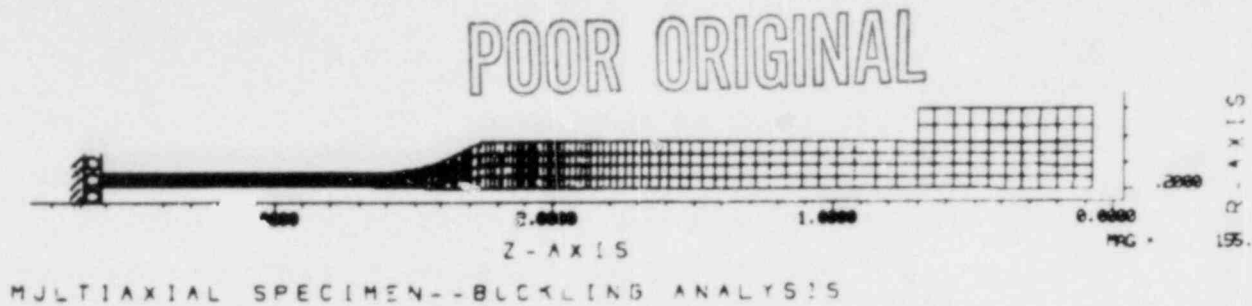
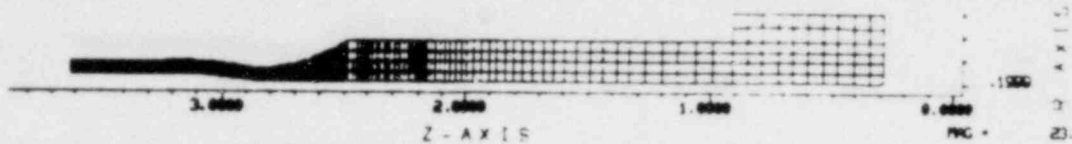


Figure 4.2-1 Finite Element Model for the Tubular Specimen

The first analysis was carried out without internal pressure. Indications were that buckling would not occur for plastic strains of less than 1%, the maximum strain anticipated in upcoming Sandia creep-fatigue experiments. The magnified deformation pattern of the specimen (Figure 4.2-2) indicates a transition region in the test section close to the fillet where significant variations in the strain occur due to shell bending behavior. This is evidenced in the contours of effective plastic strain shown in Figure 4.2-3. Here the contour labeled "I" corresponds to the greatest plastic strain; the lesser contours we labeled "A" through "H". The region with the high density of "A" labels has not yielded. Plastic strain levels to the left of the "I" contour deviate only slightly from the corresponding contour value of 0.0119 in./in. A uniformly high value of plastic strain is achieved in the majority of the test section.

In the second analysis, the specimen was pressurized to approximately half the pressure required to cause yielding before imposing axial compression. As in the first analysis, the specimen did not appear to be in danger of buckling for plastic strains of less than 1%. The magnified deformation pattern of the specimen (shown in Figure 4.2-4) indicates a more pronounced transition region near the fillet than was observed in the case without internal pressure. In addition, as is evidenced in the contour plot of Figure 4.2-5, the maximum effective plastic strain is greater and its location is shifted towards the center of the specimen. For this comparison the axial displacements in each case are equal.

POOR ORIGINAL

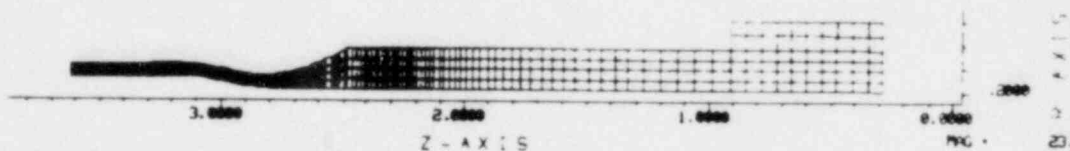


BUCKLING ANALYSIS

Figure 4.2-2 Displacement Pattern for the Room Temperature Multi-axial Specimen Under Imposed Axial Displacement Only



Figure 4.2-3 Contours of Effective Plastic Strain for the Room Temperature Multi-axial Specimen Under Imposed Axial Displacement



MULTIAXIAL SPECIMEN--BUCKLING ANALYSIS

Figure 4.2-4 Displacement Pattern for the Room Temperature Multi-axial Specimen Under Imposed Axial Displacement and Internal Pressure (2750 psi)



MULTIAXIAL SPECIMEN--BUCKLING ANALYSIS

Figure 4.2-5 Contours of Effective Plastic Strain for the Room Temperature Multi-axial Specimen Under Imposed Axial Displacement and Internal Pressure (2750 psi)

This is further evidenced in Figures 4.2-6 and 4.2-7 where comparisons of "measured" and actual data are given as a function of extensometer position. The error bars associated with the axial strain depict the range of axial strains existing within the extensometer-attachment points. Thus, the more remote the attachment points from the center of the specimen, the larger the deviation in strain from that measured. The curves associated with the hoop strain simply point out the departure from uniformity as the gage position approaches the fillet. The pressurized specimen possesses a lesser region of strain uniformity than the unpressurized one. These curves can be used for guidance in selecting locations for mounting extensometers.

Although these room-temperature analyses have not indicated a buckling problem, there is no assurance that elevated-temperature analyses of the specimen will yield the same result. Consequently, these buckling analyses need to be repeated using material-property data at elevated temperature generated from the stock reserved for specimen fabrication. Efforts will be made to complete these analyses in the ensuing quarter.

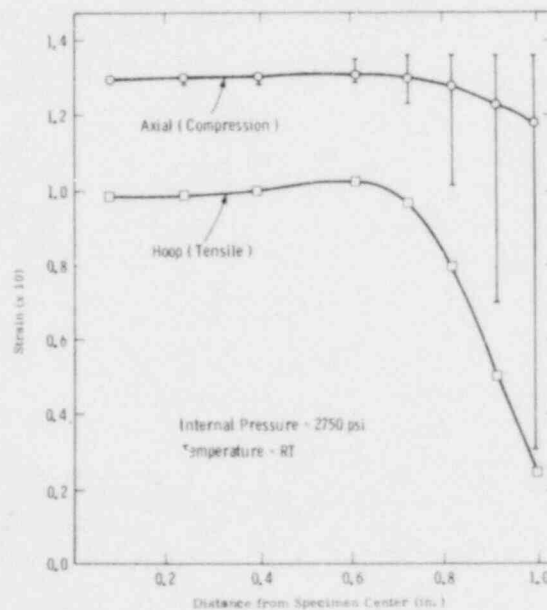


Figure 4.2-6 Test Section Strain Variations for the Room-Temperature Multiaxial Specimen Under Imposed Axial Displacement and Internal Pressure (2750 psi)

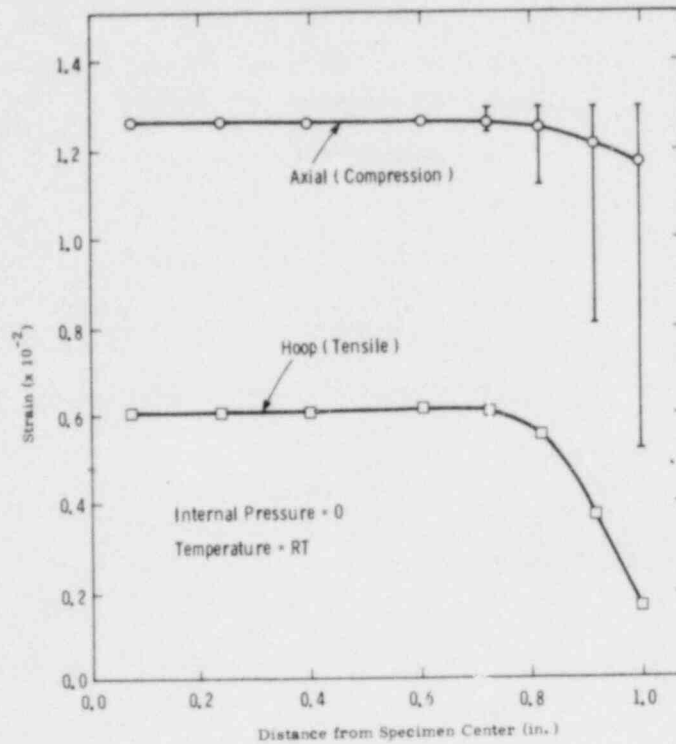


Figure 4.2-7 Test Section Strain Variations for the Room-Temperature Multiaxial Specimen Under Imposed Axial Displacement Only

4.3 Structural Analysis

Work continued on the assessment of creep-law behavior for use in piping analysis. Work to date has identified large differences in the creep response of piping elbows when different forms of creep laws are used. The PNC pipe-elbow creep-buckling experiment was chosen as the benchmark against which the various creep models could be run. The creep hold time in this test is 96 h; this is still within the primary creep regime for Type 304 stainless steel.

Three types of creep laws were considered. Two of these laws are of the Blackburn type with single- and double-exponential terms representing primary creep. The third law considered was a Norton power law on stress. The double-term Blackburn law was given by PNC as a creep model for the test. In addition, constants for the Norton power law were provided PNC from short-term creep tests. The single-term Blackburn law was provided

by Westinghouse - ARD for Type 304 stainless steel. The double-term Blackburn representation was found to have a very-high creep-strain rate during the 96-h hold. The next highest creep-strain rate was given by the power-law expression. The minimum strain rate was exhibited by the single-term Blackburn law which also gave the best correlation with the experimental results. The worst comparison came from the double-term Blackburn model. These results suggest that the better models for numerical creep analysis are the simplest mathematically.

4.4 Structural Evaluation

A technical review of the CRBRP piping document, written at Westinghouse - ARD (Report CRBRP-ARD-0185), was initiated this quarter. Basically the document attempts to assure the integrity of the piping system on three levels. At the first level, compliance with ASME Code design rules for Class 1 piping is investigated. The second level focuses on the growth of a specified surface crack throughout the duty cycle of the plant to determine whether or not the crack will develop into a through-wall crack. At the third level, if a through-wall crack does develop, the question of leak-before-break is investigated. The third-level arguments are the first to be addressed by this review.

The approach taken in the third level is basically experimental, involving two separate experiments. First, however, an attempt is made to assure that the characteristics of Types 304 and 316 stainless steel piping will be essentially the same at the end of the plant duty cycle as at the beginning. For effects such as aging, creep-fatigue interaction, and irradiation, arguments are made which support the hypothesis that these effects as well as other do not significantly affect material characteristics in this application.

Accepting these arguments, the first set of experiments attempts to determine the length of the through-wall crack in a piping elbow necessary for bulging of the elbow to occur (when the elbow bulges open, it is considered broken). Elbows are of interest because they are the most highly stressed elements of the piping system; experimental data of this

type for elbows was not available for correlation with ductile failure theories such as the plastic instability model proposed by Professor Paris. After performing a battery of tests on 4-in.-dia elbows containing a variety of through-wall cracks, correlation with the Paris plastic instability model was established for elbows. Burst pressure for each elbow was determined in the presence of an external bending moment. Using the Paris plastic instability model, the extrapolation was made to the elbows in the CRBRP primary piping system for duty-cycle loading. Results indicate that in the cold leg the critical crack length for bulging is 29.7 in. and in the hot leg, 22.3 in.

The second set of experiments addresses the behavior of a crack extending part way through an elbow under fatigue loading. These experiments were done to determine whether or not the partial crack would propagate along the surface to the critical length for bulging of a through crack before it penetrated the wall. If not, the data would support the leak-before-break concept. Several 1/6 and 2/3 scale-model elbow tests were completed wherein part-through flaws were established in the elbows along the crown. The elbows were then loaded cyclicly with an external bending moment varying from zero to some value corresponding to the desired stress range. This configuration causes ovalization resulting in unidirectional bending fatigue along the elbow crown. This bending fatigue is considered to be the primary cause of the undesirable crack propagation along the surface. Although all specimen in which crack propagation occurred developed through-wall cracks, experimental results indicate that lower stress ranges tend to produce longer cracks before penetration. However, the crack propagation rate is extremely slow for smaller stress ranges requiring $\sim 10^7$ cycles for penetration. The likelihood of a surface crack reaching the critical length for bulging of a through crack is extremely small, assuring "leak-before-break". This conclusion is affirmed by comparing the cycles and corresponding stress ranges required for penetration (in these experiments) to the expected stress ranges and their respective numbers of cycles during the plant duty cycle.

With this brief review of the leak-before-break arguments for the CRBRP primary piping system, two potential concerns exist. The first involves the arguments made to assure that material degradation will not occur throughout the life of the plant as a result of the effects identified. Secondly, the arguments are not completely convincing that a surface crack will penetrate an elbow wall before growing along the surface to a length that would bulge open if penetration occurred. The scale-model elbow experiments done to support this argument show significant variability in the results and are not comprehensive enough. No rationale is given for scaling the results to full-scale elbows. Next quarter a study in more depth will be made in order to resolve these potential concerns.

4.5 General

A meeting of the Primary System Integrity Review Group was held at Sandia on November 14, 1978. In addition to the Sandians present, J. Chow (BNL), Professor S. S. Manson (Case-Western University), R. Huddleston (ORNL), and T. J. Walker, H. Holz, and F. Litton of NRC participated in the review.

References for Section 4

- 4-1 L.M. Clarebrough et al, "Changes in Internal Energy Associated with Recovery and Recrystallization," Recovery and Recrystallization of Metals, L. Himmal, ed., 1963, p 63.
- 4-2 W. Wycisk and M. Feller-Kniepmeier, "Quenching Experiments, in High Purity Ni," J of Nucl Matls, 69 & 70 (1978).

5. LMFBR Accident Delineation (P.S. Pickard, 4424; J. Sholtis, 4424; D.C. Williams, 4425; P.W. Conrad, 4424)

5.1 Introduction

During this period, in all three of the major study areas (Engineered Systems, Accident Phenomenology, and Postaccident Phenomenology (Containment)), a significant portion of the available time was spent in the preparation of summaries and reviews of the current status and results of the Delineation Study. This work included preparation of presentations for the NRC-DOE-Japan FBR Conference, a paper for the International Meeting on Fast Reactor Safety Technology (19-23 August 1979, in Seattle, WA),⁵⁻¹ and detailed presentations to the LMFBR Accident Delineation Research Review Group at the NRC, January 31, 1979.

Additional efforts centered on preparation of a work plan of possible future investigations for the Delineation Study. A beginning was made on some of the tasks previously identified.

5.2 Engineered Systems

Efforts on the Phase II Work Plan continued during this reporting period. The Phase I Study in the Engineered Systems Area resulted in the construction of event trees for 14 identified vital subsystem failures that delineated a set of 15 initiating-accident categories. Phase I illustrated the general applicability of conventional-event/fault-tree methodology to the Engineered Systems area of an LMFBR. An absolute quantification of LMFBR initiating-accident probabilities is considered beyond the scope of this study due primarily to the lack of necessary data. Nevertheless, a preliminary quantification to roughly estimate the relative frequency of initiating-accident categories appears useful. In particular, if successful, this relative accident quantification would provide a framework of reviewing LMFBR safety research and development priorities. From the results obtained in Phase I, two general objectives were established to identify promising areas for potential future investigation in

the near term (1 to 3 yrs) during Phase II. The objectives set down include:

- Scope the requirements for a more realistic quantification of LMFBR initiating-accident probabilities.
- Provide feedback for evaluation of LMFBR safety research and development priorities.

To satisfy these objectives, Phase II efforts were aligned within four analysis categories which involve:

- a. Complete qualitative accident delineation and categorization.
- b. Expand specific areas of concern identified in Phase I.
- c. Attempt to estimate roughly the relative frequency for LMFBR initiating-accident categories and their order of sensitivity.
- d. Scope the requirements for a more realistic quantification of LMFBR initiating-accident probabilities based on all data and information obtained collectively from previous analyses.

This approach led to the identification of 15 promising tasks for possible analysis in Phase II. Table 5-1 lists the 15 tasks showing their tentative temporal order of performance and their relationship to other tasks. These 15 tasks define an arena that would require a substantial level of effort for completion. Many tasks identified are exploratory with no assurance of success. Because of the probability of encountering difficulties during the course of analysis, a firm level of effort cannot be set with confidence. A rough estimate of about 2.5 to 3 man-yrs is considered representative.

Table 5-1

LMFBR Accident Delineation Study

ESS Phase II Summary

Task	Rank* Order	Analysis Category	Task Dependency	Suggested For FY79?
Develop DHRS fault tree	1	2	None	Yes
Attempt to specify and characterize meaningful protected-accident categories	2	2	1	Yes
More extensive analysis of accident initiators	3	1	None	Yes
Qualitative assessment of common cause/mode effects between initiators and PPS functions (detection, pump trip, and SCRAM)	4	2	3	If time permits
Attempt to est DHRS cond. failure prob. for various initiators and subsystem failures (if cannot, perform qualitatively)	5	2	1,3	If time permits
Critical review of CRBR safety study (CRBRP-1)	6	3	3,4,5	If time permits
Estimate plausibility of CRBR unscrammable faults	7	1	3,4,6	Yes
Simplify ESS event trees	8	2	None	Yes
Delineation and plausibility of protected LOAs in CRBR	9	1	1,3,5,6	Yes
Evaluate CRBR TBS function and delineate LOSP initiator	10	1	None	Yes
Base case quantification and ranking of accident categories	11	3	1-10	If time permits
Estimate uncertainty intervals and perform sensitivity on base case accidents and their rank order	12	3	1-11	No
Analysis and interpretation of results and information obtained from all above tasks	13	4	1-12	Yes
Scope requirements for a more realistic quantification of LMFBR initiating accident probabilities	14	4	1-13	Yes
Reporting of results and information obtained from all above tasks	15	4	1-14	Yes
Delineation of in-core accidents at conditions other than full power	15	1	1-13	No
Delineation of ex-core accidents	15	1	None	No

*This ranking is based on a temporal ordering of task performance and does not necessarily indicate task importance.

Notes for Table 5-1 (abbreviations)

ESS	Engineered Safety System
LMFBR	Liquid Metal Fast Breeder Reactor
DHRS	Decay Heat Removal System
PPS	Plant Protection System
est.	Estimate
cond.	Conditional
prob.	Probability
CRBR	Clinch River Breeder Reactor
LOCA	Loss-Of-Coolant Accident
TBS	Turbine Bypass System
LOSP	Loss-Of-Offsite-Power

All 15 tasks obviously cannot be addressed during FY79. Table 5-1 indicates those tasks that will be addressed during FY79 and those that will be initiated if time permits. Basically, the efforts to be performed during FY79 will involve completing the delineation of the Engineered Systems area and will review areas for future study. Generally, Phase II efforts identified in this work plan would set the stage for a more realistic subsequent quantification of LMFBR initiating-accident probabilities while also providing interim data for review of LMFBR safety research and development priorities. The tasks to be treated during FY79 are indicated in Table 5-1. Work on Tasks 1, 7, 8, and 10 was initiated during March 1979.

5.3 Accident Phenomenology

The planning for future work was strongly influenced by the major conclusions of the Interim Report, especially the following:

- Quantification of the event trees in the Accident Phenomenology area (or other means of executing a quantitative probabilistic/mechanistic risk analysis) is not likely to be feasible in the near term.
- Future work in the Containment area can probably demonstrate substantial risk mitigation provided very low probabilities can be validly assigned to very severe energetics. Given these conclusions, efforts in the Accident Phenomenology area reasonably should be concentrated on questions that bear directly upon the problem of whether extremely severe energetics* can occur.

The proposed efforts in the Accident Phenomenology area can be divided into two parts as follows:

- a. Continuation of general efforts required to bring the coverage offered in the Interim Report to a more uniform level. At present, the report gives only a limited treatment of some topics (e.g., local fault-propagation accidents) that merit more detailed

*"Extremely severe energetics" means energetics sufficient to directly and rapidly cause serious impairment of containment capability including the reactor-containment building (RCB).

delineation to identify key phenomenologies requiring additional study and to set priorities for these studies.

- b. The interim report delineated ULOF and UTOP accidents to the point where key phenomenologies requiring better understanding can be identified and these investigations can be assigned priorities. These efforts are guided by placing the greatest emphasis on questions concerning the possible occurrence of severe energetics. If time and resources permit, phenomenologies assigned the highest priority will be considered in more detail than was done in the Interim Report. Experimental and/or analytical studies to improve understanding of these phenomenologies may be proposed where possible. Actually carrying out these investigations will be outside the scope of Phase II.

5.3.1 General Studies

This part of the effort may be thought of as a continuation of Phase I (filling in certain subjects that were treated inadequately in the Interim Report). Some topics that might be addressed are noted below in order of decreasing priority. Only the first two or three items are likely to be considered in any detail during FY79.

5.3.1.1 Local Fault-Propagation Accidents -- Delineation will include consideration of what physical signals (acoustic, thermal, neutronic, etc) will be generated as propagation proceeds; how these might be detected and thus used to initiate shutdown; and the safety implications of detection and shutdown at different stages of the propagation process.

5.3.1.2 Extension to Cores Other Than CRBR -- Phase I efforts concentrated on the standard CRBR core. Work should be extended to consider major differences that might arise in larger cores with higher void coefficients, and also "parfait" (heterogeneous) cores.

5.3.1.3 Categories of Protected CDAs -- This task may be treated primarily in the area of Engineered Systems.

5.3.1.4 Extensions of the Fuel Dispersal Phase Delineation

5.3.1.5 Refinement of Delineation of Unprotected CDAs Other Than UTOP and ULOF

5.3.1.6 Delineation of Accidents Initiating at Other Than Normal Operating Conditions

5.3.1.7 Further Refinement of Existing UTOP and ULOF Accident Delineations

5.3.2 Improved Definition of Key Questions Governing Severe Energetics

The Interim Report carried delineation of accident phenomenologies to the point where it is now possible to identify some key needs and to begin assigning priorities, guided especially by the need to resolve questions related to severe energetics. The first step in addressing improved definition has been to assign the various relevant phenomenologies to categories indicating the nature of the effect they might have on accident outcome, the degree to which they might exercise these effects, and a judgment as to the likelihood that additional work might show that the effect indicated would indeed be present. The categorization scheme being applied is as follows:

- a. Category A refers to phenomenologies that are directly involved in determining the severity of a disassembly. Quantitative prediction of disassembly energetics requires at least some capability to quantitatively evaluate Category A phenomenologies. Examples would include the complex of phenomenologies involved in LOF-driven-TOP sequences.
- b. Category B refers to phenomenologies that may contribute to the evolution of the accident along paths that bypass possible sequences which otherwise could lead to severe energetics at a later stage in the accident. Examples would include negative reactivity effects in the early portions of a ULOF accident (e.g., early fuel dispersal) that could slow the transient sufficiently so that a LOF-driven-TOP sequence does not develop. Quantitative evaluation of Category B phenomenologies may be required in order to determine the likelihood that a subsequent sequence leading to disassembly could arise;

quantitative evaluation is less likely to be needed in actually assessing the disassembly severity if disassembly does occur.

- c. Category C applies to phenomenologies not currently known to be relevant to the question of severe energetics, but which are known to be relevant in answering other questions important to over-all accident delineation. An example would be the question of whether fuel eventually relocates in the upward or downward direction (this information is needed for in-vessel PAHR analysis).
- d. Category D refers to questions that arise in the course of any attempt to carry out a truly mechanistic analysis, but do not have major effects of the types noted above insofar as is presently known. (Note that a D designation may reflect only a lack of knowledge rather than actual absence of important effects.)

Table 5-2 presents the assignment of phenomenology categories for ULOF accidents. A bar over the letter indicates a negative contribution (i.e., acts to reduce or prevent the effect) designated by the letter. A numeral 1 following the letter implies a large effect and a 2 indicates a lesser effect. A (+) indicates that an effect to the degree designated seems likely; a (-) indicates that it does not seem likely, but it cannot be ruled out completely. Table 5-2 gives a preliminary application of the scheme to the ULOF initiation phase; observe that a phenomenology can have more than one designation. In this table, assignments are limited to A and B categories, even though some of the phenomenologies may also have C- or D-type effects.

Application of categorization schemes based upon delineation appears to provide a useful framework for assigning priorities for further work. This does not, however, mechanize the process; judgement is still required.

Table 5-2

Assignment of Phenomenology Categories, ULOF Accidents

Accident Phase or Subphase	Phenomenology	Categories
Initiation	Axial Expansion	B2(+)
Phase (prepin failure stage)	Clad Relocation	A2(-), $\overline{B2}(+)$
	Premelt Fuel Slumping:	
	Fresh Fuel	$\overline{B2}$
	Irradiated	$\overline{B2}(-)$
	Fuel Swelling	$\overline{B1}$, $\overline{B2}(+)$
	Fuel Motion on Disruption	
	Compaction†	$\overline{B2}$; A2(-)
	Dispersal	
	Fission Gas	B1, B2
	Na Vapor	B1(-), B2
Steel Vapor	B2(-)	
	Compaction Driven by Plenum Gas	A1(-); $\overline{B1}(-)$, $\overline{B2}$
Postpin Failure Stage: LOG-Driven-TOP	Pin-Failure Characteristics	$\overline{A1}$, A2(+)
	Intrapin Fuel Motion	A2(+); A1
	Voiding Due to Fission Gas	A2
	FCI-Driven Voiding	
	Incoherent FCI (as in SAS)	A1, A2(+)
	Coherent FCI	A1*(-)
	Nonaxial Motions	A1*(-)?
	Expin Fuel Motion	$\overline{A1}(-)$, A2
	Other Rapid Material Motions (from effects not explicitly identified in the delineation to date)	A2(+), A1(-); $\overline{A1}$

† Does not include compaction due to plenum gas (next item).

5.4 Postaccident Phenomenology

During this period, efforts were directed toward developing a work plan for improvements in the Postaccident Phenomenology event trees to be made during the coming fiscal year. A draft of the work plan has been

completed; the initial tasks outlined by the work plan have been undertaken.

The work plan consists primarily of two broad areas for further study: the elaboration and clarification of in-vessel PAHR phenomenology, and more detailed examination of specific branch points of the containment-response-event trees. In addition, whenever appropriate, these trees would be altered to be less generic and more compatible with the specific design features of the CRBR.

Work on the first of these areas is now in progress and is concentrated on the development of in-vessel PAHR event trees. These will encompass all events between fuel dispersal and reactor-guard-vessel failure. Examples of phenomena that will be developed into a system of branchpoints include the character, location, and size of an in-vessel debris bed; recriticality considerations; decay-heat-removal system availability; and the character, location, and mode of any resulting reactor-vessel failure. This exercise is expected to yield a more precise set of initiators for the containment-response-event trees by producing a better-defined characterization of the state of debris and sodium after the CDA. The impact of this exercise will then be traced through the containment trees, and modifications will be made where appropriate. A preliminary version of a generic in-vessel PAHR tree has been developed and is now being reviewed.

The second area of effort will be, in effect, a final refinement of the containment-response-event trees with emphasis on demonstrating more explicitly some design features peculiar to the CRBR. Example of particular areas that would receive increased consideration would be

- Events in the reactor cavity after melt-through including the effects of cavity-liner failure
- The impact of the capabilities of specific types of upper containment-cleanup systems including partial failure effects

- o The influence of various types of sodium fires whether above or below the operating floor or within a reactor vessel with a failed head
- o The likelihood and character of the final failure mode of the upper containment building including the impact of some specific features such as the double walled structure and annulus cooling system.

The objective of these additional efforts will be to better define the timing, extent, and character of each major containment failure with the intent of obtaining a better characterization of the various forms of fluid releases to the environment.

References to Section 5

- 5-1 J.A. Sholtis, M. Rios, D.W. Worledge, P.W. Conrad, D.C. Williams, D.W. Varela, and P.S. Pickard, "LMFBR Accident Delineation Study," International Meeting on Fast Reactor Safety Technology, 19-23 August 1979 in Seattle, WA, paper to be presented.

6. TEST AND FACILITY TECHNOLOGY

6.1 ACRR Fuel-Motion Detection System (J.G. Kelly, 4423; K.T. Stalker, 1254)

6.1.1 Introduction

A fuel-motion detection system is being developed for the ACRR. The design of the system is based upon the experience gained in experiments with shielding, collimation, coded-aperture imaging, and time-resolved pseudoholography at the ACPR, SPR-II, and ^{252}Cf facilities. The system will be designed for high-spatial and temporal-resolution measurements of fuel motion in both transient and steady-state experiments, bed-leveling, and material-separation studies in the postaccident heat-removal experiments.

The ACRR fuel-motion detection system is designed to take advantage of the latest advances in framing camera design, optical-image-intensifier developments and coded-aperture imaging technology to measure fuel motion in simulated core-disruptive accidents with high temporal and spatial resolution. The coded aperture, in particular, permits the collection of more imaging gamma rays for each resolution element in the object per unit time than does a pinhole aperture with the same resolution. Thus, improved signal-to-noise ratios in the fuel-pin image can be obtained. At present, the complete system has been designed and most of the major components have arrived. The proof tests are scheduled to commence in October 1978 and will begin with assembly tests in the reactor, radiation mapping, and passive (steady-state) imaging of a fuel pin. The experiment plan was outlined in the April-June Quarterly Report.

The ACRR Fuel-Motion Detection System is now being installed in the reactor tank, and the steady-state proof tests will begin in February 1979. No major difficulties have been encountered thus far in the assembly of the components into the reactor, but some secondary problems have been encountered, delaying the initiation of the tests. These problems will be reported below.

POOR ORIGINAL

6.1.2 Dry Assembly of the Shield and Instrumentation Chambers

A sketch of the fuel-motion system is shown in Figure 6.1-1. Except for the interior parts of the chambers, all of the components were assembled in the laboratory to assure their proper fit. Figure 6.1-2 is a photograph of the assembled system taken from the side that will face the reactor.

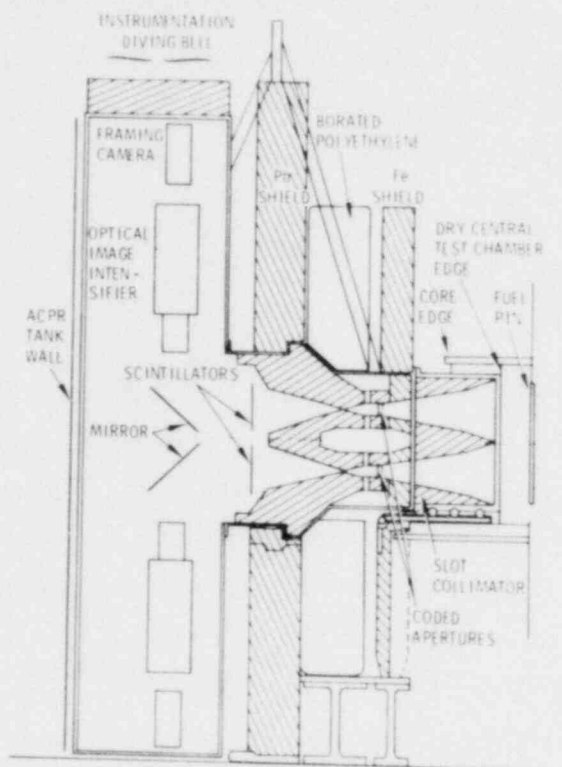


Figure 6.1-1 ACRR Fuel-Motion Detection System

At the bottom of the photograph is the 7.62-cm(3-in.)-thick stainless-steel system-support plate which is leveled on the uneven tank floor by 17 footpads. On the left and right are side plates with angled gussets to support and guide the principle parts of the shield. The collimator chamber (which will slide into the slot of the reactor core) extends through the center of the 7.62-cm-thick steel wall. The lead-shield wall is behind and extends above the steel wall. In Figure 6.1-3, the instrumentation chamber (without its top lid) can be seen behind the lead barrier.

POOR ORIGINAL



Figure 6.1-2 Assembled System Seen From Side Facing Reactor

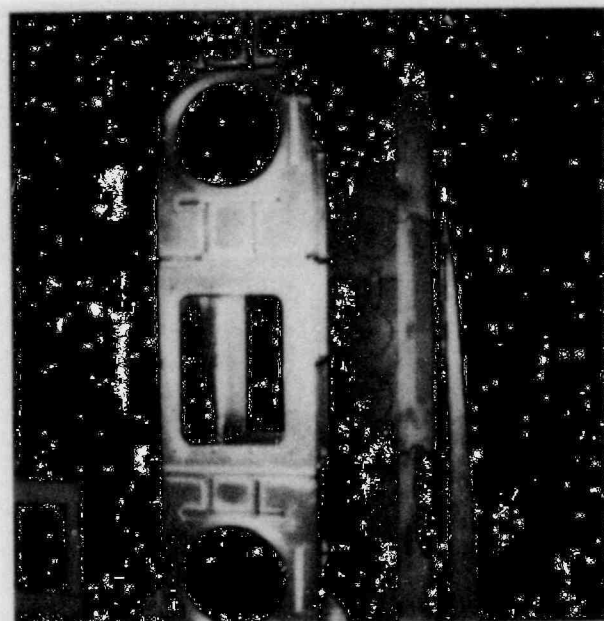


Figure 6.1-3 Lead Barrier With Instrumentation Chamber Behind

After the system was disassembled, the footpads were set according to the depths previously determined in the dry reactor tank for leveling the plate.

6.1.3 Installation of the Shield Structure into the ACRR

The shield structure is too massive to assemble into the reactor in one stage. The lead shield itself weighs 28 000 lb; the tank is so congested with components and piping that only a modest opening is available for insertion of parts. Therefore the pieces had to be assembled singly and aligned, all within the tank. The support plate was first lowered on edge and then rotated to its horizontal position between two brackets that had been welded to the tank floor. The plate was aligned and locked in place by bolts through the brackets.

The side-support frames were then lowered into the water and positioned onto alignment pins in the support plate. They were bolted into place from above. A stainless-steel table was placed onto additional alignment pins between the side frames. This table supports the front stainless-steel scatter plate and the tank containing the borated polyethylene neutron shield. The front steel plate was guided into the forward alignment slots in the support frames.

The lead shield is 20.3 cm (8-in.) thick on the front wall and 15.2 cm (6-in.) thick on the side walls. The shield has been divided into 14 parts, each encased in a stainless-steel can; they mesh together without any line-of-sight cracks. They were designed to be not only self-aligning, but also to fit onto a set of 3.175-cm (1.25-in.) stainless-steel guide rods that are screwed into the base of the support plate. Special tools were built to first screw these rods into place from the surface and then to guide the lead pieces onto these rods.

The bulk shield was completed by positioning the borated-polyethylene tank behind the stainless-steel scatter plate. The successful assembly of the primary shield structure into the reactor was an important milestone in the preparation of the Fuel-Motion Detection

System. Investigators now know that the footpads will support and level the shield load on the uneven tank floor without damage and, further, that the massive and awkward components can be assembled and aligned inside the tank. Up to placement of the borated-polyethylene tank, the assembly went very smoothly although it required twice the expected time. Some difficulty was encountered during the attempted assembly of the slot collimator and the aperture chamber into the slot in preparation for the passive imaging and radiation-field mapping experiments. These and the required remedial actions will now be briefly described.

After fuel rods are removed to form a core slot, a roller plate is hinged to the front scatter plate. This assembly will be lowered into the gap to support the slot collimator. Two problems were encountered during attempts to roll the slot collimator into place.

- a. A buildup of tolerances and some small dimensional errors had raised the roller plate slightly and the collimator chamber would not slide between the grid plates. Consequently, the chamber had to be shortened and rewelded.
- b. Some guide tabs on the side of the roller plate were so closely dimensioned that unless alignment was perfect, the chamber would not slide into the slot. Subsequently these tabs were removed so that the chamber will be aligned solely by the fuel rods, as was originally intended.

Although the aperture chamber was successively lowered into position (without the instrumentation chamber attached), leaks were discovered in the welds. Similar leaks appeared in the slot-collimator chamber. Both chambers had been tested with dye penetrant under vacuum in a swimming pool and had shown no leaks. However, when fully loaded (with lead and polyethylene) and placed in 30 ft of water, the numerous leaks appeared. When these welds were ground out and inspected, they were found to be porous and of poor quality. Subsequently, an engineering-design review was conducted to determine whether thin-walled-aluminum containers could be built in this manner and still survive the weights carried and the pressures generated. The conclusion was that with proper welds the

present designs should be more than adequate. The necessary modifications are being made.

6.1.4 Radiation Measurements Behind the Lead-Shield Wall

A series of gamma-ray dosimetry measurements have been made behind the lead shield, showing it to be very effective despite the fact that without the aperture chamber in place there is a 33 x 71.1 cm (13 x 28 in.) hole in the lead wall centered opposite the reactor.

Figure 6.1-4 shows how the lead pig used in the collimation test-module experiments of 1977 was used to characterize the radiation field behind the lead shield. The lead pig has 10.2-cm(4-in.)-thick walls, a bottom 22.9 cm (9 in.) thick and a 5.1-cm(2 in.)-thick wall opposite the collimator. Thermoluminescent detectors (TLDs) were placed at the locations noted on the sketches showing the two pig locations. The gamma-ray dose at each detector after one 277-MJ burst is shown in Table 6-1. These measurements were made without either the front steel scatter plate or the tank with the borated polyethylene in place.

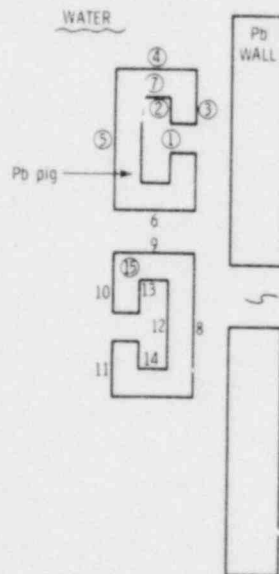


Figure 6.1-4 Lead Pig Used in Collimation Test Module Experiments of 1977

Table 6-1

Gamma-Ray Dose at Each Detector After One 277-MJ Burst

<u>Dosimeter</u>	<u>Dose (rads)</u>
1	0.10
2	0.06
3	1.20
4	Cal limits [†]
5	1.25
6	2.72
7 (side of pig)	1.33
8	8021.0
9	238.0
10	5.09
11	2.00
12	210.8
13	117.5
14	95.5
15 (side of pig)	213.9

[†]The reading was below calibration limits for this detector (~1 rad), but the charge collected indicated a small fraction of a rad.

Several significant conclusions can be made from the results in Table 6-1.

- a. Detectors 3 and 5 have almost the same reading (about 1 rad), while detector 1 inside the collimator detected only about 0.1 rad. Sandia investigators feel that most of the radiation detected by 3 and 5 is being scattered upward from the water behind the opening in the shield; only about 0.1 rad appears to come from wall penetration. Since 8×10^3 rads was measured at detector 8, the net attenuation through the shield is about 10^5 , equal to the exponential attenuation of penetrating 2-MeV gamma rays through 30.3 (8 in.) of lead. This measurement implies that

even on a very large pulse, the radiation penetrating the bulk shield should not have a significant effect on the camera film or the image intensifier. This result is very important.

- b. Detector 4 shows that very little radiation comes over the top of the shield. It measured an uncalibrated small fraction of a rad. Because of this, no lead lid will have to be built to cover the instrumentation chamber after insertion.
- c. The radiation back at the pig location is mostly from gamma rays that are easily shadow-shielded (i.e., the radiation does not scatter around corners very well). The detector at 6 saw only 0.004 times the radiation seen by detector 8 even though the former was placed only 15.24 cm (6 in.) outside of the direct view penumbra of the radiation beam.
- d. Comparison between detectors 12 and 8 shows that the attenuation through 5.1 cm (2 in.) of lead is faster than exponential for 2-MeV gamma rays, indicating (as might be expected) a softer fission spectrum averaging 1 MeV.
- e. Detectors 10 and 11, because they differ so significantly, indicate that most of their dose comes from around the sides of the pig.

The effectiveness of the collimator, mounted in the aperture chamber, has yet to be determined. This collimator-aperture chamber assembly will stop most of the gamma radiation which enters the shield opening, but it will also displace a significant amount of the water that provided much of the neutron shielding in this first test. If the lead collimator parts are found to act too much as a neutron conduit in later tests, it will be a simple matter to reduce the amount of lead and increase the amount of borated polyethylene.

6.1.5 Assembly and Testing of the Linear-Coded Apertures

The gold and platinum vanes that form the attenuating zones of the coded aperture were received in September. The vanes were individually cast, had to be filed to the correct thicknesses, and shimmed to assure proper spacing. The cast material is moderately flexible and could not

be easily machined to the proper dimensions, so this final tuning step was done by hand.

The assembled apertures were then exposed at the ^{252}Cf facility so that the effectiveness of the modulation could be measured and the accuracy of the vane spacing could be determined. A densitometer scan across the x-ray film is shown in Figure 6.1-5. The code has 15 opaque zones between the axis and one edge. The scan in Figure 6.1-5 can be compared to the code made of Ta with 10 opaque zones shown in Figure 6.1-6. This second aperture is the one used to image a fuel pin at the reactor in 1977.

Clearly the new aperture offers superior modulation of the gamma-ray signal. This can be seen by comparing the height of the central zone maximum to the minima of the adjoining zones for both apertures. In the case of the older Ta zoneplate (Figure 6.1-6), the amplitude of the minima increases toward the edge of the zoneplate. This is a consequence of making the outer zones thinner to avoid vignetting as the angle of observation at the detector plane is increased. The thinner zones allow more penetration of the attenuating zones by the incident radiation. In contrast, the zones of the new zoneplate are all the same thickness; they are beveled and angled toward the object centerline to eliminate vignetting. Thus, the valley amplitude of the minima remain about the same for all zones.

For a point source, the exposure level between zones (the peak heights) should be the same but, looking at Figure 6.1-5, it is clear that the central peak is considerably higher than are the other two. Although the ^{252}Cf source approximates a point source, the total gamma-ray source may be spread out by scattering in its container and in the transfer tube that guides it into place. This would result in a reduction in apparent modulation as seen in Figure 6.1-5. Another explanation is that there is some vignetting present that reduces the height of the maxima but does not decrease the depth of the minima. The actual modulation provided by this aperture is approximated by the difference in exposure level between the

central peak and the deepest valley level. The increase in modulation in the new aperture, especially in the outer zones, will result in increased contrast in the final reconstructed images.

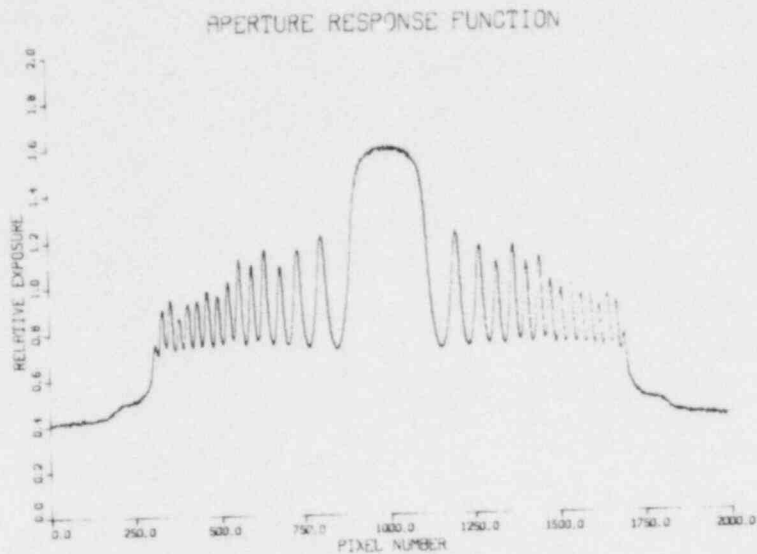


Figure 6.1-5 Densitometer Scan Across the X-ray Film (15 opaque zones between the axis and one edge)

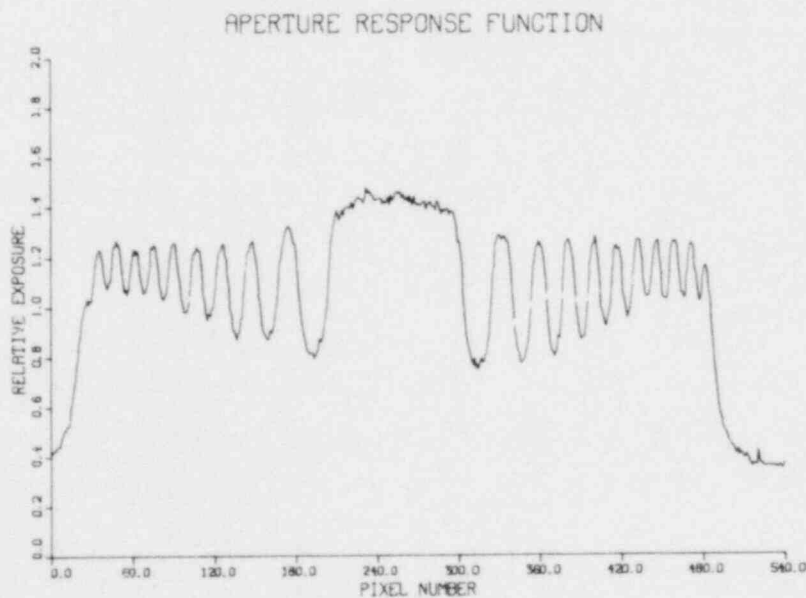


Figure 6.1-6 Densitometer Scan Across the X-ray Film (Ta Code with 10 opaque zones)

The greatest number of zones has resulted in two benefits.

- a. Because the outer zone width has remained the same yet more zones have been added, the new zoneplate has greater theoretical depth resolution.
- b. Because the new zoneplate is wider, it will have a higher solid-angle collection efficiency than the old zoneplate used in previous test geometries. This increase in signal-gathering ability will result in improved signal-to-noise ratios in the final image. This may be especially important if nonscatter background is present as is possible in the ACRR configuration.

The fact that some peaks in the outer zones of the new aperture are reduced in amplitude indicates some slight misspacing that has been hard to eliminate because of the flexibility of the vanes. This deficiency should only be of secondary importance. However, because of this shortcoming, the use of a Tungsten-copper alloy called Kennertium is being considered for future apertures. It is machinable and has a density of 18.5 g/cm^2 .

6.1.6 Assembly of Components Into the Chambers

The interior collimators and apertures were not available for fitting into the chambers until after the dry lab assembly of the system, but were inserted and aligned before the tests in the tank were conducted. The added weight may be responsible for the discovery of the chamber leaks that did not show up in the initial tests.

The active system components have been placed and aligned inside the instrumentation chamber. These included the optical support table and rails, the scintillators, lenses, image intensifiers, cameras, shields, and power supplies. These latter components require electrical cables and air hoses, both of which were subsequently run to the cable access tubes at the top of the chamber. A photograph of the chamber and closures of the cameras, intensifiers, and mirrors are shown in Figures 6.1-7, 6.1-8, and 6.1-9.

POOR ORIGINAL

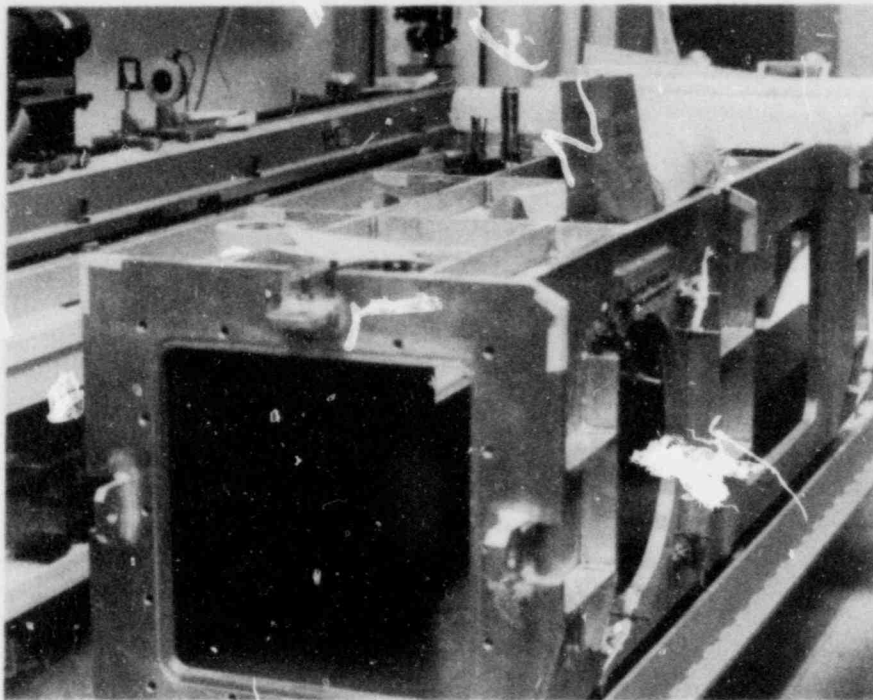


Figure 6.1-7 Instrumentation Chamber: Cameras, Intensifiers, and Mirrors - No. 1

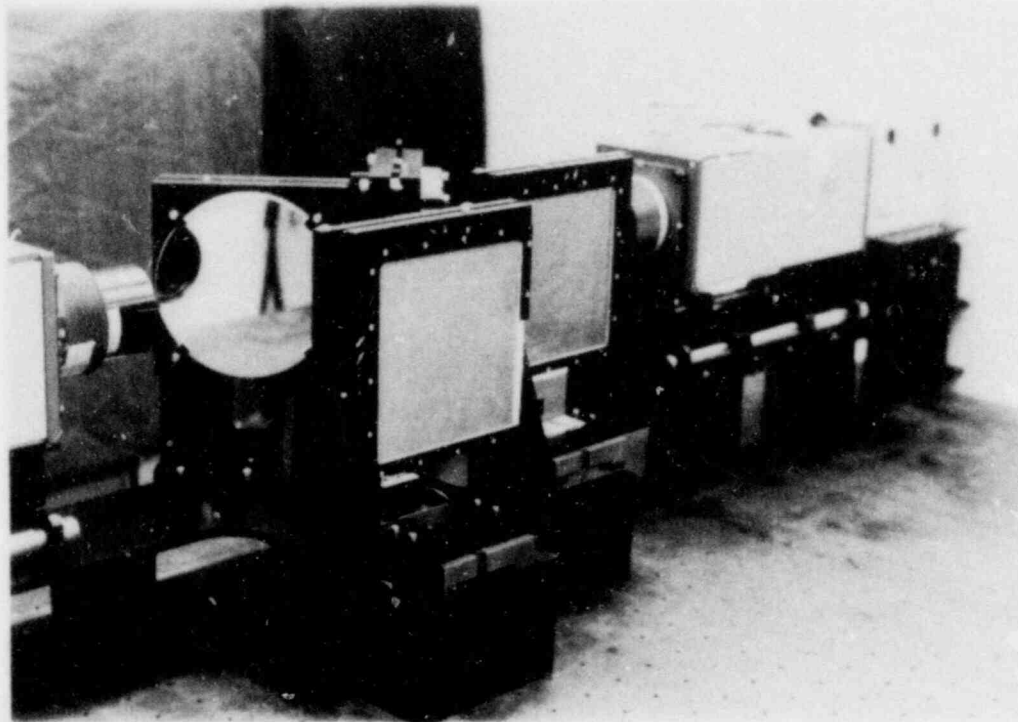


Figure 6.1-8 Instrumentation Chamber: Cameras, Intensifiers, and Mirrors - No. 2

POOR ORIGINAL

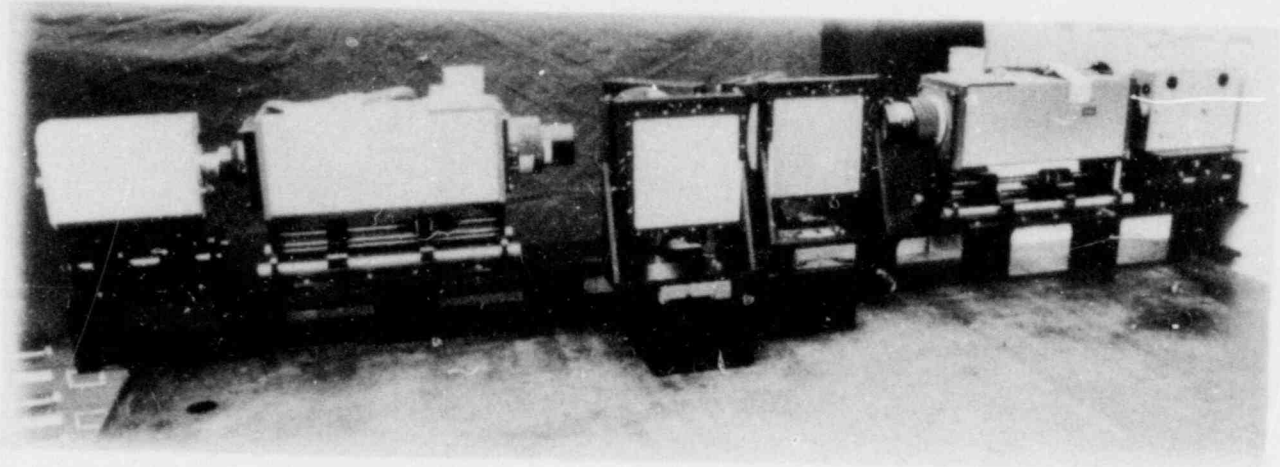


Figure 6.1-9 Instrumentation Chamber: Cameras, Intensifiers, and Mirrors - No. 3

6.1.7 Procurement of Equipment

The manufacturer of the 10^3 frames/s cameras had continued to delay delivery. Two pin-register Campbell Redlake LOCAM's were procured as backup. These operate at only 500 frames/s, but are otherwise the best available. The first of the two final medium-response image intensifiers (10^{-4} s decay time) has also been received. Two new TropeI lens systems with a higher demagnification factor (~ 4.4) have been ordered. These will permit the scintillator image to be focused into the central, more linear region of the intensifier field of view.

6.1.8 Requirements for Load-Bearing Components in the ACRR

The ACRR committee has recently defined a preliminary set of guidelines that will govern the design of components to be used for hoisting those fuel-motion-system parts that will be lowered into the reactor tank. These are subject to change in the future, but may serve as a framework for a generic set of rules now.

- a. Each lifting component must be certified and load-tested to 2.5 times the weight of the object(s) to be lifted. This will be the case no matter how many other components will be sharing this weight in parallel. (These components include lifting lugs, clevises, shackles, turnbuckles, rings, hooks, cables, straps, frames, etc.)

- b. There should be at least two such components or chains of components in parallel if the above criterion is the only one to be met.
- c. If the experimental situation demands that at some point only one component can be used to hold the object, then it must be tested and otherwise certified to carry four times the weight. The use of this component must also be separately approved by a safety committee.
- d. The component must have a safe working load of twice the weight of the object. For example, if a clevis is to be used to carry a 1000-lb weight, it must be certified as tested at 2500 lb, or it must have a calculated yield strength of 10 000 lb.

Some discussion occurred about applying criterion c to each carrying point on the object for which a break in the suspension would cause severe swinging or movement. No final decision has yet been made on that proposed condition.

6.1.9 Summary

The system is being assembled within the reactor and no serious problems have been identified. However, the assembly has proceeded more slowly than expected and more minor modifications than were expected have had to be made. The leak problem has delayed the schedule by approximately one month. This delay will not impact the overall program schedule.

6.2 Large-Scale Test Assessment (J.S. Philbin, 4452; W.E. Nelson, SAI; Jack Tills, CNSC; P.S. Pickard; 4424)

Large-scale test assessment efforts are directed toward the definition of an experimental program for providing test data having the potential to confirm analysis and conclusions drawn from smaller scale CDA experiments. These considerations include the use of existing facilities as well as the definition of requirements for new facilities or modifications of existing ones.

6.2.1 Heat-Transfer and Fuel-Element Design Considerations

A project for fuel-element design for the gas-cooled-reactor concept was initiated during this period. The complete design effort will include literature review, computational correlation, and design optimization.

6.2.1.1 Mechanical Design Considerations

The fuel elements for a gas-cooled research reactor with full-length capability must be arranged in a fairly tightpacked array in order to yield large fuel-element volume fractions (~ 0.75) for minimum reactivity requirements. Clad thickness and bowing considerations for these extra-long elements will also be important in choosing an appropriate packing fraction.

Intermediate grid spacers between the top and bottom grid plates and cladding strength can be chosen to simultaneously ensure the appropriate packing fraction and eliminate interference from adjacent fuel elements due to bowing. Specification of these parameters is in progress.

Figure 6.2-1 specifies the clearance between adjacent cylindrical fuel pins in a hexagonal array for a given fuel-element diameter and fuel-element volume fraction. The information in this family of curves can be obtained into a single curve by plotting a dimensionless ratio (separation distance divided by the fuel-element diameter) as a function of the fuel-element volume fraction (Figure 6.2-2).

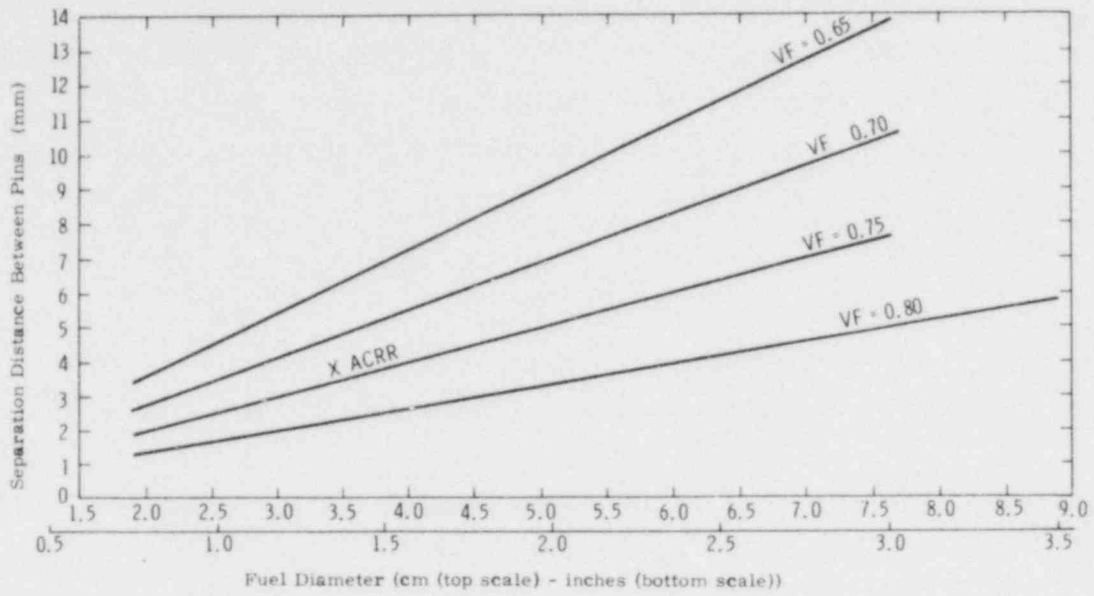


Figure 6.2-1 Clearance Between Adjacent Cylindrical Pins

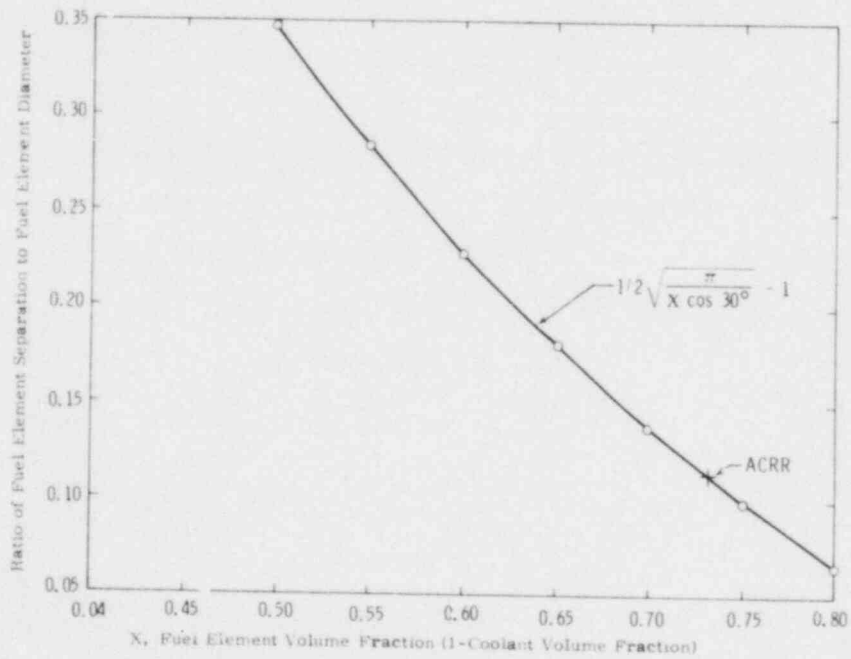


Figure 6.2-2 Dimensionless Representation of Fuel-Element Pitch Requirement

The separation distance between elements for a given fuel element and volume fraction can be increased by changing the fuel element from a cylindrical to a hexagonal shape. Large cans of fuel elements resulting in a very small coolant volume fractions (less than 0.10) are also possible if steady-state operational requirements are of very low power or of short-time duration (i.e., enthalpy limited). This is the situation in the STF-reactor design where the coolant volume fraction in the converter is only 0.06 and the reactor is to be run only as an adiabatic machine.

6.2.1.2 Heat-Transfer Analysis and Reference Calculations

The thermomechanical design effort during this quarter has involved assembling and checking out a computer-code library that can be used to calculate transient or steady-state temperature and stress profiles in candidate High Fluence Fast Pulsed Reactor (HFFPR) fuel elements. This library includes the STEALTH⁶⁻¹ family of one- and two-dimensional codes for coupled thermomechanical response, and the ONEDIM⁶⁻² code for one-dimensional nonlinear heat transfer. Each code in the library has been modified to treat specific design problems associated with the HFFPR fuel elements. STEALTH has been updated to treat thermoelastic-material response and gas-gap closure. The ONEDIM code has been expanded to include stress computation using approximating analytical stress/strain equations for fuel and clad response. In addition, a new gap model has been programmed into ONEDIM to account for gap closure.

The requirement for two temperature/stress codes, STEALTH and the expanded ONEDIM, reflect the need in a design analysis for both detailed and parametric study. In general, a detailed study is conducted using the more complex code in which simplifying assumptions are kept to a minimum (i.e., STEALTH-2D). Computation time for the complex code restricts the number of element designs that can be investigated. For the parametrics, a code such as the modified ONEDIM is well suited; it is a fast-running code that has been put on the NOS time-sharing system for interactive running.

In the thermomechanical studies, there are two main areas of concern following a reactor pulse: clad temperature and fuel/clad hoop stress. For example, in the case of a gas-cooled HFFPR, the relatively low heat-transfer coefficient means that, except for the very-high-flow velocities, clad temperatures will tend to equilibrate at the fuel temperature before appreciable cooling can take place (Figures 6.2-3 and 6.2-4). In such cases, methods for improving heat transfer and/or insulating the clad must be investigated. One of the main thermomechanical design goals for the gas-cooled HFFPR is to provide a fuel-element design that will maximize fuel-volume fraction, and operate below maximum thermal and stress limits for all anticipated transient and steady-state conditions.

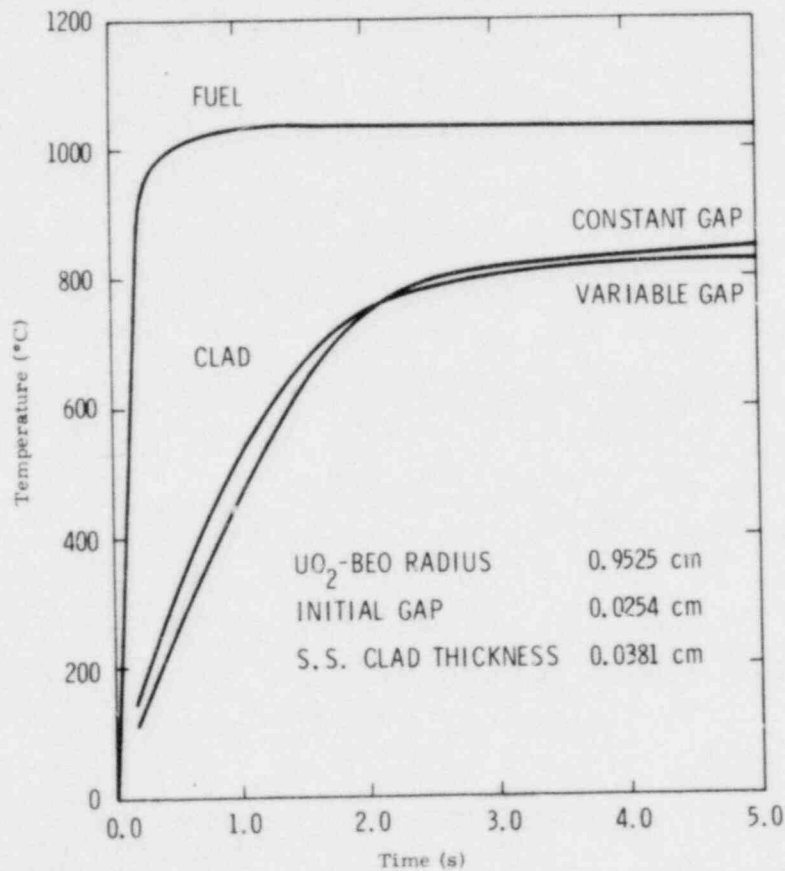


Figure 6.2-3 Centerline Fuel and Clad Temperature for 3.00 Pulse, Heat-Transfer Coefficient = $3.119 \text{ ergs/cm}^2\text{-s-}^\circ\text{C}$, Velocity of He Flow $\sim 1.219 \text{ cm/s}$. (Based on a core average fuel element)

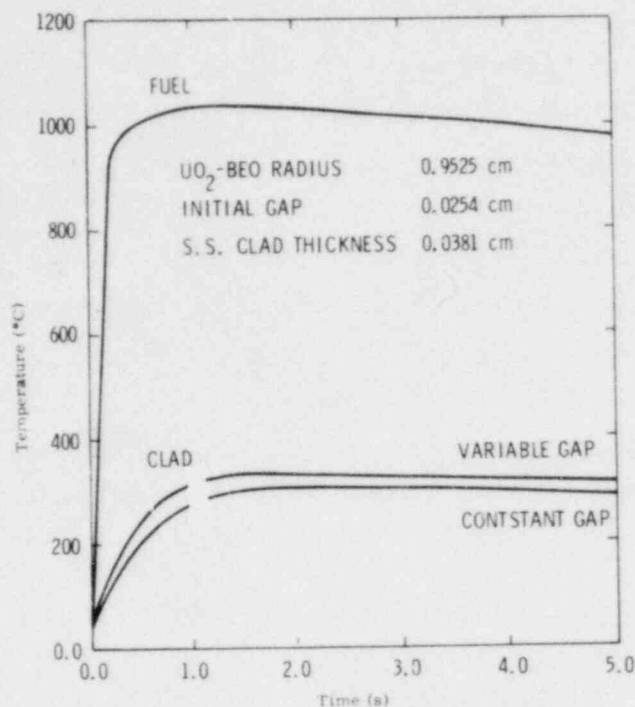


Figure 6.2-4 Centerline Fuel and Clad Temperature for \$3.00 Pulse, Heat-Transfer Coefficient = $3.119 \text{ ergs/cm}^2\text{-s-}^\circ\text{C}$, Velocity of He Flow $\sim 1.828 \text{ cm/s}$. (Based on a core average fuel element)

6.2.2 Neutronic Analysis of Large Gas-Cooled Driver Cores

A study to determine the sensitivity of maximum energy deposition in the test section as a function of the eigenvalue of the entire driver/test section in calculated assemblies was initiated but results are too preliminary to report at this time. This study is being done with a one-dimensional model using DTF-71.

Work on the neutronics evaluation of a high volume-percent Be₂C fuel (70 v/o Be₂C; 5 v/o UC₂; and 22 v/o graphite) has been dedicated to the production of cross sections for the fuel and to the development of R-θ models that include an outer cavity, radial fuel-motion-detection slots, and six control-rod locations. Initial work on kinetics modeling of the Be₂C and BeO tall-core systems has also been done. Reactivity time histories for LMFBR accident scenarios are being developed for evaluation in the PK1D and SAK kinetics codes.

Development of the R- θ models has been carried out concurrently for both BeO and Be₂C systems. Normalization of the R- θ model to the R-Z TWOTRAN II code was accomplished through the use of zone- and energy-dependent DB² terms (defined later). Table 6-2 is a comparison of some of the R-Z and R- θ models. The agreement between the R-Z and R- θ models for k_{eff} is an ~1% difference. The difference in energy deposition is ~8%.

Table 6-2
Comparison of R-Z and R- θ TWOTRAN-II Models

Geometry	Reactor Description	k _{eff}	E _{max} (j/g)	Edge to Center- line Ratio
R-Z	BeO/UO ₂ = 50/1, 45% E 35.56-cm inner cavity; no outer cavity. Cadmium fil- ter of 0.01 atoms/b-cm x 1 cm wide	1.12	1904	1.21
R- θ	Same as above	1.13	2069	1.22
R- θ	Same as above, but with 60-cm-wide outer cavity	1.12	2076	1.23
R-Z	Be ₂ C-UC ₂ -Graphite 70 v/o Be ₂ C; 5 v/o UC ₂ ; 22 v/o graphite; 50% enriched U. 35.56-cm inner cavity; no outer cavity. Cadmium fil- ter of 0.1 atoms/b-cm x 1 cm wide	1.12	1060	1.11
R- θ	Same as above	1.13	1124	1.11
R- θ	Same as above, but with 50-cm-wide outer cavity	1.12	1197	1.10

The energy and zone dependent DB² terms are calculated from data available in the macroscopic edit of TWOTRAN II. The DB² terms are calculated as:

$$DB^2 = \text{Leakage/Flux} \quad (6.1)$$

The axial effect of the DB^2 terms may be computed by summing the vertical-zone leakage and dividing by the flux for the zone. The DB^2 terms are then entered into TWOTRAN II as pseudomacroscopic absorption cross sections. They are then added into the mixture for the appropriate zone.

Care must be exercised in using the DB^2 terms if there are energy groups having a very low population; e.g., thermal groups in a cadmium filter. The extremely low population may lead to the calculation of comparatively large DB^2 terms for these groups and, if the terms are negative (leakage into the zone), one may have a substantial neutron source in that region. If the source is large enough, this will cause instabilities in the model. It is then necessary to zero out the DB^2 terms for that particular zone in order to stabilize the model.

6.3 ACRR Status (T.R. Schmidt, 4451)

In October, work was performed on the ascension-to-full-power and pulsing tests (ATPs) with the completion of parts of ATP 1, 7, 11, 12, and 14. The argon-purge system for the experiment cavity was completed since it was modified to accommodate the electrical conduits for the instrumentation patch panels that run in the same raceway in the floor. The base plate and the shield-support gussets for the fuel-motion-detection system were installed in the ACRR tank.

During November, tests were initiated on 15.24-cm (6-in.) stacks of BeO fuel to examine its behavior at temperatures up to 2273 K (2000°C). Forty-nine pulses were given to several fuel stacks. The core configuration was adjusted by adding seven elements on the core flat toward the radiography tube location. Ten maximum pulses were given to a fresh-fuel element to be later destructively examined. The core was slotted, requiring the removal of 13 fuel elements and transient rod A.

In December, after several checks of fuel-motion hardware in the slotted core and various reactivity measurements, the core was returned to its

unslotted configuration. Six arming, fusing and firing (AF&F) systems were exposed and 20 shots were given to UO_2 -BeO experiments. The reactor was shut down on the 18th in order to paint the high bay over the end-of-year holidays.

In January, several irradiations were performed for weapon components and outside contractors. In addition, the series of UO_2 -BeO fuel irradiations in the cavity were continued. Trial-fittings in the loading tubes were made for the data acquisition system of the aerosol experiment; several days were devoted to check-out and nondestructive testing of the fuel-motion detection hardware. The heat transfer in one of the instrumental fuel elements started changing, indicating that air was leaking in. This apparently faulty fuel element was replaced with a spare instrumented element and additional instrumented elements were ordered.

During February, most of the activity involved the fuel-motion-detection system. The in-tank shielding was completed and several steady-state irradiations were performed with and without a fuel pin to determine backgrounds and signal-to-noise ratios. The new lower section of the neutron radiography tube was manufactured and tested. Assembly of the tube was completed and it will be installed early in April. Initial steps were taken to order the higher reactivity-worth transient rods. The current rods are worth \$2.95 and the new rods will be worth approximately \$4.25. A second set of two rods will be ordered later for use with a slotted core as soon as a standard slotted core is developed.

In March, the slotted core was reconfigured to reduce the imbalance in reactivity-worth of the control and transient rods. The neutron radiography tube was installed. The standard core was also reconfigured to facilitate the changeover to the slotted core and to minimize the influence on core safety and control instrumentation. The core was then recalibrated and dosimetry was performed for upcoming weapons and PBE experiments. PBE-13S was performed.

Summarizing, all of the startup tests have been completed and most of the characterization of the reactor has been completed. A major use of the facility has been devoted to the fuel-motion-detection system with other users being phased in around the slotted core operations. The fuel and control systems are operating as designed without any significant problems.

References for Section 6

- 6-1 Ronald Hofmann et al, STEALTH: A Language Explicit Finite Difference Code for Solids, Structural and Thermalhydraulic Analysis, EPRI NP-260 (Oakland, CA: Science Applications Inc., August 1976; prepared for Electric Power Research Institute, Palo Alto, CA.
- 6-2 V.K. Gabrielson, B.W. Grange, and K.D. Christian, ONEDIM - A Computer Code for Solving One-Dimensional, Nonlinear Heat-Transfer Problems, SCL-DR-69-99 (Livermore, CA: Sandia Laboratories, 1970).

DISTRIBUTION:

U. S. Nuclear Regulatory Commission
(380 copies for R7)
Division of Document Control
Distribution Services Branch
7920 Norfolk Avenue
Bethesda, MD 20014

U. S. Nuclear Regulatory Commission (4)
Division of Reactor Safety Research
Office of Nuclear Regulatory Research
Washington, DC 20555
Attn: C. N. Kelber, Asst Director,
Advanced Reactor Safety Research
R. T. Curtis, Chief
Analytical Adv Reactor Safety Res, ARSR
M. Silberberg, Chief
Experimental Fast Reactor Safety
R. W. Wright
Experimental Fast Reactor Safety

U. S. Department of Energy
Office of Nuclear Safety Coordination
Washington, DC 20545
Attn: R. W. Barber

U. S. Department of Energy (2)
Albuquerque Operations Office
P. O. Box 5400
Albuquerque, NM 87185
Attn: J. R. Roeder, Director
Operational Safety Division
D. K. Nowlin, Director
Special Programs Division
For: C. B. Quinn
D. Plymale

University of Michigan
Nuclear Engineering Department
Ann Arbor, MI 48104

General Electric Corporation (7)
310 De Guigne Drive
Sunnyvale, CA 94086
Attn: J. O. Bradfute, Mgr
Dynamics and Safety
R. A. Meyer, Mgr
Analytical Engineering
S. M. Davies, Mgr
Conceptual Design Study

DISTRIBUTION (cont):

J. W. McDonald, Mgr
Containment & Radiological Evaluation
N. W. Brown, Mgr
Licensing & Systems Eng
M. I. Temme, Mgr
Safety Criteria & Assessments
K. H. Chen,
M/C S-54

W. E. Nyer
P. O. Box 1845
Idaho Falls, ID 83401

Projekt Schneller Brueter (4)
Kernforschungszentrum Karlsruhe GMBH
Postfach 3640
D75 Karlsruhe
West Germany
Attn: Dr. Kessler (2)
Dr. Heusener (2)

Institut de Protection (3)
et de Surete Nucleaire
CEN Fontenay-aux-Roses
B. P. 6
92260 Fontenay-aux-Roses
France
Attn: M. Tanguy
M. Schmitt
M. Cogne

Safety Studies Laboratory (3)
Commissariat a L'Energie Atomique
Centre d'Etudes Nucleaires de Cadarache
B. P. 1, 13115 Saint Paul lez Durance
Bouches-Du-Rhone
France
Attn: M. Bailly
M. Meyer-Heine
M. Penet

Centre d'Etudes Nucleaires de Grenoble
B. P. 85 - Centre de Tri
38401 Grenoble, Cedex
France
Attn: M. Costa

DISTRIBUTION (cont):

H. J. Teague (3)
UKAEA
Safety and Reliability Directorate
Wigsnaw Lane
Culcheth
Warrington, WA3 4NE
England

R. G. Bellamy
Reactor Fuels Group
AERE Harwell
Oxfordshire, OX11 0RA
England

R. G. Tyror, Head
Reactor Development Division
UKAEA - Atomic Energy Establishment
Winfrith, Dorchester
Dorset
England

Joint Research Centre (2)
Ispra Establishment
21020 Ispra (Varese)
Italy
Attn: R. Klersy
H. Holtbecker

Power Reactor & Nuclear Fuel (3)
Development Corporation (PNC)
Fast Breeder Reactor Dev Project (FBR)
9-13, 1-Chome, Akasaka
Minato-Ku, Tokyo
Japan
Attn: Dr. Mochizuki
Dr. Watanabe (2)

1100 C. D. Broyles
Attn: J. D. Plimpton, 1110
T. L. Pace, 1120
G. L. Ogle, 1125

1537 N. R. Keltner
1537 R. U. Acton
1537 T. Y. Chu
1550 F. W. Neilson
Attn: O. J. Burchett, 1552
J. H. Gieske, 1552

2150 C. B. McCampbell
3434 B. N. Yates
4000 A. Narath

DISTRIBUTION (cont):

4231 J. H. Renken
 4231 J. A. Halbleib
 4231 J. E. Morel
 4400 A. W. Snyder
 4410 D. J. McCloskey
 4420 J. V. Walker (5)
 4421 R. L. Coats
 4421 J. E. Gronager
 4421 G. W. Mitchell
 4421 J. B. Rivard
 4422 D. A. Powers
 4422 J. E. Smaardyk
 4422 D. W. Varela
 4423 P. S. Pickard
 4423 A. C. Marshall
 4423 D. A. McArthur
 4423 K. O. Riel
 4424 M. J. Clauser
 4424 J. T. Hitchcock
 4424 P. J. McDaniel
 4424 M. E. Senglaub
 4424 J. A. Sholtis
 4424 D. C. Williams
 4425 W. J. Camp
 4425 W. M. Breitung
 4425 F. Briscoe
 4425 R. J. Lipinski
 4425 M. L. Schwarz
 4425 M. F. Young
 4426 G. L. Cano
 4426 J. G. Kelly
 4426 H. L. Scott
 4426 K. T. Stalker
 4426 W. H. Sullivan
 4426 S. A. Wright
 4441 M. L. Corradini
 4442 W. A. von Rieseemann
 4450 J. A. Reuscher
 4451 T. R. Schmidt
 4452 M. F. Aker
 4723 D. O. Lee
 5500 O. E. Jones
 5530 W. Herrmann
 5534 D. A. Benson
 5800 R. S. Claassen
 5820 R. E. Whan
 5821 N. E. Brown

DISTRIBUTION (cont):

5830 M. J. Davis
5835 C. H. Karnes
5846 R. A. Sallach
5846 E. K. Beauchamp
8266 E. A. Aas
3141 T. L. Werner (5)
3151 W. L. Garner (3)
For: DOE/TIC (Unlimited Release)
3154-3 R. P. Campbell (25)
For: NRC Distribution to NTIS